ScuDo
Scuola di Dottorato ~ Doctoral School
WHAT YOU ARE, TAKES YOU FAR

Doctoral Dissertation
Doctoral Program in Material Science and Technology (33rd Cycle)

Laser Powder Bed Fusion of AlSi10Mg+4Cu and AlSi10Mg alloys

Federico Bosio

* * * * * *

Supervisors
Prof. Mariangela Lombardi, Supervisor
Ass/Prof. Aijun Huang, Co-Supervisor

Doctoral Examination Committee:
Prof. E. Bassoli, Referee, Università degli Studi di Modena e Reggio Emilia
Prof. R. Casati, Referee, Politecnico di Milano

Politecnico di Torino
March 2021

I hereby declare that, the contents and organisation of this dissertation constitute my own original work and does not compromise in any way the rights of third parties, including those relating to the security of personal data.

…………………………………..…

Federico Bosio
March 2021

Summary

Laser Powder Bed Fusion (LPBF) is one of the most used additive manufacturing techniques, which enables the production of metallic parts by selectively melting consecutive layers of powder according to 3D model data. Apart from its inherent advantages related to the high design freedom, customized manufacturing and limited material waste, LPBF also has several barriers that prevent this technique from entirely succeeding in the manufacturing market. On the one hand, the rapid solidification induced by laser heating opens the possibility to develop new alloys specifically designed for LPBF with performances superior to the conventional counterparts. Nevertheless, today, only a limited palette of metallic alloys is available in the marketplace. On the other hand, the low productivity of LPBF results in the high production cost of additively manufactured parts. In particular, this limited productivity is often related to the small size of a producible component. Therefore, the overall purpose of the thesis is to help overcome the above mentioned LPBF barriers.

The first study of this thesis reports the experimental results on a novel AlSi10Mg+4Cu alloy processed by LPBF. In this work, 4 wt.% of Cu powder was mixed with a pre-alloyed AlSi10Mg powder to improve hardness and strength of AlSi10Mg. Afterward, AlSi10Mg+4Cu alloy was directly synthesized *in-situ* by exploiting the intense laser energy during LPBF manufacturing. Single scan tracks were then used as a tool to quickly evaluate the alloy processability. Once defined the suitable process window by analyzing scan tracks characteristics, the chemical composition, the microstructure, and the mechanical properties of as-built and heat-treated samples were investigated. A T5 protocol was used to heat-treat as-built samples with the purpose of fully exploiting the alloy precipitation potential generated upon the rapid cooling.

Experimental results showed that AlSi10Mg+4Cu alloy was successfully consolidated by LPBF, exhibiting a densification level up to 99.16 % after the process parameters optimization. Moreover, the overall chemical composition of the printed alloy reflected the theoretical one thanks to the mixing effect of the local convective flows arising during melting. However, local segregations of Cu were found owing to the different physical properties of the starting powders creating local inhomogeneities, which in turn resulted in localized hardness peaks. Generally speaking, the addition of Cu was effective in improving the hardness of AlSi10Mg. This was mainly due to the enhanced contribution of super-saturated solid solution and precipitation strengthening mechanisms to the total strength of the alloy. The microstructure morphology of as-built specimens revealed the presence of fine α-Al cells surrounded by a dual eutectic formed by Si and ϑ-Al$_2$Cu phases. Direct aging enabled the solutes diffusion and a progressive hardening without affecting the fineness of the Al-Si/Al$_2$Cu eutectic network. The maximum hardness increment was achieved upon 1 h at 175 °C, and the corresponding microstructure was constituted by a mix of $\theta''/\theta' + \theta$-Al$_2$Cu precipitates and Si phase. As for the hardness, as-built and directly aged tensile samples returned superior yield and ultimate tensile strength values compared to AlSi10Mg counterparts. Finally, the fracture mechanism of AlSi10Mg+4Cu was characterized by ductile-brittle behavior.

The second study of the thesis aimed at solving the issues related to the production of large AlSi10Mg components by adopting the heated building platform strategy. Two main aspects were tackled. On the one side, the inevitable presence of internal residual stresses that can cause the job failure during long printing time and, on the other side, the *in-situ* aging of the processed alloy above the heated platform. To this end, the platform temperatures preventing cracks and distortions were firstly determined. Then, the *in-situ* aging behavior was investigated for samples processed under various platform temperatures and holding times. Our results revealed that the platform temperatures of 150 and 200 °C can effectively prevent cracks and minimize distortions. Besides, using 150 °C, AlSi10Mg samples can reach the peak hardness with a holding time less than 13 h. In comparison, samples produced with a holding time longer than 13 h at 150 and 200 °C showed an obvious over-aging response and, thus, lower hardness. However, such hardness impoverishment was recovered by using a T6-like heat-treatment.

Acknowledgment

I would like to acknowledge the Department of Applied Science and Technology (DISAT) of Politecnico di Torino for my PhD project's financial support and for the third-level PhD lectures. My deep gratitude goes to the Monash Centre for Additive Manufacturing (MCAM) in Melbourne, Australia, for the stimulating scientific collaboration carried out during this PhD project.

I would like to express deep gratitude to my Supervisor, Professor Mariangela Lombardi, for her constant scientific and financial support to this thesis's research works and her positive attitude when things get hard. I learned a lot from her work ethic and management skills. I am also grateful for her moral encouragement and the numerous on-line meetings we had when I was overseas.

Special thanks go to my boss at MCAM, Professor Aijun Huang, for having me with his research group for more than one year. At MCAM, I could experience a completely new world and work approach. This has been one of the most important experiences I had during my PhD path. My deep gratitude also goes to Prof. Xinhua Wu and all the MCAM's colleagues for their support. Special thanks are dedicated to Mr. Haopeng Shen for the fruitful cooperation and valuable scientific advice. Moreover, I would newly express my heartful gratitude to Aijun for his assistance and empathy during the Covid19 outbreak. I will certainly keep in my soul this great experience! Thanks.

My gratitude especially goes to Prof. Diego Manfredi for his valuable scientific suggestions and his passion for the Materials and Engineering Science. He has definitely been one of my major inspirational guides in the additive manufacturing research world.

I would like to thank all the Professors and colleagues who with I've worked through these years, especially: Prof. Paolo Fino, Prof. Daniele Ugues for having introduced me to the academic research at the end of my Master thesis, Prof. Livio Battezzati for his charism, Emilio for his passion and competence in metallurgy, Hamed for having been a point of reference during scientific paper's drafts, and 'my friend' Andrea for the scientific discussion we had during our coffee breaks. A final 'thank you' goes to Alberta and Silvia.

Finally, from the bottom of my heart, I would love to thank my parents, Maria Grazia and Valter, for their unconditional love. My nonna and my cousin's family. My close friends, Alessandro, Francesca and Andrea, and all the persons indirectly involved in this experience.

To my grandad and my
loving parents

Contents

List of Tables

List of Figures

Preface

I. Additive Manufacturing

In recent decades, a novel manufacturing route has been flourishing in the industry, paving the way to a new manufacturing era, also known as the 'third industrial revolution'[1]. The term 'Additive Manufacturing' (AM) refers to a family of manufacturing technologies creating three-dimensional objects in a layer fashion manner. The real breakthrough brought by AM is the new concept of manufacturing. In fact, contrarily to the traditional methods of manufacturing where objects are produced in molds and then finished by subtracting the excess material, AM is 'a process of joining materials to make objects from 3D model data, usually layer upon layer' in an additively way [2]. Outside the industry and research, the term AM is used interchangeably with 3D printing, although the former refers to the manufacturing of metallic components, and the latter refers to the production of polymers/non-metallic objects.

The additively manufacturing process begins with the creation of a digital 3D CAD model of the object to be built. Alternatively, the desired object geometry can be retrieved by reverse engineering techniques, such as computer tomography. Once the CAD model is created, it must be converted into a .STL file, which provides instructions of how to slice the object geometry in several individual layers. Afterward, the printing machine progressively builds the three-dimensional object layer by layer, following the .STL file specification. After manufacturing, the printed objects have a 'near net shape', minimizing the post-processing operations, which rely on the final application and the used AM technique [3].

Over the past decades, materials that have been processed by AM techniques varied from polymers to ceramics and metals. Initially, the first AM technique developed in the early 80s, known as stereolithography (SL), foresaw the use of photocurable polymers [1]. Nearly a decade after, 3D Systems, widely renowned as one of the primary producers of 3D printing systems, commercialized a novel technology called Selective Laser Sintering (SLS) [4]. By this technique, a powder bed of polymer powders was selectively sintered using a laser energy source. The advent of AM techniques making use of metals took place shortly thereafter. In 1995, EOS Gmbh introduced into the market the first Direct Metal Laser Sintering (DLMS) system, by which it was possible to sinter a metal powder bed directly [5]. Since those days, Metal Additive Manufacturing (MAM) has grown rapidly, leading to the development and commercialization of various MAM techniques. According to the ASTM Standard F2792-12a, MAM technologies fall into two main classes, namely Directed Energy Deposition (DED) and Powder Bed Fusion (PBF) [2].

DED is an additive manufacturing process where a focused thermal energy source is employed to melt metal powders, which are blown onto the building platform using feeding nozzles [6]. Numerous DED systems have been developed over the years. They have been commercialized by the name of Direct Metal Deposition (DMD), Direct Light Fabrication (DLF), and Laser Engineered Net Shaping (LENS^{TM}). DED technologies have been mostly used for repairing, cladding, and re-manufacturing of damaged components.

In the PBF process, a thermal energy source selectively melts the regions of a powder bed [7]. In this regard, PBF technologies mainly differ for the energy source employed to melt the metal powder bed. Based on the energy source, PBF technologies have been classified in Electron Beam Melting (EBM) and Laser Powder Bed Fusion (LPBF). The EBM process was patented and commercialized by Arcam AB in 2000 and makes use of an electron beam energy to fuse the material. Differently, the LPBF technique, which is the process used in the work of the thesis, utilizes focused laser energy to consolidate metal layers and create the 3D object progressively. Nowadays, LPBF plays a leading role in the market and, therefore, several LPBF machines were commercialized over the years. It is worthwhile to mention that, based on the machine manufacturer, the LPBF process is referred to a different patent, as shown in Table 1.

Table 1 The leading manufacturers of LPBF systems and the related LPBF process nomenclature.

Company	LPBF Process
EOS GmbH	Direct Metal Laser Sintering (DMLS)
Renishaw	Laser Powder Bed Fusion (LPBF)
Concept Laser	LaserCUSING®
Realizer	Selective Laser Melting (SLM)
SLM Solutions GmbH	Selective Laser Melting (SLM)
Trumpf	Laser Metal Fusion (LMF)
3D Systems	Direct Metal Printing (DMP)

II. Advantages and applications of AM

Thanks to the additive nature of such technologies, AM can offer several advantages compared to the conventional casting processes. The principal AM advantages are briefly summarized below:

- *Design freedom*. AM opens new possibilities to design lightweight objects with virtually unlimited complexity and improved functionality, such as internal channels or lattice structures. Moreover, monolithic parts can be directly manufactured without the need for joining or post-process assembling.

- *Limited material waste*. AM offers the possibility of manufacturing parts with a 'near-net-shape', thus reducing the material waste and limiting the post-process steps as well as the time-to-market and production costs.
- *Customized manufacturing*. Since AM requires a digital model of the part to be built, it is possible to rapidly adapt the component design modifying the digital model according to the customer specifications.

Hence, due to the remarkable advantages of AM technologies, additive manufacturing has expanded its applications across various industries over the last decades [8]. Manufacturing companies have produced, among the others, AM parts for health, aerospace, automotive, and energy applications (Fig. 1).

The health sector has experienced a growth of 25% every year since 2009, reaching a high manufacturing readiness level in the production of dental and biomedical components [9,10]. The target products, which were produced by AM technologies so far, are mainly dental implants, orthopedic prosthesis, scaffolds, and drug delivery systems (Fig. 1a).

After the health sector, aerospace currently constitutes the second largest sector into the global AM market (16%) with a share that is supposed to reach \$1bn in 2021 [11]. A great advantage offered by AM in the aerospace sector is the opportunity of reducing the component weight, limiting the buy-to-fly ratio without sacrificing part performances. As an example, the weight of a belt buckle was reduced by 55 % after topological optimization and AM manufacturing [10]. Thus, the usage of such parts in an Airbus A380 would mean a weight reduction of 72.5 Kg, which in turn would result in a significant abatement of fuel consumption and CO_2 emissions (Fig. 1b).

The automotive industry is the third important sector in the AM market. Being this sector strictly dependent on mass production, AM technologies are not yet fully exploited. However, this field is expected to account for 20% of the total 3D printing market by 2025, with a predicted business of \$4.3 bn [12]. Nowadays, the most relevant applications of AM parts in the automotive sector are for high-end value cars used in motorsport (Fig. 1c).

The energy sector has been viewed as one of the most promising application fields for AM. In fact, the global turbine market for energy applications is expected to be \$191.87 bn in 2020 [13]. Among all the benefits offered by additive manufacturing, AM processes represent a fast solution for repairing damaged turbines or blades. Also, the full design freedom of AM allows the production of turbine blades (Fig. 1d) with complex internal structures, which provide excellent performances at extreme working temperatures.

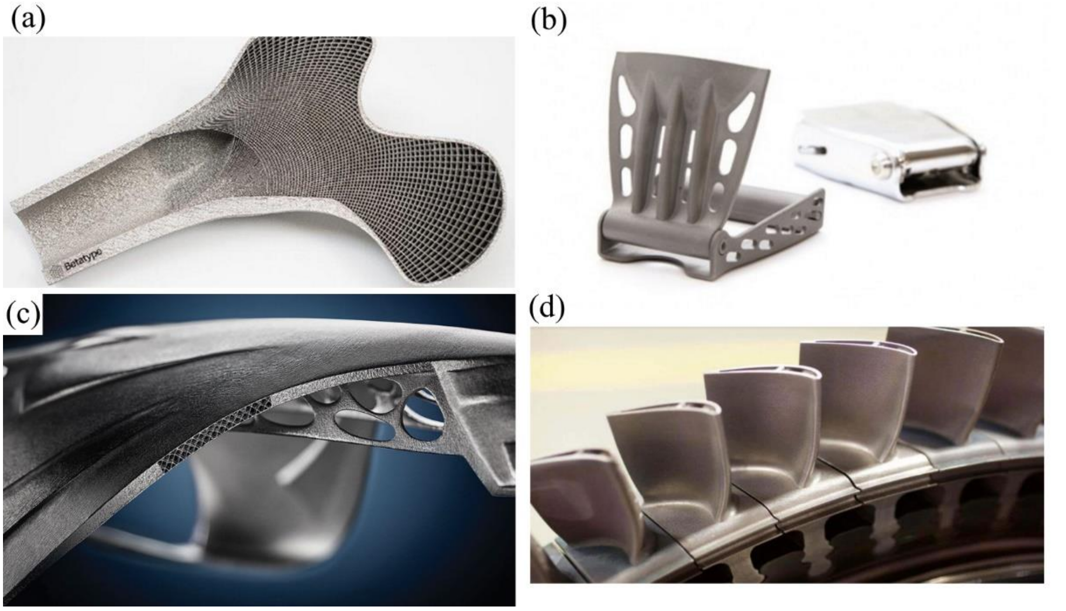

Fig. 1 Selection of printed 3D parts used for (a) bio-medical, (b) aerospace, (c) automotive and (d) energy applications. In detail: (a) orthopaedic implant [14], **(b) belt buckle** [15], **(c) car wing** [16] **and (d) gas turbine blades** [17].

III. Barriers and challenges of AM

Although the advantages mentioned above, AM also has several barriers that prevent additive processes from entirely succeeding in the manufacturing market. Regarding this, in 2014, renewed experts of AM have defined the AM roadmap in Europe to pin down the significant barriers and establish future research challenges for the global AM development [18]. The principal AM barriers to overcome were defined within the strategic research agenda of Ref. [18], and are summarized as follow:

1. *Limited material palette*. There is the need to develop materials specifically tailored for AM processes with performances similar or superior to the conventional counterparts. As an example, nowadays, only a limited number of metallic alloys is available in the marketplace for AM, such as titanium, nickel, steel, and aluminum alloys, and few systems reached a high readiness level (TRL 7-9) [19]. The cause of this was found to be the high lead time for the development and testing of new materials [20]. As suggested by Bourell et al. [21], quick screening methodologies would be necessary to rapidly answer why some materials are processable with AM, and some are not.

2. *Low productivity*. AM is advantageous over conventional manufacturing processes when producing a limited number of parts of high complexity. However, the layer-wise nature of AM often results in a very slow build rate and limited productivity [18]. As a consequence of this, AM becomes disadvantageous in case of higher volume production. A further aspect limiting the AM productivity is

the maximum size of a producible component, which depends on the building chamber size. The limited productivity is, thus, one of the major causes of the high production costs related to AM parts. Machine producers and researchers should step up their efforts on this aspect to make AM attractive also over large volume production.

3. *Poor process control and repeatability*. In AM, the possibility to achieve predictable and replicable operations is quite critical since these technologies have several process parameters to be tuned [18]. In line with this, the interchange-ability of process parameters between different AM machines is quite critical as well. In fact, once a set of process parameters is optimized for a specific material-machine system, a new process optimization must be performed when changing AM machine, wasting machine time and material.
4. *Improvement of material recycling*. Research efforts on improving the material recycling/reuse would be especially appreciated in metal AM. In fact, the powder cost is the second largest cost index associated with the production of metal AM parts [22]. AM experts and technicians are called to develop strategies for recycling material, considering for example the powder reuse or the atomization of end-of-life parts for the production of AM feedstock.

In conclusion, the depicted AM scenario indicates that the major research opportunities rely not only on the technology and production aspects but also on the used materials. In particular, the development of materials specifically designed for AM is a challenge of current interest both in academic and industrial areas. Only by expanding the material palette of AM, indeed, it would be possible to fully exploit the market prospects of AM in various industrial sectors.

IV. Research objectives

The overall goal of this Ph.D. project is to contribute to overcoming some critical AM barriers. On the one side, the thesis focusses on the development and characterization of a novel aluminum alloy, thus helping to expand the AM material palette. On the other side, the work deals with the production of large-scale components made of aluminium. This latter part of the thesis provides practical recommendations for improving the production of large aluminum components by AM.

Due to the different topics addressed in this dissertation, the results of this thesis are divided into two sections. The former section covers the development and characterization results of a mixed AlSi10Mg+4Cu alloy, which have been conducted at the Integrated Additive Manufacturing (IAM) center at Politecnico di Torino. The latter section on the production of large aluminum parts presents the results of the experimental activities performed during the visiting period at the Monash Centre for Additive Manufacturing (MCAM) in Melbourne, Australia. In both experimental projects, the Laser Powder Bed Fusion (LPBF) process was used to manufacture the aluminum samples.

IV.I Section I: the development and characterization of a mixed AlSi10Mg+4Cu alloy for LPBF

Aluminum alloys are a class of materials with a high strength-to-weight ratio, making these alloys suitable for automotive and aerospace applications [23]. Nevertheless, the aluminum alloys currently processed by LPBF are relatively few (i.e., AlSi10Mg, Al12Si, AlSi7Mg), and they were originally designed for foundry techniques [24]. Therefore, the resultant performances of these alloys are often mediocre compared to the ones achievable by fully catching the opportunities offered by the LPBF rapid solidification.

For this reason, it was decided to add 4 wt.% of Cu to an AlSi10Mg alloy in order to improve the hardness and strength of AlSi10Mg. To this aim, Cu powder was mixed with a pre-alloyed AlSi10Mg powder and the AlSi10Mg+4Cu alloy was directly synthesized *in-situ* during manufacturing. Single fusion lines of AlSi10Mg+4Cu, also known as Single Laser Tracks (SSTs), were used as a tool for a quick evaluation of the alloy processability. Once defined the optimum process parameters by SSTs analysis, the microstructure and mechanical behavior of as-built and heat treated bulk samples were investigated.

The research objectives of this section are:

- To strengthen the base AlSi10Mg alloy by adding 4 wt.% of Cu.
- To exploit the peculiar characteristics of the LPBF process for the *in-situ* synthesis of a mixed AlSi10Mg+4Cu alloy.
- To quickly assess the processability of the alloy and determine the main process parameters through SSTs evaluation.
- To study the microstructure, chemical composition, and mechanical properties (i.e., hardness and tensile behavior) of the processed alloy.
- To explore various heat-treatment strategies for AlSi10Mg+4Cu alloy.

IV.II Section II: the production of large aluminium components by LPBF

The manufacturing of large scale components of aluminium involves critical challenges to solve before printing. In this section, two main aspects will be tackled. On the one hand, it is well established that the rapid solidification of LPBF induces internal residual stresses, which in turn may lead to cracks and support distortions, and eventually to the job failure [25]. Thus, considering the high printing time required to produce large components, this is a crucial aspect to be considered before manufacturing. On the other hand, one has to face the age hardening nature of the processed Al alloy, i.e. AlSi10Mg. Indeed, when an heated platform is used to alleviate the internal residual stresses over long printing time, a possible *in-situ* aging can be induced [26]. Therefore, the research objectives of this section are:

- to identify the platform heating temperature range able to mitigate the internal residual stresses.
- to evaluate the *in-situ* aging response of AlSi10Mg over long production times.
- to determine the holding time limit above which *in-situ* over-aging takes place.
- to explore a possible remedy to the *in-situ* over-aging by performing post-process heat-treatments.

V. Thesis structure

This thesis consists of six chapters divided in two bibliographic chapters and two results sections, according to the scheme of Fig. 2.

The content of each chapter is briefly summarized as follow:

Chapter 1 - This chapter provides a comprehensive overview on the LPBF process covering different aspects of this technology. After a brief description of the process characteristics, the LPBF process parameters are reviewed with a special focus on their effect on the densification mechanism. Then, the chapter highlights the importance of the powder feedstock on the final quality of LPBF*ed* parts, and provides a description of the physical interactions occurring between laser and powder during printing. In conclusion, the principal defects arising from LPBF are identified and discussed.

Chapter 2 - This chapter presents a literature review on aluminium alloys processed by LPBF. The chapter provides a description of microstructure, heat-treatment strategies and mechanical properties of LPBF*ed* Al alloys. A special focus is given to the development of Al alloys specifically tailored for LPBF, being one of the research topics of this thesis.

Chapter 3 - The chapter contains the first part of the results of the experimental work performed on the mixed AlSi10Mg+4Cu alloy. After a brief introduction on the challenges in the development of new alloys for LPBF, different aspects related to the AlSi10Mg+4Cu alloy, such as its processability, microstructure, chemical homogeneity and nano-hardness distribution, are addressed and discussed.

Chapter 4 - This chapter reports the second part of the experimental work on AlSi10Mg+4Cu alloy. Varied heat-treatment strategies for the developed alloy, namely direct aging solutions at different temperatures, are investigated in this chapter studying their effect on mechanical properties of AlSi10Mg+4Cu.

Chapter 5 - This chapter contains the research work conducted on the manufacturing of large components of AlSi10Mg produced by LPBF. Specifically, the influence of the platform heating strategy on both cracks/distortions formation and *in-situ* aging occurrence is discussed.

Chapter 6 - This chapter summarizes the key findings of the thesis and reports some closing remarks/recommendations for future works.

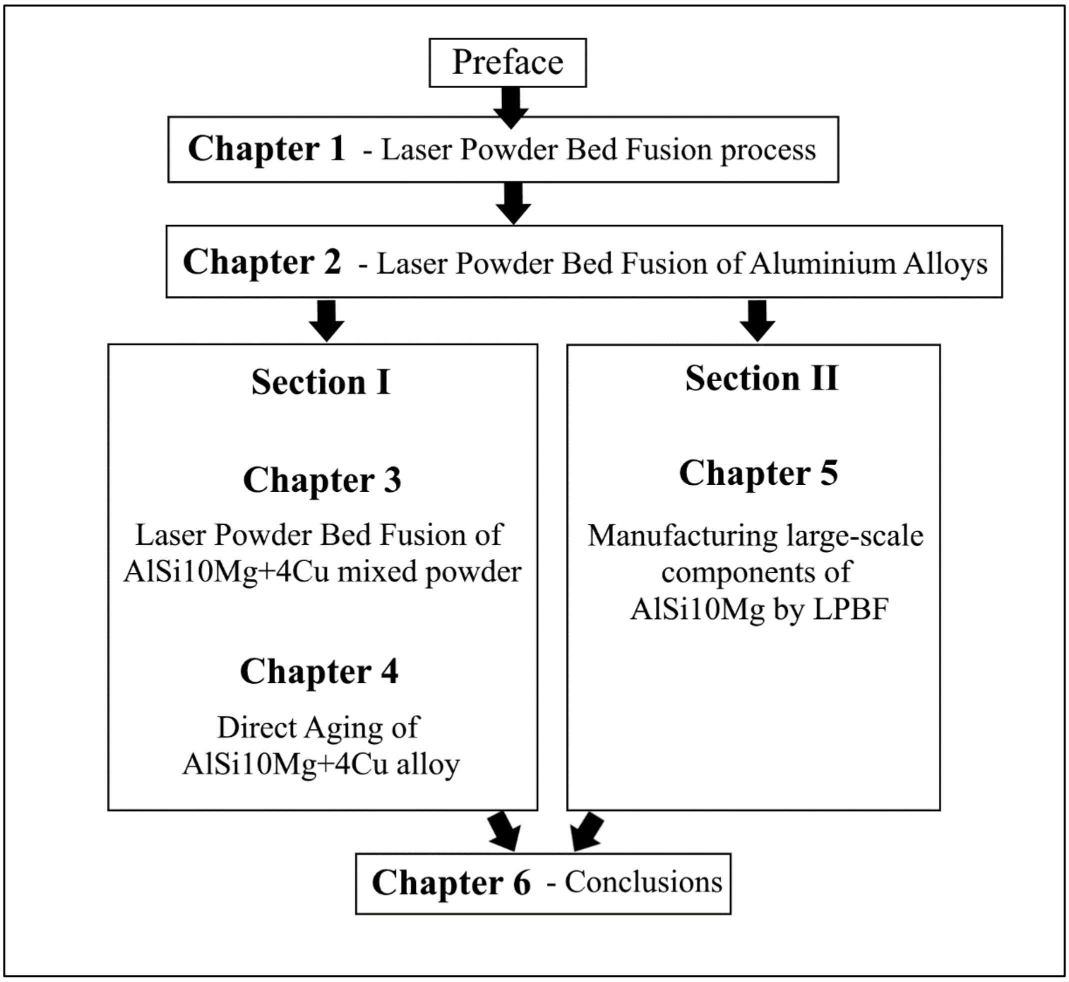

Fig. 2 Schematic representation of the thesis structure.

Chapter 1

Laser Powder Bed Fusion Process

The Laser Powder Bed Fusion (LPBF) process has been the laser-based additive manufacturing (AM) technique most extensively used by industrial companies and research labs through the last two decades. Originally referred to as Direct Metal Laser Sintering (DMLS, EOS GmbH) or Selective Laser Melting (SLM, SLM Solutions GmbH), nowadays, the technique is universally acknowledged as laser powder bed fusion as declared in the ISO/ASTM 52900:2015(E). According to the same standard, a 'powder bed fusion' technique is defined as an 'additive manufacturing process in which thermal energy selectively fuses regions of a powder bed' [27]. LBPF offers, nowadays, a powerful alternative to the conventional manufacturing processes for medium-low batch productions. Thanks to its ability to produce near net-shaped metal parts with complex geometries and high design freedom, LPBF is considered as a key enabler for reducing production time and costs, meanwhile increasing the part functionality. The final applications of the produced parts can range from aerospace to automotive and defense, from biomedical to jewelry. The most processed alloy systems are titanium alloys, Al-Si casting alloys, nickel-based superalloys, stainless steels, and cobalt-chromium alloys.

In this chapter, the LPBF technique will be firstly described starting from its technological aspects, namely the process characteristics (Section 1.1) and the process parameters (Section 1.2). Besides, the effect of the powder properties on the final quality of LPBF components is described (Section 1.3). Then, an overview on the physical interactions between the laser and powder is provided (Section 1.4). Finally, the formation mechanisms of the main defects occurring during LPBF are presented in Section 1.5.

1.1 Process characteristics

The LPBF is schematically depicted in Fig. 3. A 3D CAD model of the final components is converted in.STL file and sliced in several layers ahead of starting LPBF. At the beginning, the process uniformly lays down a powder layer of a predefined thickness over the building surface by using a powder spreading system, also known as a recoater blade. Once the first powder layer has been homogeneously spread, a focused laser beam is directed onto the laid material selectively melting the region of interest according to the .STL drawing of the building part. After that, the build platform descends of one layer thickness to allow the reacoting process and the deposition of a new layer. After completing the layer deposition, the powder is leveled and metallurgically bonded with the previous layer. The same process is repeated until the whole part will be built in a layer fashion manner along the vertical direction. At the end, the as-built part undergoes some post-processing operations, including the powder removal from the building chamber, varied heat-treatments, the clearance of support structures, and the surface finishing [28].

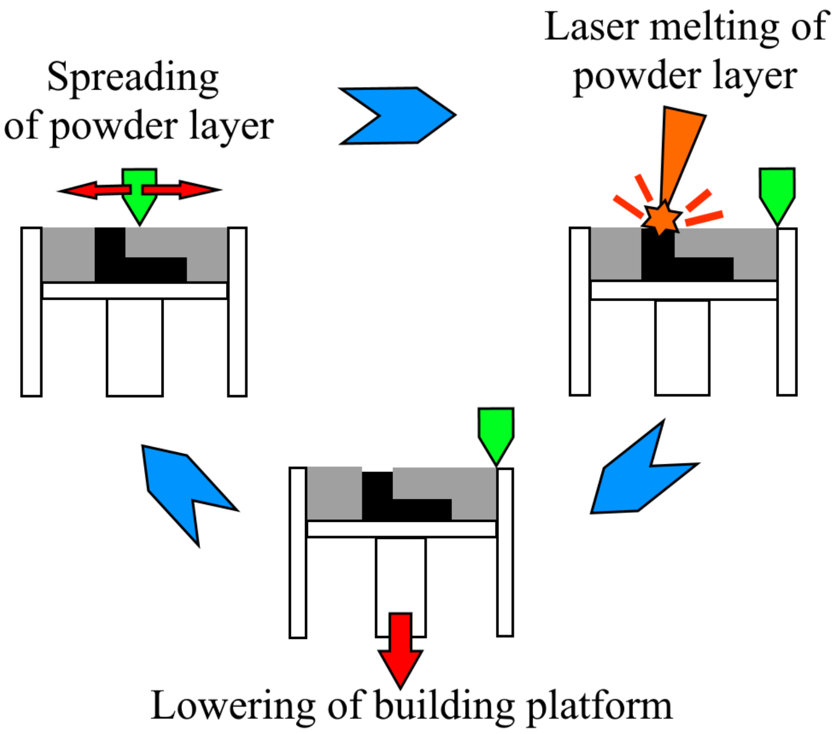

Fig. 3 Schematic illustration of the laser powder bed fusion process.

To obtain fully dense and defect-free final products, some preventive measures must be adopted throughout the LPBF process. On one side, the process chamber is purged with inert gas as Argon or Nitrogen at room temperature (RT) to constantly keep the oxygen content below 0.1 % and minimizing oxidation phenomena [29]. However, it must be noted that the residual oxygen in the process chamber promotes, otherwise, the formation of oxide layers on the powder surfaces, which in turn implies the porosity formation [23]. The inert gas also plays an important role in blowing away by-products formed from the evaporation of fine powder particles during melting (plume) or from the powder spatter [30]. On the other side, the LPBF machine can be provided by a heatable building platform that can be heated up to a temperature higher than RT to alleviate the internal residual stresses and avoid the cracking of support structures [31]. The heated building platform can also be used for pre-heating powder and releasing powder moisture before LPBF, as a general practice [32].

As far as the laser source is concerned, Nd:YAG and CO_2 lasers with a spot size of 200 – 300 μm have been employed in the earliest machines of this technology [33]. Because of their scarce melting efficiencies, due to the low laser power, and the resulting porous LPBF*ed* components, new machines equipped with high-power fiber and Yb-based lasers have been introduced into the market over the past ten years [34]. Over the years not only the laser efficiency has been improved, but also the machine build volume has been enhanced to increase the LPBF productivity. To this regard, actually the Concept X Line 2000 R machine is the largest commercial volume machine with a build volume of $800 \times 400 \times 500$ mm^3 and two lasers of 1000 W [34]. Large-scale components for aerospace and automotive industries can be produced benefiting from the larger building volume and faster building rate.

1.2 Process parameters

The LPBF process is a very complex AM technique, and, by implication, to produce near fully dense parts with satisfying performances several technological parameters require attention [35]. The main process parameters are summarized in Table 2. To better understand the influence of these process parameters on the consolidation behaviour, one can refer to the schematic operational sequence of LPBF reported in Fig. 4. The consolidation of the part starts from the melting of an individual single scan track (SST). The formation of each SST is directly governed by the interaction of the laser power and speed with the powder bed. Being the final part made by vertical stacking of single layers, which in turn consist of several single scan tracks horizontally overlapped, also the powder layer thickness and the hatching distance play a key role for the densification. As a consequence of this, all the process parameters need to be carefully optimized, and only their proper combination can guarantee a full density [36].

Table 2 Main LPBF process parameters influencing performances of manufactured components.

Process parameters
Laser Power (P)
Scanning Speed (v)
Hatching distance (h_d)
Layer thickness (t)

Scanning strategy
Platform heating temperature (*T*)
Processing atmosphere
Gas flow rate

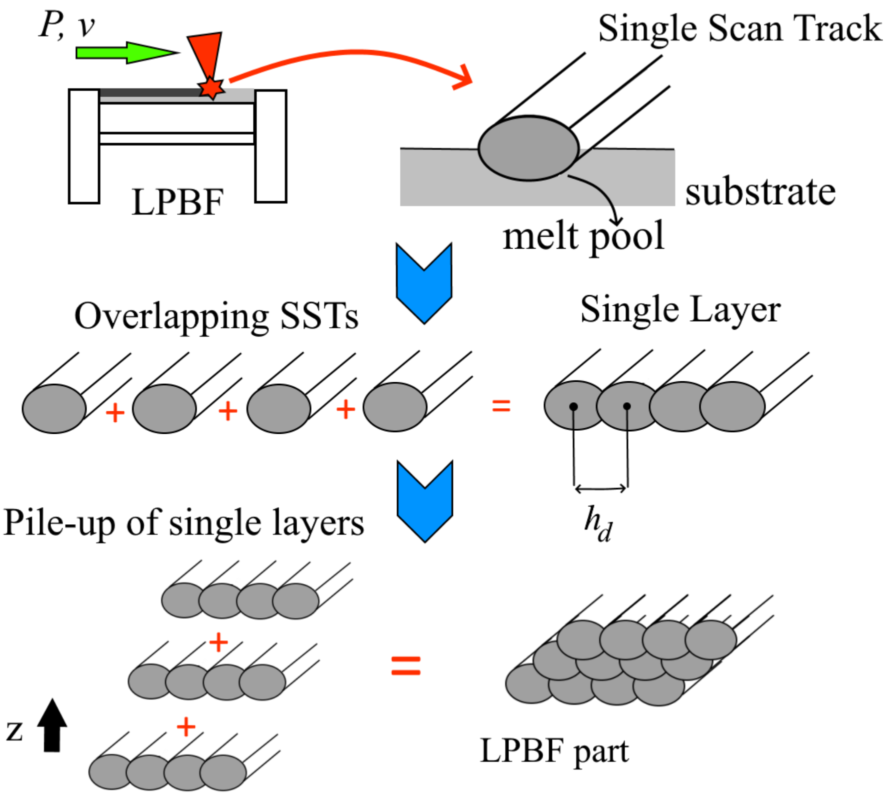

Fig. 4 Schematic illustration of the sequence used by the LPBF process to additively build the final object.

In this section, the most relevant LPBF process parameters are described. The effect of the process parameters on the final density and performances of the built part is also reported with reference to the published works in literature.

1.2.1 Laser Power

The selection of the laser characteristics for processing alloys by LPBF may significantly influence the final density and the surface roughness of printed parts [37].

In the early day of this technology, former LPBF machines were equipped with CO_2 lasers delivering a power rate in the range of 50 and 200 W at a wavelength λ of 10.6 μm [38]. If the sintering of polymer powders was possible using these prototypes, CO_2 lasers were not able to completely densify many metal alloys given that their absorptance is typically at λ between 10 nm and 1 μm [38,39]. Therefore, this implies that lasers with high power and operating at lower λ are fundamental to fully melt alloys and counteract the rapid heat dissipation throughout LPBF [40,41]. For these reasons, producers introduced into the market

LPBF machines equipped by Nd:YAG lasers operating at λ of 1.06 μm, achieving a higher level of absorptance for the processed alloys [39]. For instance, Tolochko et al. found that the absorptance of powder metals processed by Nd:YAG laser is 1.5-2.5 times higher than that obtained using shorter wavelength radiation [39]. Nevertheless, the very high thermal conductivity and low absorptance (*A*) exhibited by some alloys, e.g., Cu (*A* of 59 %) and Al alloys (A_{AlSi10Mg} of 9 %), require a quite high laser power coupled with very low scanning speed [42,43]. In the case of Al alloys near fully dense samples were obtained with 300 W of power and 500 mm/s of scanning speed. In this regard, to increase the production rate of aluminium alloys, Buchbinder and co-workers developed an LPBF prototype machine equipped with 1 kW Nd:YAG laser, defining the technique as 'high power selective laser melting' [42]. By increasing the laser power values up to 900 W, they were able to enhance the scanning speed up to 2100 mm/s, achieving higher production rates with a satisfying level of densification (above 99.5 %) [42] (Fig. 5).

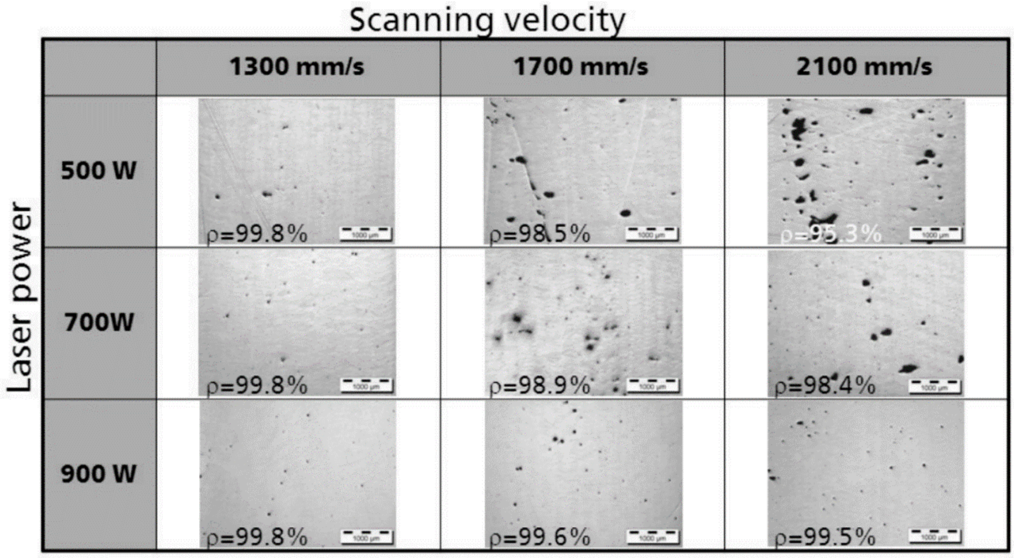

Fig. 5 Effect of the increased laser power and scanning speed values on porosity of AlSi10Mg alloy processed by high-power SLM.

An additional laser characteristic to consider when processing high reflective alloys is the laser spot size that defines the powder bed surface subjected to the laser irradiation [43]. The laser spot size for Nd:YAG laser varies from 35 to 180 μm, and it is usually set at 100 μm. Increasing the laser power and keeping constant the lase spot size can lead to excessive energy absorption by the material at the incidence point. This results in the higher evaporation of powder particles that contaminate the powder bed with plume and sputter, and the formation of the keyhole defects, as described later in Section 1.5.1 [44,45]. As a consequence of this, working at higher power levels required an enlarged laser spot size to avoid the aforementioned defects. On the other side, when dealing with the laser spot size, the accuracy of printed parts can be negatively affected by the wider melt pools obtained with high *P* level and larger beam size. To address this issue, the skin-core strategy has been adopted by many LPBF technicians [46]. According to this strategy, the part core can be produced with a wider beam diameter enhancing the production rate, while the skin (outer part) is processed using a small beam diameter for better accuracy [43].

1.2.2 Scanning Speed

Scanning speed, also called ‘scanning velocity’ or ‘scan speed’, is generally defined as the laser velocity at which the laser moves on the powder bed. However, this definition of scanning speed better suits when considering LPBF systems equipped with continuous lasers where the speed is defined by a single parameter [47]. This is the case of EOS GmbH, SLM Solutions GmbH, Realizer GmbH, and other LPBF producers, while Renishaw Plc prefers lasers with pulsed emission [48]. In pulsed LPBF printers, the laser is delivered in a point-by-point fashion (not continuously), and the scanning speed is thus defined as the ratio between two factors: the point distance of two subsequent melting points and the exposure time at each point [47,48].

Laser scanning speed combined with the other process parameters influences the consolidation behaviour in terms of melt pool characteristics [44]. Being the melt pool the key constitutive element of the LPBF process (Fig. 4), its shaping features are of particular importance when the proper operating window of the processed alloy has to be defined [49]. Generally speaking, when the laser power is kept constant, and the scanning speed is varied, the molten pool aspect ratio accordingly changes because of the different amount of energy absorbed by the powder bed [50–52]. This effect is qualitatively depicted in Fig. 6. When low scanning speed is adopted, a significant penetration of the laser under the layer of powder is achieved, featuring deep molten pools with a ‘keyhole’ shape and high aspect ratio [52]. By gradually increasing the scanning speed value to a medium-range, the melting mode slightly changes from ‘keyhole’ to the ‘conduction’ one revealing dual-half melt pool with elliptic shape [49]. In this regime, the molten pool geometry reveals an aspect ratio in the range of 0.4 – 0.6 [53]. By further increasing the laser scanning speed, the laser does not deliver enough energy to fully melt the powder layer leading to shallow melt pools with scarce growth and depth [54]. In this last case, the lack of fusion defects may arise in the printed part [55].

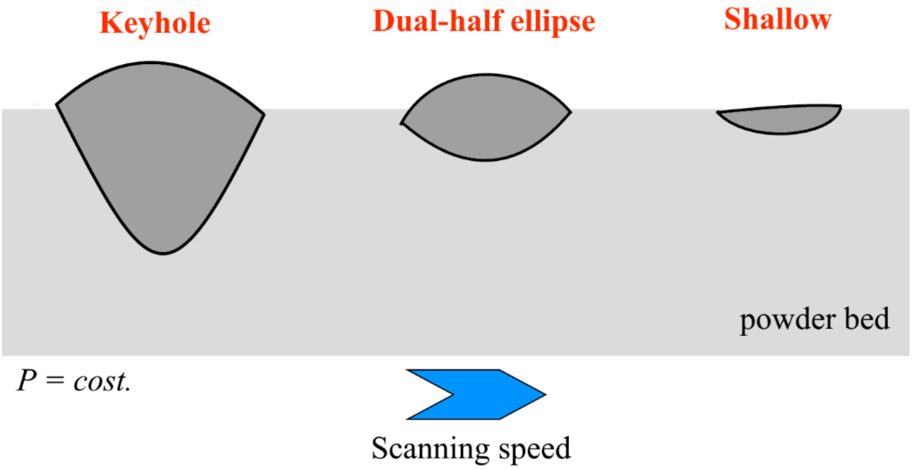

Fig. 6 Effect of scanning speed on the melt pool shape at constant laser power.

As far as the printed parts are concerned, numerous studies in literature have been shown the influence of scanning speed on densification and defects demonstrating that the higher the scanning speed employed, the lower is the densification level achieved [42,56–59]. For instance, Read et al. obtained the lowest densities when using high scanning speed at each power level. Besides, Aboulkhair et al. observed varied defects by processing AlSi10Mg at different scanning speeds. In fact, by using slow scan speed values, rounded pores due to the gas entrapment emanating from powder were found in the sample core. On the other side, lack of fusion defects with irregular shapes arose due to the insufficient energy delivered. Finally, the scanning speed plays a crucial effect on the surface roughness. As an example, Maamoun et al. found that, by increasing the scanning speed, the surface roughness of as-built AlSi10Mg samples increased accordingly [57]. This behavior was attributed by Authors to the faster solidification rate at higher scanning speed, which might lead to the formation of un-melted zones or balling defects.

1.2.3 Hatching distance

The hatching distance (also called ‘hatch distance’ or ‘scan spacing’) describes the distance between two consecutive laser single scan tracks during the manufacturing process. It is measured from the melt pool center of one track to the center of the consecutive one [60]. Hatching distance value plays a crucial role when a good overlapping with adjacent tracks has to be guaranteed to prevent process porosities [53,61,62]. This parameter is usually set according to the laser spot size and layer thickness. However, in the process optimization for density, one must also consider the laser power and the scanning speed values because they have a direct influence on the single scan tracks dimensions [63]. In fact, starting from the measurement of a single scan width, the hatching distance can be empirically determined by the Eq. (1.1):

$$h_d = w \cdot (1 - \varphi) \tag{1.1}$$

where w is the measured single scan track width and φ is the desired overlapping grade between two neighboring single scan tracks [64]. This equation is schematically depicted in Fig. 7. The higher the hatching, the lower the overlapping of melt pools is. This relationship should be considered when a good hatching distance has to be set to minimize porosity [53]. Several studies published over the past ten years showed a significant increase in porosity of printed parts caused by increasing hatching, which in turn formed gaps between nearby single scan tracks [40,49,57,59,65]. Other studies reported, instead, how this parameter affects the surface roughness. For instance, the research of Nie at al. revealed that smooth single layers of SLM*ed* Al-Cu-Mg were produced with 65 % of single scan tracks overlapping [64]. This number of SSTs overlap was achieved by using a P, v, and h_d of, respectively, 200 W, 5 m/min and 90 µm in a self-developed SLM machine (LSNF-I). Also, Calignano et al. according to their systematic statistical study showed that a small hatching distance of 0.10 mm coupled with 120 W of power and 900 mm/s of speed was the optimum value for the surface roughness of AlSi10Mg components processed by an EOSINT M270 [37]. Furthermore, the hatching distance together with scanning speed and layer thickness governs the build rate of LPBF [43].

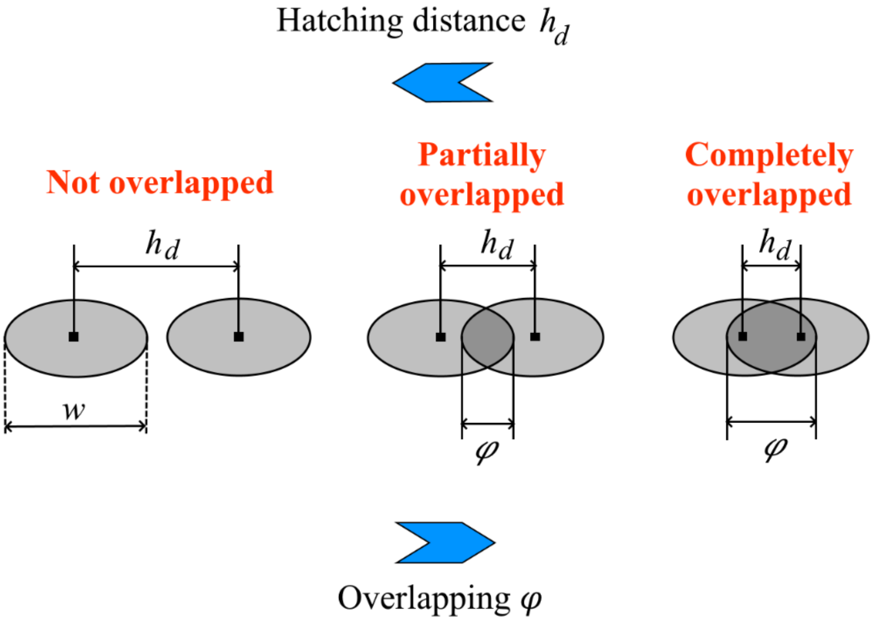

Fig. 7 Different overlapping grades of adjacent single tracks according to the employed hatching distance.

1.2.4 Layer thickness

Since components in LPBF are manufactured in a layer-by-layer manner, the layer thickness is an important parameter of this technique. As far as the laser-powder interaction is concerned, the powder layer thickness determines the amount of powder will be consolidated by a single scan track [33]. On the other hand, the layer thickness directly affects surface smoothness, production rate, and porosity of printed parts [60].

The layer thickness value is generally selected considering the size distribution of the used powder [46]. It is often set to a number equal to d_{50} of the cumulative powder size distribution [53,66]. Notwithstanding this common general practice, some explanatory researches on the effect of the layer thickness on single scan track morphology and densification mechanisms have been carried out to find the proper layer thickness value [33,63,67–69]. In this regard, Yadroitsev et al. observed that 316L single scan tracks, produced by a SLM machine PM 100, were continuous for a layer thickness lower than 100 µm coupled with a P of 50 W, and v in the range 0.10-0.28 m/s [67]. On the contrary, with the increment of the layer thickness from 100 to 350 µm, discontinuous tracks featuring balling defects were observed to a large extent. In a further study, they also put in evidence how the layer thickness influences the melt pool geometrical features [33]. It was found that, by using thinner powder layers, it was possible to achieve good penetration into the substrate and thus a significant remelting of previous layers, favoring the densification. This was also observed by Olakanmi et al. achieving higher densities at lower layer thickness values for Al-12Si aluminum powders [69]. However, the melt pool height in Ref. [33] was limited to tens of microns requiring more layer to manufacture the final object.

The effect of the layer thickness, as a rule of thumb, is described in Fig. 8. Thinner layers guarantee high density because of a better bonding with underlying layers, low shrinkage, and satisfying surface finishing because of small gap sizes related to the ‘staircase effect’ [70]. However, several layers are required to produce the final part and higher building time is needed. Thicker layers, on the other side, enhance productivity but excessive layer thickness values can lead to delamination, rough surfaces with a significant staircase effect, and lack of fusion porosities [71,72].

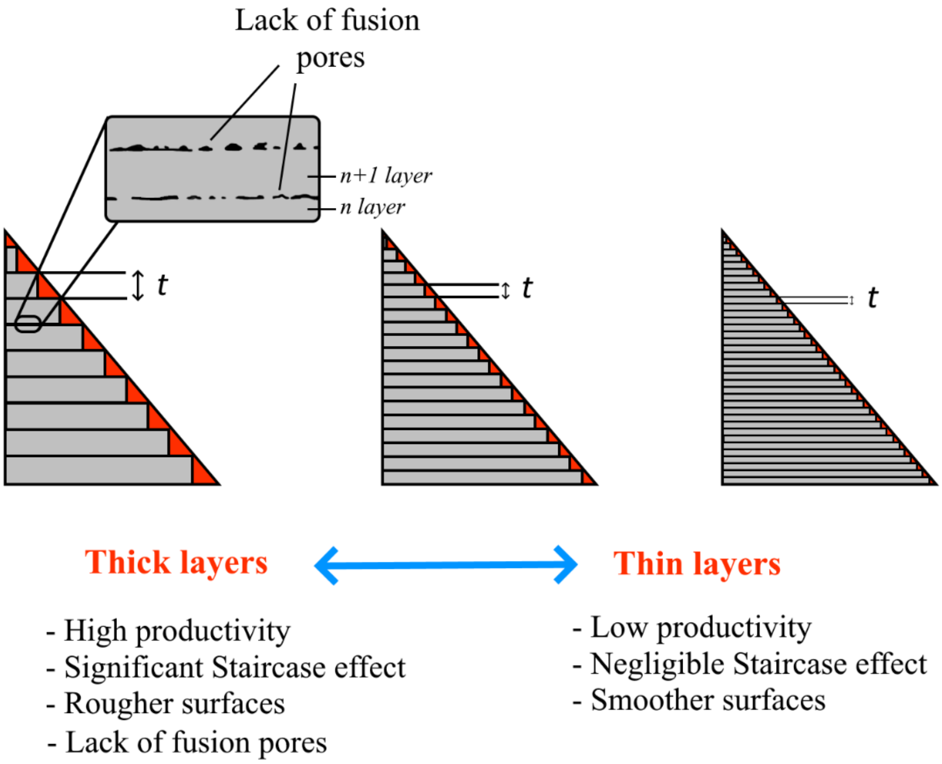

Fig. 8 Effect of layer thickness on LPBF*ed* part characteristics.

1.2.5 Hatch patterns and scanning strategies

The ‘hatch pattern’ or ‘scanning pattern’ describes the geometrical path followed by the laser tracks in a single layer while the ‘scanning strategy’ refers to the method adopted to stack the layers in LPBF process, e.g. the difference in the alignment of the track between consecutive layers [36,46,73]. Some examples of the most common hatch patterns and scanning strategies available for LPBF are illustrated in Fig. 9. The scanning strategy can be ‘unidirectional’ with tracks oriented either along the X or Y-axis. The orientation of single scan tracks does not change among layers. On the opposite, if an ‘alternating XY’ strategy is selected, the direction of scanning varies between layers, following first X and then Y-axis. In ‘both X and Y’ strategy, each layer is scanned twice, once along X and then along Y-axis, while layers are rotated of a certain angle to the previous one in the ‘rotated’ scanning strategy. Differently from the abovementioned options, the ‘island’ strategy requires a partition of the whole layer surface in several sectors with a fixed size. In this case, the scan pattern is rotated at an angle of 90° compared to the neighboring sectors.

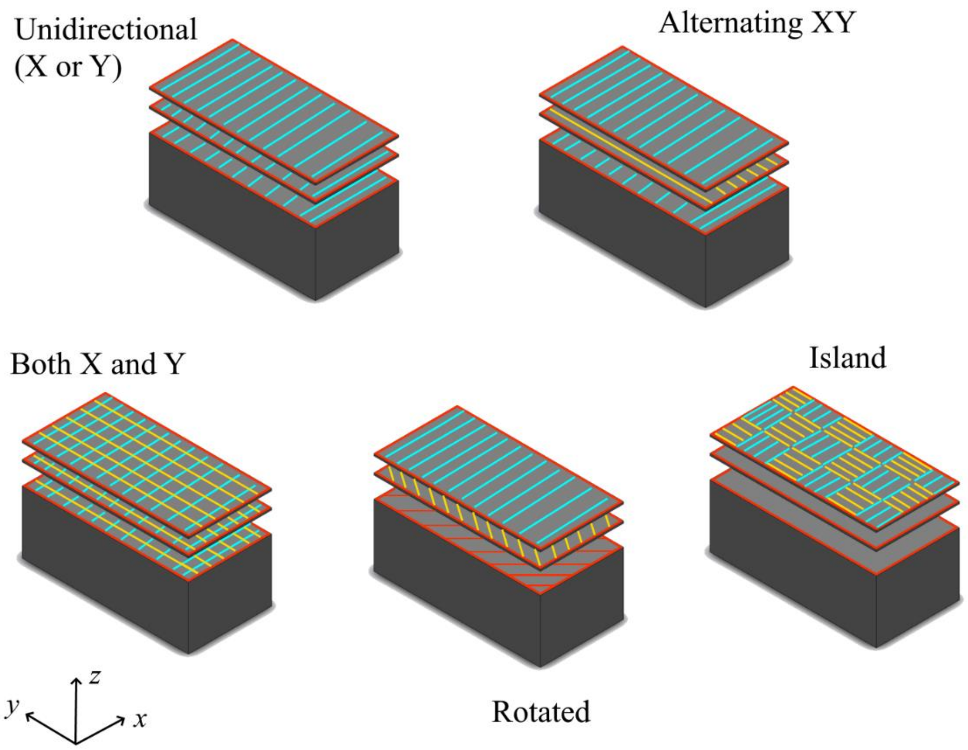

Fig. 9 Hatch patterns and scanning strategies adopted in LPBF.

Scanning strategies have been mainly employed to mitigate the residual stresses [74,75], to control the crystals texture [76,77] and to reduce inner porosities [55] of LPBF*ed* parts. As far as the residual stress is concerned, it is well established by earlier works that the scanning strategy affects the thermal gradients of parts being manufactured, which in turn influences the internal residual stresses. Referring to this, Mercelis and Kruth observed that a partition of the scanned surface in several sectors (similar to the 'island' scanning strategy) yields to lower residual stresses if compared to unidirectional X or Y patterns [74]. The main reason behind this result was the random consolidation of the sectors which were not connected to neighboring sectors during melting. By doing so, the stress level at sectors border was zero being the material free to shrink. This fact has been corroborated in Ref. [75] by Wang et al. By processing AlSi10Mg via SLM, they concluded that a island scanning strategy significantly reduced residual stress values in both X- and Y- directions when comparing results with the ones obtained through a unidirectional strategy. Considering the crystallographic texture, Thijs et al. processing AlSi10Mg by SLM obtained a lowered <100> fiber texture along building direction using the alternating XY scanning strategy with a rotation angle of 90° [76]. This rotation between layers induced the formation of a weak <100> cube texture making the tensile properties of printed parts more isotropic. Furthermore, also the microstructure of other LPBF alloys can be modified by a specific scanning strategy. For example, Kurzynowski and co-workers comparing the microstructure of 316L steel produced with alternating XY and both X and Y strategies found less segregation of δ-ferrite in the latter microstructure [77]. Lastly, improving densification is a further possible benefit of using specific hatch patterns. For example, it was demonstrated that a double exposure scanning strategy with the first scan at reduced power (referred to as 'pre-sinter' strategy) was efficient in minimizing the keyhole pores of a SLM*ed* AlSi10Mg alloy.

1.2.6 Platform heating temperature

Heating the building platform is a common method employed to lower the steep thermal gradient of LPBF and reduce the internal residual stresses [25,78]. This can be possible because of a heater element placed underneath the mounting plate able to raise the building platform temperature (T) level at a higher operating temperature. The operating temperature can be raised to 200 °C or more depending on the used LPBF system. However, it is known that the operating building platform temperature hinges either on the building plate material conduction or the processed alloy. For this reason, the real operating T can be different from the set temperature requiring constant monitoring throughout the LPBF process [79].

If the platform heating, on the one hand, acts in reducing the thermal stresses arising from rapid cooling, on the other hand, the microstructure of the processed alloys undergoes an in-situ heat-treatment induced by the heat emanated from the building platform [80,81]. Regarding this, the optimal building platform temperature must be selected considering both aspects. It should be able to minimize the thermal stress without deteriorating the microstructure or, even better, to replace a post-process heat-treatment [26].

Table 3 provides a list of the main works that have dealt with the platform heating effects over the last decade. From the results presented in Ref. [25], it was revealed that a platform heating of 250 °C drastically reduced cracks and distortions of AlSi10Mg cantilevers produced with an EOSINT M270. However, a remarkable hardness loss occurred at this T due to an accelerated coarsening of Al-Si eutectic texture. Similarly, Casati et al. investigated the effect of the hot platform strategy on the hardness of an AlSi10Mg alloy processed by an EOS M290 system [26]. They observed a loss of aging response after LPBF attributable to a possible in-situ direct aging occurred throughout the process. Moreover, Mertens et al. using an in-house developed SLM machine equipped with an enhanced heating module, achieved improved tensile properties for H13 steel at 400 °C [82]. The main reason behind this was ascribed to the in-situ formation of a strong bainite phase at $T > 350$ °C. They claim the possibility to use this alloy in the as-built condition without the need for post-process heat-treatments. Nevertheless, using the same T in a further work [81], they observed that grain coarsening took place at the bottom of samples of a nickel Hastelloy X alloy processed at 400 °C for 32 hrs. This means that also the holding time above the heated platform can significantly affect the resultant microstructure [26].

Table 3 Results of main recent works dealing with the effect of the platform heating strategy on varied LPBF alloys.

Alloy	LPBF system	Producer	T [°C]	Findings	Refs
AlSi10Mg	EOSINT M 270	EOS GmbH	100, 150, 200, 250	- Distortions in cantilever samples are nearly zero at 250 °C - At $T > 200$ °C microstructure coarsening	[25]
Al-12Si	SLM 250 HL	SLM Solutions	200, 300, 400	-Not homogeneous microstructure along building direction with platform heating	[83]
AlSi10Mg	EOS M 290	EOS GmbH	160	-Loss of aging response upon LPBF using the heated platform at 160 °C	[26]
AlZn5.5MgCu (7075)	SLM 250 HL	SLM Solutions	40, 200	-T of 200 °C is not sufficient to prevent hot cracks	[84]
M2 High Speed Steel (HSS)	M3 Linear	Concept Laser	100, 180	-Reduced thermal gradient achieved by heating at 180 °C	[85]
H13 tool steel	In-house developed SLM	KU Leuven	100, 200, 300, 400	-Improved mechanical properties obtained at 400 °C -Additional post-process heat-treatment can be avoided	[82]
18Ni300 Maranging steel	AM250	Renishaw	170	-Platform heating of maranging steel does not provide any improvement in density	[86]
Ti6Al4V	In-house developed SLM	KU Leuven	100, 200, 300, 400	-Platform heating at 400 °C reduced residual stresses of 50 % and induced ß-phase formation	[87]
Ti6Al4V	SLM125	Renishaw	370, 470, 570, 670, 770	-Decomposition of α^{I} martensite to α+ß at 570 °C	[88]
W	Aconity*One*	Aconity3D GmbH	600, 800, 1000	-Potentially lower crack occurrence at 1000 °C	[89]

1.2.7 Process atmospheres

The processing environment of LPBF is an important aspect to consider in process optimization. It is tightly related to the formation of defects namely pores, oxides, and thus to the overall impoverishment of mechanical properties [23]. LPBF components are usually printed in a building chamber purged with inert gas to keep the oxygen level below 0.1 % and minimize oxidation. This is quite significant when powder highly susceptible to oxidation such as aluminum or steel alloys are manufactured [41,90–92]. The types of purging gas typically pumped into the building chamber are primarily argon, nitrogen, and helium. These atmospheres were adopted by Wang et al. to manufacture Al-12Si parts by SLM [29]. The Authors did not found any statistical differences in terms of average density or hardness between samples. However, clusters of rounded pores were revealed using He atmosphere. Even though the pore size was less than 50 μm, these voids, therefore, had a detrimental effect on the ductility and tensile strength of the processed alloy. The origins of pores formation under He atmosphere was not described in Ref. [29]. A possible theoretical description has rather been provided by Zhang et al. which studied the influence of different shielding gas mixtures on the densification mechanism of 316L powder processed by SLM [32]. They obtained near fully dense specimens under Ar, N_2, and mixtures thereof while, on the opposite, density remarkably dropped down to 90 % using He and its mixtures. The theoretical explanation of this behavior relies on the varied plasma conditions above the molten material. Because of the low specific gravity and the high ionization energy of He, the plasma plume generated under He atmosphere is located farther from the melt pool than the ones produced by Ar and N_2. As a consequence, the melting efficiency was obstructed by the plasma plume and lack of fusion porosities were generated throughout the process. Besides, the process atmosphere used for LPBF has also been studied to improve the process stability and productivity of Ti-6Al-4V alloy [93]. This has been possible using argon-helium mixtures as shielding gases. Differently from previous researches [29,32], it was argued that these gas mixtures enhanced the laser heat input. The mechanism related to this was ascribed to the efficient removal of process by-products offered by the argon-helium mixtures.

1.2.8 Gas flow rate

Gas flow rate of the shielding gas purged into the building chamber is another crucial process parameter influencing the part quality of LPBF*ed* parts. In addition to as previously discussed in 1.2.7, the gas flow of the inert atmospheres is crucial for removing the process by-products from the melt pool area and enable the laser to properly melt the powder [94]. Insufficient removal of laser plume and spatter may lead to a reduced laser melting efficiency caused by the increased interaction of laser with these process by-products [95]. Moreover, the gas flow speed has to be homogeneous across the whole powder bed and its values lie in a specific range [30]. The lower speed limit of this range corresponds to a speed value below which the redeposition of removed particles onto a powder bed area occurred (Fig. 10a). On the opposite, the upper limit corresponds to a speed value above which the pick-up of fresh particles of the powder bed occurred (Fig. 10c). Both scenarios have been related to different mechanisms underneath the formation of lack of fusion porosities [30,94,96]. It is thus worthwhile to set up the gas flow speed within this value range and ensure a uniform gas flow across the powder bed (Fig. 10b). For these reasons, several studies have been carried out to evaluate the gas flow speed effect on the quality of printed parts [45,94,97–99]. Bidare et al. reported that the jet of vaporized material can be efficiently removed by a cross-flow but the effectiveness was reduced at higher laser power values [97]. Ladewig et al. observed a consistent beam attenuation, also known as ‘splashy process’ [95], at low flow gas rate due to the presence of by-products on the powder bed [94]. Consistently with Ref. [94], Anwar and Pham obtained better tensile properties for an LPBF*ed* AlSi10Mg alloy by doubling the gas velocity [45]. Indeed, a higher gas speed velocity can wipe more efficiently the powder bed from spattered particles. As far as the flow uniformity is concerned, Ferrar et al. optimized the setup of the gas inlet achieving a homogeneous flow speed distribution across the building area and, accordingly, density and strength were improved [99]. Recently, Shen et al. studying the powder behavior of commercial LPBF alloys under varied levels of gas flow speed, developed a model to predict the particle pick-up speed [30].

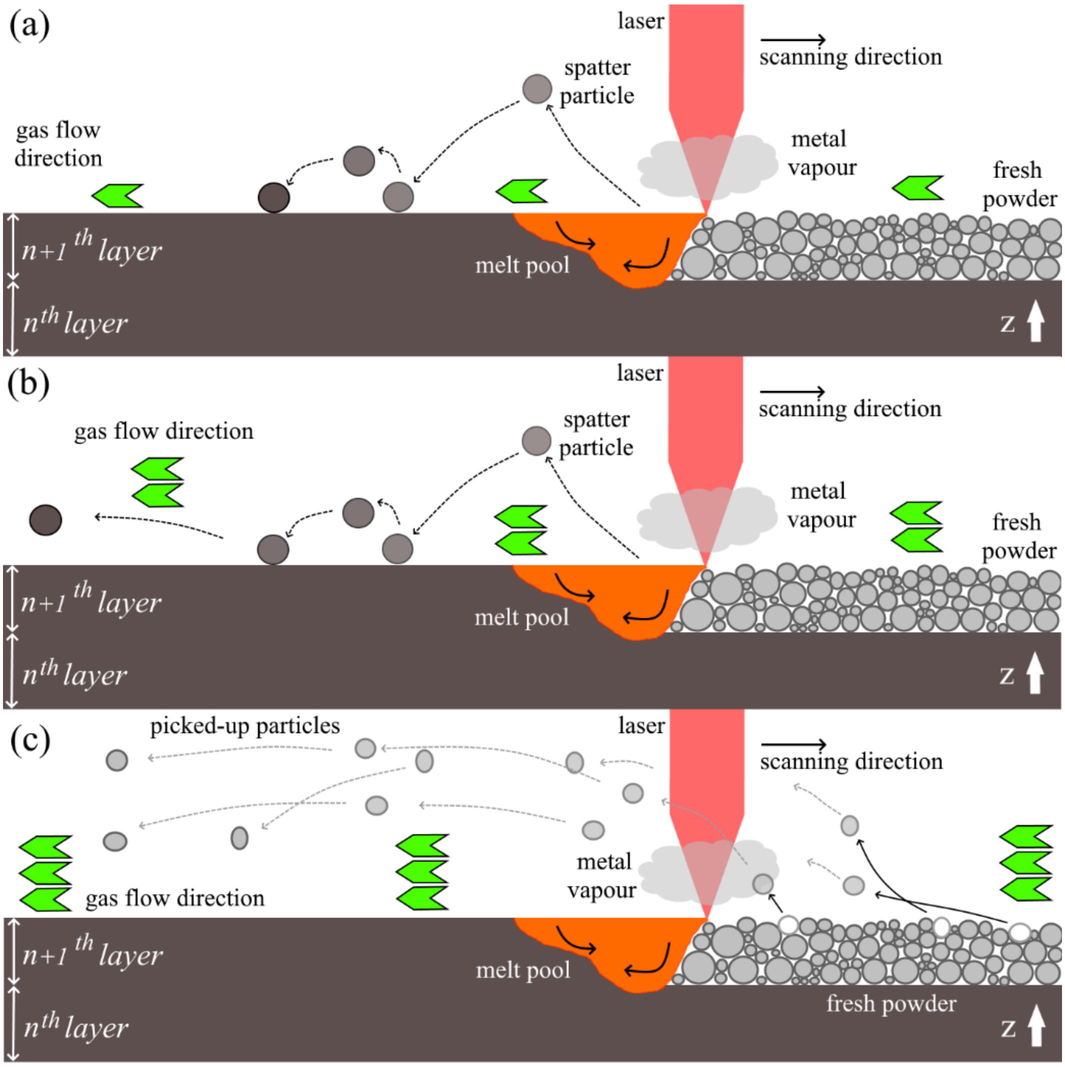

Fig. 10 Overall effect of gas flow speed on powder bed; (a) lower, (b) optimum, and (c) excessive speed scenarios.

1.2.9 Linear, surface, and volume energy density

As described in previous sections, a large number of process parameters influence the density and the mechanical properties of printed parts. Related to this, Yadroitsev et al. even argued that at least 130 parameters need to be tuned for a comprehensive LPBF optimization [33]. Due to this huge number of process parameters, researchers are wont to report density results using the energy density parameters. These parameters namely linear energy density (*LED*), surface energy density, and volumetric energy density (*VED*) have been often used because multiple factors are considered at once.

The linear energy density (*LED*) is defined as the energy delivered by the laser power P over the scanning speed v (P/v) with a unit of *J/mm*. The *LED* parameter has been generally employed as a tool for identifying a preliminary P and v operating window through the analysis of single scan tracks [100]. Yadroitsev et al. before manufacturing single scan tracks of 904L steel, studied the effect of laser energy input on a building platform without the powder bed. By observing the remelted volume per unit time formed by the fusion lines, they found a greater remelting rate at a lower *LED*. This was mainly ascribed to the high *v* coupled with a significant *P* [51]. Besides, varied morphologies of AlSi10Mg single tracks were classified into five types according to the used *LED* [100]. At a low *LED* level, the input energy was not sufficient to consolidate the powder, and the resultant scan tracks were merely fusion lines on the building substrate (Fig. 11a) [51,68] or discontinuous tracks featuring 'balling' phenomena (Fig. 11b) [101]. By increasing the energy to a medium value, 'thin and stable' tracks were achieved (Fig. 11c). They were employed in the definition of the first operating window for some Al-based LPBF alloys. Finally, by further increasing *LED*, 'irregular' or 'too thick' tracks were formed due to the excessive laser power or the very low scanning speed.

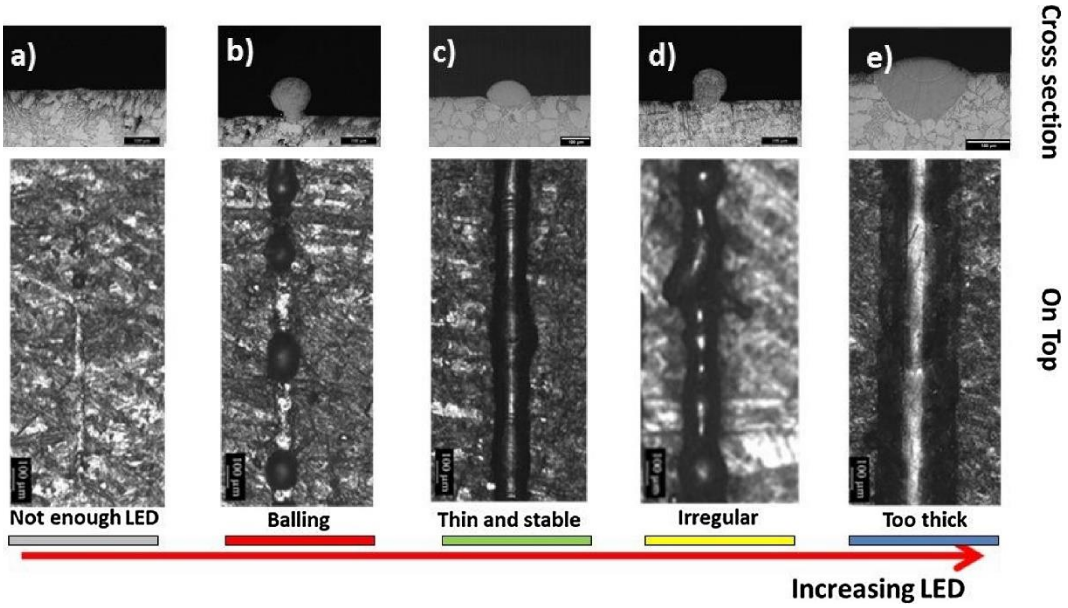

Fig. 11 Scan tracks morphologies classified according to the used linear energy density [100].

The surface energy density is defined as the delivered laser *P* on the specific area given by the product of *v* with the powder layer thickness *t* ($\varphi = P/v \cdot t$). The metric unit is J/mm^2. This parameter has been adopted when the studied factors are laser power, scanning speed, and layer thickness, thus excluding the hatching distance. It was used by Olakanmi et al. to define the operating windows for Al-Si, Al-Mg, and Al alloys, that corresponded to the 'good consolidation' region between 12 and 30 J/mm^2 [102]. These surface energy density values were obtained from a *P* between 100 and 240 W, *v* in the range of 80-200 mm/s, and *t* of 0.25 mm.

The volumetric energy density (*VED*) is expressed by Eq. (1.2):

$$VED = \frac{P}{v \cdot h_d \cdot t} \quad \left[\frac{J}{mm^3}\right] \tag{1.2}$$

where *P* is the applied laser power, *v* the scanning speed, h_d the hatching distance, and *t* the layer thickness, respectively. According to Eq. (1.2), *VED* corresponds to the energy applied to a specific volume of processed powder. In the very early days of LBPF, Simchi et al. correlated the sintering rate of varied ferrous powders to the applied laser energy values [103]. The Authors observed better densification at higher energy input. Similarly, Ciurana et al. concluded that *VED* values above 151 J/mm^3 were necessary to consolidate continuous single scan tracks of CoCrMo alloy, after experiencing varied P, v and h_d combinations using a Kondia HS-1000 machine [104]. Several other research works have been focused on the correlation between *VED* and the final density level [59,105–107]. Broadly speaking, all the aforementioned works showed the possibility to manufacture parts minimizing residual porosities when LPBF parameters met a well-defined *VED* process window. Nevertheless, if the *VED* approach is adopted as a design parameter, one must consider that the same *VED* value can correspond to significantly different parameters and, thus, its effect on processed alloy could change [36,52,54,59,108]. Scipioni Bertoli et al., as evidence of that, using a *VED* of 242 J/mm^3 resultant from five different combinations of power and speed values obtained either irregular or continuous tracks of 316L steel using a customized SLM machine [108].

1.3 Powder for LPBF

The LPBF process requires metal alloys in pulverized condition as raw material. It is, therefore, easy to understand how the quality of the feedstock used to manufacture parts plays a crucial role on the final component properties. Thus, the used powder must have specific requirements to yield satisfying performances in terms of density, surface roughness, and mechanical properties. To manufacture a reproducible component with reliable properties, the knowledge of the powder characteristics is, therefore, as important as the handling of the process parameters.

In this section, the most relevant powder properties, such as the morphology, the particle size distribution, and the chemical composition are described and thereof effect on part properties discussed. Additionally, sub-sections containing the main powder atomization methods as well as the issue related to powder recycling are presented as well.

1.3.1 Powder atomization techniques

The quality of the powder tightly depends on the production technique. A number of techniques can produce metal powders. However, LPBF preferably requires high-quality powder with spherical particles and a size distribution in the range of 20-45 μm [109]. Therefore, among these many techniques, the most common routes of powder production for LPBF are the gas and plasma atomization (Fig. 12) [110]. This is due to their specific process characteristics by which highly spherical particles are produced differently to other techniques as water atomization [111].

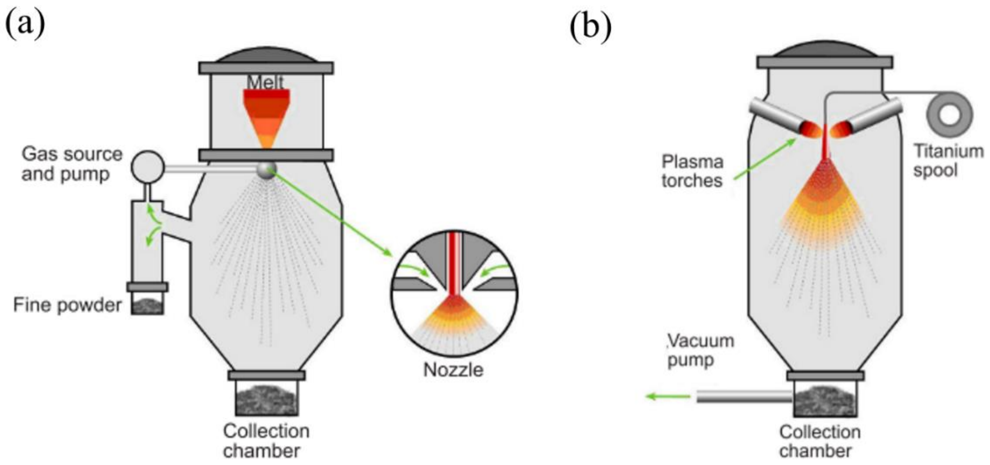

Fig. 12 Schematic representation of (a) gas and (b) plasma atomization (adapted from [112]**).**

The gas atomization is broadly the most used method to produce powders for LPBF (Fig. 12a). In this process, ingots or bars of the raw material are melted via vacuum induction melting furnaces installed above the atomization chamber. Once the chemical composition is homogeneous, the liquid metal directly flows into a refractory nozzle where it undergoes the atomization process induced by high-pressure jets of gas [110,112]. To achieve the desired particle size, careful control of the gas speed is required. Indeed, before starting the production of a good quality powder, technicians have to finely tune the ratio between the injected gas and the molten metal. This parameter is technically known as the gas-to-metal ratio (G/M) and it influences productivity [113]. As an example, a higher G/M, which means the higher gas speed at a constant metal quantity, yields to an even higher fraction of fine powder. Thus it is important to regulate its value to increase the process efficiency, reduce the material waste, and consequently, the final powder cost.

Indeed the presence of an inert atmosphere, such as argon or nitrogen, pumped into the atomization chamber, reduces the risk of oxidation making possible the production of highly reactive alloys as aluminum and titanium. As observed by Murr and Starr, the specific gas media used in the process, however, does influence the powder particle microstructure and accordingly on the final printed parts [114,115]. In their studies, it was detected a higher content of γ-austenite in 17-4 PH steel powder obtained using a nitrogen media when compared to the powder composition upon production in argon, being the nitrogen a γ stabilizer.

Plasma atomization is the other process generally used to produce LPBF powders with an extremely spherical shape [116]. On the whole, the workflow of this process is similar to the gas atomization one. However, some differences can be perceived when observing the processes drawings thoroughly in Fig. 12. Concerning the used feedstock, differently from gas atomization, plasma atomization uses either a wire, as depicted in Fig. 12b or powder. Moreover, in this process, melting and atomization takes place in a single step using plasma torches as atomization media. This process also offers the possibility to produce finer particles with an average size of 40 µm favoring the powder flowability and the packing density on the powder bed [112].

1.3.2 Extrinsic powder properties

The characteristics of printed parts such as the densification level and the dimensional accuracy are strictly correlated to the quality of the powder bed. It must be devoid of surface defects, homogeneously spread onto the building platform, and with a constant thickness throughout the whole manufacturing process. To ensure these conditions, once the main process parameters have been optimized, the assessment of the extrinsic powder properties, namely powder morphology and powder size distribution, is highly recommended.

The powder morphology generally refers to the shape of particles which constitute the used powder [112]. As briefly outlined in the previous section, the atomization technique has a significant impact on particle shape and dimension [113]. LPBF requires the use of spherical, regular, and equiaxed particles rather than irregularly shaped particles that cannot guarantee good powder bed properties, thus promoting defects during printing [111]. This is one of the main reasons behind the higher cost of the spherical powder obtained via gas and plasma atomization (Fig. 13a) compared to the water atomized ones (Fig. 13b). However, some research groups have attempted to use water atomized powder for producing steel components showing contradictory results [111,117,118]. Starting from the results of Li et al., a higher density was achieved using gas atomized 316L powder, whereas, as expected, several lack of fusion pores were revealed adopting the water atomized ones [111]. The Authors explained their findings referring to a higher powder bed packing density obtained using spherical atomized particles and consequently a better densification after consolidation. Contrarily to the previous findings, both Paulosek and Letenneur et al. achieved almost fully dense samples with relatively high mechanical tensile properties by processing the same water atomized iron-based powders via two different LPBF systems [117,118]. Apart from the unprofitable morphology of water atomized powder, even spherical particles could have defects limiting the powder spreading. This is the case of the so-called satellites [119]. Satellites are very small particles generated by the gas atomization process and clung on the bigger sized particles via adhesive forces [119,120] (see arrows in Fig. 13a).

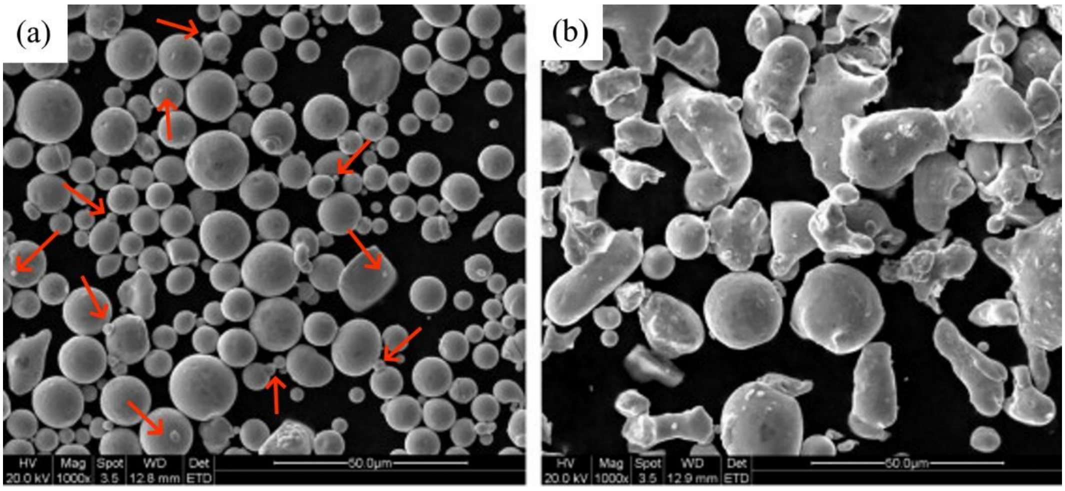

Fig. 13 SEM images showing the morphology of (a) nearly spherical gas atomized and (b) elongated water atomized particles of 316L powder. Satellites on gas atomized particles are indicated by arrows (adapted from [111]**).**

The particle size distribution (*PSD*) of a specific powder describes the relative number or volume amount of detected particles according to their size. The particle size distribution typically refers to three diameter values, namely d_{10}, d_{50}, and d_{90}, which correspond respectively to the diameter of 10, 50, and 90 % of the total particles of the investigated population. A *PSD* curve is commonly determined using different techniques, mainly sieving, laser light diffraction, and high-resolution microscopy [109]. Diameter values measured from the PSD curve have a significant impact on both the used layer thickness and the quality of the surface finishing. When the used layer thickness value is greatly larger than d_{50}, there is the risk to just spread on the powder bed the larger fraction of particles. As a consequence, the resultant powder bed would have a poor stacking density with voids among the larger particles. On the other hand, when the layer thickness is excessively lower than d_{50}, the recoater could potentially push away the larger particles creating grooves or segregations onto the powder bed. The desired powder bed should be regularly spread without defects formed by the recoating process and with the finer fraction of *PSD* filling gaps among larger particles [121]. For this reason, being the nominal powder size for LPBF between 15 and 45 μm [109], a layer thickness of 30 μm has been widely used by the LPBF community [46,56,59,76].

Both particle morphology and particle size distribution influence the powder flowability, which is one of the crucial requirements for LPBF powder [112]. The flowability is defined as the capacity of a powder to flow under a specific set of conditions [109]. Broadly speaking, spherical shaped particles possess a higher flowability than the irregular ones. Moreover, a powder distribution with a significant fraction of fine particles can also negatively affect the particle motion. In fact, short cohesive forces as the electrostatic or Van der Walls forces are more prominent in the case of large surface areas, as in the case of fines particles.

1.3.3 Intrinsic powder properties

The intrinsic properties refer to the inner characteristics of the processed powder, such as the powder chemistry or the presence of powder internal porosities [109]. Investigation of such properties would be very important as they directly influence the characteristics of the processed parts.

It is widely known that powder contamination is an issue in LPBF, especially when highly reactive alloys as aluminum, magnesium, and titanium ones are processed [122]. Due to their micrometric size, a long exposure of these fine powders to an external environment rich in oxygen could greatly promote oxidation reactions [123]. For this reason, as mentioned in Section 1.2.7, the building chamber of the LPBF machine is purged with inert gas to reduce the amount of oxygen that would otherwise trigger the oxidation phenomena. Accordingly, the overall oxygen content must be reduced to 0.1 – 0.2 % and kept within this range while processing [41]. However, it has been demonstrated that this amount of oxygen is low enough to process stainless steel and titanium alloys but it still induces the formation of thin oxide layers when processing aluminum alloys. Consequently, these oxide layers have several detrimental effects on the processability and, thus, on the final characteristics of printed objects [122]. First, oxide skins covering the single track could be disrupted by high laser power, and the residual oxide chips are translated into the melt pool, causing melt pool instabilities and promoting the formation of balling defects [41,124]. Second, oxide layers can provoke a scarce surface wettability and, therefore, poor adherence between consecutive layers leading to a lack of fusion porosities [41]. Third, as a consequence of the previous two considerations, the presence of incorporated oxides significantly impacts the tensile properties as well as the fatigue resistance of an alloy [125]. Corroborating this, several sub-micron oxides whose formation has been ascribed to the disruption of the oxide skins during LPBF were found in AlSi10Mg parts [125]. In this study, Tang et al. observed that the fatigue life limit of their AlSI10Mg was mainly controlled by micro-sized oxides located at the pore boundaries. One way to minimize the presence of residual oxides into the matrix is processing at high laser powers, as suggested by Louvis et al. [41]. This would promote the disruption of skin oxides and then their dissolution stirred by the Marangoni forces into the melt pool. Nevertheless, thin oxide skins between the laser tracks can still be present after laser passing (Fig. 14).

The other issue contaminating powder is represented by the formation of hydroxides upon particle surfaces in the presence of moisture and humidity [122]. Differently from oxides, adsorbate particles tend to promote the chemical interactions of particles favoring the formation of powder agglomerates. Therefore, the flowability will suffer for this, and as a result, it would be more difficult to obtain a homogeneous powder bed in these conditions. Besides, the adsorbed hydroxides can be easily broken up by the laser beam releasing hydrogen gases, which can be entrapped in the melt, forming gas bubbles [126,127]. Drying the powder before LPBF is a simple procedure that helps to prevent hydrogen gas porosities [127,128]. By pre-heating powder up to 200 °C, the number of hydrogen porosities in AlSi10Mg halved [127]. Similarly, Al-12Si powders were heat-treated for 60 min at 100 °C before processing achieving higher densities when compared to non-dried samples [128]. However, care must be taken when pre-drying powder of aluminum. As an example, Rao et al. observed early in-situ aging phenomena in a SLM*ed* A357 alloy processed with a platform heating of 80 °C [80]. Drying powder in a temperature interval of 100-200 °C could enhance precipitation reactions of the alloy since in its powder state.

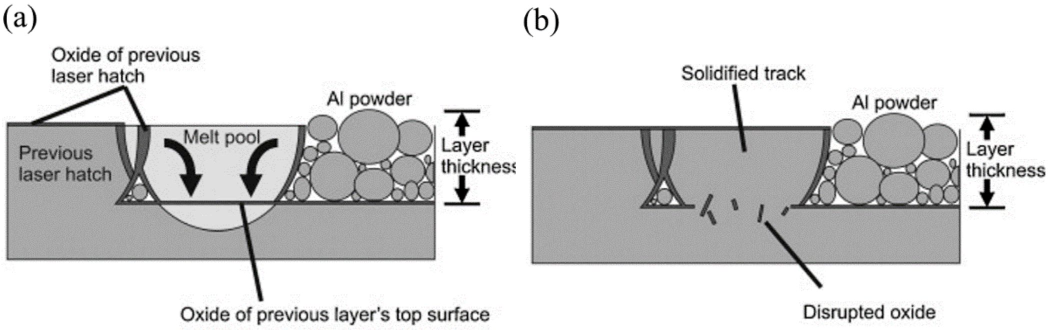

Fig. 14 Schematic mechanism of oxide skin disruption throughout LPBF; (a) the laser beam generates the melt pool and Marangoni convection takes place in the melt pool and (b) the thin oxide layer underneath is disrupted afterward (adapted from [41]**).**

The dissociation of hydroxides absorbed on the powder surface is not the only source increasing the final density level. The powder may contain internal pores consisting of atomization gas, which were trapped during atomization [119]. As obvious, these gases would be released upon laser melting and thus generating additional gas porosities in printed parts. The proper way to alleviate this issue is to prevent porosities formation while producing the powder. More detail about the atomization mechanism causing the gas entrapment into powder can be retrieved in Ref. [129].

1.3.4 Powder recycling

Powder recycling is one of the main attractive aspects of LPBF. The reusing of unmelted powder after a job is a common practice in research centers and companies. Being atomized powder very expensive, the powder reuse helps in minimizing the material waste and thus knocking down the process-related costs. According to Tofail et al., indeed, the powder cost is the second biggest cost of manufacturing by LPBF [22]. Despite LPBF could theoretically guarantee the reutilisation of all remaining powder, the recycle efficiency was approximately estimated to be 95% [130]. In fact, as observed by Aboulkhair et al., the remaining 5% corresponds to the fraction of powder discarded by sieving, mainly consisting of partially melted particles, such as coarsen laser spatter particles [23].

Once the powder waste has been discarded, care must be taken when reusing the sieved fraction since it could exhibit different characteristics when compared with the virgin powder [109]. Regarding this, a slightly coarsened particle size distribution has been noticed upon powder recycling by several LPBF users [130–132]. Seyda et al., as an example, observed an average particle size coarsening from 37.4 μm to 51.18 μm after recycling 12 times Ti6Al4V powder [131]. Likewise, Strondl et al. noticed a more significant fraction of coarse particles after recycling Ti6Al4V powder just one time [132]. The explanation of this can be manifold.

On the one hand, by a technological point of view, small powder particles could have been blown away in the gas stream (see Section 1.2.8) remaining in the atmosphere and being thus unavailable for recycling [132]. Besides, coarser particles may have been pushed in the overflow bin by the powder recoater if the layer thickness is not adequately calibrated with the average size of powder (see Section 1.3.2) [132]. On the other hand, the presence of agglomerates formed by partially sintered particles is likely a possible explanation [131]. The effects of the broad particle size distribution could be an improved powder flowability and a better apparent density [131]. However, the packing density of the powder bed may be affected by this because the voids between larger particles are unlikely filled by the fine fraction. Such powder properties must be continuously monitored after each usage to assess if the powder is suitable for a further job.

Powder contamination is a hazardous effect of powder recycling [122]. The powder is frequently exposed to the air during the sieving process, and, therefore, this could cause oxides. Relating to this, the surface of spattered particles of 316L steel, AlSi10Mg and Ti6Al4V alloy that potentially could not be sieve out in the sieving process, have been deeply investigated by Simonelli et al. [123]. Selective oxidation phenomena were observed on 316L and AlSi10Mg particle surfaces after sieving (Fig. 15). The investigated oxides contained chemical elements featuring an excellent affinity to oxygen and thus more inclined to oxidation. Moreover, surface oxides can be disrupted by the laser energy in further reuses and embedded into the molten pool upon the rapid cooling [23,41]. As described in 1.3.3, powder oxides have a detrimental effect on the densification mechanism forming layer oxides in LPBF*ed* parts [41]. As such, the higher porosity found in AlSi10Mg samples built with recycled AlSi10Mg powder has been ascribed to the formation of oxide layers [133]. These oxides also acted as brittle particles with adverse influence on tensile performances [133]. However, powder contamination can be alleviated by adopting strict preventive steps, as do not leave the powder for a longer time in contact with air while sieving powder for reuse. For instance, Mamooun et al. did not found any significant differences between virgin and recycled AlSi10Mg powder after 18 reuse cycles [134].

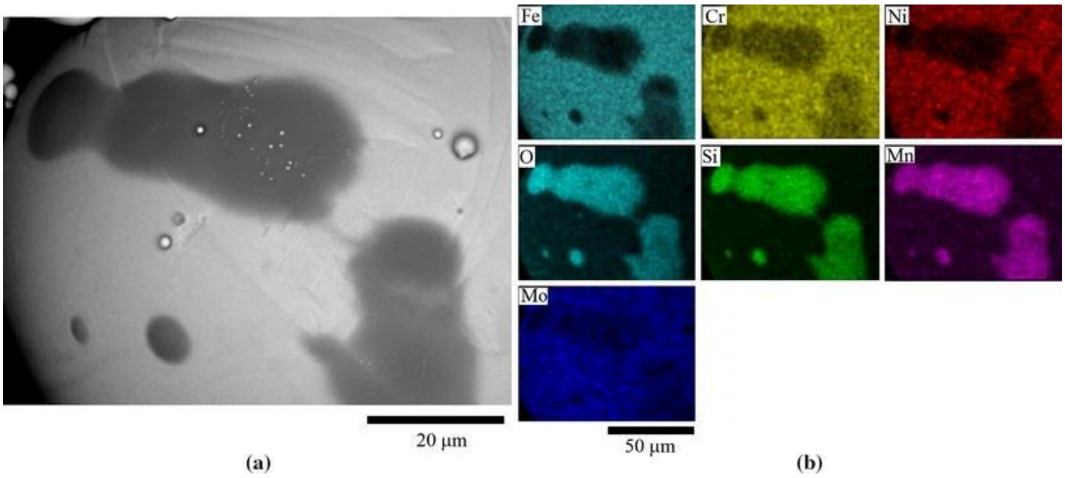

Fig. 15 (a) SEM and (b) EDS investigations on the surface of 316L steel spattered particles. It is clearly visible the presence of oxides patches on the powder surface consisting of mainly Si and Mn [123].

1.4 Physical interactions in LPBF

The laser melting process can be considered as the result of physical interactions between laser and powder bed (Fig. 16). These physical phenomena include the laser absorption, the heat transfer through radiation, convection, and conduction, the material phase transformations, and the melt pool flow induced by a surface tension gradient [135]. Three key stages represent the main laser-powder interactions occurring during LPBF: heating, melting, and consolidation of the powder bed [33,136,137].

In the heating stage, a fraction of the total laser energy is absorbed, increasing the temperature of the powder bed surface. Then, the absorbed heat is dissipated into the surrounding areas by conduction through the previously consolidated powder layers. Also, in this phase, heat is transferred by convection (in the molten pool) and evaporation. The heating process goes on until the powder bed will absorb the amount of heat required to reach the melting temperature of the processed alloy. When the melting stage begins, a liquid melt pool is rapidly formed. Here, a local temperature fluctuation creates a surface tension gradient, which in turn origins the melt flow. Such melt material is mixed into the liquid pool by the thermocapillary flow, also known as Marangoni convection. When the extracted heat from the melt pool becomes higher than the absorbed heat, the melt pool rapidly cools down to the ambient temperature, and thus a consolidated powder layer is formed.

In the next sub-sections, an overview of the principal physical interactions taking place in LPBF is given. The physical phenomena related to fluid behavior, such as wetting, thermocapillary effects, and capillary instabilities will be first described. Besides, the evaporation phenomena is explained paying attention to the impact of the recoil pressure on the melt pool dynamics. Finally, the solidification process will be described focusing on the varied solidification mechanisms that may be encountered during cooling.

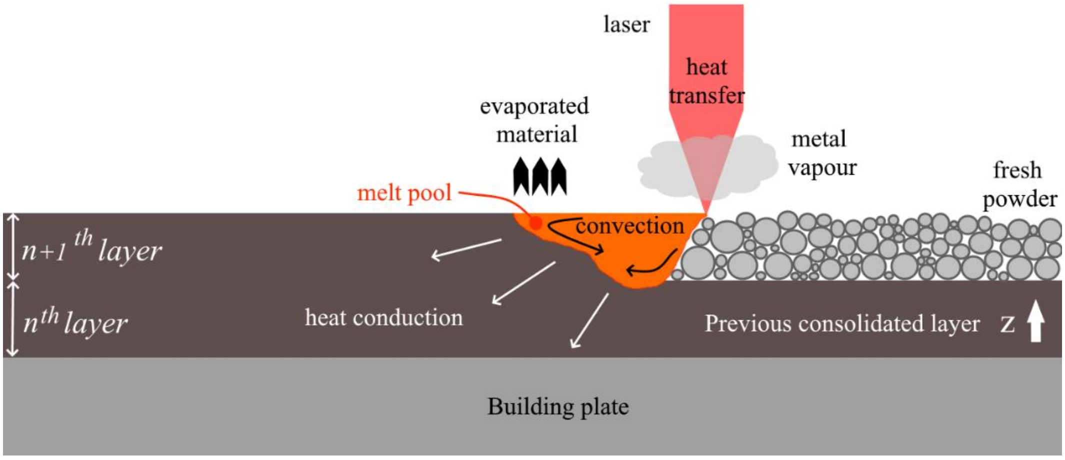

Fig. 16 Schematic representation of a layer consolidation process throughout LPBF.

1.4.1 Wetting

In LPBF, heating the powder bed leads to the formation of a melt pool. The melt pool is considered as the fundamental 'brick' upon which the whole 3D 'building' is manufactured. Based on many studies, it can be inferred that the melt pool shape and its size significantly affect the densification mechanisms and the overall mechanical performances of printed parts [53,64,138]. Consequently, the wetting behavior of the processed alloy has a significant impact on the melt pool characteristics [71]. Also, this property determines the spreadability of the molten alloy during printing.

The ideal wetting behavior of a liquid on a solid substrate can be defined by Eq. (1.3), widely known as the Young equation [139]:

$$\cos\theta = \frac{\gamma_{SV} - \gamma_{LS}}{\gamma_{LV}} \tag{1.3}$$

where θ is the contact angle formed by a liquid drop on a smooth and chemically homogeneous substrate at a given pressure and temperature; and γ_{SV}, γ_{LS}, γ_{LV} are the surface tensions related to solid-vapor, liquid-solid and liquid-vapor interfaces, as depicted in Fig. 17.

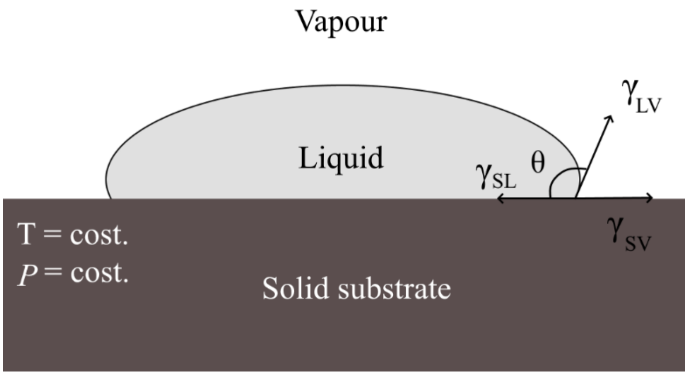

Fig. 17 Wetting of a liquid drop on a solid substrate.

It is worth to point out that the Young equation requires perfect smoothness and chemical homogeneity to be valid [139]. In LPBF, however, the boundary conditions are more complicated than the ideal condition defined by the Young equation. First, the building substrate or the underneath consolidated layers are not theoretically smooth [37]. In the case of the deposited layer, indeed, the powder particles create a slight surface roughness. As a consequence, the apparent contact angle can be different than the actual melt pool contact angle. Second, the liquid alloy wets a solid layer with a similar chemical composition [71]. As evidenced by Schiaffino and Sonin, this particular condition, defined as 'homologous wetting', involves simultaneous non-equilibrium phenomena, such as heat transfer, fluid flows, and a dynamic solidification front at the liquid-solid interface [140]. Third, oxidation of the substrate can negatively affect the melt pool wettability [71]. The liquid alloy could not wet the layer underneath because of the low surface energy typical of metal oxides. Thus, molten metal may prefer to reduce its specific surface by forming a spherical drop, giving rise to balling defects.

1.4.2 Thermocapillary flow

In LPBF, the temperature distribution at the melt pool surface is not homogeneous, creating a significant temperature gradient $\frac{dT}{dx}$. Consequently, a liquid-vapor surface tension gradient $\frac{d\gamma_{LV}}{dT}$ is formed likewise [28,141]. It is known from the literature, indeed, that the surface tension gradients $\frac{d\gamma_{LV}}{dT}$ of most metals or alloys have a strong dependence on the temperature T [139]. Hence, thermocapillary fluid flows may arise in the melt pool from regions at lower surface tension to areas at a higher surface tension. The intensity of such flow is generally quantified by the dimensionless Marangoni number M_a, defined by Eq. (1.4) [139]:

$$M_a = \frac{d\gamma_{LV}}{dT} \cdot \frac{dT}{dx} \cdot \frac{L}{2\eta\delta} \tag{1.4}$$

where L represents the characteristic length of the melt pool, η is the alloy viscosity, and δ the diffusivity.

The direction of Marangoni flows is defined by the sign of the liquid-vapor surface tension gradient $\frac{d\gamma_{LV}}{dT}$, as depicted in Fig. 18. When $\frac{d\gamma_{LV}}{dT}$ is negative (Fig. 18a), the surface tension γ_{LV} shows a higher relative value at the pool edge (colder area) and, on the contrary, a lower one in the middle region (hot area). Thus, an outward melt flow following the radial direction from the center to the melt pool border is formed. Besides, a shallow and wide molten pool is generated [28]. This phenomenon takes place for many pure metals and alloys, which exhibit a negative linear relationship of surface tension γ_{LV} vs. the increasing temperature T [142]. When $\frac{d\gamma_{LV}}{dT}$ is positive (Fig. 18b), the surface tension γ_{LV} is higher in the area showing higher T (the melt pool center), originating an inward fluid flow from the edge to the center of the melt pool. Consequently, a deep and narrow melt pool is formed [28]. This latter scenario is characteristic of alloys with a high amount of ‘surface-active elements’ such as oxygen and sulfur in iron melt pool [143–145]. However, when an excessive content of active elements is present in the melted alloy, the melt pool shape may change. Concerning this, Niu and Chang studied the origins of the single scan track instabilities obtained processing steel powders via selective laser sintering (SLS) [145]. It was shown that steel powder featuring a higher oxygen content were more prone to consolidate in ball shapes. They ascribed this behavior to the larger inward Marangoni convection induced by the positive surface tension due to the oxygen dissolution in the alloy. Similarly, the oxidation phenomena greatly affects the thermocapillary flow [141,144]. Oxidation is more significant at the melt pool border, and it remarkably lower down the surface tension on this area, thus promoting large inward melt flows and balling defects as well [144].

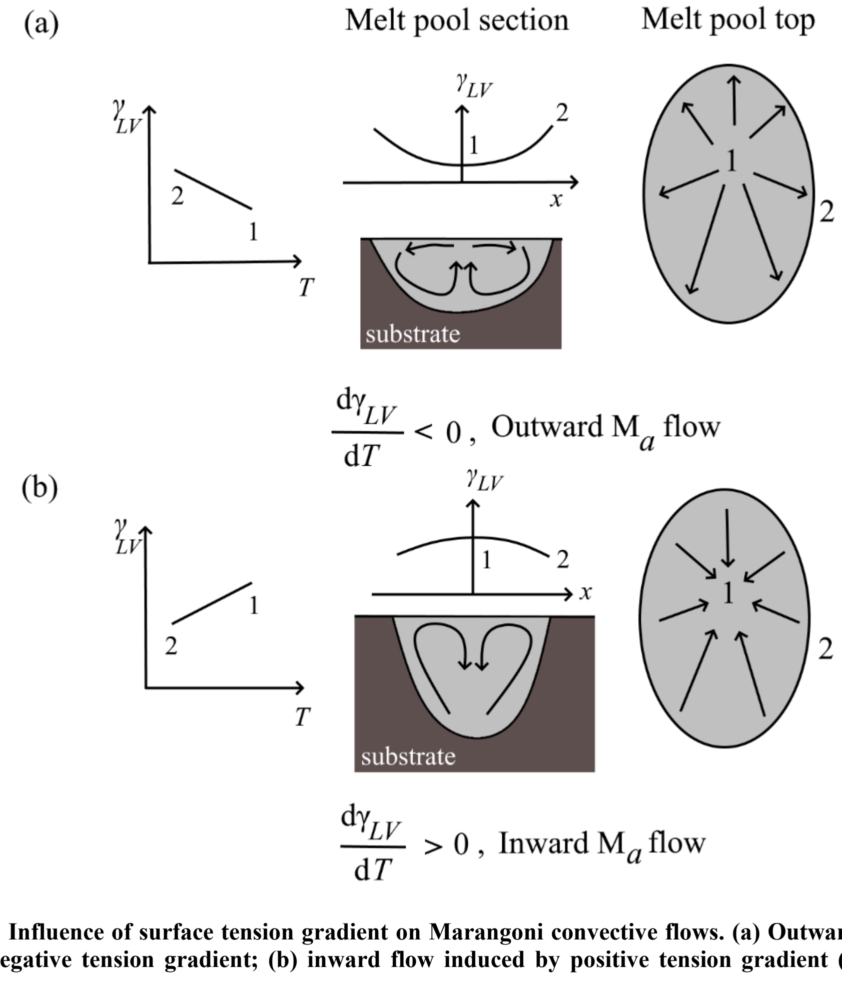

Fig. 18 Influence of surface tension gradient on Marangoni convective flows. (a) Outward flow caused by a negative tension gradient; (b) inward flow induced by positive tension gradient (adapted from [144]).

1.4.3 Capillary instability

The capillary instability, also known as Plateau-Rayleigh instability, describes the phenomenon of the rupture of a free cylinder of fluid into multiple droplets

[146]. The driving force of this phenomenon is represented by the fact that the liquid tends to lower the total surface free energy of the system, forming droplets with a reduced surface area. The cause behind the capillary instability is the presence of small perturbations in the free fluid cylinder that may vary its circumference. According to the Plateau theory, a circular liquid cylinder becomes unstable when the axial harmonic perturbation has a wavelength higher than the cylinder circumference [146]. Generally speaking, the instability occurs when a sector of the free fluid stream excessively grows owing to the perturbation and, thus, its size exceeds the original cylinder circumference, as illustrated in Fig. 19. The stability criterion for a fluid stream of a radius r disturbed by a wavelength of length λ is expressed by Eq. (1.5) [146,147]:

$$\lambda < 2\pi r \tag{1.5}$$

which corresponds to Eq. (1.6) after replacing the radius value r with the cylinder diameter D:

$$\frac{\pi D}{\lambda} > 1 \tag{1.6}$$

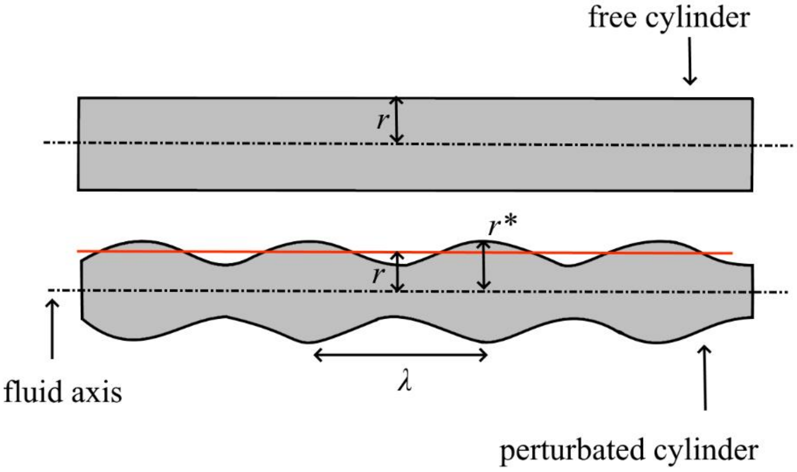

Fig. 19 Schematic representation of a fluid cylinder in the free state and the perturbated state.

In LPBF, the capillary instability may occur immediately after the melting of a single scan track, giving rise to humping [148] or balling defects [51,149]. In this specific case, however, the melt pool is not a free circular cylinder being in contact with the substrate or a layer underneath. Therefore, a segmental cylinder with a circular segment as cross-section is formed (see Fig. 20a). Accordingly, also the stability criterion of Eq. (1.6) changes into the more complex Eq. (1.7), as suggested by Yadroitsev et al. [51]:

$$\frac{\pi D}{\lambda} > \sqrt{2}\sqrt{\frac{\phi(1+\cos 2\phi)-\sin 2\phi}{2\phi(2+\cos 2\phi)-3\sin 2\phi}} \tag{1.7}$$

where ϕ is the angle defining the extent of contact with the substrate. The segmental cylinder is stable when the ϕ ranges between 0 and $\frac{\pi}{2}$ and, it may form droplets when higher than $\frac{\pi}{2}$. For ϕ equals to π, the cylinder is circular but still attached to the substrate, which is different from the ideal theory of Plateau-Rayleigh. Thus, replacing ϕ with π in Eq. (1.7), the limit of stability for the melted single scan track is obtained and given in Eq. (1.8).

$$\frac{\pi D}{\lambda} > \sqrt{\frac{2}{3}} \tag{1.8}$$

This adapted instability limit has a lower value than the one of the starting Plateau-Rayleigh theory.

The study performed by Yadroitsev also revealed that at very high scanning speed values, the capillary instability of the liquid single scan track is promoted [51]. As can be seen in Fig. 20b, by increasing the speed, the contact angle of stainless steel single scans shifts from $\frac{\pi}{2}$ at 0.06 m/s to π using 0.20 m/s, thus forming a ball in the latter case. Hence, it is reasonable to argue that the maximum scanning speed limit value is related to the lack of contact between the scan track and the substrate.

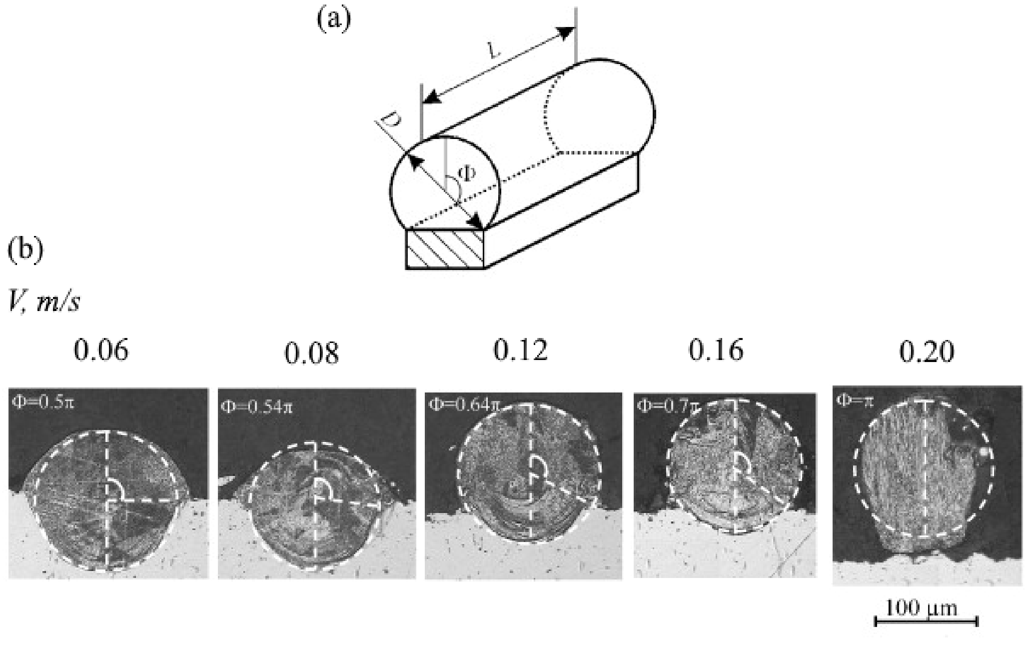

Fig. 20 (a) Segmental cylinder with a segmented cross-section bound by the substrate; (b) SS 904 L melt pool cross-sections processed at different scanning speed values. The contact angle increases as the scanning speed is increased (adapted from [51]**).**

1.4.4 Recoil pressure

In LPBF, the evaporation of the processed material is often observed due to the high energy density delivered by the irradiating source [150]. The intense irradiation of the laser, indeed, significantly increases the surface temperature of the molten pool. Once the melt pool temperature exceeds the boiling point temperatures of the inner chemical elements, evaporation gets started. Consequently, the high number of evaporated particles will form a vapor plume located on the melt pool surface, exerting intense pressure on it. Then, a recoil pressure P_r is caused due to the difference of the vapour plume pressure and the atmospheric pressure. The direction of the recoil pressure is normal to the melt pool surface [150] (Fig. 21).

The recoil pressure P_r depends on the equilibrium vapor pressure P_s, which in turn depends on the melt temperature T_s, as shown in Eq. (1.9) [150,151]:

$$P_r = AP_s(T_s) = AB_0 {T_s}^{-1/2} e^{(-U/T_s)} \tag{1.9}$$

where A is a numerical constant, B_0 the vaporization rate constant and U a parameter related to the latent heat of evaporation.

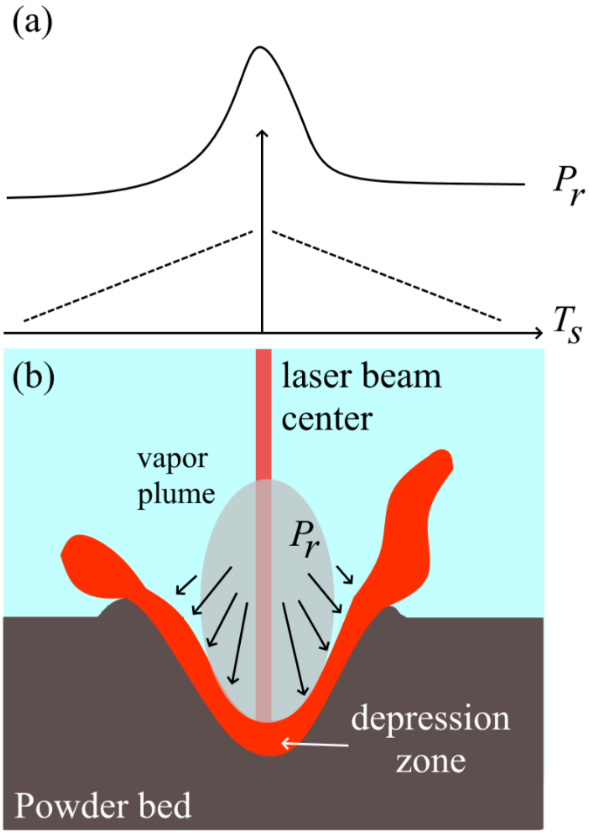

Fig. 21 (a) Recoil pressure dependence on temperature ([152]) and (b) the schematic representation of the vaporization-induced recoil pressure on the molten pool.

Considering that P_r is exponentially dependent on the melt temperature, the recoil pressure dominates the fluid flow dynamics in the areas of the melt pool at the highest temperature, i.e. the area exposed to the center of the laser beam [152] (Fig. 21a). As a consequence of this, when using high power, the recoil pressure quickly increases in that area with severe effects on the melt pool shape and dimension [153]. On the one hand, a depression zone is formed in the melt pool center, pushing the liquid alloy at the melt pool edge with a high velocity (Fig. 21b). Therefore, it follows that the melt pool diameter is enlarged with a mechanism similar to the outward thermocapillary flows (Section 1.4.2) [153]. On the other hand, the vapor-induced surface depression also allows the heat dissipation into the material depth, promoting the melt pool penetration [96]. Thus, a V-shape melt pool may form. When an excessive laser power is used, this latter effect can be exacerbated, causing further evaporation at the melt pool cavity. Afterward, when the depression collapses during cooling, gases can be entrapped in the melt pool cavity, forming the so-called keyhole pores [96]. This mechanism of pore formation (keyholing), indeed, is a consequence of the keyhole melting mode, which occurs at high laser intensities, as observed in welding and drilling [154]. Apart from keyholing, an intense recoil pressure can also trigger the spatter formation mechanism [96]. As noted by Khairallah et al., the liquid metal located at the depression front is spilled either at the melt pool edge or ahead of the laser beam with a very high velocity (4 m/s). Consequently, the ejected liquid will be deposited onto the colder powder bed, forming spatter particles upon consolidation.

1.4.5 Solidification

Solidification is generally defined as the material transition from liquid to solid. In LPBF, this phenomenon happens when the extracted heat from the liquid melt pool is higher than the absorbed heat from the laser source. In this scenario, the melt pool rapidly cools down, and it becomes undercooled to a large extent. Consequently, the solidification gets start almost instantly driven by the high degree of undercooling ΔT [155].

During this transition, the nucleation of crystals at the solidification front is possible when the energy barrier ΔG for the nucleation of a crystal is overcome, as shown by Eq. (1.10):

$$\Delta G > \frac{4\pi {\gamma_{LC}}^2 {T_m}^2}{3(\Delta H_m \Delta T)^2}(2 - 3\cos\theta + \cos\theta^3) \tag{1.10}$$

where γ_{LC} is the surface tension at the crystal-liquid interface, T_m the equilibrium melting temperature, ΔT the undercooling number, ΔH_m the latent heat of melting of the processed material, and θ the contact angle [155]. As can be deduced from Eq. (1.10), the high undercooling ΔT produced by the rapid solidification process significantly decreases the energy barrier for crystal nucleation. Furthermore, the molten pool completely spreads on the previously consolidated material, thus reducing the contact angle θ near zero. Both factors promote the nucleation of crystals at the melt pool boundary. Hence, the crystal seeds first nucleate upon grains of the underlying solid substrate and then grow inheriting the existing crystallographic orientation, as depicted by Fig. 22 [155,156]. The described mechanism of crystal growth initiation is called epitaxial solidification, and it has been widely studied in welding as well as in additive manufacturing technologies [76,157].

Once crystals started the epitaxial solidification, they grow into the liquid melt. As known from metallurgy literature, some metal grains have a preferential growth direction [158]. As an example, Liu reported that the preferred growth direction of grains in a LPBF*ed* AlSi10Mg alloy is <100> [159]. Consequently, the crystals nucleated at the melt pool border, and oriented along the easy growth direction, grow faster at the expense of the less optimal oriented ones. Due to this mechanism, also referred to as competitive growth (Fig. 22), unfavoured crystals will be smothered between large crystals and cannot further grow. Apart from the competitive growth, the extent of the crystal growth and its solidification mode mainly depend on two factors: the growth rate R and the temperature gradient G [155].

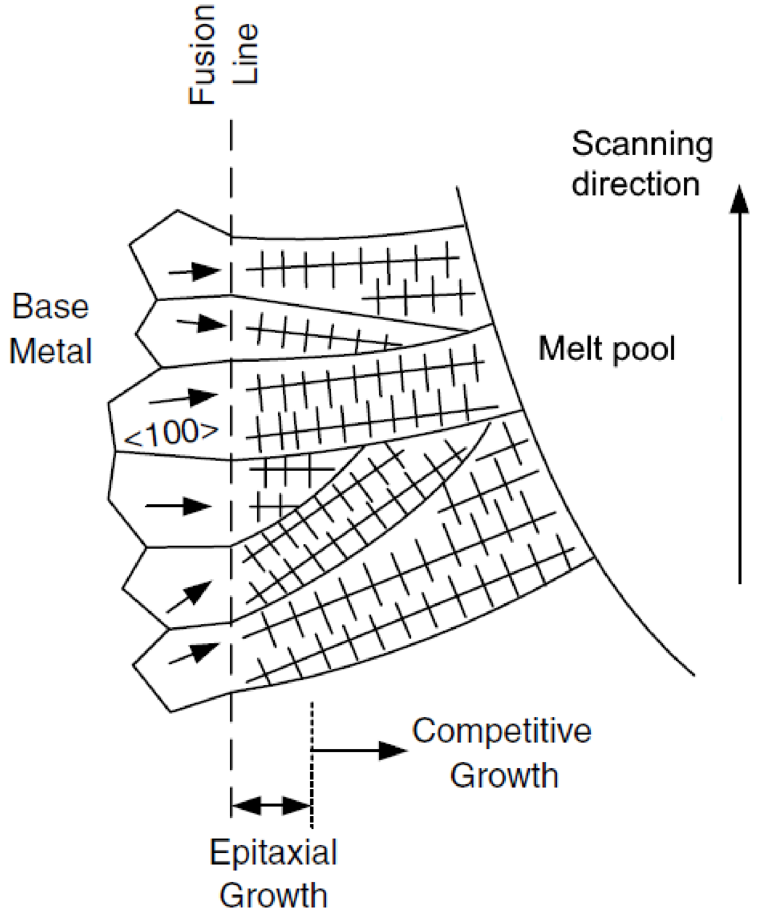

Fig. 22 Epitaxial solidification and competitive growth at the melt pool boundary (adapted from [155]**).**

The growth rate R, also called solidification rate, is given by the ratio $\frac{dx}{dt}$, which corresponds to the displacement dx of the crystal solidification front in the time unit dt [158,160]. According to Eq. (1.11), the growth rate is directly dependent on the scanning speed V and the angle α formed between the scan direction and the normal to the melt pool border:

$$R = V\cos\alpha \tag{1.11}$$

Two general conclusions can be drawn by Eq. (1.11). First, the growth rate is generally higher when processing at elevated scanning speeds. Second, the growth rate has not a constant value along with the melt pool border. Regarding this, the R value varies according to $\cos\alpha$ function and it reaches the minimum value at the fusion line and the maximum at the centerline, as illustrated in Fig. 23.

The temperature gradient G is defined by the ratio $\frac{dT}{dx}$ and refers to the temperature variation dT in a space interval dx of a melt pool. Considering the small volume of the melt pool and the elevated local temperatures during melting (1000-4000 K), the temperature gradient quickly gets close to 5-20 K/µm in LPBF [161]. However, as for the growth rate R, also the thermal gradient G changes in the melt pool area. This fact is due to the nature of the laser source. In the case of a Gaussian laser type, indeed, the highest melt temperature T_{max} is reached at the melt pool front while the lowest T_L at the melt pool border [160]. Consequently, assuming a quasi-elliptical melt pool shape (Fig. 24), the temperature gradient value is greater at the fusion line than that at the centerline. Therefore, G and R values change in opposite directions along the melt pool boundary [136].

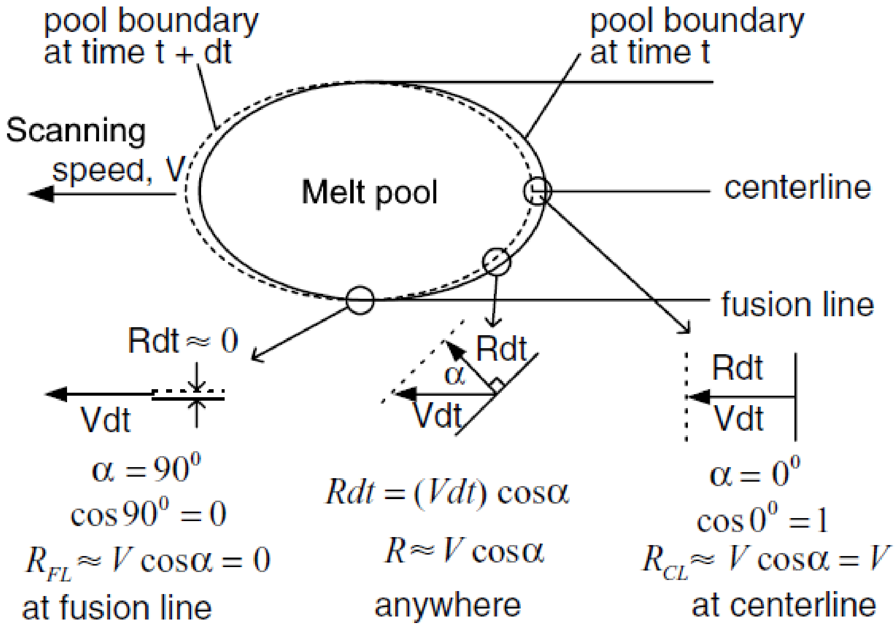

Fig. 23 Growth rate variation along the melt pool border [160].

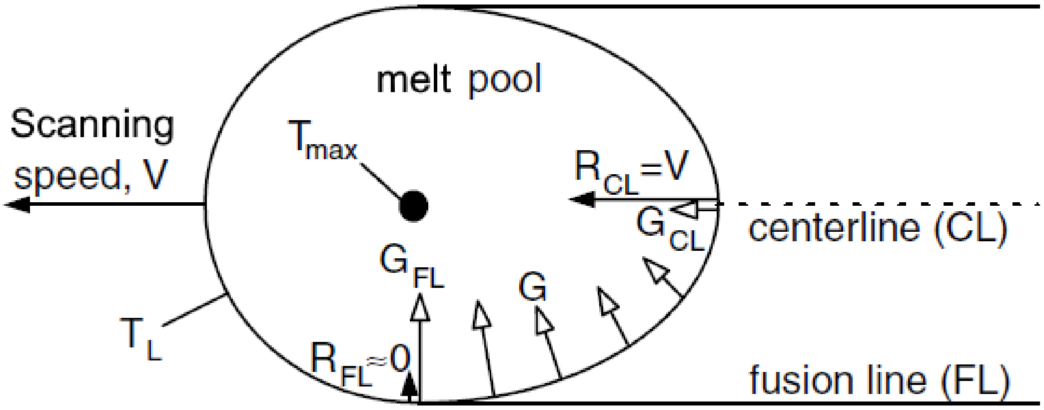

Fig. 24 Temperature gradient variation along the melt pool border [160].

The combined effect of R and G plays a vital role on the overall microstructure upon solidification. Specifically, the product $G \times R$ refers to the cooling rate (K/s) of the melt during solidification [156]. It is given by the ratio $\frac{dT}{dt}$ and describes the temperature variation in the time unit. As such, the cooling rate directly determines the amount of undercooling, which in turn affects the size of the solidified structure [162]. This effect was observed by many investigators [91,133,163].

Other than the cooling rate effect, which determines the fineness of the microstructural features, the G/R ratio affects the microstructure as well [162]. In this latter case, the number of G/R directly governs the solidification mode, which can be planar, cellular, columnar dendritic or equiaxed dendritic (Fig. 25) [156,162]. According to the Chalmer's theory of constitutional undercooling [164], the solidification front is generally planar but it can break-down by a severe thermal undercooling. Therefore, in LPBF, the planar front is easily broken by the high ΔT achieved during the rapid solidification. Consequently, cellular or dendritic architectures coexist with the liquid phase in the undercooled areas of the melt, namely the melt pool regions where the melt temperature is below the liquidus temperature T_L [162].

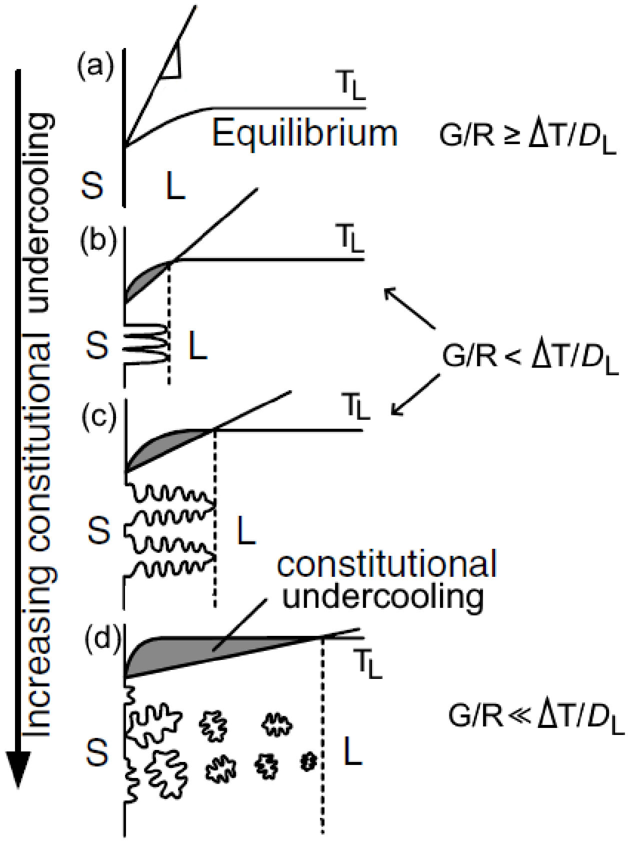

Fig. 25 Effect of the G/R ratio on the solidification mode: (a) planar, (b) cellular, (c) columnar, and (d) equiaxed dendritic (adapted from [162]**).**

The G/R ratio is defined by Eq. (1.12):

$$\frac{G}{R} = \frac{\Delta T_0}{D_L} \tag{1.12}$$

where ΔT_0 is the temperature solidification range and D_L is the diffusion coefficient of the solute atoms at the solidification front in the near liquid region [162]. The G/R ratio corresponds to the slope of a line on the liquidus temperature T_L vs. the solidification front distance diagram, as depicted in Fig. 25a. When a planar interface is growing, the G/R ratio is higher than the $\Delta T_0/D_L$ value (Fig. 25a). This is the steady-state condition for a planar growth. When the G/R value decreases, the G/R line may intersect the $T_L$curve forming a constitutional undercooled area. Consequently, the planar front is locally destabilized and protrusions start growing into the liquid undercooled regions (Fig. 25b). Thus, a cellular structure is formed. If the G/R value further decreases, the constitutional undercooled region can expand and the native cellular structure can evolve in a columnar architecture with side branches, forming the columnar dendrites (Fig. 25c). If the temperature gradient continues to decrease, the high constitutional undercooling promotes the spontaneous nucleation in the liquid and the subsequent growth of equiaxed dendrites (Fig. 25d).

1.5 Defects

Defects are common issues in LPBF. Although the LPBF process offers the possibility to manufacture near net shape components, this technology is regulated by many factors such as the process parameters (Section 1.2), the powder properties (Section 1.3) and the laser-powder physical interactions (Section 1.4).

The factors mentioned above may influence, for example, the densification level leading to the formation of varied types of porosities. The main types of porosities and their formation mechanisms are described in sub-section 1.5.1. Furthermore, the high-temperature gradient of LPBF coupled with the presence of internal residual stresses formed upon cooling may also induce internal cracks in the material. The cracking mechanism is then presented in sub-section 1.5.2. This section describes two further LPBF defects such as the balling (sub-section 1.5.3) and the spattering (sub-section 1.5.4), both detrimental for part performances.

The distortion of manufactured parts caused by internal residual stresses represents a further typical defect of LPBF. The mechanisms behind the residual stress formation and the related part distortion is described in Section 5.4, being part of the experimental activities of the thesis.

1.5.1 Porosities

The most common defect in the printed components is porosity, regardless of the processed alloy. Based on their formation mechanisms and characteristics, the porosities can be classified into three types: gas-related pores, lack of fusion pores, and keyhole pores.

Gas pores, also known as metallurgical or hydrogen pores, are of small size (less than 10 μm), featuring almost a spherical shape [165] (Fig. 26a). A gas pore is generally formed when a gaseous matter has been entrapped into the molten alloy upon solidification. Varied mechanisms imply the formation of such type of pores. One cause has been identified in the process gas trapped within the gas-atomized particles since it may be released during the powder melting [129]. Still related to the powder properties, the presence of moisture on powder surfaces produces gas pores as well [127]. As discussed in Section 1.3.3, the chemical bonds of adsorbed hydroxides are broken up by the intense laser beam energy, releasing hydrogen gas. In particular, considering aluminum alloys, the powder moisture could react with the molten aluminum leading to the formation of alumina oxides (Al_2O_3) and hydrogen as by-products of the chemical reaction. Furthermore, it has been found that a low packing density of the powder bed can promote the gas pores formation as well [165]. The gas existing among powder particles, indeed, may not come out of the molten pool before solidification due to the high cooling rate of LPBF. Apart from the powder properties, also the process atmosphere induces the retention of gas porosity [166]. For instance, Elmer et al. found that welds produced by using an inert shielding gas, such as Ar, showed a higher number of pores compared to the ones obtained using the N_2 atmosphere.

In fact, being Ar insoluble in the liquid metal, it may be entrapped as a gas bubble unless it quickly floats out of the melt pool. On the contrary, the high reactivity of N_2 in stainless steel alloys does not result in pores formation. Lastly, the high local temperature reached under the laser beam may have detrimental effects on porosity, increasing either the gas solubility in the liquid metal or the vaporization of low melting alloy elements [167].

Lack of fusion pores generally possess an irregular shape with a large size (up to 100 µm or more) (Fig. 26b). The origins of these pores are related to the improper coupling of the process parameters, as described in detail in Section 1.2. They are ‘fusion errors’ caused by an insufficient energy density delivered to the powder bed [165]. Thus, the low energy hinders the formation of optimal metallurgical bonds between the neighboring single scan tracks or the layers underneath [49]. As a result, irregular and sharp voids are formed, and occasionally unmelted particles can be entrapped therein. The lack of fusion voids can be minimized by adopting process parameters suitable for a proper melt pool shape, which ensures a sufficient penetration and a proper overlapping with the adjacent tracks [168]. Broadly speaking, this would be possible working within the conduction regime at a quite high laser power values coupled with medium-low scan speeds [169]. However, one must be careful when tuning power and speed values to achieve the desired melt pool shape. The reason is that it could accidentally shift to the keyhole regime and encounter in keyhole porosities when an excessive energy density is deployed [54].

The keyhole pore appears as a large cavity with a size up to 100 µm at the bottom part of the melt pool [170] (Fig. 26c). Keyhole porosities are produced processing at a high laser intensity. The formation of keyhole porosities is the direct consequence of the intense recoil pressure generated at a high power level due to the metal evaporation (see Section 1.4.4) [96]. During melting, indeed, the molten metal collapses on itself and the gaseous metal vapor gets trapped into the melt pool depth. Consequently, a melt pool featuring a narrow and deeper corridor with a large cavity at the end is formed.

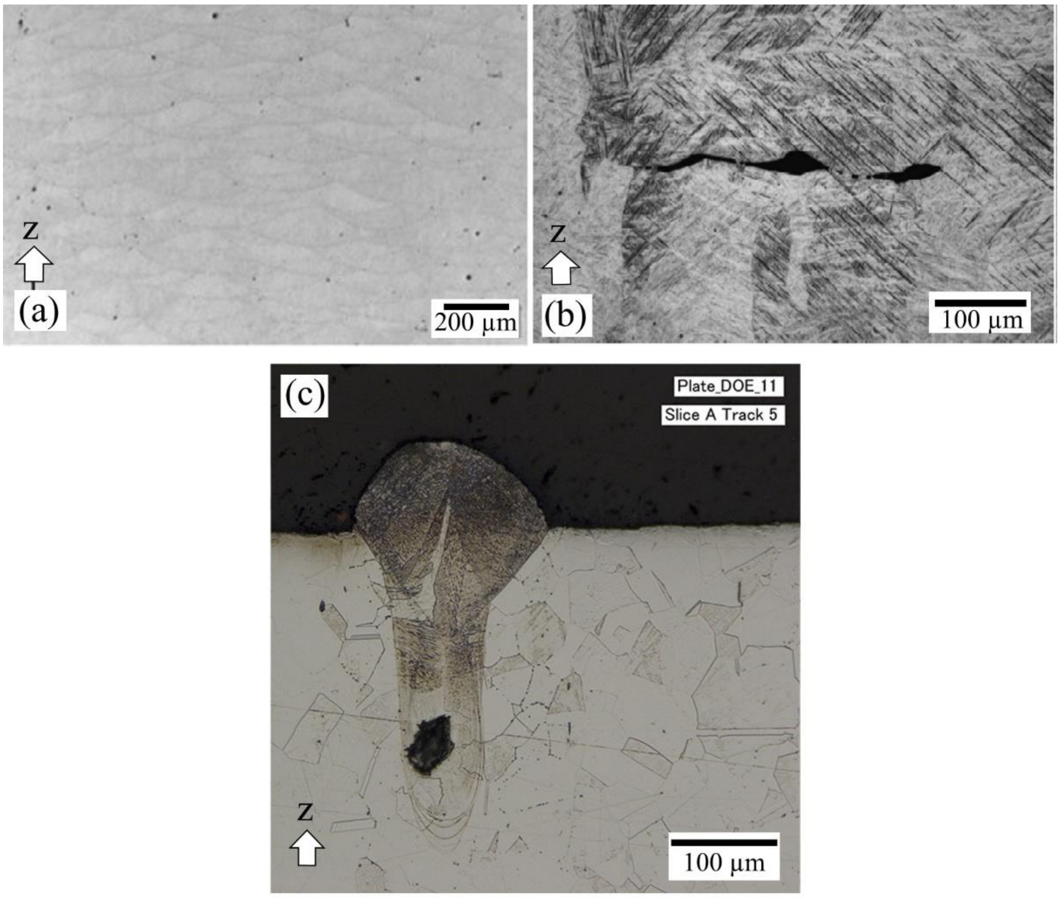

Fig. 26 Types of porosities that may be encountered upon solidification. Low magnification micrographs of (a) hydrogen porosities in SLM*ed* AlSi10Mg alloy [127]**, (b) lack of fusion voids between two layers of a SLM*ed* Ti6Al4V alloy** [171]**, and (c) keyhole pore in a melt pool of 316L steel processed by LPBF** [170]**.**

1.5.2 Cracking

In LPBF, the processed alloy experiences a rapid transition from the melt to the solid-state because of the high-temperature gradient and the resulting cooling rate. Consequently, thermal residual stresses are formed upon cooling and the crack formation and propagation may be triggered. Similarly to laser welding, a cracking mechanism, known as liquation cracking or hot tearing, has been identified in some LPBF alloys [165].

Liquation cracking has been found in alloys which develop a dendritic microstructure during cooling [172,173]. It generally occurs in the mushy zone of a melt pool, namely a semi-solid region near the molten pool where the solid dendritic architecture coexists with its interdendritic liquid. The cracking mechanism gets start at the final stage of the solidification process when dendrites are fully grown in grains and just divided by a thin film of liquid (Fig. 27). At this stage, the solidified dendrites would contract upon solidification, however, the contraction can be inhibited by the presence of tensile stresses induced by rapid cooling. As a consequence, solidified dendrites tend to shrink in the direction of the tensile stresses and a crack may form and propagate through the intergranular region as depicted in Fig. 27.

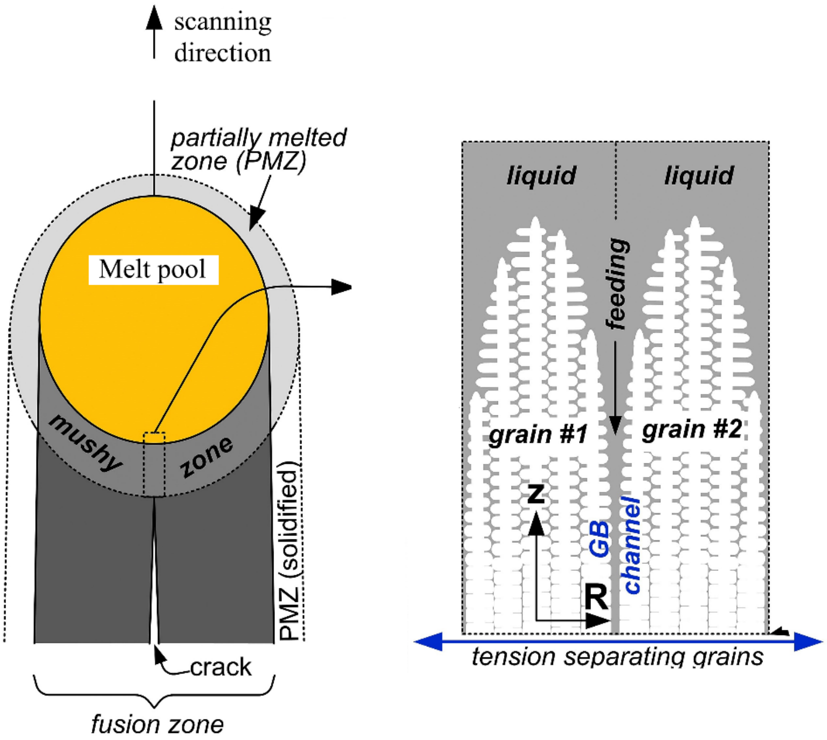

Fig. 27 Mechanism of crack initiation (adapted from [173]**).**

The liquation cracking depends on the tendency of the alloy to liquate during LPBF [172]. The higher the liquation extent, the greater is the possibility of encountering liquation cracking. The liquation tendency during LPBF increases when the alloy has a high solidification range. This phenomenon has often been observed in the high strength age-hardenable alloys [174]. The presence of elements such as Cu, Mg, and Zn yields indeed to extended solidification ranges. Furthermore, the tendency to liquation is also induced by the presence of segregations at the grain boundaries, which liquates at low melting points, as observed for some nickel superalloys [175].

It has been demonstrated that the liquation cracking has a detrimental effect on the mechanical properties of manufactured parts [23]. Therefore, researchers have worked to find some remedies for liquation cracking [174,176,177]. An effective strategy is to dilute the composition of the master alloy by adding chemical elements in order to increase the eutectic phases with low melting points. Regarding this, Montero Sistiaga and co-workers successfully inhibited the formation of the cracks in the wrought 7075 aluminum alloy by adding 4 wt% of Si [176]. The reason for their result is twofold. On the one hand, Si decreased the alloy melting temperature, forming a second eutectic at a lower temperature. The cracks formed at the last stage of solidification were then filled by the low melting point liquid eutectic. On the other hand, the dendrites growth has been limited by the grain refinement effect of Si. Later on, Martin et al. reported an alternative approach for manufacturing crack-free Al 7075 alloy components by LPBF [174]. They decorated the particles surfaces of the master alloy with fine Zr particulates, which induced a grain refinement effect in the master alloy microstructure.

1.5.3 Balling

Balling has been classified as an unfavourable defect related to the laser technologies. The formation mechanism of the balling phenomena involves the complex fluid dynamic behavior of the molten pool [178]. As thoroughly discussed in Section 1.4, the physical properties of a melt fluid, namely wetting, thermocapillary flow and capillary instability, contribute collectively to the balling defects formation. Based on the mechanisms of balling formation, two types of balling have been identified by Gu and Shen in the Direct Metal Laser Sintering (DMLS) of 316L powder [101].

The first type of balling refers to the appearance of coarsened balls induced by a poor liquid formation during LPBF. Generally speaking, this phenomenon occurs when the energy density transferred to the powder bed is not enough for a full powder melting. Specifically, this scenario is induced when processing with low laser power or slow scan speed as well as by using a layer thickness largely higher than the powder bed height (Section 1.2). In these conditions, a liquid-solid mixture with a high viscosity is formed, thus promoting the formation of sintering necks or metal balls along the single scan track cylinder, as shown in Fig. 28a,b.

The second kind of balling is related to the formation of by-products balls flanking the scan track cylinder. It occurs when a consistent amount of melt is produced by processing at a high laser power coupled with a relatively high scanning speed. Due to the high scanning speed, the molten cylinder has a reduced diameter and, consequently, the liquid instability increases under the capillary instability effect (Section 1.4.3). In these conditions, the melt tends to splash from the melt cylinder surface, generating small spherical balls as depicted in Fig. 28c. Finally, at even higher scanning speed, the scan track will break into several droplets once overpassed the stability limit for the liquid cylinder [51].

The balling phenomenon has disadvantageous effects on the quality of printed parts. First, a consistent number of pores result from the presence of discontinuous scan tracks and metal balls [144]. The spread powder of the subsequent layer, indeed, may drop between the consolidated metal balls, giving rise to lack of fusion defects when shallow melt pools are formed during LPBF. Second, balling affects the surface quality of manufactured parts [68,179]. Therefore, a mechanical post-process treatment is often performed to improve the surface roughness and eliminate surface defects, such as surface metal balls, satellites and un-melted powders [179]. Lastly, in the case of an unusual metal balls formation, balls tend to hamper the movement of the recoater blade and may act as a wedge on the material underneath.

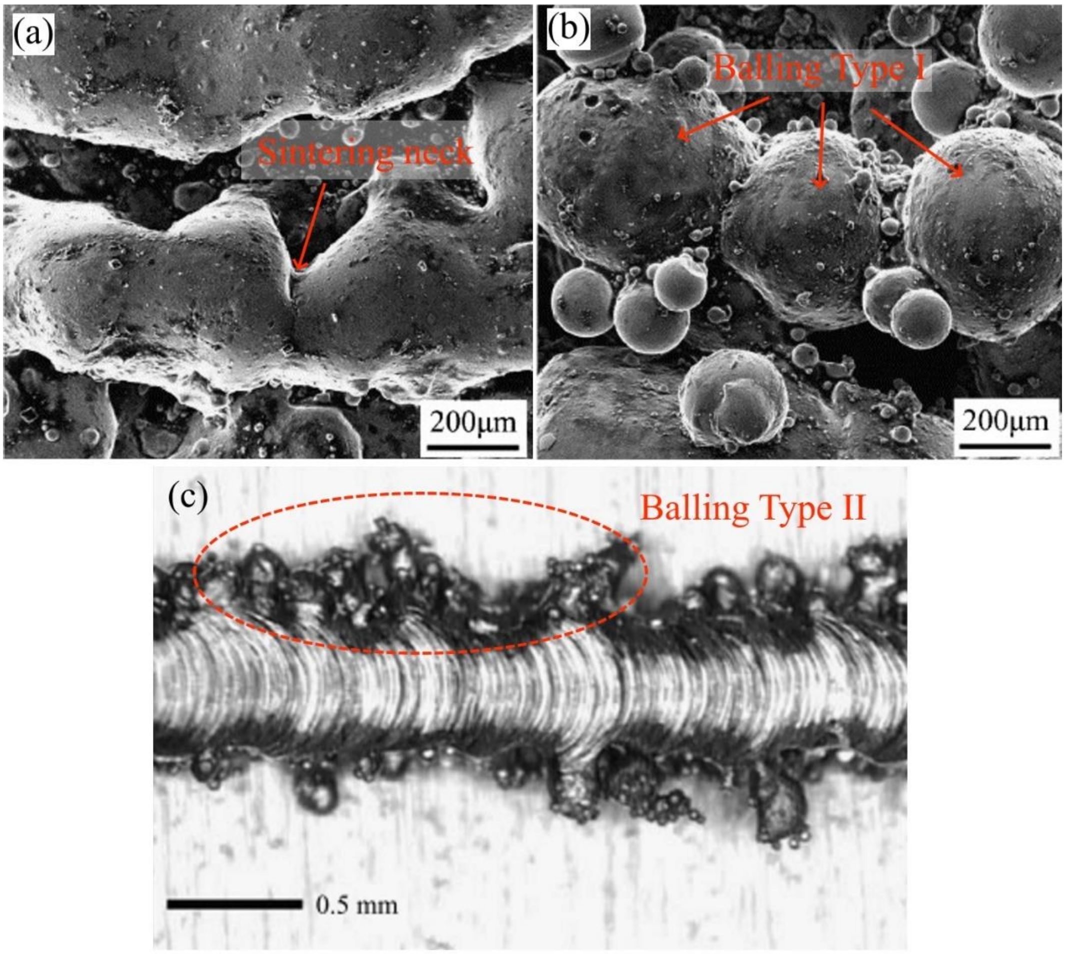

Fig. 28 (a) Sintering neck caused by an incomplete fusion process and (b) balling type I in single scan track of a Cu-based alloy [180]**. Similar type of balling has been identified by the Authors processing steel powder in Ref.** [101] **; (c) balling type II on a Inconel 625 scan track** [181]**.**

1.5.4 Spattering

Spattering has been commonly observed in traditional laser-based technologies such as welding, drilling, cutting and, also, in LPBF. The term ‘spattering’ refers to the mechanism of spatter formation (Fig. 29) [182].

As described in Section 1.5.4, the high energy density applied in a local area of the powder bed during LPBF creates a high recoil pressure on the molten pool. Later on, this high recoil pressure combined with the outward thermocapillary flow causes the melt ejection from the melt pool. This primary metallic jet is then crushed into small droplets under the laser irradiation effect, creating the droplet spattered particles. They still have a spherical shape but often exhibit a larger size compared to starting particles. Apart from the metallic jet, sideways gaseous jets made of conveyor vapor and un-melted particles are formed as well. Unlike the droplet spatters, these particles, known as the ‘sideways spatter’, maintain a similar particle size and shape [183].

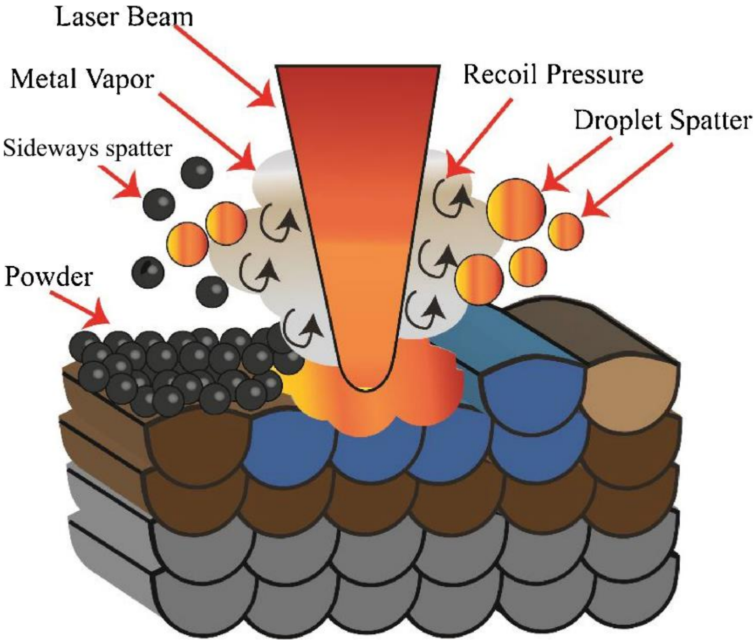

Fig. 29 Spatter formation from a metallic jet induced by the recoil pressure [182].

Once the spatter particles are created, they are conveyed away from the melt pool by the gas flow (see Section 1.2.8) [30]. If the laser scanning is in the opposite direction of the gas flow, spatter particles will be deposited onto the newly consolidated layer [45,184]. In this scenario, large spatter particles could cause severe issues during reacoting, such as the removal of the material underneath or the formation of grooves into the spread powder bed [94]. Furthermore, large spatter particles can worsen surface roughness when processing the skin parts.

On the contrary, when the gas flow has the same direction of the laser scanning, spatters will mix with the starting particles present in the powder bed particles ahead of the laser front, as depicted in Fig. 30a [45,184]. Here, a spatter particle (‘spatter A’ in Fig. 30a) with a size close to the layer thickness will melt, but this would not be possible, for example, when its size is much larger than the powder bed thickness (‘spatter B’ in Fig. 30b). In the latter scenario, the un-melted particle will get trapped as inclusion after the deposition of the subsequent layer (Fig. 30c,d).

Laser spattered particles can oxidize in-flight before landing on the powder bed [123]. This aspect represents a severe issue to face when recycling powder, as discussed in Section 1.3.4. Due to the ceramic patches on spatter surfaces, the spatter inclusion can act as crack initiation site under cycling loading fatigue tests. Regarding this, Aboulkhair et al. detected a spatter particle enriched in Mg, Si, and O_2 on the fractured surface of an AlSi10Mg sample processed by LPBF [185]. Still, iron-oxide spatters have been observed as embedded particles in fractured surfaces of LPBF*ed* 316L samples [183]. They are supposed to be the cause of their significantly low elongation to failure performance.

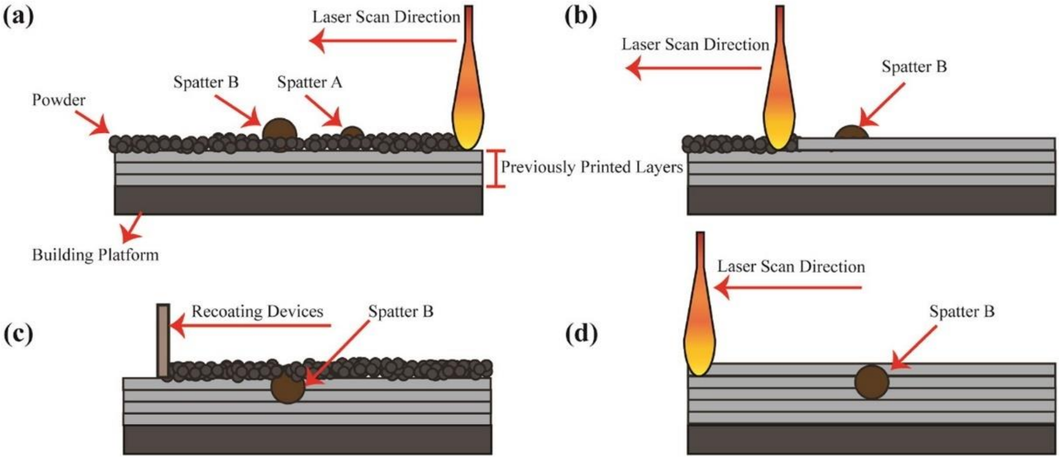

Fig. 30 Mechanism of the spatter particle entrapment during the recoating process [184]**.**

Chapter 2

Laser Powder Bed Fusion of Aluminium Alloys

Al-based alloys have received great consideration by the industries over the last decade, so as to be the second class of materials mostly printed by LPBF. As a consequence, a wide number of researches investigated processability, microstructures, heat-treatments, and mechanical properties of LPBF*ed* Al alloys. Therefore, the goal of this chapter is to provide a comprehensive state of the art on Al alloys processed by LPBF and contextualize the experimental results of the thesis.

After a summary of the main Al alloy systems for LPBF (Section 2.1), the metallurgy of Al alloys is revealed, describing the peculiar microstructures and the strengthening mechanisms of LPBF Al alloys (Section 2.2). Then, the chapter will go through the description of various post-process heat-treatment strategies, mainly T6, direct aging, and annealing (Section 2.3). Specifically, the influence of heat-treatments on the as-built microstructure is presented, and correlated with the change of the mechanical performances after heat-treatment (Section 2.4). Lastly, a particular focus has been given to the development of Al alloys specifically tailored for LPBF (Section 2.5).

2.1 Al alloys for LPBF

Aluminum alloys (Al alloys) have been employed in a wide range of industrial sectors such as aerospace, military defense, and automotive. Their properties guarantee a good strength coupled with a relatively low density, making them suitable for demanding applications where light-weight and high strength are required at the same time. Apart from these properties, aluminium has also a high thermal conductivity and a good corrosion resistance for applications as electrical conductors or salt-water service components, respectively [186].

The opportunity to manufacture complex structures with a high strength-to-weight ratio and thermal conductivity has driven the research on LPBF of aluminium alloys over the last decade. LPBF of Al alloys, as an example, has been widely employed to manufacture high-performance heat exchangers, lattice structures, and other advanced componentry [73,138]. Notwithstanding this, processing Al alloys has been found quite challenging because of the inherent properties of aluminium powder.

Al powder is generally characterized by scarce flowability, high conductivity along with a high reflectivity/low absorption, as shown in Table 4. Being the LPBF a layer by layer process, the poor flowability may cause severe issues in the recoating process leading to a non-homogeneous deposition of the powder bed and, thus, to the porosity formation. Besides, the high reflection of Al powder (91 % of Nd:YAG lasers) requires the adoption of high power lasers to melt the alloy completely [42]. Furthermore, the laser energy needed for the heating and melting is rapidly conducted away from the molten pool to the surrounding areas because of the high thermal conductivity of Al alloys [187]. Lastly, Al powder reacts quickly with oxygen forming oxide patches on the powder surfaces or oxide layers around the melt pool [41,123].

Table 4 Comparison of Al powder properties with stainless steel and titanium alloys [188].

LPBF alloy	Flowability (s/50gr)	Thermal Conductivity (W/m·K)	Reflectivity (%)
AlSi10Mg	No flow	172	91
AISI 316L SS	14.6	21.4	60
Ti6Al4V	47	6.7	53-59

Despite all the issues which limit the processability of Al alloys, near fully dense parts of cast aluminum alloys such as AlSi12 [189], AlSi7Mg [56] and AlSi10Mg [46] have been manufactured with promising results (Table 5). This has been possible because Al-Si cast alloys have a Si content percentage near the eutectic and, accordingly, they have a good castability along with low shrinkage and high strength. In addition, the presence of a small content of Mg in AlSi7Mg and AlSi10Mg alloys induces an alloy hardening thanks to the Mg_2Si precipitation after natural or artificial aging [190]. For these reasons, Al-Si alloys have been adopted for the LPBF production of critical aerospace components as well as wheels and transmission parts of cars.

On the contrary, wrought aluminium alloys as high-strength 2*xxx* (Al-Cu, Al-Cu-Mg) [191] and 7*xxx* (Al-Zn-Mg) [84] Al alloys are not still successfully processable by LPBF. Regarding this, researchers have made attempts in processing such alloys, but their processability is significantly hindered by the liquation cracking (Section 1.5.2). Al alloys as 2024 and 7075 contain elements as Cu and Zn, which widen the alloy solidification range, thereby increasing the susceptibility to cracking (Table 5). Recently, it has been found that an effective prevention for cracking is tailoring the alloy chemical composition with the purpose of shortening the solidification range [176].

Table 5 Chemical composition of alloying elements for some LPBF Al alloys [192,193].

Alloy	Si	Fe	Cu	Mn	Mg	Cr	Zn	Ti	Other	Solidification range [°C]
AlSi12	11-13.5	<0.7	<0.1	<0.5	<0.1	-	<0.1	<0.15	Pb < 0.1; Sn < 0.05	582-574
AlSi10Mg	9-11	<0.6	<0.1	<0.6	0.15-0.40	-	<0.1	<0.2	Pb < 0.1; Sn < 0.05	595-555
AlSi7Mg	6.5-7.5	<0.15	<0.05	<0.03	0.45-0.6	-	<0.05	<0.2	0.04-0.07 Be	615-555
2024	<0.5	<0.5	3.8-4.9	0.3-0.9	1.2-1.8	<0.1	<0.25	<0.15	-	638-502
7075	<0.40	<0.50	1.2-2.0	<0.30	2.1-2.9	0.18-0.28	5.1-6.1	0.2	-	635-477

2.2 Metallurgy of LPBF Al alloys

The peculiar microstructure obtained through LPBF and the strengthening mechanisms associated with Al alloys are presented in Sections 2.2.1 and 2.2.2, respectively. The deepening of both topics enables a better comprehension of the alloy response to various heat-treatment and the resultant mechanical properties.

2.2.1 Microstructure

The combined effect of the growth rate R with the temperature gradient G governs the solidification mode and, thereby, the microstructure of Al alloys obtained upon consolidation (Section 1.4.5). Since LPBF implies a very high cooling rate (10^3-10^8 K/s) [189], a unique microstructure consisting of fine grains and metastable phases is produced, leading to attractive mechanical performances. The LPBF microstructure is extremely finer than the corresponding microstructure produced via conventional foundry techniques [190,194].

The typical morphological texture of an AlSi7Mg alloy is shown in the isometric view of Fig. 31a [56]. Similar morphological textures have been also observed for LPBF AA-2024 [191], AlSi10Mg [46], AlSi12 [83] and AA-7050 [195] alloys at low magnifications.

Considering the XY plane, the laser tracks are usually oriented along with the laser scanning direction imposed by the scanning strategy. The macro-structure observed on this plane, furthermore, reveals the extent of bonding between the single scan tracks of the same layer. As far as the XZ plane is considered, the morphologic texture typically exhibits a ‘fish scale’ pattern with stacked melt pool cross-sections [190]. Besides, in this plane, it is possible to observe the degree of penetration of a melt pool across the layers underneath, and the overlapping extent with the neighboring scan tracks.

Higher magnification micrographs in Fig. 31b,c reveal that the solidification mechanism for Al alloys of 3*xxx* series, such as AlSi7Mg, is mostly cellular/columnar-dendritic [56]. As previously described in Section 1.4.5, the severe constitutional undercooling induced by the rapid solidification breaks the planar solidification front. Consequently, protrusions start growing into the liquid area forming α-Al cells and/or columns. At this point, the excess Si is rejected from the dendrite solidification front to the liquid nearby. The Si-rich liquid, then, forms a Si fibrous architecture, also known as the Si eutectic, around α-Al structures. Due to the heat extraction direction, columnar dendrites epitaxially grow from the laser fusion line to the melt pool centerline. Therefore, elongated cells decorated by eutectic Si are identified along the building direction (Fig. 31b). In contrast, the corresponding cross-sections (i.e. cells) are observed on the XY plane (Fig. 31c).

Independently of the observation plan (XY or XZ), three regions can be identified across the melt pool [56,76,196]. The first zone is a fine cellular-dendritic structure observed at the melt pool core. The fineness of the cells is estimated at around 0.4 μm. Moving from the melt pool core to the boundary, a coarser cellular-dendritic structure with an average cell size of 0.7 μm is observed at roughly 5 μm from the melt pool border. Then, moving outside the melt pool, the heat-affected zone (HAZ) is found. Such area surrounds the melt pool boundary and corresponds to a remelted region between adjacent melt pools. Here, the eutectic cells are broken due to the coarsening of the Si phase and the formation of Si particles.

This gradient of microstructure has been explained by Li et al., considering the temperature distribution within the molten pool during melting [189]. According to their simulation results for a binary Al-12Si system, the peak temperature reached in the melt pool core is about 1439 °C, which is significantly higher than the temperature range of Al-Si liquidus line (577-660 °C) [197]. Thus, the alloy completely melts, and the resultant high cooling rate will drive the microstructure towards fine equiaxed homogeneous cells. Moving from the melt pool core to the boundary, the temperature decreases, and Al-rich and Si-rich zones coexist within the melt pool. Then, an Al-rich matrix supersaturated with Si atoms and decorated by silicon nano-particles forms after the rapid cooling. Due to the high cooling rate, Marola et al. estimated that the solubility limit of Si in α-Al matrix has been enhanced from 1.59 at% to 4 at% for an LPBF*ed* AlSi10Mg [196]. In line with this, by computing the Al lattice parameters for an as-built and heat-treated LPBF*ed* AlSi7Mg alloy, Casati et al. found that 1.2 at% of Si solute atoms was present in as-built samples produced without heating the building platform [198].

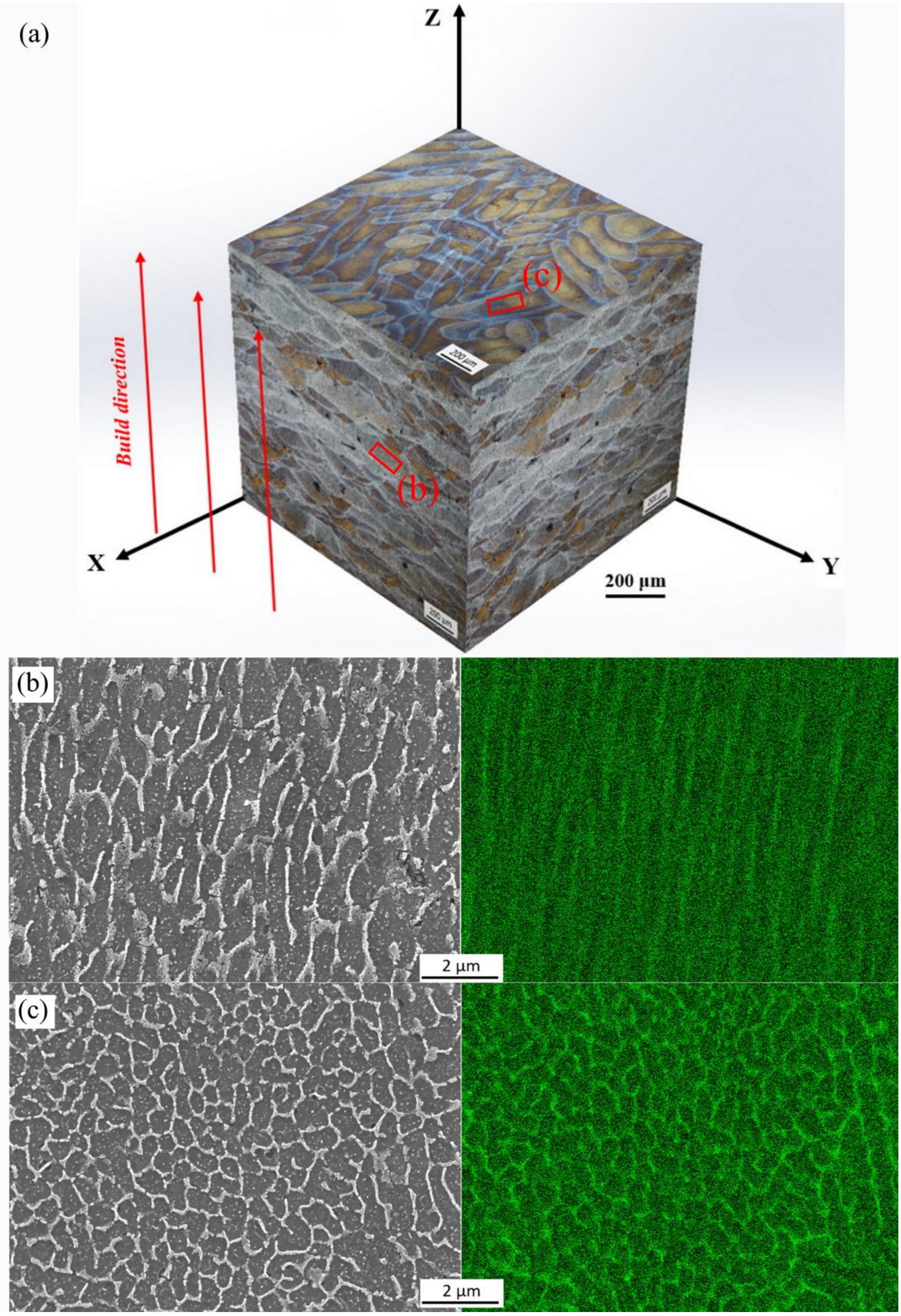

Fig. 31 (a) Isometric view of the microstructure of an as-built AlSi7Mg alloy processed by SLM; the high magnification microstructures in XY (b) and XZ (c) planes with the corresponding EDS maps for Si [56].

The directional solidification occurring in the melt pool during cooling (Section 1.4.5), causes a crystallographic texture [76]. At the track centerline, indeed, elongated grains epitaxially grow along the <100> direction, which is an ‘easy growth’ direction for Al crystals. Nevertheless, when the heat flow is not directed favorably to <100> direction, new crystal nuclei form and, then, the competitive growth of the grains get started along the heat flow direction. In this regards, This et al. studied the effect of varied scanning strategies on the AlSi10Mg crystal texture [76]. By using the unidirectional scanning strategy, a strong <100> fibre texture along the laser scanning direction was obtained, increasing the anisotropy of the alloy. On the other hand, a weak cubic texture along the building direction formed by using a 90° scanning strategy. Generally speaking, the adoption of a rotated scanning strategy (Section 1.2.5) reduces the crystallographic texture of the processed Al alloy, leading to more isotropic properties [46,76].

A detailed investigation of the as-built microstructure of an AlSi10Mg alloy manufactured by LPBF has been carried out by Le Zhou et al. [190]. They observed the cell-dendritic microstructure of the alloy via transmission electron microscope (TEM) (Fig. 32a-c). The grain consists of several primary Al cells with a size between 500 nm and 2 μm (Fig. 32a). Along the boundaries of these Al cells, a very fine eutectic phase mixture is observed. The cell boundary is mainly rich in Si, as shown in Fig. 32b. Some traces of Mg and Fe have been found as well. A quantitative analysis performed on the cell boundaries revealed the occasional presence of the π-$Al_8Si_6Mg_3Fe$ phase. The eutectic border has a thickness of roughly 50-300 nm decorated with tiny Si particles depicted in Fig. 32c. In addition, the inset of Fig. 32a shows some needle-shaped Si particles within the Al cells. Their length varies between 50 and 300 nm, whereas the width is just about tens of nm.

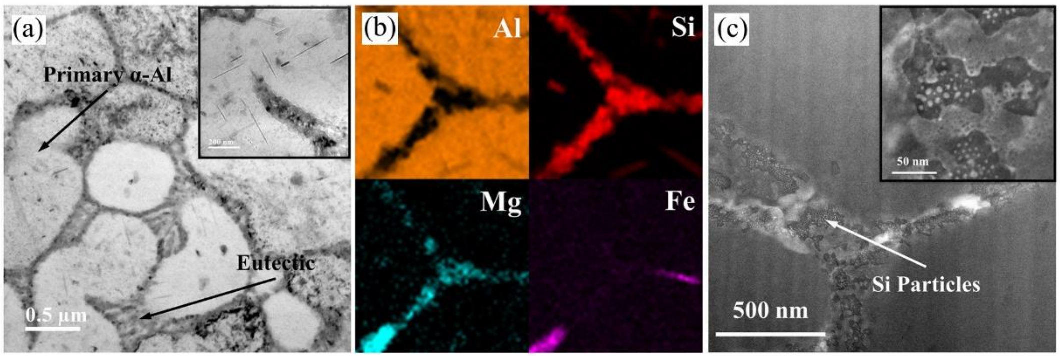

Fig. 32 TEM investigation of an as-built AlSi10Mg alloy: (a) the Al cells decorated by a fine lamellar eutectic structure and an inset which shows the needle-shaped precipitates; (b) map of the main alloying element at the melt pool boundary; (c) Si nano-particles at the triple eutectic point (adapted from [190]**).**

2.2.2 Strengthening mechanisms

The strength of Al alloys can be considered as the sum of varied mechanisms [199]:

$$\sigma_{YS} = \sigma_{GBS} + \sigma_{SSS} + \sigma_{SCS} + \sigma_{PS} \tag{2.1}$$

where σ_{YS} is the yield strength and σ_{GBS} is the contribution of the grain boundary strengthening; σ_{sss} is the contribution due to the supersaturated solid solution; σ_{SCS} represents the solute clustering strengthening and σ_{PS} is the contribution from the precipitation strengthening.

In the next sub-sections, the referred strengthening mechanisms are briefly described.

2.2.2.1 Grain boundary strengthening

The grain boundary strengthening ('GBS') occurs when dislocations interact with grains and subgrains boundaries. The grain boundary, indeed, acts as a pinning point to the dislocations slip, thereby it hinders the dislocation propagation and causes the formation of dislocations tangles. The GBS mechanism is commonly ruled by the Hall-Petch equation (2.2) [200]:

$$\sigma_{GBS} = \sigma_0 + \frac{k_y}{\sqrt{d}} \tag{2.2}$$

where σ_0 represents the friction stress of the pure alloy, k_y is the Hall-Petch slope, and d is the mean grain size. Therefore, fine and ultrafine grains promote the GBS mechanism because of a more effective obstruction of the dislocations motion [201].

Due to the fine dimensions of the microstructural features achieved by LPBF, this GBS contribution to the overall strength may be quite significant. However, some Al alloys designed specifically for LPBF have been modified by adding Sc and Zr to further improve the overall strength. In particular, in these alloys, the refinement effect is due to the formation and precipitation of nano-sized Al_3X (X = Sc and/or Zr) particles [24,202].

2.2.2.2 Solid solution strengthening

The solid solution strengthening ('SSS') arises when alloying elements are in solid solution within the base alloy. This mechanism of strengthening is particularly significant when there is a mismatch between the size of solute and solvent atoms. The alloy lattice is then locally distorted by the solute atoms and, consequently, crystallographic-dependent residual strains form. The dislocations motion is hindered by the presence of these solute-induced residual strains, thus increasing the overall hardness and strength of the base alloy [200].

The solid solution strengthening contribution to the overall alloy strength is given by Eq. (2.3) [203]:

$$\sigma_{sss} = \sum_i A_i {C_i}^{\beta_i} \tag{2.3}$$

where A_i, C_i and β_i refer respectively to SSS constant, concentration and power-law coefficient of each solute species.

Table 6 summarizes the maximum solid solubility concentration for some alloying elements in pure cast Al at the eutectic temperature. As can be seen, only a few elements have significant equilibrium solubilities in Al, such as Cu, Li, Si, Mg, Ag, and Zn. However, other elements, which show a solid solubility lower than 1 at%, still play a key role in the overall strengthening. This is the case of Zr, which has been commonly used to refine the grain size in Al cast alloys.

Table 6 Maximum solid solubility of alloying elements in pure aluminium at the equilibrium. (*) The maximum solubility occurs at the eutectic temperature for all elements with the sole exception of Zr, for which occurs at the peritectic temperature [200].

Solute	Temperature* [°C]	Maximum equilibrium solubility	
		[wt%]	[at%]
Cu	548	5.65	2.4
Li	600	4.2	16.3
Mg	450	17.4	18.5
Mn	658	1.82	0.9
Si	577	1.65	1.59
Ag	566	55.6	23.8
Zn	443	82.8	66.4
Zr	660.5	0.28	0.08

Due to the rapid solidification of LPBF, the maximum solid solubility reached upon cooling overpasses significantly the one measured at the equilibrium (Table 6). Therefore, a supersaturated solid solution is formed after manufacturing. The increased solid solubility limit of some elements have been calculated for rapidly solidified Al alloys in Ref. [204] and reported in Table 7. As far as an as-built AlSi10Mg alloy is concerned, Si content of 2.2 at% has been found in α-Al, which greatly exceeds the maximum solubility in cast Al-Si alloys [205]. Similarly, the high content of Si (2.5 wt%) in solid solution has also been detected in a SLM*ed* A357 alloy [206]. In this work, Yang and co-workers found that the contribution of the Si solute atoms to the overall alloy strength was 27.5 MPa, whereas the Mg solute content (0.56 wt%) contributed to 9.5 MPa [206]. Furthermore, Jia et al. investigated the strengthening mechanisms of a high strength Al-Mn-Sc alloy processed by SLM [203]. The research group concluded that the solid solution strengthening induced by Mn and Mg accounts for 24% (135 MPa) of the total yield strength (560 MPa) of their alloy.

Apart from the extension of the solubility limit to a higher level, rapid solidification techniques, such as melt spinning (MS) and LPBF, allows to bring in solid solution elements with an inherent low solubility in Al such as Cr, Fe and Ni (Table 7), making possible to design novel alloy composition with enhanced mechanical and thermal performances.

Table 7 Extended solid solubility limit upon rapid solidification processing [204].

Solute	Maximum equilibrium solubility		Reported extended solubility	
	[wt%]	[at%]	[wt%]	[at%]

Cu	5.65	2.4	40-42	17-18
Mg	17.4	18.5	34-38	36-40
Mn	1.82	0.9	12-18	6-9
Fe	0.05	0.025	8-12	4-6
Ni	0.04	0.023	2.4-15.4	1.2-7.7

2.2.2.3 Solute clustering strengthening

Solute clustering is a metallurgical phenomenon, which occurs during the natural aging of age-hardenable Al alloys [200]. Al alloys are more prone to natural aging when they form a super-saturated solid solution (SSSS) upon cooling. The natural aging, indeed, gets start with the decomposition of the super-saturated solid solution immediately after the alloy consolidation. When a SSSS decomposes, solute atoms may diffuse within the Al matrix lattice and gather in disordered clusters. As depicted in Fig. 33, solute clusters are formed by 20 to 50 atoms in number and do not have a defined structure. Therefore, they cannot be classified as precipitates, even though they contribute to increasing the overall strength of the alloy by pinning dislocations similarly to the precipitates.

The solute clustering strengthening (SCS) contribution to the alloy strength can be estimated by Eq. (2.4) [207]:

$$\sigma_{SCS} = C_{clusters} \cdot r^{\frac{1}{2}} \cdot {f_{r_{clusters}}}^{\frac{2}{2}} \tag{2.4}$$

where $C_{clusters}$ represents the clustering strengthening coefficient, r is the cluster radius, and $f_{r_{clusters}}$ is the volume fraction of the clusters. Being the clusters size very small, the effect of the radius cluster on the yield strength in Eq. (2.4) can be considered negligible. Thus, the most influential factor is the volume fraction of clusters formed during natural aging as well as the cluster distribution in the alloy.

Researches have been conducted on the natural aging of Al alloys over the years [207–209]. It has been observed that 90% of the total natural aging response of a cast Al-Si-Mg alloy occurs within one day. It has also been pointed out that such alloy is stable after four days of natural aging [207,208]. Still, a yield strength increment from 100 to 213 MPa was achieved after 100 h at 22 °C for water quenched A357 casting alloy [208]. Based on the results of Ref. [208], Yang et al. evaluated the contribution of the SCS mechanism on the yield strength of an as-built SLM*ed* A357 [206]. Since an as-built alloy after rapid solidification likely has high natural aging potential, the clustering contribution for the SLM*ed* A357 was estimated at around 115 MPa, which accounts for about 50% of the as-built yield strength.

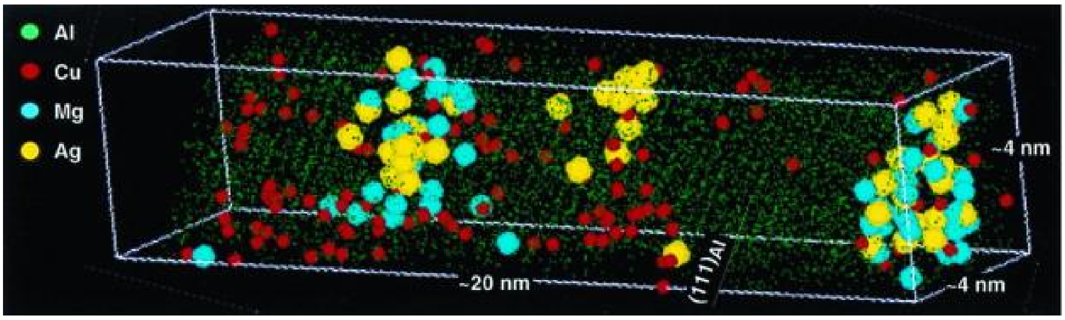

Fig. 33 Solute clustering in Al-1.9Cu-0.3Mg-0.2Ag alloy aged at 180 °C for 5 s [210].

2.2.2.4 Precipitation strengthening

The precipitation strengthening is a strengthening mechanism induced by the interference of precipitates with the movement of a dislocation along with the slip plane [200]. During aging, indeed, the disordered clusters evolve into the coherent Guinier-Preston (GP) zones and further precipitates thereof, creating local strains around particles, which in turn hinder the mobility of dislocations.

The contribution of the precipitation strengthening to the overall alloy strength depends on the precipitate size, as illustrated in Fig. 34a. The maximum strengthening is achieved at the transition between the two main mechanisms of dislocation-particle interaction, i.e. the cutting and the by-passing mechanism.

The cutting mechanism takes place when the coherent GP zones are located along the slip direction of a glide dislocation (Fig. 34b). In this scenario, the dislocation would encounter the precipitate, which acts as a barrier, and the only way to move forward would be to go through the particle. Therefore, if the available surface energy is high enough, the dislocation will shear the precipitate and move on. The resulting strengthening contribution to the alloy strength is given by Eq. (2.5) [199]:

$$\sigma_{PS-cutting} = \frac{3.1\gamma^{\frac{3}{2}}}{b^2} \cdot \left(\frac{rV_p}{G}\right)^{\frac{1}{2}} \tag{2.5}$$

where γ is the surface energy at the anti-phase boundary, b is the Burger vector, G is the shear strength, r and V_p are the average radius and the volume fraction of precipitates, respectively.

As it can be inferred from Eq. (2.5), the cutting mechanism induces a significant yield strengthening when a high volume fraction of fine precipitates is evenly dispersed in the matrix. Moreover, the maximum strengthening is expected to be when the distance among precipitates is around 10 nm, i.e. equivalent to the minimum curvature radius of a gliding dislocation.

Once the precipitates coarsen due to aging, the particle size exceeds the critical value for the cutting-bypassing transition. Therefore, the principal mechanism for strengthening is now the by-passing mechanism (Fig. 34c), also known as the Orowan mechanism.

The by-passing mechanism has been proposed by Orowan (1949) to depict the interaction mechanism between a gliding dislocation and coarse and widely spaced spherical precipitates [199]. In this scenario, the easiest way for the dislocation to proceed is to bow out between the precipitates and re-join, leaving dislocation loops around particles. The Orowan strengthening can be expressed by the following formula:

$$\sigma_{PS-Orowan} = \frac{0.8\,Gb}{2\pi(1-\upsilon)^{\frac{1}{2}} \cdot L} \ln\left(\frac{2r}{r_0}\right) \tag{2.6}$$

where υ is the Poisson ratio, L is the interparticle spacing and r_0 is the core radius of the dislocation.

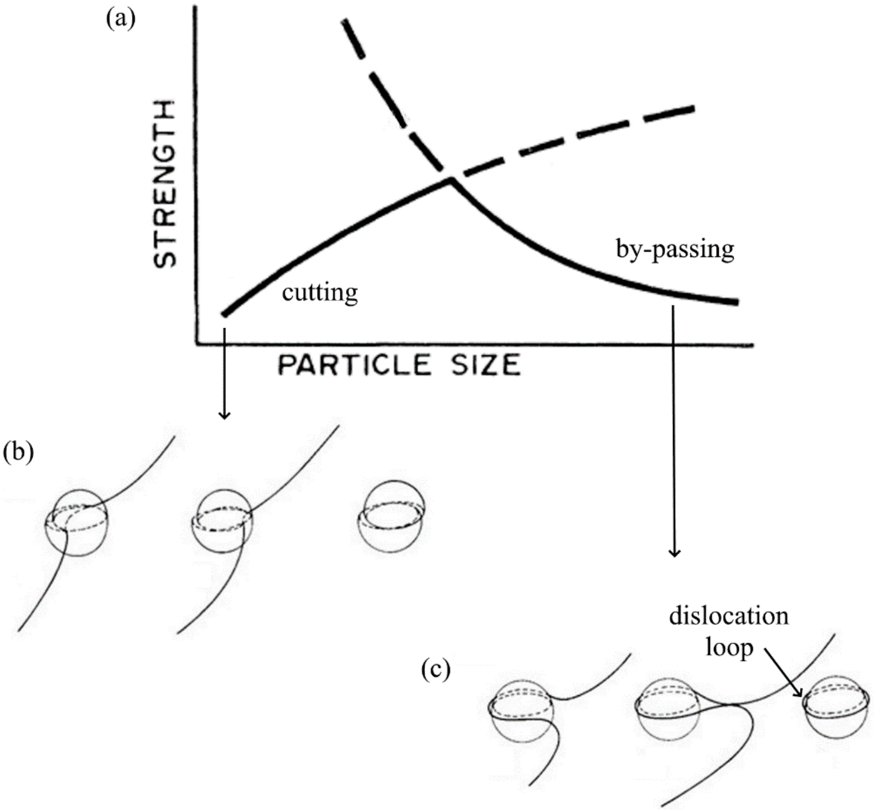

Fig. 34 (a) Relationship between the strength and the precipitate size for a age-hardenable Al-alloy; (b) particle cut by a dislocation (cutting mechanism) and (c) particle by-passed by a dislocation (by-passing mechanism) (adapted from [200]**).**

2.3 Heat-treatment strategies

In this section, the principal heat-treatment strategies for heat-treating Al parts are described. Particular emphasis on the metallurgical principles of aging is first given in Section 2.3.1. The leading families of Al alloys are, indeed, susceptible to the age-hardening. Therefore, T6-like and T5 heat-treatments exploit the aging response of Al alloys to increase hardness and strength by precipitation strengthening. Apart from strengthening heat-treatments, solution and annealing are common thermal strategies to soften and relieve the internal residual stresses of Al alloys. These heat-treatments for LPBF Al alloys are described in Sections 2.3.2 - 2.3.4.

2.3.1 Metallurgical principles of aging in Al alloys

The aging heat-treatment also referred to as age-hardening, has been widely adopted to increase the hardness and the strength of heat-treatable Al alloys. Aging occurs in those Al alloys, which contain hardening alloying elements such as Ag, Cu, Mg and Zn. Aging of Al alloys typically involves a sequence of diffusion-controlled transformations to form precipitates from the decomposition of a super-saturated solid solution (SSSS) [200,211]. The precipitation-hardening sequences of the primary age-hardenable Al alloys are summarized in Table 8.

Table 8 Precipitation sequences for age-hardenable Al alloys [211].

Alloy	Precipitation sequence
Al-Ag	GP (spheres) → γ'(plates) → γ (Ag_2Al)
Al-Cu	GP (discs) → θ'' (discs) → θ' (plates) → θ ($CuAl_2$)
Al-Cu-Mg	GP (rods) → S' (laths) → S ($CuMgAl_2$)
Al-Zn-Mg	GP (spheres) → η' (plates) → η ($MgZn_2$) (plates or rods)
Al-Mg-Si	GP (rods) → β''→ β' (rods) → β (Mg_2Si) (plates)

According to the foundry post-processing route, a SSSS is achieved upon solutioning and rapid quenching. Thus, a large amount of solute is retained into a stable *fcc*-α phase at room temperature. If the alloy is held at room temperature, i.e. naturally aged, or heated-up and kept in the temperature range of 140-190 °C for a certain period of time, i.e. artificially aged, the diffusion of solute atoms gets start.

As a consequence of the solute diffusion at a short distance, GP zones firstly form. GP zones are solute-rich groups of ordered atoms fully coherent with the *fcc*-α matrix. In the case of Al-Cu alloy, GP zones have a disc shape with a diameter of 10 nm and thickness of two atomic layers, as shown by the inset A in Fig. 35 [212].

At this point, the aging process involves the formation of the so-called transition phases [211]. The transition phases are metastable crystal structures which precede the equilibrium phase. The reason behind the formation of these phases is the low activation energy for the nucleation. Thus, the system prefers to go through the transition phases rather than directly form the stable phase from the SSSS.

As an example, the transition phases θ'' and θ' precede the stable θ (Al_2Cu) phase in the binary Al-Cu alloy (Table 8). θ'' nucleates at the stable GP zones sites. The crystal structure is composed of a tetragonal cell, which is fully coherent with the matrix lattice, as shown by inset B of Fig. 35. At longer aging times, θ' plates form by the in-situ nucleation on the matrix dislocation. The crystal structure of θ' has non-coherent (100) and (010) planes whereas the (001) plane is partly coherent with the α-matrix. When θ' keeps growing, the crystal structure evolves in a complex semicoherent configuration, partially losing the coherency with matrix (inset C, Fig. 35). Furthermore, θ' grows at the expense of the less-stable θ''. Lastly, at higher aging times, the θ phase nucleates at the interfaces between θ' and the matrix. The θ phase has a chemical composition near to Al_2Cu and generally exhibits a large and incoherent body-centered crystal structure (inset D, Fig. 35).

The hardness response to the artificial aging of a cast Al-4Cu alloy is depicted in Fig. 35 [213]. Immediately after quenching, the main impedance to the dislocation motion is represented by the super-saturated solid solution (Section 2.2.2.2), but the hardness is still quite low. Later, the hardness increases because of the formation of the coherent GP zones. At this stage, the main contribution to strengthening is due to the cutting of GP zones by the gliding dislocations, as explained in Section 2.2.2.4. At even higher aging times, a hardness peak is reached when the fully coherent θ'' phase nucleates. Once the θ' is formed, the distance between precipitates becomes larger and dislocations may blow between them, thereby leading to a hardness decrease. Eventually, further aging coarsen θ'particles and promotes the precipitation of incoherent θ, reaching the overaged condition.

The aging response of an alloy depends on the temperature of the aging heat-treatment, as illustrated in Fig. 36 for the Al-Cu alloy. The maximum hardness increment is achieved when the aging temperature is below the metastable solvus line of the GP zones. In this way, the complete hardening precipitation sequence occurs and the full precipitation potential is exploited, achieving a high hardness level. In this scenario, a hardness peak is reached at a relatively high aging time when the presence of θ''phase is such to effectively hinder the dislocations motion. On the other hand, if the aging is performed at a temperature between the GP zone and θ''solvus lines, GP zones dissolve and the precipitation sequence will start immediately with the θ'' phase. In this context, θ'' phase would not be finely dispersed in the α-matrix due to the lack of the nucleation sites provided by GP zones and, thereby, a lower hardness level is obtained. Being the nucleation rate dependent on the temperature, the hardness peak is reached at a relatively low aging time.

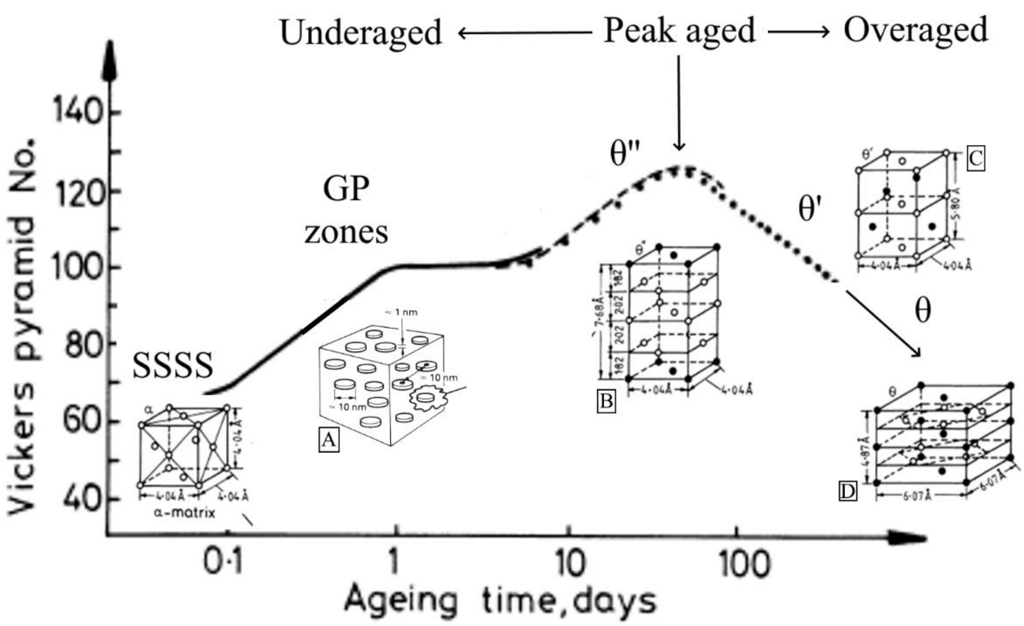

Fig. 35 Hardness response of Al-4Cu alloy aged at 130 °C. Insets represent the crystal structures of precipitates nucleated during aging (adapted from [213]**).**

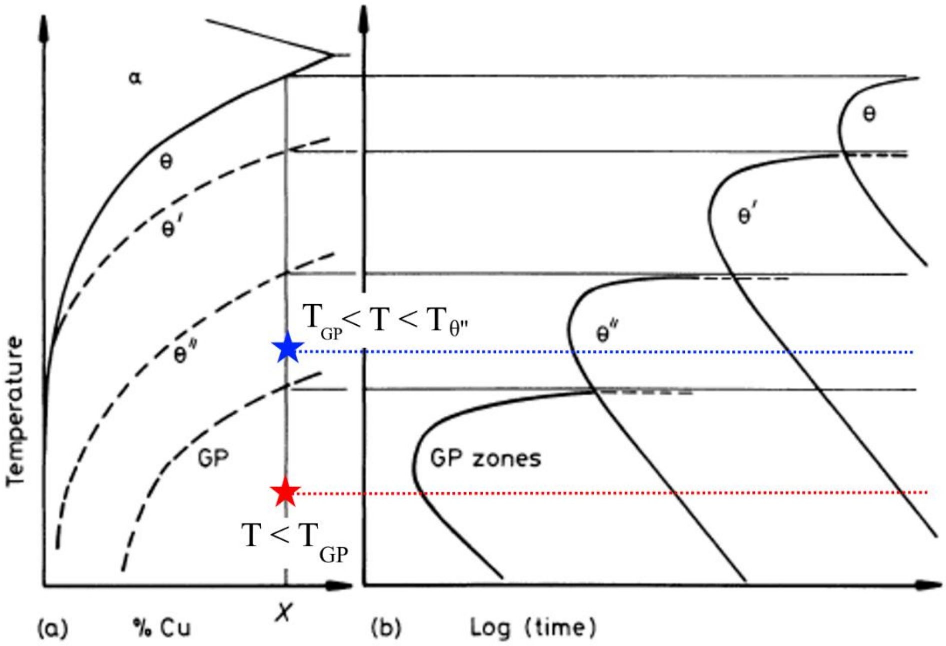

Fig. 36 Effect of the aging temperature on the aging response of a Al-Cu alloy. (a) the metastable solvus lines of GP zones and transition phases and (b) the TTT diagram (adapted from [211]**).**

2.3.2 T6-like heat-treatment

The T6-like heat-treatment ('T6') is standard practice for heat-treating cast Al alloys and typically involves three stages [214]:

1. Solution heat-treatment to dissolve any precipitates or alloying elements. The solution temperature must fall within the α-phase region of the processed Al-alloy. The solution time is chosen to dissolve the alloying elements and precipitates into the Al-matrix.

2. Quenching in water or oil media to obtain a SSSS.
3. Artificial aging to induce the nucleation of evenly dispersed particles and increase the strengthening of the alloy.

The effect of T6 on the microstructure and mechanical properties of LPBF*ed* Al alloys has been widely investigated over the years [215–219].

Li et al. described the microstructural evolution of the AlSi10Mg alloy after each stage of heat-treatment [215]. The as-built microstructure consisted of α-Al matrix cells surrounded by a fibrous Si eutectic. Once the alloy undergoes the solution heat-treatment, the Si network breaks and the cell boundaries become blurred or disappear entirely. The Si in excess comes out from the SSSS and, consequently, Si particles nucleate. The size and density of these Si particles depend on the solution temperature. The higher the solution temperature, the greater is the size of the precipitates. On the contrary, the particle density decreases due to the coalescence of smaller particles. Si particles keep growing during the subsequent artificial aging, although a peak of hardness eventually occurs due to the nucleation of transition phases only detectable at higher magnifications (Table 8).

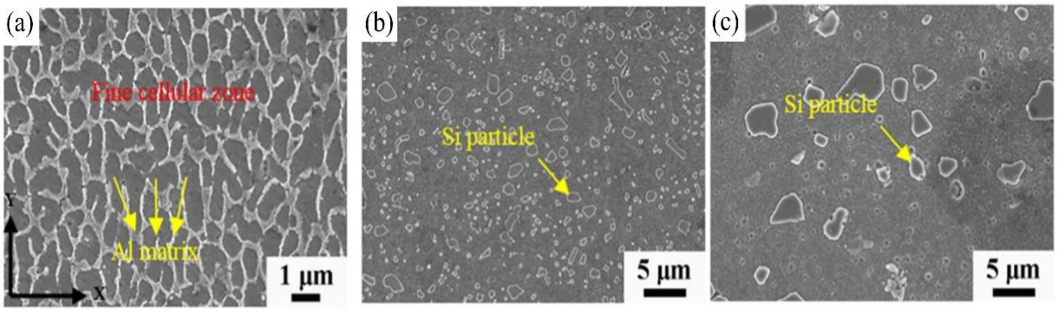

Fig. 37 Micrographs of (a) as-built, (b) solution heat-treated (500 °C for 2 h), and (c) artificially aged (500 °C for 2 h + 12 h at 180 °C) AlSi10Mg alloy processed by LPBF (adapted from [215]**).**

Aboulkhair et al. assessed the effect of T6 heat-treatment on the mechanical performances of an SLM AlSi10Mg alloy [217]. Based on their results, little benefits are achieved when compared to the as-built properties, as schematically depicted in Table 9. Considering the decrease in hardness and strength and the increment of elongation, the alloy appears softened after T6. This softening is mostly due to the rupture of the Si eutectic architecture and the coarsening of Si particles. Hence, the grain boundary and the solid solution contributions to the overall strengthening of the alloy can be considered negligible. In the heat-treated condition, indeed, the alloy is mostly strengthened by the Orowan mechanism, leading to a lower precipitation hardening response [220].

Therefore, on the one hand, T6 produces a hardening effect on cast AlSi10Mg alloy while, on the other hand, it softens the LPBF as-built alloy. This different behavior is attributed to a significantly different solute content, type of precipitates, and grain size of the starting microstructures [190,216]. According to these evidences, the heat-treatment strategy should be designed explicitly considering the unique microstructure achieved by LPBF.

Table 9 Effect of T6-like heat-treatment (1h at 520 °C + w.q. + 6h at 160 °C) on the mechanical properties of SLM AlSi10Mg alloy [217]. **The mechanical properties variation is expressed in percentage.**

Property	**Effect of T6-like heat-treatment (%)**
Nano-hardness	↓ -(16 ± 1)
Micro-hardness	↓ -(20 ± 1)
Ultimate tensile strength	↓ -(12 ± 5)
Yield tensile strength	↓ -(11 ± 1)
Tensile elongation at failure	↑ +(179 ± 57)
Compressive strength at 25% strain	↓ -(56 ± 0.003)
Yield compressive strength	↓ -(47 ± 2)

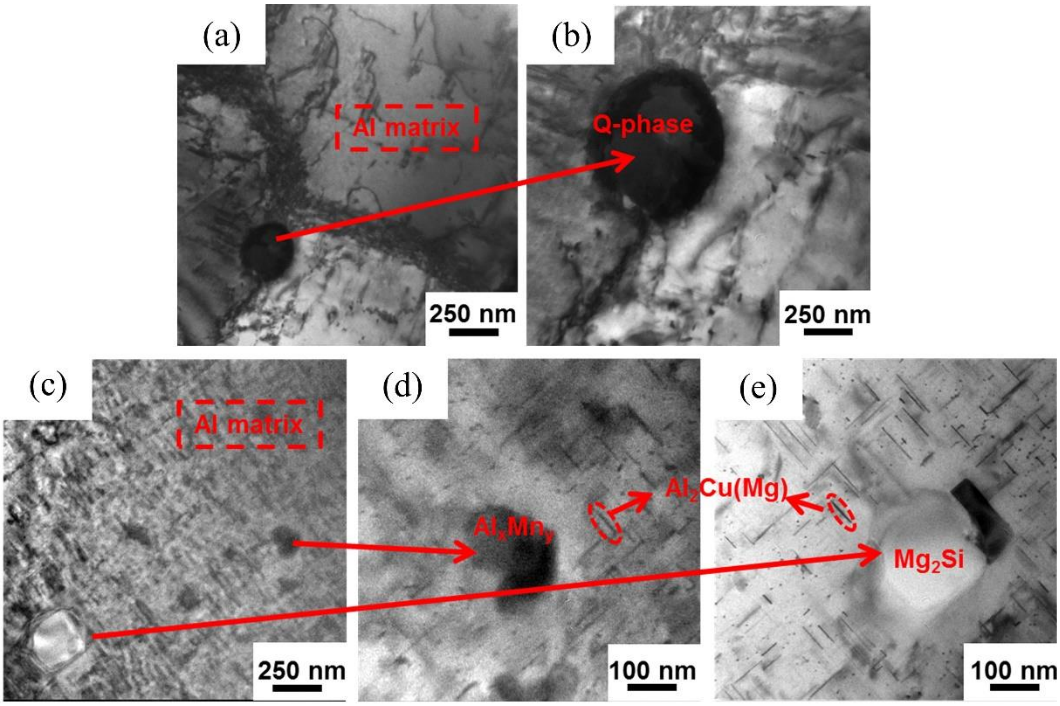

Fig. 38 TEM investigation on (a,b) the as-built and (c-d) the heat-treated Al-3.5Cu-1.5Mg-1Si [219].

Notwithstanding the results of Ref. [217] on AlSi10Mg, the T6-like heat-treatment has been found likewise effective in the strengthening of 2*xxx* Al alloys [218,219]. This was mainly due to the significant precipitation potential of this alloy family, which are enriched of various hardening elements, such as Cu and minority elements, e.g. Mg, Mn and Si. In this regard, Wang et al. heat treated an Al-3.5Cu-1.5Mg-1Si alloy manufactured by SLM [219]. After T6-like heat-treatment, both yield and ultimate strength values significantly increased, while ductility was preserved. The quaternary Q phase formed upon solidification, indeed, decomposed into the finer Mg_2Si, Al_xMn_y and nano-$Al_2Cu(Mg)$ precipitates after T6, as illustrated in Fig. 38. Hence, a consistent precipitation strengthening was achieved, enhancing the mechanical properties.

2.3.3 Direct aging (T5) heat-treatment

The direct aging heat-treatment, also known as T5 temper [214], is a standard protocol to heat-treat cast Al alloys. Differently from T6-like heat-treatment, T5 provides for artificial aging without the need of previous solutioning. Therefore, starting from the as-fabricated condition, the alloy will result directly strengthened by precipitation hardening.

Considering the peculiar microstructure and the high level of supersaturation of as-built LPBF alloys, direct aging heat-treatment has been recently acknowledged as a profitable solution to heat-treat LPBF component [24,177,221–223]. Especially, the direct aging response of the age-hardenable A357 alloy has been widely investigated over the last years [221–223].

Aversa et al. were among the early LPBF users to test the direct aging on an as-built A357 alloy processed with various platform heating temperatures [221]. In this study, the aging behavior has been found intimately related to the platform heating. The lower the platform heating, the higher was the precipitation hardening effect. A peak hardness of roughly 137 HV was achieved upon 3 h at 170 °C for samples processed at 100 °C. The depletion of the SSSS in samples built at higher platform temperatures was the primary cause of the poor direct aging response. Therefore, as-built alloys with relatively high solute content are prone to be strengthened by T5.

Later, Casati and Vedani compared the aging response of an A357 alloy heat-treated by both T5 and T6 solutions [222]. The highest hardening was exhibited by the directly aged samples. A maximum hardness (≈ 137 HV), indeed, was achieved at 160 °C after 4 h, which is remarkably higher than the one obtained upon T6 (≈ 110 HV). To explain this hardness difference, they carried out a thermal analysis on as-built and solutionized samples. The exothermic peaks of both conditions showed the typical precipitation sequence of cast Al-Si-Mg alloys (Table 8). However, the signal attributed to the formation of β'' precipitates was shifted at a lower temperature and appeared more intense in the as-built alloy. The β'' nucleation, indeed, gets start earlier in LPBF samples, due to the fast Si diffusion promoted by the high number of vacancies formed after rapid cooling. Moreover, homogeneous nucleation of β'' is favored by the high degree of supersaturation, thereby increasing the hardening level of T5 alloy.

Still, Rao et al. observed the precipitation pathway of an A357 alloy directly aged at 165 °C [223]. In their work, T5 gives better results in terms of hardness than that of the T6 counterpart, as formerly observed by Ref. [222]. The added value of Rao's work was the phase identification at the peak-aged condition conducted using TEM analysis. The selected area electron diffraction pattern (SAED) of Fig. 39 shows the presence of multiple Si particles with nanometric size, exhibiting both random and specific orientations (e.g. the Moiré fringes). The Authors claim that these Si particles were generated by the quick diffusion within the SSSS of Si atoms and the subsequent aggregation. Contrarily to the theory of Casati and Vedani [222], they believe that the formation of (Mg + Si) clusters and β'' phase is improbable at the peak-age as the Mg diffusion rate is very slow compared to Si.

Although the direct aging gives a higher level of hardness than T6, it typically results in a low degree of stress relieving and a poor ductility. Consequently, crack and distortions may arise during the production of large-scale components with a complex shape [224].

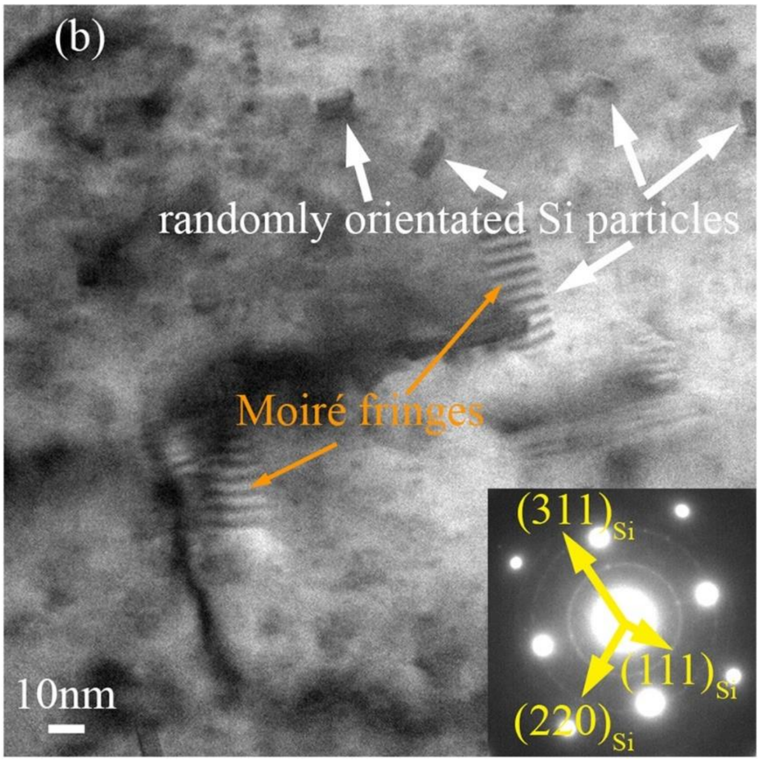

Fig. 39 TEM image showing the randomly oriented Si particles for a SLM*ed* A357 alloy directly aged at 165 °C for 2 h [223]**.**

2.3.4 Annealing

Immediately after cooling down, the as-built alloy is heavily stressed by a considerable amount of solute content [156]. Consequently, the LPBF component often undergoes an annealing heat-treatment to minimize the internal residual stresses. Annealing, also referred to as 'stress-relieving' among LPBF users, can be performed before the detachment of parts from the building platform. This procedure helps to prevent part distortion and/or buckling after cutting.

The degree of relaxation relies on annealing temperature and time. The temperature range for annealing is between the upper limit temperature of artificial aging and the lower temperature for solution heat-treatment [225]. A good reduction of residual stress is achieved by heating the alloy from 260 to 415 °C, regardless of the Al series. The time required for annealing depends on the adopted temperature. For instance, an overaged Al-Si alloy is nearly annealed as the solid solution has been entirely depleted during artificial aging. However, this condition is reached after longer times when working in the temperature range of artificial aging, i.e. 140 - 190 °C. On the contrary, if the temperature is set above the upper limit of annealing (T > 415 °C), the time required for softening is significantly reduced, but excess relaxation may occur. In this latter case, the annealing becomes similar to a solution heat-treatment [215].

Table 10 reports the effect of an annealing heat-treatment on the mechanical properties of an LPBF AlSi10Mg alloy [226]. The heat-treatment was performed at 300 °C for 2 h. An overall reduction of the strength tensile values was achieved upon annealing. On the contrary, the elongation at failure is remarkably higher due to matrix softening, showing an increment up to 83% for the Z direction. Besides, Mamooun et al. noticed a hardness decrease of roughly 33.3% by applying the same heat-treatment strategy on an as-built AlSi10Mg alloy [134].

Table 10 Effect of annealing heat-treatment (2 h at 300 °C) on the mechanical properties of a AlSi10Mg alloy [226]**.**

Property	Direction	Effect of annealing heat-treatment (%)
Tensile strength	XY	↓ - 25
	Z	↓ - 23.9
Yield strength (Rp 0.2 %)	XY	↓ - 14.8
	Z	↓ - 4.2
Modulus of elasticity	XY	↓ - 6.7
	Z	↓ - 14.3
Elongation at break	XY	↑ + 33.3
	Z	↑ + 83.3

The overall softening of the alloy is caused by a microstructural modification, which occurs during the annealing heat-treatment [216,227]. Regarding this, Prashanth et al. observed the microstructure evolution of a SLM*ed* Al-12Si alloy by increasing the annealing temperature [216]. As the annealing temperature is increased from 200 to 500 °C, the fish-scale pattern observed in the as-built alloy (Section 2.2.1) gradually dissolves. Initially, Si particles start to grow at the grain boundaries at a medium temperature. By further increasing the temperature, the Si eutectic structure breaks and spheroidization of Si particles occurs. Eventually, the Si particle density decreases, whereas their particle size becomes larger by further raising the annealing temperature. A similar microstructure has been observed in solutionized AlSi10Mg alloy with poor mechanical properties [215]. Therefore, the annealing should be designed specifically for the processed alloy.

In this context, Fiocchi et al. developed ad-hoc annealing treatments for a SLM*ed* AlSi10Mg alloy [228,229]. The temperature of their annealing (244 °C) was set between the β''solvus temperature and the Si spheroidization temperature. By doing so, the annealed microstructure experienced the precipitation of the stable Mg_2Si without the disruption of the Si network. Consequently, a good degree of stress relieving was achieved without losing excessive strength [229].

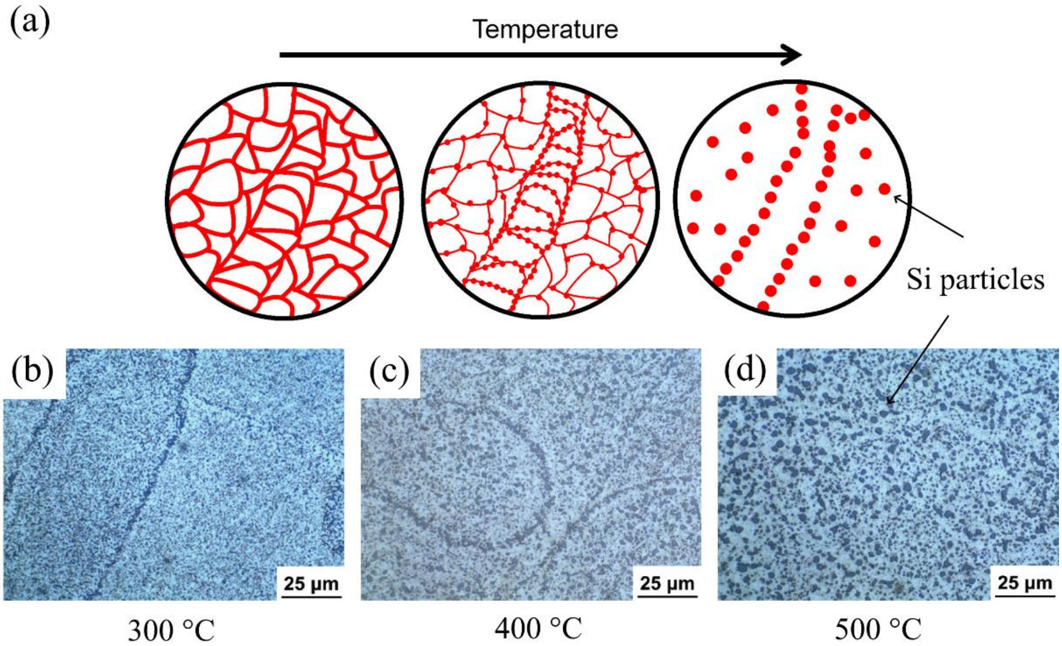

Fig. 40 (a) Schematic evolution of the AlSi10Mg microstructure with annealing temperature. Low magnification micrographs annealed at (b) 300, (c) 400 and (c) 500 °C (adapted from [216]**).**

2.4 Mechanical properties

In this section, an overview of the principal mechanical properties for LPBF Al parts is given.

Strength related properties, such as hardness (Section 2.4.1), tensile (Section 2.4.2) and fatigue (Section 2.4.3) of LPBF parts overpass those of the cast counterpart due to the unique microstructure arising after rapid solidification. Accordingly, the LPBF alloy behaves better when it undergoes intense static loads, although its ductility is quite low. This is confirmed by the higher hardness and tensile performances achieved in the as-built condition when compared to cast parts. To improve ductility, annealing or solution heat-treatments are commonly adopted. These heat-treatments have a twofold effect on the mechanical behavior. First, the alloy results softened by the Si particle spheroidization. Hence, ductility is first increased at the expense of the strength. On the other hand, solution heat-treatment erases almost entirely the LPBF macrostructure and its fibrous crystallographic texture. Consequently, mechanical properties are more isotropic upon heat-treatment.

Lastly, Section 2.4.4 will go through the other mechanical properties which have been studied less intensively over the years.

2.4.1 Hardness

The Vickers micro-hardness ('HV') is commonly used to estimate the mechanical properties of LPBF parts, such as strength and ductility [230]. The test procedure is relatively easy, and significant results can be obtained in a short time. On the contrary, a bottleneck for the micro-hardness test is represented by the sample preparation. The tested sample, indeed, needs to be flat since a slight misalignment often results in consistent data scattering. This is a consequence of the micro-scale nature of HV hardness.

The chemical composition greatly affects the hardness value of Al alloy, regardless of the manufacturing technique. The pure Al is generally a soft metal, thus chemical elements, namely the hardeners (Section 2.3.1), are commonly alloyed within Al matrix to increase strength and hardness through precipitation hardening. To this regard, Zuback and DebRoy found a linear dependence of the as-built hardness of LPBF*ed* parts on the Al alloy chemical composition [231]:

$$\mathrm{HV} = 37.99 + 19.47\mathrm{Ag} + 2.85\mathrm{Cu} + 23.36\mathrm{Fe} + 24.47\mathrm{Mg} + 30.00\mathrm{Mn}$$
$$+ 5.43\mathrm{Si} + 20.86\mathrm{Ti} + 19.06\mathrm{Zn} \qquad (2.7)$$

where each chemical element is expressed in weight percent and is comprised in the following ranges: 0 ÷ 0.5 wt % Ag, 0 ÷ 5.3 wt % Cu, 0 ÷ 0.8 wt % Fe, 0 ÷ 1.95 wt % Mg, 0 ÷ 0.55 wt % Mn, 0 ÷ 12.2 wt % Si, 0 ÷ 0.064 wt % Ti and 0 ÷ 0.1 wt % Zn.

Apart from the chemical composition, multiple factors affect the hardness of LPBF*ed* aluminum alloys. For instance, the usage of different machines may lead to different hardness values for similar Al alloys [220,229]. Moreover, the densification level negatively influences the hardness as well. As an example, although the hardness measurement is apparently performed on a dense sample area, porosities may be hidden beneath the surface. Then, the resulting hardness diagonals may be larger and the material appears softer. Still, the process parameters can be the cause of a hardness variation [232]. By using a higher level of scanning speeds (Section 1.2.9), a consistent fraction of solute atoms is retained in the super-saturated solid solution and, consequently, an increased HV level is reached.

The solidification phenomena, which occur within the melt pool during consolidation, may lead to local micro-hardness fluctuations. In this regard, Liu et al. measured the hardness profile along Z direction of a SLM*ed* AlSi10Mg alloy [159]. Results of Ref. [159] show a significant hardness decrease (ΔHV ≈ 40) moving from the top surface to 300 μm inside of the sample. The reason for this trend was attributed to the different cooling rates experienced by the material during consolidation. Different cooling rates result in a gradient microstructure with different mechanical properties. The higher cooling rate reached in the last deposited layers forms finer Si particles and several subgrains, which in turn give high hardness. Moreover, a gradient of hardness along the building direction can also be caused by the different exposure time at a temperature able to induce precipitation hardening, e.g. a building platform temperature above 150 °C for Al alloys [26,233].

Table 11 summarizes the HV values of LPBF Al-Si alloys and the hardness variation with the heat-treatment. As can be noticed, Al parts produced by LPBF exhibit a higher hardness than their cast counterparts [194,234]. This is attributable to the unique microstructure resulting from the LPBF technology (Section 2.2.1).

Fig. 41 shows the effect of the heat-treatment previously described on the hardness. The significant data scattering of the as-built condition corroborates the idea that several factors affect the hardness of additively manufactured Al alloys. The HV values for as-built Al-Si alloys relay on a range between 105 and 150 HV. Annealing and solutioning soften the Al-Si alloy to different extents. Annealing is performed at a lower temperature range with respect to solutioning. The very fine microstructure is partly retained in the former, whereas the rupture of the Si network occurs in the latter. When the LPBF Al-Si alloy undergoes a T5, the peak-age is reached at roughly 144.2 HV, which is noticeably higher than the as-built average, i.e. 125 HV. On the other hand, artificial aging after solutioning leads a hardness increase, but the T6-HV mean value is slightly lower than that of as-built (see Section 2.3.2).

Table 11 As-built and heat-treated Vickers hardness of LPBF Al-Si aluminum alloys compared to the cast counterparts.

Alloy	HV					Ref
	As-built	**Annealing**	**Solution HT**	**T5**	**T6**	
AlSi7Mg	121			137		Aversa et al. [221]
	103		78	137	113	Casati et al. [222]
			60	150	115	Rao et al. [223]
AlSi12	145-150					Bai et al. [235]
	135		65			Prashanth et al. [236]
AlSi10Mg	138	74				Fiocchi et al. [229]
	120	78	62		115	Maamoun et al. [134]
	119					EOS [226]
	127					Kempen et al. [237]
	136			152		Kempen et al. [44]
		105-108				Manfredi et al. [5]
		94				Rosenthal et al. [238]
	140-150					Buchbinder et al. [42]
	106-112					Takata et al [239]
	132	88	60			Takata et al. [240]
	110		62-68		96	Aboulkhair et al. [220]
	125				103	Aboulkhair et al.

			[217]
AlSi10Mg Die-cast	95-105	133	Rogers et al. [234]

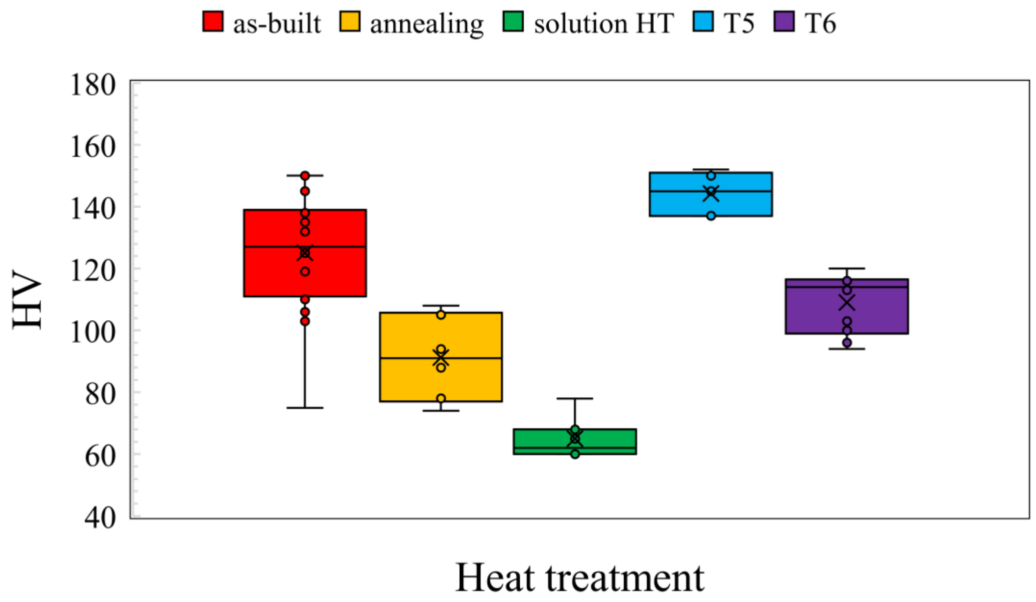

Fig. 41 Effect of the heat-treatment on the Vickers hardness of Al-Si alloys (obtained from values in Table 11).

The hardness of heat-treatable Al alloys is affected by the natural aging [222,241]. Thus, it must take care of the elapsed time between the LPBF production (or eventual heat-treatment) and the hardness measurement. To have comparable results, it is a good practice to set a specific time interval between production/heat-treatment and measurements. The natural aging is consumed within one week after LPBF or quenching. It is possible to avoid the solute clustering phenomena by storing samples at a low temperature (-5 °C).

2.4.2 Tensile properties

As for the hardness, the tensile properties of LPBF Al alloys are superior to the wrought or cast ones [194]. The improved strength is attributable to the fine microstructure of LPBF materials, the presence of a super-saturated solid solution and, eventually, sub-grain boundaries and nano-precipitates that hinder the dislocations slip.

The value interval of yield (YS), ultimate strength (UTS) and fracture strain (ε) of an LPBF alloy can occasionally be quite broad as several factors related to the LPBF system, raw powder and process parameters may affect the tensile behavior [23].

The sample orientation during manufacturing influences the microstructure evolution within tensile parts [35,79]. Hence, the directional pile-up of scan tracks/layers and the texture orientation causes an anisotropic tensile behavior.

The tensile performance depends on the direction of the applied load with respect to the layers orientation. As an example, samples oriented along the building direction consist of several stacked layers, whereas the ones built horizontally provide for a few layers. Therefore, the latter samples possess higher mechanical properties because of the few interfaces between layers, which act as slipping surfaces.

This behavior has been corroborated for the AlSi10Mg alloy by Hitzler et al. [79]. By studying the tensile behavior of seven differently oriented configurations, they noticed an overall lower ductility for vertical samples ($\varepsilon \approx 3.20\text{-}3.97$ %). On the contrary, the higher strength was obtained in configurations with a small build height and layers parallel to the load direction (UTS ≈ 366-399 MPa). Interestingly, a quite low strength occurs for samples built at 45°. In this case, slipping of α-Al atomic planes is triggered by the presence of the layers interfaces oriented along the (111) slip direction.

Apart from the build orientation, other process parameters, namely the scanning strategy and the platform heating, impact the tensile performances. As far as the scanning strategy is concerned, Prashanth et al. found that the island scan strategy (Section 1.2.5) leads to the best elongation at break (≈ 4.5%) for a SLM*ed* Al-12Si alloy, due to a meander propagation of the crack during failure [83]. Moreover, they noticed a significant reduction in ductility and ultimate strength adopting a contour strategy. It was suggested that an untimely failure occurs when a crack forms and propagates along the contour-core interface due to the different melting patterns and melt pools size of these regions. Still related to the scan strategy, Kempen et al. suggested to operate in the ‘ghost vector’ mode to avoid the keyhole pores formation in the proximity of the outer skin. These pores were the primary reason for the failure of their AlSi10Mg tensile specimens [20].

The platform heating strategy enhances the ductility while decreases YS and UTS. In Ref. [83], the Authors observed a strength drop for Al-12Si alloy with increasing the platform heating temperature from 200 to 400 °C. Specifically, this behaviour was correlated with the higher content of free Si detected in samples manufactured at higher platform temperatures.

The fracture mechanisms of Al-Si alloys have been studied either for as-built and heat-treated conditions [215,242,243].

Considering the as-built state, nano-sized eutectic silicon particles pin the gliding dislocations, thus increasing strength and reducing the plasticity. Cracks randomly originate near voids or brittle oxides and then propagate until failure. The fracture surface typically does not show evidences of track/layer detachment, but only shallow dimples appear, as depicted in Fig. 42a,c.

When an annealing or solution heat-treatment is performed, the nano-Si particles coarsen and the particle number is reduced due to Ostwald ripening. Thus, plasticity is enhanced thanks to the weak pinning action of precipitate towards dislocations. Failure occurs when the coarser Si precipitates crack, acting as brittle inclusions. The crack path follows the single track/layer interfaces where the presence of larger Si particles is prominent. The fracture surface exhibits a visible track/layer debonding and well-dispersed ductile dimples, respectively at low (Fig. 42b) and high magnifications (Fig. 42c).

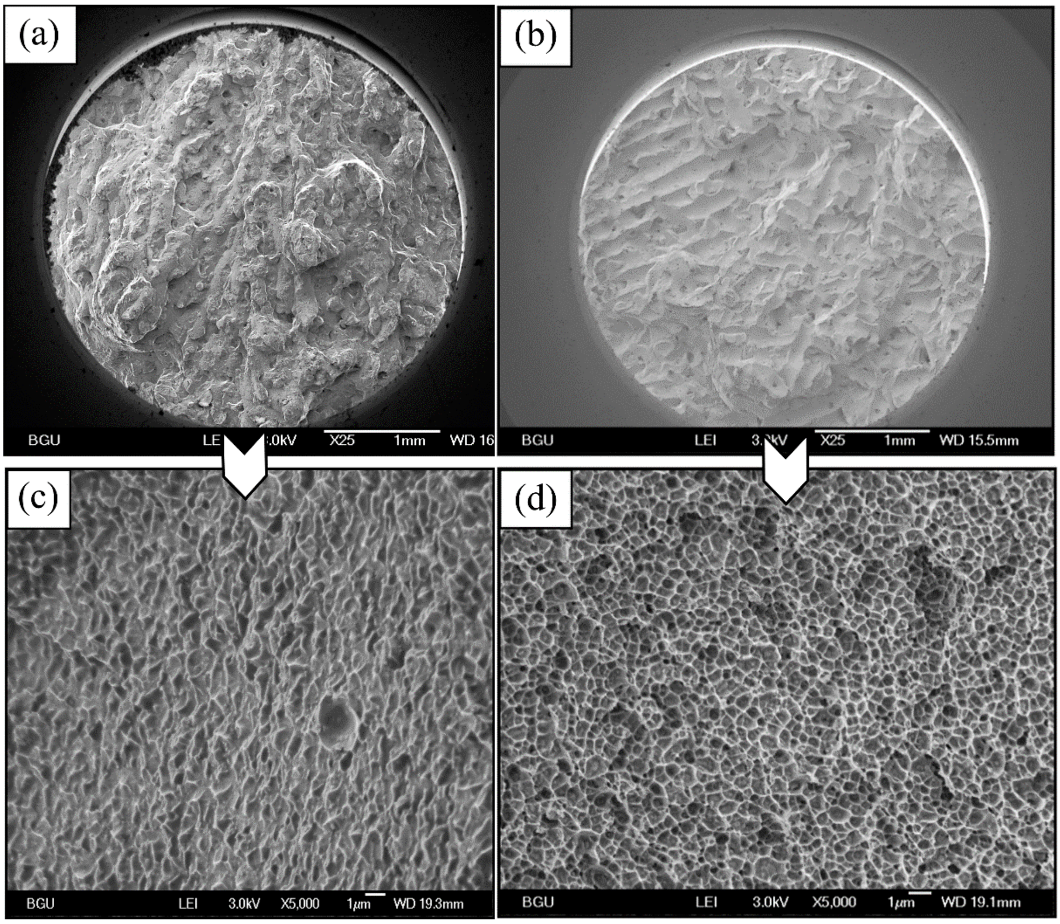

Fig. 42 Fracture surfaces of (a,c) as-built and (b,d) annealed AlSi10Mg alloy processed by SLM (adapted from [242]**).**

2.4.3 Fatigue behaviour

The fatigue life of additively manufactured components is often inferior to their cast counterparts [244]. This behavior has been ascribed to the various defects arising from LPBF (Section 1.5), which act as origin sites for crack nucleation. Specifically, the most influencing defects on the fatigue performance of LPBF*ed* Al alloys are summarized as follow:

- all the types of porosities irrespective of their origin [23]. On the one hand, lack of fusion pores can act as severe stress raisers because of their irregular shape, thereby promoting crack nucleation and growth. On the other hand, although gas pores possess a rounded shape, these defects might grow pronouncedly under cycling loading, leading to untimely failure. Lastly, fatigue failure may also occur in the presence of sub-surface pores likely caused by the adoption of a contour strategy [245].

Regarding this, Siddique et al. recommended a remelting of the contour for fatigue applications to avoid these pores [246].

- sub-micron oxide inclusions formed by the decomposition of the native oxide film covering the contaminated powder particles [41]. Oxides were found at the boundary between the crack origin area and the growth region on the fracture surfaces of LPBF*ed* AlSi10Mg alloy [125]. High laser power, as well as intense energy densities, might help to reduce the oxide presence, thus increasing the fatigue life.
- unmelted powder particles entrapped between stacked layers and hard spatter particles embedded in the soft Al matrix [185].
- poor surface roughness of as-built parts due to the presence of balling, satellites, and partially melted powder particles on the external skin [185].

As for tensile properties, both build orientation and platform heating affect fatigue performances.

Considering the build orientation, Tang and Pistorius obtained lower fatigue life by testing vertically built AlSi10Mg specimens [125]. Similarly, Mower and Long achieved a longer fatigue life for specimens horizontally produced made of a similar Al alloy [244]. The anisotropic fatigue behavior observed in both researches is related to the grain texture arising from LPBF [247]. When the load is perpendicular to the build direction, the crack quickly grows between the elongated <100> grains as shown in Fig. 43a, leading to premature fatigue failure. On the opposite, a higher crack growth resistance is expected when the load is applied perpendicularly to the building direction. The crack, indeed, experiences a more tortuous path because it propagates in a zig-zag mode between the vertically elongated grains (see Fig. 43b).

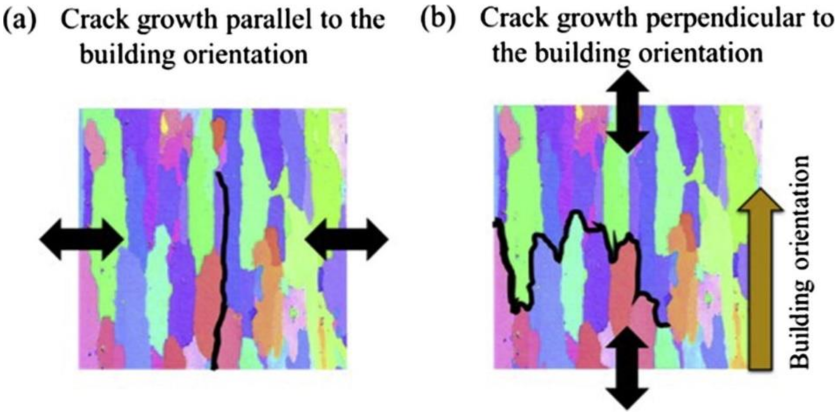

Fig. 43 Crack growing mechanisms (a) parallel and (b) perpendicular to the building direction [247].

As far as the effect of platform heating is concerned, fatigue performances can be enhanced by using a base plate heating [248,249]. Siddique et al. described the crack propagation behavior of a SLM*ed* Al-12Si alloy processed with and without platform heating [248]. In this work, the reduced number of pores in samples built with the heated platform significantly reduced the crack initiation at lower stresses. Once the crack nucleates at a higher stress amplitude, the crack propagation is slower for samples built with the heated platform. In fact, grains were coarsened by the reduced cooling rate, increasing the crack path to failure.

The fatigue life of LPBF*ed* components can be boosted by several surface finishing methods, primarily shot peening, sandblasting or machining, and/or through heat-treatments [179,185,249]. As an example, shot peening on as-built AlSi10Mg specimens increased the fatigue strength of about 270 %, exceeding the strength level of conventionally manufactured parts (+ 50%) [179]. The high compressive stresses induced on the sub-surface layers, together with the partial closure of small pores, contributed to the fatigue strength improvement. Nevertheless, some sub-surfaces pores might emerge after surface finishing with detrimental effects on fatigue, as observed by Aboulkhair et al. [185]. Moreover, Brandl et al. first study the impact of a T6-like heat-treatment on the high cycle fatigue behaviour of an AlSi10Mg alloy [249]. Due to the Si dendrites spheroidization, crack nucleation, as well as the propagation, is reduced upon T6. Being the material softened by T6, the ductility is increased and the fatigue resistance improved as well.

2.4.4 Other mechanical properties

Table 12 provides a brief overview of those mechanical properties which have been studied less intensively over the years.

The fracture toughness describes the ability of the alloy to counter the crack propagation. Hitzler et al. found that K_{IC} values for a SLM*ed* AlSi10Mg remarkably exceed those of the wrought alloy, although SLM alloy has a lower ductility [250]. This improvement can be explained considering the peculiar LPBF macrostructure. The presence of stacked melt pools, showing occasionally different orientations, prolongs the crack path to failure increasing the fracture toughness [251]. As for tensile and fatigue properties, the LPBF crystallographic texture causes an anisotropic toughness behavior. Vertically built samples showed the lowest K_{IC} in Ref. [250].

The impact resistance refers to the amount of energy absorbed by the material upon collision with a metal impactor. Charpy impact pendulum is commonly used for impact tests [252]. Similarly to the fracture toughness, the impact resistance for LPBF Al alloy is comparable or 1.5 times superior to that of conventionally manufactured parts [252–254]. The better impact strength is induced by the finer and more homogeneous LPBF microstructure.

The creep resistance of an alloy is the evaluation of its mechanical properties performed at relatively high temperatures for a prolonged time. Regarding Al alloys, it is endorsed that creep occurs in a temperature range between 200 and 300 °C. Uzan et al. evaluated the creep behavior of an AlSi10Mg alloy at various temperatures (225-300 °C) and stresses (117-147 MPa) [255]. The higher the adopted temperature/load, the faster was the creep phenomenon. At higher temperatures, the creep mechanism was triggered by dislocation gliding within primary Al grains.

The compressive behavior refers to the alloy performance under a compressive load. Aboulkhair et al. demonstrated that compressive properties can be significantly affected by the length-to-diameter ratio of tested specimens [23]. Buckling and barrelling might occur owing to the ductile nature of aluminum. Compressive yield strength surpasses that of cast counterparts up to three times. Besides, ceramic reinforcements as TNM or TiB_2 particles have been found able to further improved the compressive performances of a eutectic Al-12Si alloy.

The wear resistance of an alloy is the ability to resist a significant amount of sliding, rolling, and friction forces. Since Al alloys are generally classified as ductile materials, the wear resistance of these alloys is not relatively high compared to other materials, such as steel or cemented carbides [256]. For this reason, although the wear resistance of Al alloys has been enhanced after LPBF, metallic reinforcements were added to the Al matrix to achieved better wear properties [257].

Table 12 Overview on the less studied mechanical properties of LPBF Al alloys.

Properties	Alloy	Findings	Refs.
Toughness	AlSi10Mg	- vertically built samples show the lowest toughness	Hitzler et al. [250]
	Al12Si	- enhanced toughness compared to the cast counterpart -melt pool boundaries increase tortuosity of crack path	Suryawanshi et al. [251]
Impact	AlSi10Mg	- impact energy for SLM*ed* AlSi10Mg is comparable to T6-A360 cast alloy	Raus et al. [253]
	AlSi10Mg	- dynamic tensile strength exceeds that of cast counterpart by a factor of four - improved impact behavior after LPBF because of the fine homogeneous microstructure	Zaretsky et al. [254]
Creep	AlSi10Mg	- creep tests at 225-300 °C under applied load in the range 117-147 MPa - creep mechanism involves the dislocation motion in primary aluminum grains	Uzan et al. [255]
Compression	Al12Si+TNM	- enhanced compressive strength at the expense of ductility due to TNM reinforcements	Prashanth et al. [257]
	Al12Si/ Al12Si + TiB_2	- improved compression behavior due to the grain refinement induced by TiB2 particles	Xi et al. [258]
Wear	Al-50Si	- higher Si content leads to higher wear resistance	Kang et al. [259]
	Al12Si + TNM	- TNM reinforcement improves wear properties	Prashanth et al. [257]

2.5 Expanding the Al alloys palette for LPBF

The most printed Al alloys are mainly based on the Al-Si system that offers excellent castability and weldability. However, these alloys, which are borrowed from the foundry industry, do not show outstanding mechanical performances. In other words, although the Al-Si alloys processed by LPBF showed returns higher than the cast counterparts, it is believed that the full potential of LPBF has not yet been exploited entirely. Similarly to Al-Si alloys, high strength Al alloys, as those of 2*xxx* and 7*xxx* series, have been directly processed by LPBF. However, the high strength Al alloys possess large solidification ranges that may induce severe liquation cracking during printing. For these reasons, there has been a growing interest in expanding the Al alloys palette for LPBF.

Various strategies have been adopted in terms of alloy design to increase processability and performances of Al alloys. The next sub-sections will go through these strategies, describing first the effects of the addition of transition metals and rare earth elements (Section 2.5.1), and, then, the modification of pre-existing high strength Al alloys (Section 2.5.2). Moreover, this section also focuses on the attempts made by previous researchers to reproduce aluminum matrix composites by LPBF (Section 2.5.3). Finally, some Al alloys developed by mixing blends of powders are presented in Section 2.5.4.

2.5.1 Al alloys containing Transition Metal (TM) and Rare Earth (RE) elements

Transition metal (TM) and rare earth (RE) elements are characterized by reduced diffusion rate and low solid solubility. The low diffusion rate is an essential requirement for high-temperature applications (e.g., aerospace sector), while the limited solid solubility represents a drawback. Nevertheless, rapid solidification processes, such as LPBF, expand the solubility limit of such elements, retaining more solute atoms in solid solution. Thus, TM and RE elements have been added to existing Al alloys with the purpose of exploring new compositions specifically tailored for LPBF [24,260–262].

Scandium (Sc) possess properties which make the alloying of this element very attractive for the aerospace industry [224]. First, Sc has a low density coupled with a remarkable precipitation strengthening [263]. The enhanced super-saturated solid solution formed upon LPBF can decompose into fine $L1_2$ fully coherent Al_3Sc precipitates via direct aging heat-treatment. Precipitation occurs in the temperature range of about 250-350 °C, which is significantly higher than the aging temperature of heat-treatable Al alloys (140-190 °C). The high degree of coherence of Al_3Sc precipitates makes them stable up to roughly 350 °C. Second, Sc-precipitates act as nucleation sites for new Al grains, improving the grain refinement. Besides, such grain refinement effect may also reduce the liquation cracking phenomena in the high strength Al alloys [264]. The refined microstructure accommodates the thermal stresses and allows liquid feeding to the solidification front. Lastly, Sc controls the grain growth resistance at high temperatures owing to the Al_3Sc particles, which act as pinning points towards gliding dislocation at the grain boundaries [265].

The thermal stability of Sc-precipitates can be significantly enhanced by adding a small amount of *zirconium* (Zr) [266]. The effect of Zr is to modify the structure of Sc-precipitates. Al_3Sc particles, indeed, will absorb a certain fraction of Zr, forming an external shield of composition $Al_3(Sc_{1-x}Zr_x)$. Accordingly, being the Zr diffusion rate lower than that of Sc, coarsening at elevated temperatures is delayed, and the alloy outstandingly performs even at high temperatures.

However, the high cost of Sc powder limited the application of Sc containing- alloys to the production of high-value components [224]. This is the case of the aerospace industry, where the powder cost represents just a portion of the total cost of the aircraft component. Scalmalloy®, developed by the Airbus group, has been the first alloy specifically designed for the LPBF process [260]. This alloy, indeed, has been created by adding 0.8 wt% of Sc and 0.3 wt% of Zr to an Al-Mg cast alloy. Scalmalloy® has attracted much attention among researchers due to its newly conceived designing approach and outstanding mechanical properties.

Microstructural investigations performed on LPBF*ed* Scalmalloy® revealed that this alloy mainly consists of a bimodal microstructure [267]. Very fine equiaxed regions at the melt pool boundaries alternate with <100> elongated grains within the melt pool cores. The origin of this microstructure was explained in detail by Spiering et al. in Ref. [267]. The grain refinement effect of $Al_3(Sc_1Zr_{1-x})$ particles promotes the formation of fine equiaxed regions at melt pool boundaries. It was argued that the precipitation of Sc-containing particles from the super-saturated solid solution occurs at the remelted zones when neighboring and overlying tracks are produced. These particles can act as crystal seeds for the epitaxial growth of α-Al grains towards the melt pool core, i.e., in the opposite direction of the heat flux. However, the density of such $Al_3(Sc_1Zr_{1-x})$ particles is quite low during LPBF because the maximum temperature reached in the melt pool exceeds the dissolution temperature of $Al_3(Sc_1Zr_{1-x})$ [267]. Therefore, highly coarsed and elongated α-Al grains epitaxially grow along the <100> direction towards the melt pool core.

Fig. 44 illustrates the compositional effect of Sc addition to Al-Mg-Zr alloy for the production of Al-Mg-Sc-Zr alloy with a chemical composition similar to Scalmalloy® [264]. Grain refinement and annihilation of cracking can be noticed in Sc-containing alloy. Also, the research' Authors investigated the effect of thermal-related process parameters on the resultant microstructure for both alloys [264]. As the platform temperature and energy density are respectively increased to 200 °C and 154.2 J/mm^3, a nearly equiaxed structure is achieved in the Sc-containing alloy. This has been ascribed to the reduced heat flux, and the increased remelted areas, which in turn induced a consistent $Al_3(Sc_1Zr_{1-x})$ precipitation during remelting.

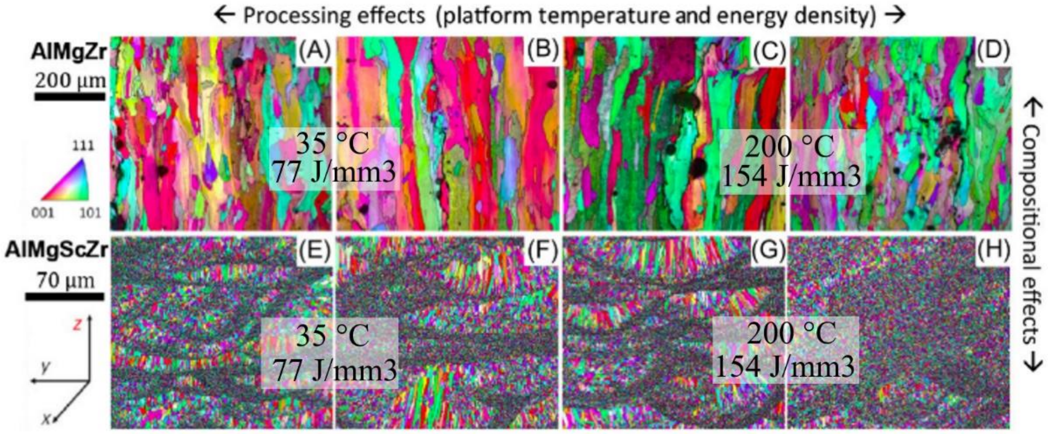

Fig. 44 Comparison of crystallographic textures of Al-Mg-Zr and Al-Mg-Sc-Zr alloys processed under different process conditions. Platform temperature was set at 35 °C and 200 °C. VED was fixed at 77 J/mm^3 and 154 J/mm^3 (adapted from [264]**).**

Contrarily to the other classes of Al alloys, the bimodal microstructure of Scalmalloy® produces just a slight anisotropy of mechanical performances [268]. This behavior can be attributed to the absence of preferential directions for the crack growth, which are inhibited by the extremely fine α-Al grain regions. In the as-built condition, Scalmalloy® showed a YS of 287 MPa, UTS of 427 MPa, and elongation of about 17 %. Considering the heat-treated condition, an increment of YS from 287 up to 470 MPa was observed upon aging at 325 °C for four hours. Ductility, on the opposite, slightly decreases but still showing a quite high value (≈ 14%).

Although Sc has shown remarkable precipitation strengthening in Al forming trialuminides precipitates, purchasing this element is quite expensive, and the availability on the market is limited [262]. Among RE elements, *erbium* (Er) has been regarded as a possible alternative element to Sc due to its capability to form Al_3Er precipitates with $L1_2$ structure [269]. These precipitates showed a good affinity with Zr in Al-Er-Zr cast alloys, which makes them thermally stable at elevated temperatures as well as effective retardants of crystallization [270]. Besides, Er is cheaper than Sc. Unfortunately, according to the binary Al-Er diagram phase, the maximum solubility of Er in Al at the eutectic temperature is just 0.045 at.%, much lower than Sc (0.23 at%). This implies that the maximum volume fraction of Al_3Er precipitates at RT is 0.18%, which is reasonably less than that of Al_3Sc (0.92%) [271]. However, the steep cooling rate of LPBF may help to retain more Er atoms in solid solution within fcc-Al, making Er a potential candidate for replacing Sc for future applications.

Battezzati and co-workers, studying the processability of single scan tracks of a binary Al-3wt% Er alloy, found higher nano-hardness in as-built tracks compared to the cast counterpart [163]. However, their research did not aim at replacing Sc with Er but was limited to explore new promising Al compositions for LPBF.

Jia et al. investigated two ternary alloys, such as Al-Sc-Zr and Al-Er-Zr, with the purpose of replacing Sc with Er in future works [262]. The direct aging curve for Al-Sc-Zr alloy in Fig. 45a shows outstanding precipitation strengthening and thermal stability at elevated temperatures. A hardness of about 107 HV was achieved after 168 h at 300 °C without traces of overaging. On the contrary, the hardness of the Er-containing alloy steadily decreased down to 80 HV upon 168 h. The reason behind these different aging behaviors is twofold.

On the one hand, although the solubility of Er was enhanced with rapid cooling, Er likewise precipitates out from solid solution after LPBF, forming trialuminides much larger than those found in the as-built Al-Sc-Zr alloy (Fig. 45b,c). Whereas, in the case of Al-Sc-Zr alloy, most of Sc is expected to be in solid solution with Al, increasing the precipitation potential of this alloy. On the other hand, the diffusivity of Er at 300 °C (aging temperature) is higher than that of Sc [272]. The large precipitates found in as-built Al-Er-Zr alloy grow faster during heat-treatment, thereby leading to a premature overaging and poor thermal stability (Fig. 45d,e). Therefore, the overall results revealed that Sc is hardly replaceable by other TM or RE elements [262].

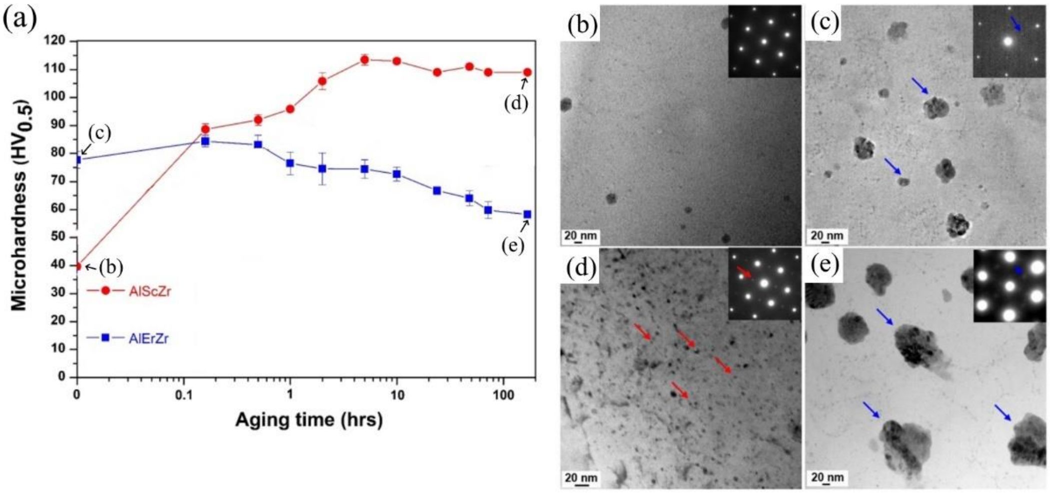

Fig. 45 (a) Aging responses of LPBF*ed* Al-Sc-Zr and Al-Er-Zr at 300 °C and (b-e) representative TEM micrographs: (b) as-built Al-Sc-Zr, (c) as-built Al-Er-Zr, (d) directly aged Al-Er-Zr for 168 h and (e) directly aged Al-Er-Zr for 168 h (adapted from [262]).

The MCAM research group has paved an alternative way to develop high strength Al alloys for LPBF [24,203,273]. Instead of replacing Sc, they considered the idea of alloying other elements into Al-Sc alloys. Thus, *manganese* (Mn) was added to fully exploit the rapid solidification nature of LPBF. The pursued criteria for the Mn selection has been the following:

- Mn is highly soluble upon LPBF and may provide a remarkable precipitation potential upon aging.

- Mn does not affect the equilibrium solubility of Sc in the fcc-Al matrix.
- Mn should not form any precipitates with Sc. In this way, the $Al_3(Sc, Zr)$ fine precipitates together with the possible Mn-rich particles will effectively strengthen the alloy.
- the diffusion kinetic of Mn at the aging temperature for Al-Sc alloys is two orders of magnitude lower than that of Sc. Hence, it would be possible to enhance solid solution strengthening of the alloy even after the heat-treatment.

The microstructure, strengthening mechanisms, and precipitation kinetics of this newly conceived Al-Mn-Sc alloy have been deeply investigated by Jia et al. in Refs. [24,203,273]. Similarly to Scalmalloy®, the as-built microstructure exhibited a bimodal microstructure [24]. TEM investigations revealed the presence of two kinds of reinforcing precipitates: the well-known $Al_3(Sc,Zr)$ phase within the fine Al grains as well as the Al_6Mn phase at the grain boundaries [203]. The as-built YS was about 431 MPa. After direct aging of 5 h at 300 °C, the alloy reached a yield strength of roughly 571 MPa accompanied by 18.1% of elongation at failure, which are the highest tensile properties achieved by an LPBF*ed* Al alloy [23]. Interestingly, the idea of exploiting the solid solution strengthening by adding Mn has been rewarded since this mechanism contributed to 24% (134 MPa) of the total YS after heat-treatment.

2.5.2 Modification of existing high strength Al alloys

High strength Al alloys have been hardly processed via LPBF because of their high susceptibility to liquation cracking. These alloys, indeed, contain age-hardening elements, which enlarge the alloy solidification range whereby cracking is enhanced.

The 2*xxx* Al alloys are commonly adopted for aerospace applications. Cu is the primary alloying element, which contributes to the high strength by precipitation strengthening. To minimize the presence of cracks, researchers have made attempts by tuning first the LPBF process parameters [191,218,274]. However, changing the local heat input by using remelting or meander strategies turned out to be ineffective for the production of crack-free parts of 2618 Al alloy [274]. Only a careful control of the heat energy input delivered to the processed alloy has shown acceptable results in terms of cracks elimination [218]. As an example, Wang et al. produced fully dense and crack-free samples of an Al-3.5Cu-1.5Mg-1Si, adopting low power (≈ 200W) and scanning speed (≈ 200 mm/s) [218]. Similarly, Zhang et al. claimed that high volumetric energy densities are needed to prevent cracking in their processed Al-Cu-Mg alloy with a chemical composition similar to AA 2024 alloy [191]. However, they had to sacrifice productivity to avoid cracking in both cases.

A pioneering approach for reducing hot tearing cracks consisted in the modification of existing 2*xxx* alloys. In this context, Zhang and co-workers mixed 2wt% of pure chemical Zr with 2024 alloy powder [275]. Low-magnification micrographs on polished cross-sections of the un-modified 2024 alloy revealed that almost crack-free samples were obtained at low scanning speed (5 m/min). Increasing scan speed resulted in a consistent hot tearing phenomenon. The addition of Zr suppressed cracking at a large extent and enabled the production of crack-free samples at higher scanning speed (15 m/min). Thus, Zr enhanced the productivity up to three times, widening the process window of 2024 alloy. The reason for this behavior can be attributed to the grain refinement effect of Zr. A bimodal microstructure reminiscent of Scalmalloy® was observed in the Zr-modified 2024 alloy. Several Al_3Zr precipitates were found at the melt pool boundaries, presumably acting as potent crystal nuclei for the growth of α-Al grains during solidification. Besides, the fine Al_3Zr particles assisted the liquid feeding to the solidification front even at a higher scanning speed, which means steeper cooling rates.

Severe liquation cracking has also been found in 7*xxx* Al alloys, where Zn is the main alloy element. Many research works on this alloy system have shown large columnar grains accompanied by intracolumnar cracks in LPBF*ed* alloys [176,276]. It is believed that the absence of liquid between columnar grains and tensile residual stresses are the cause of cracking. Recently, researches have aimed at improving the processability of 7*xxx* Al alloys by decreasing the alloy solidification range and/or refining the grain size [176,177,276].

First, Montero Sistiaga et al. added 4wt% of Si to 7075 Al alloy [176]. The columnar cracks appearing in the 'tel quel' alloy have been eliminated with the Si addition. The effect of Si was twofold. On the one hand, it reduced the alloy solidification range by lowering the alloy melting point. On the other hand, it acted as a grain refiner, promoting the formation of ultrafine-grained regions at the overlapping areas. The analogous effect was later observed in Ref. [276] by mixing 50 vol% of AlSi10Mg with 50 vol% of Al-7075 powder. Recently, also Casati et al. developed an Al-Zn-Si-Mg-Cu alloy, which showed no cracks, good aging response as well as mechanical properties [177].

Le Zhou et al. proposed another solution to process a crack-free Al-6Zn-2Mg alloy via LPBF [277]. They introduced 1wt% of (Sc + Zr) to the master alloy to mimic the typical bimodal microstructure of Scalmalloy®. As for the previous works, cracking was inhibited by the refinement effect of the alloying element additions.

The grain refinement, helpful to prevent cracking, can also be induced via the dispersion of nano-particles on the powder particle surfaces. For instance, Martin et al. coated 7075 particles with ZrH_2 zirconium nucleants [174]. The introduction of these nanoparticles induced nucleation and precipitation of Al_3Zr particles, which in turn change the solidification mode from columnar to equiaxed dendritic.

Mechanical properties of the Zr-modified 7075 are remarkably higher than those of LPBF*ed* 7075 and AlSi10Mg, and comparable to that of the wrought 7075 alloy.

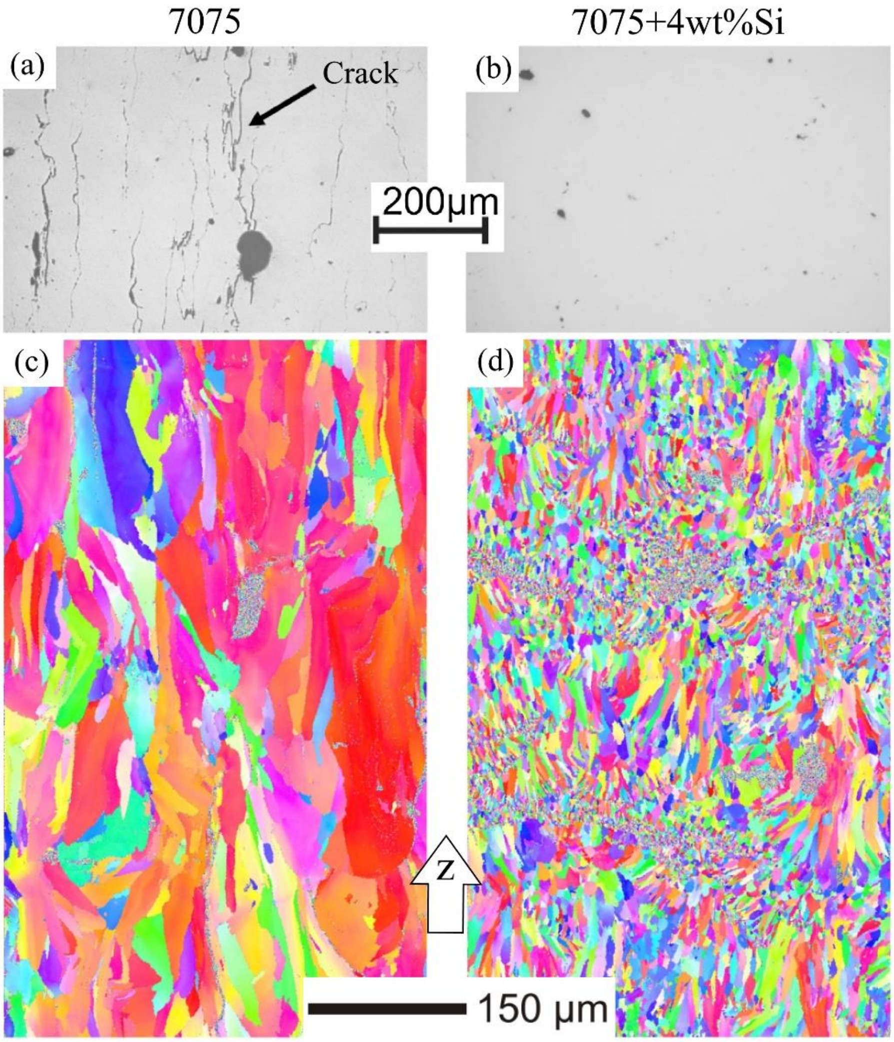

Fig. 46 Effect of 4 wt.% Si addition to 7075 Al alloy processed by LPBF. (a,c) The presence of cracks and coarse and elongated grains in as-built 7075 alloy; (b,d) near fully dense 7075 alloy + 4wt.% Si without appearance of cracks and with refined microstructure.

2.5.3 Aluminum matrix composites

Aluminum matrix composites (‘AMCs’) represents another way to increase the performances of LPBF Al alloys. For this reason, research groups and companies have devoted much attention to the development of AMCs by LPBF over the years [278,279]. The addition of ceramic reinforcements to Al systems has been shown to enhance significantly the mechanical performances, especially hardness, strength, and wear, as well as conductive properties. However, embrittlement may be induced when ceramic reinforcements are not bonded adequately with the Al matrix [24]. These weak bonds may act as initiation sites for crack propagation, thereby anticipating the failure of the part.

The LPBF technology enables the in-situ production of AMCs, exploiting the LPBF process characteristics to evenly disperse the ceramic reinforcements into the Al matrix. Therefore, AMCs parts containing oxides, carbides, or borides have been successfully produced and tested [279–281].

To achieve a high densification level for AMCs, Aversa et al. reasonably advised to operate at higher energy density than that adopted for the Al matrix [282]. The introduction of particle reinforcements, which can agglomerate into the melt pool, increases the alloy viscosity, which in turn hinders the spreading of the melted phase at low energy densities. Thus, increasing the energy density contributes to a better AMCs densification. However, when VED is increased excessively, agglomeration of reinforcement particles as well as softening of the Al matrix may occur, with a detrimental effect on AMCs' strength [282]. Therefore, two criteria must be observed to optimize the process parameter of AMCs: the high level of densification and the homogeneous dispersion of ceramic particles.

Han et al. firstly synthesized Al_2O_3-Al composite powders via high-energy ball milling [280]. Near fully dense components were obtained at relatively high energy density (317.5 J/mm^3) and a scanning speed of 300 mm/s. SEM investigations revealed that Al_2O_3 ceramic particles were evenly dispersed within the Al matrix. This contributed to improving the yield strength and micro-hardness of respectively 36.3 and 17.5% compared to the pure Al.

Similarly, starting from composite powder blends obtained by ball milling, Chang and Gu developed two reinforced AlSi10Mg alloys with SiC and TiC particles [281,283]. The SiC-containing AlSi10Mg alloy consisted of two types of reinforcement phases [283]. On one side, there were the unmelted SiC particles; on the other, the Al_4SiC_4 phase formed at high energy densities. The Authors believed that the latter reinforcing phase was responsible for the high mechanical properties of this Al-based composite. The TiC-reinforced AlSi10Mg alloy consisted of α-Al cells surrounded by TiC particles segregated along the cell boundaries [281]. The distribution of the TiC phase was found to change with the applied energy density. The steep temperature gradient induced at higher energy densities, indeed, creates significant thermocapillary flows, which can improve the dispersion of TiC particles. TiC-rings surrounding α-Al cells were noticed at a relatively high energy density (≈ 240 J/mm^3). This ring structure enhanced hardness, strength and elongation, without compromising the ductility.

Kruth and co-workers manufactured near fully dense and crack-free TiB_2-AlSi10Mg components via SLM [279]. Differently from previous researches, AMC parts were produced starting from pre-alloyed powder of AlSi10Mg decorated by nano-TiB_2 particles. TEM micrographs revealed the presence of well-dispersed TiB_2 particles and nano-Si precipitates within equiaxed α-Al grains. Both precipitates showed a high degree of coherency with the Al matrix, increasing the yield strength from 396 MPa (AlSi10Mg, Ref. [44]) to the 530 MPa of TiB_2-AlSi10Mg. Ductility was admirably preserved (≈ 15.5 %).

2.5.4 Customized powder blends of Al alloys

Gas-atomized powder is generally recommended to additive manufacture parts with high densification and homogeneous chemical composition (Section 1.3). In this regard, it has been estimated that the cost of gas-atomized powder is the second largest cost associated with LPBF production [22]. Moreover, few companies can gas-atomize powder in a short time. Thus, exploring new Al alloys compositions customized for AM processes may be rather expensive and time-consuming.

The powder blending represents a low-cost way to synthetize new Al alloys with high degree of flexibility in the chemical composition [284]. Once the alloy chemical composition is defined, the required powders are mixed within rotating jars and, then, *in-situ* alloyed during laser melting. Physical phenomena, such as thermocapillary effect and/or recoil pressure, will help to synthesize the alloy under the laser exposure. Powder blending has been used by some research groups to modify/adapt existing Al alloys or explore novel Al compositions for LPBF [66].

For instance, Aversa et al. produced Al-Si-Ni samples via LPBF by blending pre-alloyed AlSi10Mg powder with a pure chemical *nickel* [66]. The mixing ratio was selected, aiming at having a mean composition for the Al-Si-Ni alloy near the eutectic point (10.98 wt% Si, 4.9 wt% Ni at 567 °C). Near-fully dense samples were then produced, adopting the optimized process parameter of the master AlSi10Mg alloy. SEM micrographs revealed a heterogeneous microstructure consisting of un-melted particles of Ni. It was argued that these un-melted particles were caused by the incomplete fusion of Ni powder agglomerates. However, most of Ni atoms forms trialuminides precipitates (Al_3Ni) of sub-micrometric size, located preferentially along the melt pool boundaries. The chemical composition measured within the melt pool, instead, was more homogeneous and near the nominal one. The addition of Ni to AlSi10Mg alloy was found beneficial in terms of hardness. The Authors noticed an HV increment of roughly 33% compared to the master alloy. However, significant residual stress distortions were found in as-built cubic samples [285].

Similarly, the Al339 alloy has been in-situ synthesized, starting from pre-alloyed powder batches of Al-Mg and Si-Cu-Ni [286]. The mixing ratio of 84.75 (Al-Mg):15.25 (Si-Cu-Ni) was accurately calculated with Thermo-Calc. The Al319 powder blend was then mixed in jars, which contained zirconia balls to separate the powder agglomerates. Thus, bulk samples were produced via SLM. The microstructure consisted primarily of Al-rich cells decorated by brighter architectures, presumably formed by Al_2Cu, Al_3Ni, and Mg_2Si compounds precipitated out from the super saturated solid solution upon cooling. Precipitates were more concentrated at the melt pool boundaries.

Later, Wang et al. used an SLM machine for the in-situ manufacturing of Al-*x* Cu samples from various powder mixtures [287]. XRD analyses conducted on both powder mixtures and massive samples revealed that peaks related to pure Cu were no longer visible after LPBF. Thus, it is reasonable to suppose that Cu atoms were partly retained in the Al matrix and partly precipitated as Al_2Cu phase upon LPBF. Nevertheless, unmelted Cu particles were still detected in the as-built Al-6/40wt% Cu alloys. The microstructure around solute-rich areas was inhomogeneous, showing six zones at decreasing Cu content. Generally speaking, the lower the Cu addition, the more homogeneous the microstructure was.

Contrarily to the previous researches, Bartkowiak et al. evaluated the possibility of developing customized blends of high strength Al alloys by understanding first the consolidation behavior of single laser tracks [288]. Single scan microstructures were characterized by very fine α-Al cells with intermetallic phases dispersed homogeneously in the Al matrix. Neither cracks nor porosities were detected in both alloy systems. Based on these encouraging results, the Authors indicated this method as a possible way to quickly develop novel Al compositions for LPBF using few powders.

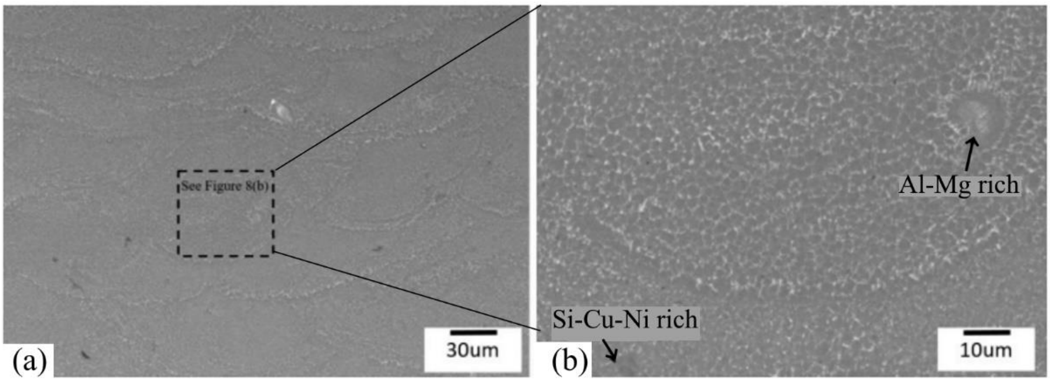

Fig. 47 (a) Fish-scale microstructure of an in-situ alloyed Al339 alloy; (b) high magnification micrograph showing some inhomogeneous areas enriched of Al-Mg or Si-Cu-Ni (adapted from [286]**).**

Chapter 3

Laser Powder Bed Fusion of AlSi10Mg + 4Cu mixed powder

The results showed in this chapter are partially published in the following articles:

- F. Bosio, A. Aversa, M. Lorusso, S. Marola, D. Gianoglio, L. Battezzati, P. Fino, D. Manfredi, M. Lombardi, A time-saving and cost-effective method to process alloys by Laser Powder Bed Fusion, Mater. Des. (2019) 107949. doi:10.1016/j.matdes.2019.107949.
- S. Marola, D. Gianoglio, F. Bosio, A. Aversa, M. Lorusso, D. Manfredi, M. Lombardi, L. Battezzati, Alloying AlSi10Mg and Cu powders in laser Single Scan Tracks, melt spinning, and Laser Powder Bed Fusion, J. Alloys Compd. 821 (2020) 153538. doi:10.1016/j.jallcom.2019.153538.

3.1 Introduction

Laser powder bed fusion paved the way for developing novel alloy compositions with peculiar characteristics, which cannot be achieved with conventional manufacturing processes (Section 2.5). Although there has been an increased demand for new alloys compatible with LPBF, the material palette available in the marketplace is quite limited [289]. The most widespread families of alloys are, indeed, Al-Si cast alloys, stainless steel, nickel-based superalloys, titanium and, recently, high-entropy alloys [290–294]. Hence, the development of new materials for LPBF is, nowadays, one of the main challenges of this field [174].

Developing new alloys for LPBF, however, generally requires high economic resources due to the cost of starting powders. Whenever a novel alloy system is investigated, there is, in fact, the need for ad-hoc pre-alloyed powder, which can be quite expensive and difficult to purchase in the marketplace within a short time [295]. To test new alloys, blending different commercial powder for the *in-situ* alloy synthesis under laser exposure can be a fast and cheap strategy (Section 2.5.4). Despite its flexibility, the powder mixing of various elements results often in fluctuations of composition owing to different melting points and thermal properties of constitutive elements [66,176,276,286,296].

Once the suitable powder blend is produced, the alloy process parameters must be optimized. For this purpose, single scan tracks (SSTs) could be employed. As described in Section 1.2, SSTs involve the laser scanning of powder along a single fusion line to assess the alloy processability. The quality of printed parts is strictly related to the characteristics of each laser track due to the nature of LPBF manufacturing [137]. For this reason, SSTs have been widely investigated over the years to quickly assess the processability of LPBF Al alloys [68,100,288,297]. Previous works in literature stated that power and speed values for LPBF could be already determined by studying SSTs, using a small quantity of powder [44,67,180,298,299]. However, to produce 3D parts, it is essential to evaluate the impact of other process parameters on porosity, such as the hatching distance and the scanning strategy (see Sections 1.2.3 and 1.2.5). To do so, time-intensive DoE experiments are generally performed, and a great amount of specimens is produced [59,62,300].

This chapter presents the results of an AlSi10Mg alloy modified with 4 wt.% of Cu powder, a typical amount giving hardening in 2*xxx* Al series [200]. The main reason for this composition choice was to exploit both solid solution and precipitation strengthening mechanisms promoted by the addition of Cu. As regard to the solid solution strengthening, previous works reported an increased solid solubility limit of Cu in rapidly solidified Al alloys (Section 2.2.2.2). Furthermore, also considering that our Cu addition is lower than its typical solid solubility limit in Al (i.e. 5.65 wt.% [200]), a highly supersaturated solid solution was expected in the as-built alloy. As for precipitation strengthening, the idea was to exploit the supersaturated solid solution by post-process heat treatments with the purpose of promoting the precipitation of hardening phases containing Cu (Section 2.3.1).

The starting powder was obtained by mixing AlSi10Mg and Cu powder. The alloy was then synthesized *in-situ* during LPBF. The alloy processability was investigated by producing single scan tracks (SSTs), and bulk samples with unidirectional and rotated scanning strategy. After the definition of the alloy process window, near fully dense bulk samples with porosity lower than 1.5% were successfully produced. Differently from recent works [64,297], it will be demonstrated that a complete set of power, speed, and hatching distance values can be already defined by studying SSTs. According to the presented results, a time-saving and cost-effective method to process alloys by LPBF is proposed.

Furthermore, the microstructure and the chemical homogeneity of AlSi10Mg+4Cu alloy were also evaluated at both single scan and bulk sample levels. Results revealed the presence of a eutectic formed by Si particles interconnected by Al_2Cu precipitates as well as the occurrence of Cu segregations. A preliminary assessment of mechanical properties was then performed by studying the hardness behavior of the alloy. In this regard, nano-indentation and Brinell tests were carried out to evaluate the effect of Cu on nano- and macro-hardness, respectively. A significant hardness increment induced by solid solution and precipitation strengthening was revealed.

3.2 Materials and Methods

3.2.1 AlSi10Mg and Cu powder mixing

AlSi10Mg composition was modified by adding 4wt% of Cu [200,211]. Therefore, gas-atomized powder of AlSi10Mg and high purity Cu (HCP Cu), supplied respectively by EOS Gmbh and Sandvik Osprey LTD, were mixed in a weight proportion of 96:4. Mixing was carried out in ceramic jars rotating at 60 rpm for 24 h. To prevent the deformations of particles and preserve the powder flowability, grinding media were not used during mixing. The chemical compositions of the master powders, as well as the calculated composition of AlSi10Mg+4Cu mixed powder, are reported in Table 13.

Table 13 The chemical composition of the used powders (wt%). †the mean composition of AlSi10Mg+4Cu mixed powder was computed from AlSi10Mg and Cu powder compositions.

Alloy	Si	Fe	Cu	Mn	Mg	Ti	O	Al
AlSi10Mg	9-11	≤ 0.55	≤ 0.05	≤ 0.45	0.2-0.45	≤ 0.15	-	Bal.
HCP Cu	-	-	≥ 99.96	-	-	-	≤ 0.04	-
AlSi10Mg+4Cu†	8.6-10.6	≤ 0.55	4	≤ 0.45	0.19-0.43	≤ 0.15	≤ 0.04	Bal.

AlSi10Mg+4Cu mixed powder was first investigated using a Field Emission Scanning Electron Microscope (FESEM) Zeiss SupraTM 40 to evaluate particle morphology. Then, the powder size distribution (PSD) was determined using a laser granulometer Frisch Analysette 22 Compact, and calculated using the volumetric assumption.

A representative micrograph of AlSi10Mg+4Cu mixed powder is shown in Fig. 48a. The mixed powder particles showed mostly spherical shape, pointing that the mixing technique did not damage them. It was also observed some occasional satellites and a significant fraction of fine particles (mostly AlSi10Mg particles) that tend to adhere to the largest ones, forming agglomerates with a size of 20-30 µm. Cu particles with a size in the range 15-25 µm were visible among the darker AlSi10Mg particles, as pointed by the white arrows. It is worth noting that a decent dispersion of Cu particles was achieved after mixing. However, chemical inhomogeneities might be found after LPBF owing to the low absorptance of Cu powder [301], and the high cooling rates of LPBF [161].

The PSD distribution of AlSi10Mg+4Cu mixed powder is depicted in Fig. 48b. The characteristic particle diameters of AlSi10Mg+4Cu powder are 13.3, 28.2 and 44.8 µm, corresponding to 10% (d_{10}), 50% (d_{50}) and 90% (d_{90}) of the PSD, respectively. The average powder size lies within the typical size interval of powders for LPBF [302] and, thus, the AlSi10Mg+4Cu mixed powder can be considered suitable for the LPBF production.

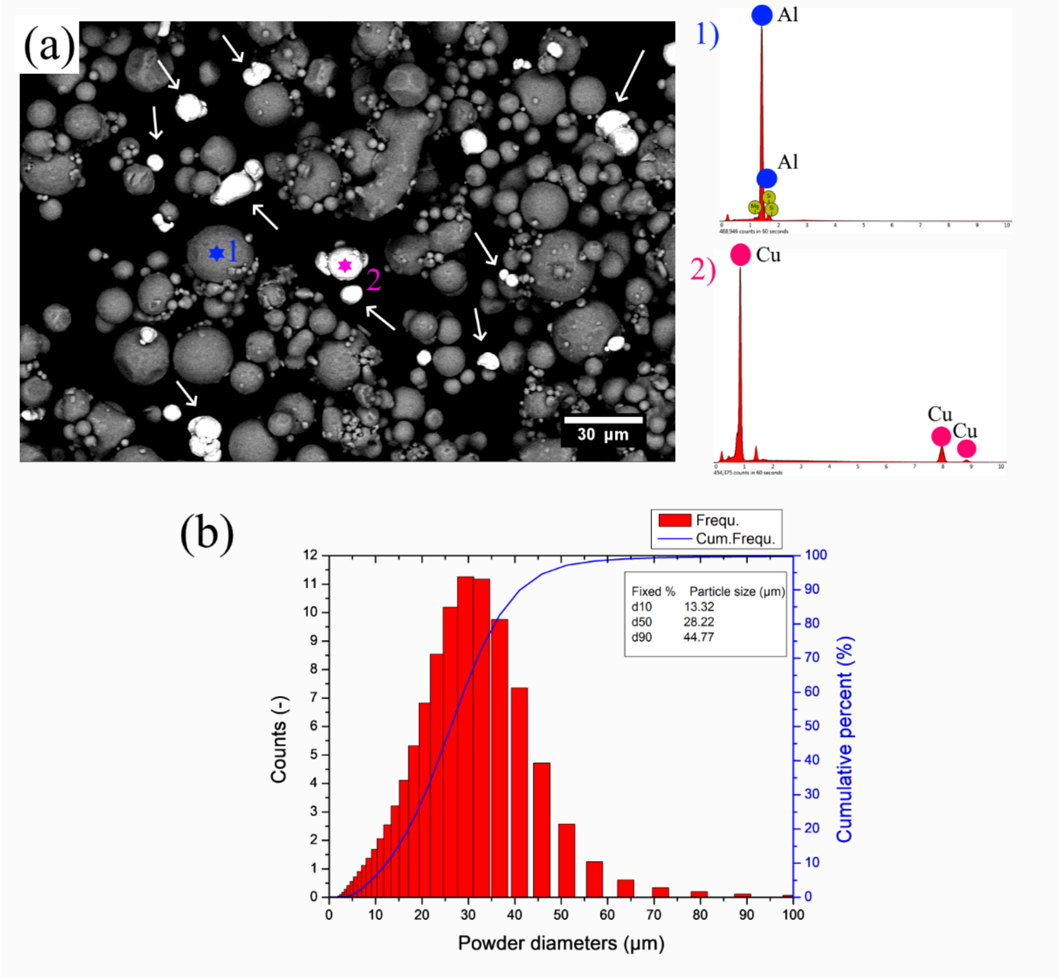

Fig. 48 (a) Representative micrograph of AlSi10Mg+4Cu powder obtained by FESEM. Insets show the EDS point analysis performed on 1) AlSi10Mg and 2) Cu particles, respectively. (b) The particle size distribution calculated with volumetric assumption.

3.2.2 Preparation and characterization of Single Scan Tracks (SSTs)

Once the starting powders were mixed, SSTs of AlSi10Mg+4Cu were manufactured using an EOSINT M270 Dual-mode LPBF system (EOS Gmbh). The system was equipped with a Yb-fiber laser with a wavelength of 1070 nm, a continuous power up to 200 W, a spot of 100 µm and a scanning speed of a maximum 7000 mm/s. The building chamber was flushed and filled by argon to minimize the powder oxidation. The building platform was heated at 100 °C with the purpose of reducing thermal stresses between the plate and deposited SSTs [221].

Following the method set up by Aversa et al. on various Al-based alloys [100], a building platform with removable discs of AlSi10Mg was used for SSTs production (Fig. 49a). The disc diameter was 40 mm. The chemical composition of the disc was intentionally selected as near as possible to the processed alloy to prevent any chemical contamination of the melt pool composition after consolidation. In this way, the dilution of the alloy chemical elements through the substrate should be limited. To produce the SSTs, a powder layer was deposited on the disc by using the self-developed recoater of Fig. 49b. The thickness of the powder layer was set at 50 µm, considering the real layer thickness obtained when 30 µm of building platform displacement is used. For all the experiments, the length of each SST was 9 mm. Once the layer was homogeneously deposited on the disc (Fig. 49c), SSTs were manufactured according to the selected power (P) and speed (v) values (Fig. 49d,e).

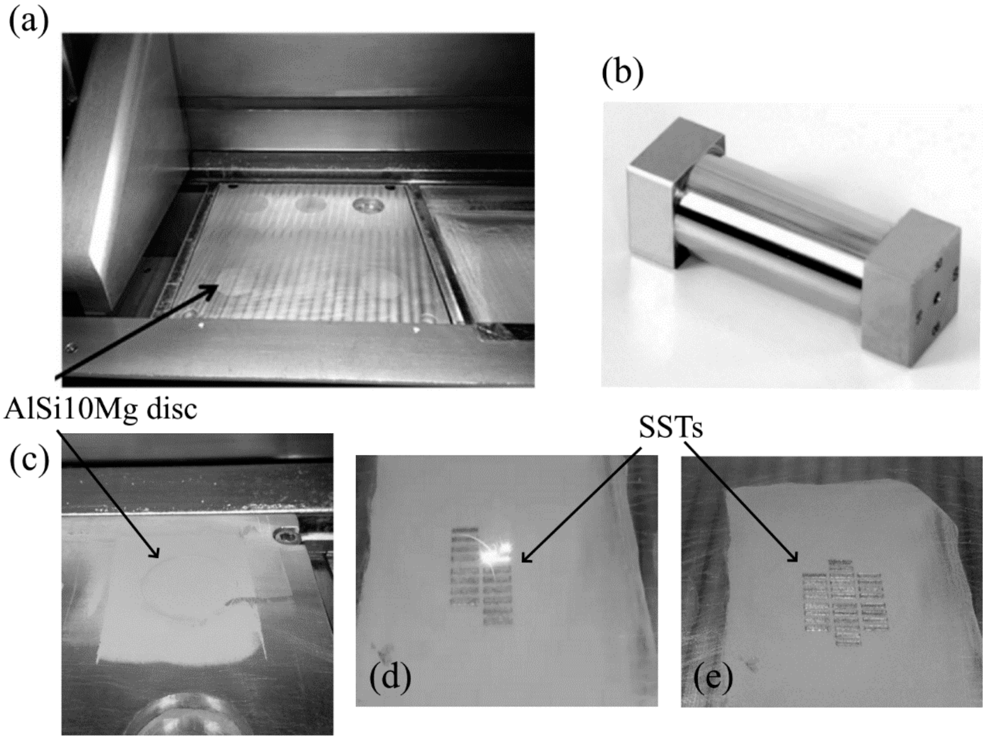

Fig. 49 (a) The modified building platform with the removable AlSi10Mg discs; (b) self-developed recoated used to spread the powder on the disc surface; (c) a deposited powder layer; (c) the melting and (d) the consolidation of SSTs.

SSTs were firstly produced to assess the processability of the mixed AlSi10Mg+4Cu powder and, then, to determine the alloy process window. Two batches of scan tracks were manufactured in two jobs by fixing the P and v values of Table 14.

Table 14 Power (P) and speed (v) values used for the production of AlSi10Mg+4Cu single scan tracks.

Job	$P \times v$ matrix	P [W]	v [mm/s]
n°1	5×5	100, 130, 160, 180, 195	300, 600, 800, 1200, 1500
n°2	3×4	160, 170, 180	700, 800, 900, 1000

A matrix of 5P × 5v for a total of 25 combinations was adopted for the first SSTs job. According to the Authors' recent research on the SSTs investigation of Al alloys [100], the first SSTs job was considered as a quick preliminary investigation of the alloy processability, thus wide P-v intervals were chosen. Specifically, the P-v region, which showed stable and regular tracks for the AlSi10Mg alloy of Ref. [100], was used as a starting point of this work. The manufactured SSTs were first evaluated by on-top analysis using an optical microscope (OM) LEICA DMI 5000 M. Specimens for the cross-sections characterization of SSTs were, afterward, cut from the disc, polished following the standard metallographic route for Al alloys and observed by OM. The investigated melt pool was taken in the middle of SST to assess a reliable shape, which was not affected by the border instabilities of the laser source [303]. The geometrical characteristics of melt pools, namely the width (w), the total height (h), the penetration in the substrate (d), and the growth (g), were determined by post-processing the melt pool OM micrograph via ImageJ software, as depicted in Fig. 50. The total height to width ratio (h/w) and the growth to depth ratio (g/d) values were used as the two leading shape indicators to define the alloy process window.

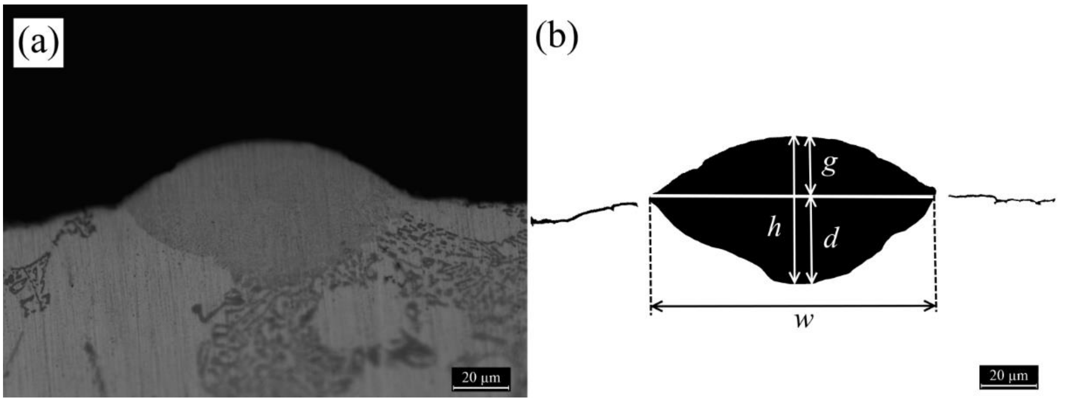

Fig. 50 (a) Low magnification micrograph of a melt pool and (b) its binary image after processing with ImageJ. The dimensions used to assess the melt pool geometrical features are labeled in Fig. 50b.

The second SSTs job was designed to finely tune the alloy process window. Hence, a narrow 3P × 4v matrix with intervals of, respectively, 10 W and 100 mm/s, was adopted in the region of stable and regular tracks. Differently from the first SSTs job, a detailed on-top assessment was carried out on SSTs surfaces via a Scanning Electron Microscope (SEM) Phenom XL . The whole SST length was investigated. Five micrographs were taken for each SST. Then, the SSTs width (w) was computed through ImageJ. For each SST (12 combinations), the i-laser track width w_i (with i- from 1 to 12) was determined as the average of 250 measurements, according to the method depicted in Fig. 51.

Furthermore, the melt pools produced within the selected process window were characterized according to the following sequence of experimental activities. First, the distribution of Cu was evaluated through compositional maps, which were performed on the melt pool cross-sections. Compositional maps were obtained using a Phenom XL SEM equipped with the Energy Dispersive X-ray Spectroscopy (EDS) detector. Then, nano-indentation tests were conducted to assess the hardness at a nano-scale using a TI950 Hysitron nano-indenter. Therefore, a nano-indentation grid was performed on the same cross section investigated by EDS. The grid was adapted to cover completely the melt pool surface with the indentation imprints at a distance of 7.5 µm from each other. Finally, to reveal the microstructure, melt pool specimens were immersed in a diluted Keller solution (20% Keller reagents + 80% H_2O) for 10 s and observed via FESEM. No further polishing was performed between analyses in order to investigate the same melt pool cross section and, eventually, correlate experimental results.

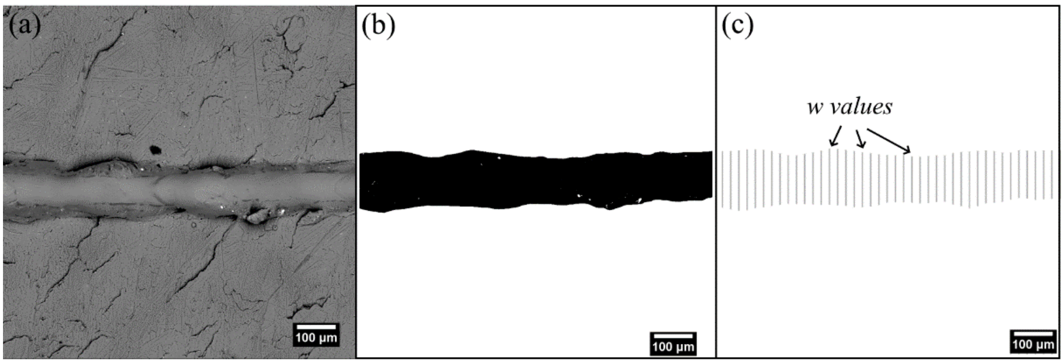

Fig. 51 The protocol adopted to determine the average single scan track width (*w*): (a) SEM micrograph of an SST sector (5 sectors were considered for each SST to cover the whole SST length); (b) the binary single scan track image and (c) the width bars (achieved by the superimposition of a grid with Fig. 51b).

3.2.3 Production and characterization of bulk samples

Bulk samples with dimensions of 10×10×10 mm^3 (Fig. 52) were manufactured using the LPBF process parameters summarized in Table 15. Specimens were built by using a layer thickness of 30 µm, which was comparable with the mean particle size of AlSi10Mg+4Cu powder (≈ 28 µm, Fig. 48b). As for SSTs experiments, the building platform was heated at 100 °C during printing.

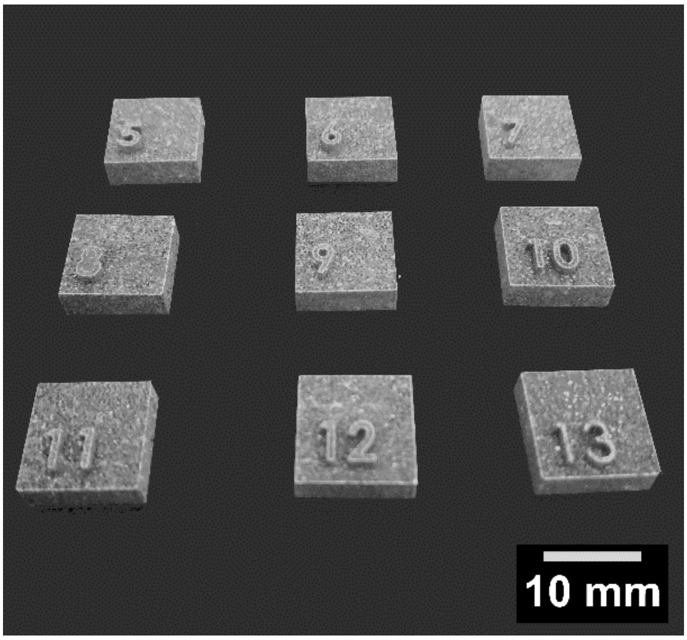

Fig. 52 Bulk samples of AlSi10Mg+4Cu manufactured using the process parameters defined after SSTs investigations.

Table 15 Factors and levels employed in the DOE of the two jobs of bulk samples.

Job	Scanning strategy	P×v×h_d matrix	P [W]	v [mm/s]	h_d [mm]
n°1	Unidirectional, 0°	3×4×3	160, 170, 180	700, 800, 900, 1000	0.08, 0.12, 0.14
n°2	Rotated, 67°	2×4×2	170, 180	700, 800, 900, 1000	0.12, 0.14

As reported in Section 1.2.5, various scanning strategies can be adopted for LPBF. For the first job, the unidirectional scanning strategy was employed to clearly understand the impact of changes of P, v, and hatching distance (h_d) on the alloy density level and, also, to evaluate the overlapping of adjacent SSTs. A full factorial DOE consisting of 2 factors with 3 levels (P and h_d) and 1 factor with 4 levels (v) was adopted, returning the total of 36 P×v×h_d combinations (Table 15). The power and speed values were borrowed from the second job of SSTs, whereas the Eq. (3.1) was used to define the h_d levels [64]:

$$\varphi = \frac{w-h_d}{w} \cdot 100 \tag{3.1}$$

where φ is the overlapping degree of adjacent SSTs. Thus, it has been possible to set three h_d values corresponding to distinct overlapping conditions φ, notably not-overlapped ($\varphi < 0$ %), partially overlapped ($0\ \% \le \varphi \le 20$ %) and completely overlapped tracks ($\varphi > 20$ %). Moreover, considering the fluctuations of w_i values of the second job's SSTs, it was decided to use the mean SSTs width $\bar{w} = \sum w_i/12$ in Eq. (3.1).

To measure the density level of the first job's samples, as-built specimens were cut from the building substrate via electrical discharge machining (EDM). Then, the outer skin was grinded using abrasive papers. Therefore, density was assessed according to the Archimede's principle using a YDK 01 Sartorius measuring set. Three measurements for each sample were considered [304]. The theoretical density of AlSi10Mg+4Cu alloy was determined through the volumetric rule of mixtures (ROM) [305], and its value was estimated to be equal to 2.74 g/cm^3. All the results from the first job of bulk samples were processed through Minitab 17 to perform the analysis of variance (ANOVA), and to investigate the influence of process parameters on density. A strict p-value (significance level) less than 0.005 was selected. Furthermore, XZ sections of each sample were polished and observed by OM and SEM to examine the occurrence of internal defects.

After that, a second job was designed to produce bulk samples using a rotated scanning strategy of 67°. As described in Section 1.2.5, adopting the rotation strategy helps to reduce internal stress and leads to more isotropic properties [46,76]. Before the job, a full factorial DOE based on 2 factors with 2 levels (P and h_d) and 1 factor with 4 levels (v) was adopted (Table 15). Density of samples was newly investigated by the Archimede's method. Later on, the as-built microstructures were observed by FESEM. Phase identification was conducted by X-Ray Diffraction (XRD), and the precipitation sequence was determined by Differential Scanning Calorimetry (DSC) analysis. XRD patterns were acquired in the 2θ range from 20° to 140° with steps of 0.0167° using a PANalytical X'Pert PRO diffractometer (λ_{Cu} = 1.5418 Å). DSC was conducted using a TA Q100 calorimeter, adopting a heating rate of 20 °C/min from 50 to 660 °C. Similarly to the melt pool characterization, compositional maps and nano-indentation grids were performed on the same sample area. Finally, the hardness was also evaluated at a macro-scale by applying a load of 62.5 Kg using an EMCO TEST M4U 025 hardness tester. The Brinell hardness number (HB10) was determined as the average of 5 measurements, according to ASTM E10-18 [306].

3.3 Results

3.3.1 Single Scan Tracks

3.3.1.1 Finding the process window

In this section, the process window of the AlSi10Mg+4Cu mixed alloy was defined, evaluating the properties of the produced SSTs.

Fig. 53 presents the low magnification micrographs of SSTs top surfaces.

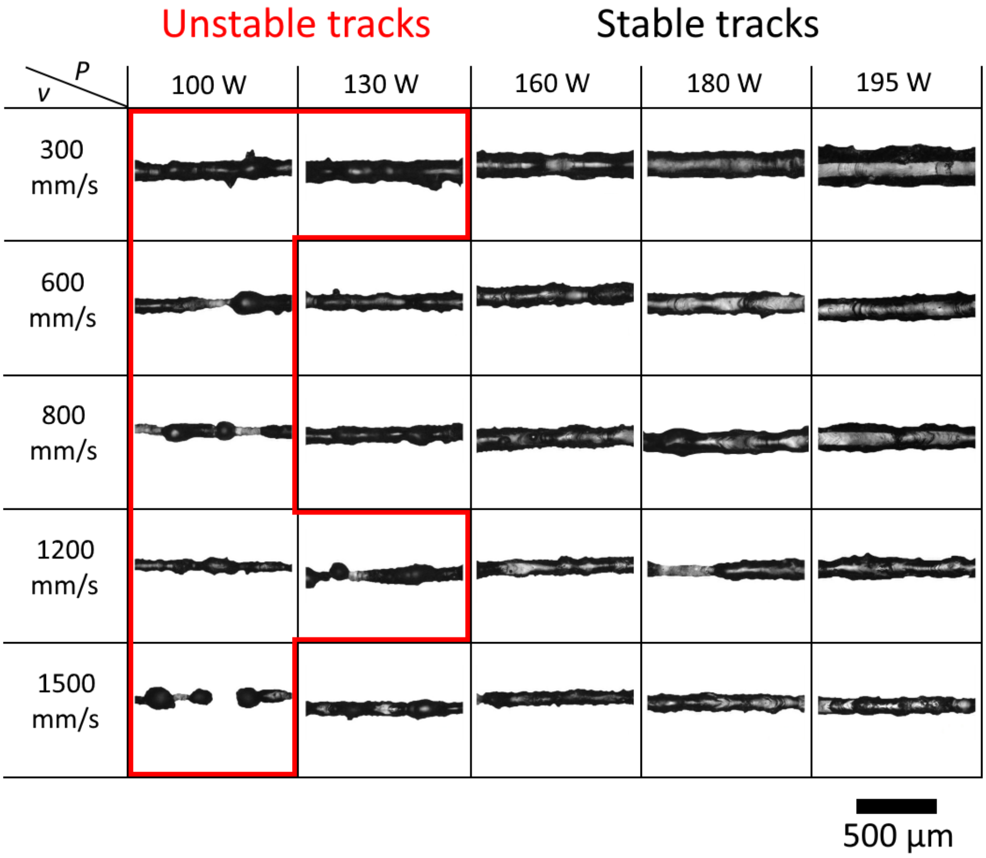

Fig. 53 Top surfaces of single scan tracks manufactured according to power and speed values of the first SSTs job.

Two main types of scan tracks were identified across the whole range of used parameters:

(I) Unstable SSTs.

At low laser power values ($P \leq 130$ W), the alloy processability was limited. SSTs, indeed, mostly resulted in irregular surfaces. By using the lowest scanning speed, the laser energy delivered to the powder was sufficient to consolidate continuous scan tracks. However, the top-surfaces showed some spiked prominences along the scan track sides caused by the partial melting of the powder, as depicted in Fig. 54a,b.

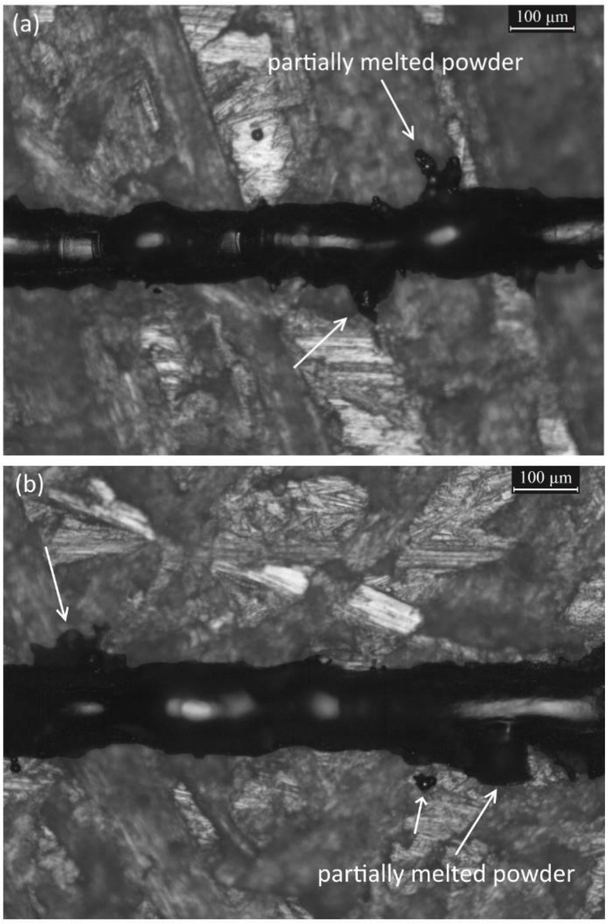

Fig. 54 Partially melted powder observed along the scan track borders of SSTs built with (a) 100 W and (b) 130 W at a constant scanning speed of 300 mm/s.

By increasing the scanning speed value, SSTs displayed the tendency to be more discontinuous, and a preliminary balling phenomenon arose. Here, the scan track surfaces showed sectors with bulged balls alternated with tight necking areas. A representative example is reported in Fig. 55a. These surface morphologies could be likely attributed to a pronounced fluid capillary instability that occurred at elevated scanning speeds [51]. According to the stability criterion of the free fluid cylinder (Section 1.4.3), indeed, a liquid cylinder becomes unstable when an axial harmonic perturbation has a wavelength higher than the liquid circumference [146]. Consequently, by increasing the scan speed, SSTs circumference progressively decreases, and the formation of discontinuities on melted tracks is promoted to a great extent. Finally, by further increasing the speed at 1500 mm/s with the power of 100 W, the fusion line split into drops (Fig. 55b). The combined effects of the capillary instability at high v and the reduced amount of liquid formed at low laser energy might be the causes.

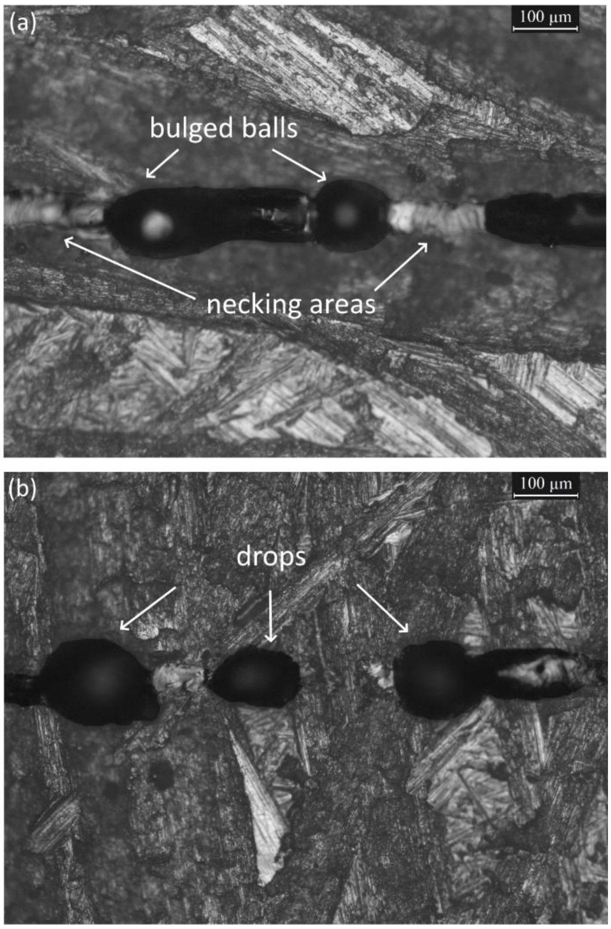

Fig. 55 Effect of the fluid capillary instability at high scanning speeds on the SSTs morphology: (a) discontinuities and (b) metal droplets identified on SSTs built at 800 mm/s and 1500 mm/s, respectively, with a constant power value of 100 W.

(II) Stable SSTs.

At relatively high powers (160-195 W), continuous and regular tracks free of pronounced balling defects were produced regardless of the used scanning speed. However, some of these tracks exhibited minor irregularities, such as a slight hump effect [148] at 180 W - 800 mm/s (Fig. 56a) and a remarkable heat affected zone at 195 W - 300 mm/s (Fig. 56b). Nevertheless, these SSTs can be considered acceptable at this point, since the on-top analysis aimed at investigating the presence of significant macro-defects after SSTs manufacturing.

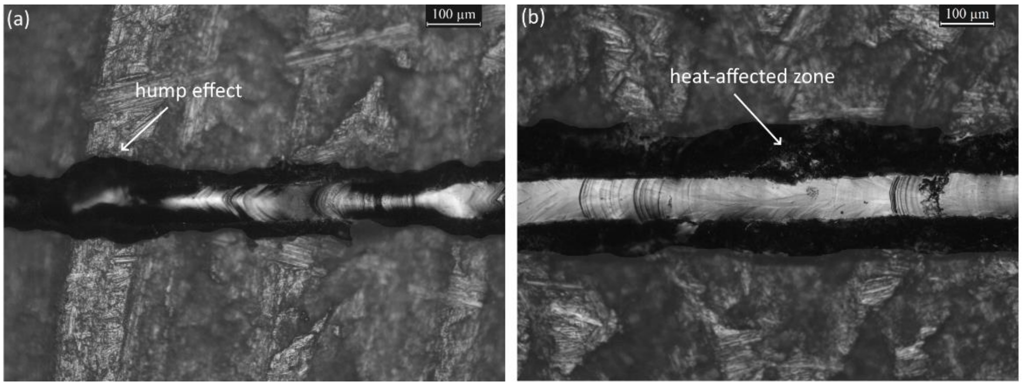

Fig. 56 Minor irregularities observed on the surfaces of 'stable' single scan tracks: (a) hump effect (180 W- 800 mm/s) and (b) pronounced heat affect zone (195 W-300 m/s).

Once the on-top surfaces of SSTs were qualitatively observed, the corresponding melt pool cross-sections were afterward investigated. Fig. 57 visually emphasizes the shape differences among the studied melt pools, while Table A 1 summarizes the geometrical dimensions and shape indicator values.

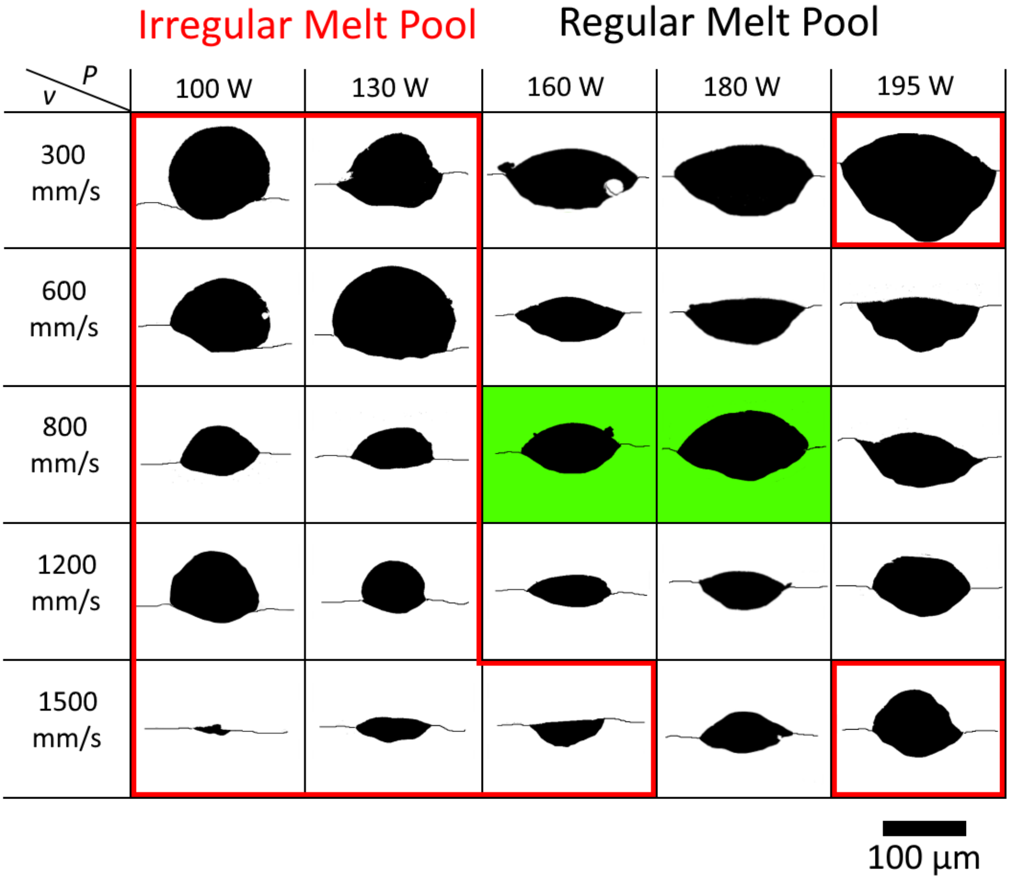

Fig. 57 Melt pool cross-sections of single scan tracks manufactured in the first SSTs job.

As can be seen in Fig. 57, the melt pools can be classified as:

I) Irregular melt pools.

When the applied power value was lower than 130 W, and scanning speeds up to 1200 mm/s, the laser energy was not enough to completely melt the disc substrate underneath. Therefore, shallow melt pools with rounded shapes were consolidated. These melt pools had an *h*/*w* ratio higher than 0.63, confirming the fact that the melt pool shape was nearly spherical. Moreover, these melt pools had both asymmetrical positions on the substrate, with a *g*/*d* ratio ≥ 1.47, and a limited penetration. On the other hand, using the highest scan speed coupled with power values up to 160 W, splashed melt pools with extremely low growth were formed as a consequence of a short laser-powder irradiation time.

When the highest laser power (195 W) is combined with both the lowest (300 mm/s) and highest (1500 mm/s) scan speed, irregular melt pools were formed. In the former case, a V-shaped melt pool with a deep and convex profile was produced due to the high amount of applied energy density. No traces of keyhole pores were found at the bottom part of melt pools built at 195 W and 300 mm/s. However, to prevent any keyhole phenomena during LPBF (Section 1.5.1) [96], this *P*-*v* condition was excluded from the alloy process window, as described later. Finally, in the case of the melt pool produced at 195 W and 1500 mm/s showed a more spherical geometry and a poor penetration, owing to the fast laser-material interaction.

II) Regular melt pools.

Quite regular melt pools were produced working at power values between 160 and 195 W. It is evident from the melt pool silhouettes of Fig. 57 that all these exhibited a quasi-elliptical profile, showing an *h*/*w* ratio between 0.39 and 0.62. This elliptical shape was very similar to the one adopted by Tang et al. to predict the lack of fusion porosities in AlSI10Mg LPBF*ed* parts. Moreover, this melt pool shape has been frequently associated with stable scan tracks consolidated in the conduction regime [50,51,100]. Two melt pools with optimum shapes were then selected (see the green box in Fig. 57). In fact, when the used laser powers are 160 or 180 W at the constant scan speed of 800 mm/s, the melt pools were elliptical and symmetrical with a *g*/*d* ratio of 1.06 and 1.14, respectively. Besides, they were sufficiently deep to re-melt the underlying substrate while avoiding keyholing; hence, they can be referred as optimum parameters.

Based on the results presented so far, the processing map for the AlSi10Mg+4Cu alloy was established and reported in Fig. 58.

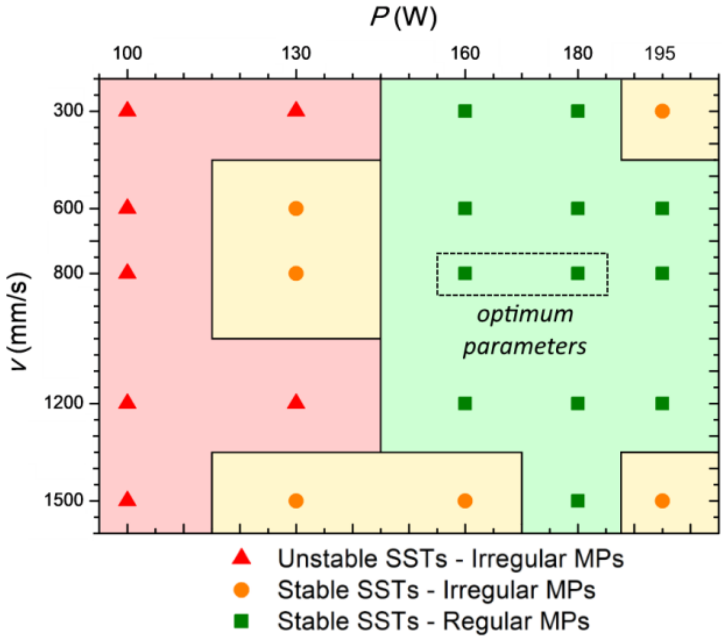

Fig. 58 Processing map of AlSI10Mg+4Cu mixed alloy defined upon the first SSTs job.

Three varied *P*-*v* areas can be identified in Fig. 58. First, unstable SSTs and irregular melt pools formed where poor laser energy was adopted for SSTs manufacturing. Consequently, single scans showed visible melting defects, such as balling and lack of fusion sectors, and the corresponding melt pools exhibited a pronounced asymmetry on the substrate. These *P*-*v* combinations were not considered for further trials. Second, stable SSTs with irregular cross-sections were produced using the *P*-*v* combinations of the yellow areas in Fig. 58. In these cases, the continuity of the fusion lines was preserved, but melt pools did not have the optimal shape. These parameters were excluded for further trials as well. Third, stable SSTs and regular melt pools were manufactured using the good *P*-*v* combinations corresponding to the green area of Fig. 58. Within this area, the *P*-*v* couples produced with *P* of 160 W and 180 W at a constant *v* of 800 mm/s were selected as a starting point to design the second job of single scan tracks (dotted box in Fig. 58).

After that, the optimal process parameters defined above were finely tuned through the characterization of the second batch of SSTs. The *P*-*v* combinations surrounding the optimum parameter values of Fig. 58, were considered for this purpose.

Fig. 59a provides the representative SEM micrographs of SSTs surfaces of the second single scan track job. Obvious macroscopic defects as metal droplets, ripples, and lack of fusion areas were not present. Although all the produced SSTs were continuous and regular, the morphology of fusion lines slightly changed with the process parameters. The laser tracks produced at 160 and 170 W were quite linear and smooth. The SSTs' continuity was preserved when the laser power increased to 180 W, even though wavy shaped fusion lines with bulge surfaces appeared. The reason for this might be attributed to the more intense laser irradiation attained at a higher power level, which likely created a significant temperature gradient on the scan track/melt pool surface. Consequently, a strong surface tension gradient could have triggered inward thermocapillary flows from SSTs sectors at lower surface tension to the areas at higher surface tension, thus leading to the observed bulged scan sectors (Section 1.4.2) [141,142].

Regardless of the used power and speed combinations, it must be observed that some partially melted powder particles were found on the scan tracks surface (Fig. 59b). Some particles pointed by black arrows had a greyscale color, and they were likely AlSi10Mg particles. On the other hand, brighter spots with dimensions ranging from 3 to 9 µm were also identified. An EDS line performed on one of these areas revealed a significant content of Cu (see inset of Fig. 59b). Considering the size, they could be Cu powder particles, which were partially melted during LPBF.

Finally, the mean width values w_i of each SST were measured and labeled in Fig. 59a with the corresponding standard deviations. The mean width value $\overline{w}$ ($\sum w_i/12$) of all SSTs was determined and found equal to 131 µm. Then, this value will be used to determine the degree of overlapping between SSTs and to define the h_d values for bulk samples manufacturing.

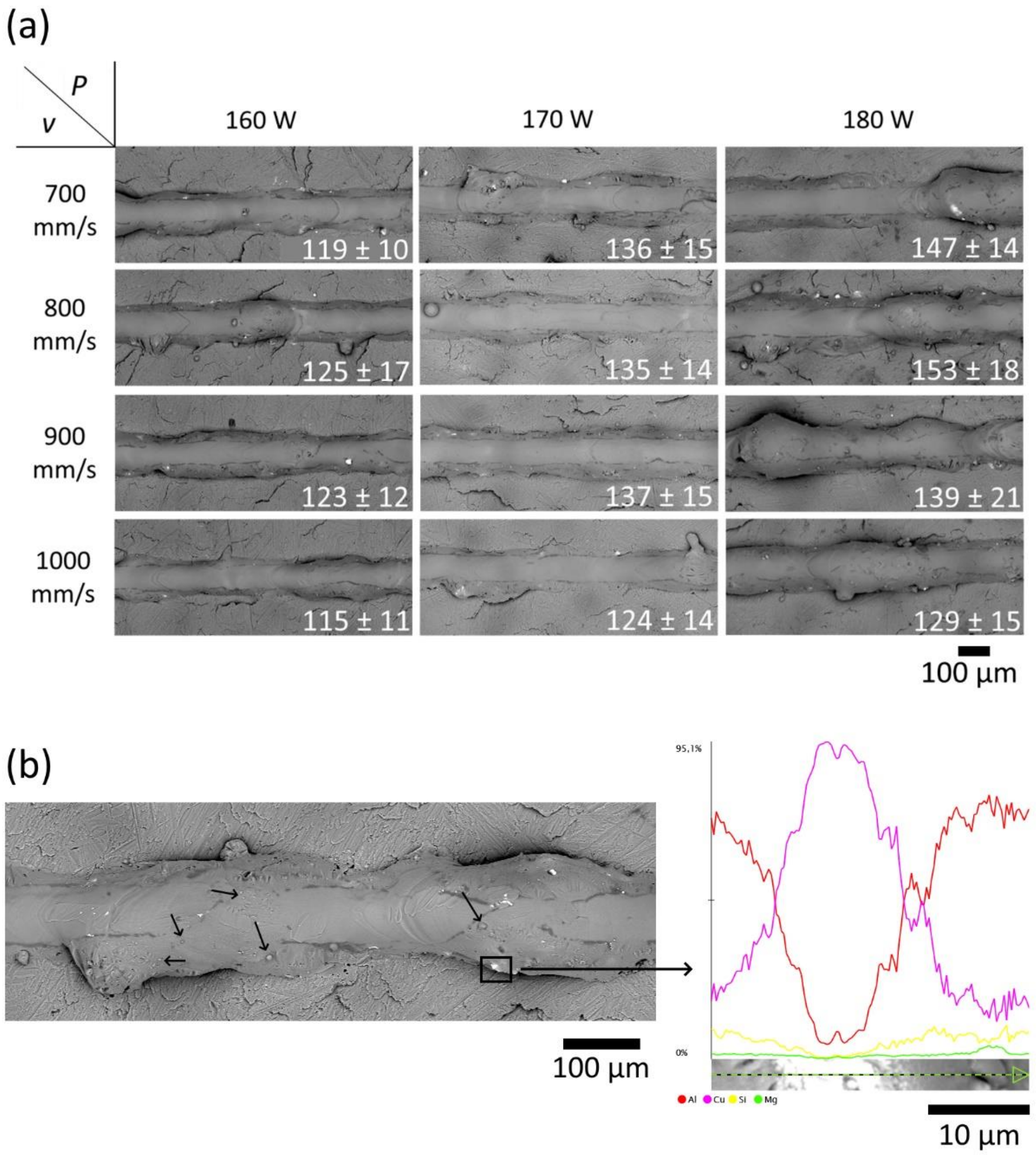

Fig. 59 (a) SEM investigation on surfaces of single scan tracks produced in the second SSTs job. The width values w_i of each single scan track are labeled on the bottom-right corner of each *P-v* box. (b) Closed-view of a single track surface with partially melted powder particles, and the inset showing the results of an EDS line on a Cu-rich area.

3.3.1.2 Melt pool microstructure

After the definition of the alloy process window, the melt pool microstructure of stable and regular single scan tracks was investigated.

Fig. 60a depicts the melt pool cross-section produced with *P* and *v* of 180 W and 700 mm/s, respectively. As can be seen at low magnification, the melt pool showed a regular and elliptical shape. A spherical pore was also noticed near to the top. It is worth to mention that similar pores were observed within other melt pools. The origin for this pores can be twofold. On the one hand, it was possible that a bubble generated by the processing gas was entrapped into the turbulent melt flow [29]. On the other hand, the intense laser irradiation induced the evaporation of volatiles chemical elements, especially Mg [299], which in turn were not able to split out from the melt pool due to the ultra-fast solidification. However, apart from pores, other defects were not observed in the investigated melt pool cross-sections.

From a further inspection of Fig. 60a, it can be appreciated the microstructure difference between as-cast substrate and fused laser scan track. Cast AlSi10Mg showed the typical Al dendritic structure (light grey) surrounded by a thick eutectic phase (dark grey), which were formed by blocky shaped Si and Fe-rich needle shaped precipitates. Conversely, the AlSi10Mg+4Cu scan track exhibited a finer microstructure induced by the high cooling rate of LPBF.

A closer inspection at high magnification revealed the presence of a completely fibrous eutectic with fine cells of size between 0.4 and 0.7 µm (Fig. 60b,c). The cell morphology appeared inhomogeneous and quite interrupted. The fraction of eutectic was estimated to be 25 ± 4% (calculated by image analysis).

To investigate the effect of Cu addition on the microstructure, EDS analysis was conducted on the melt-pool cross section (Fig. 61). BSE-SEM micrograph of Fig. 61a reveals the presence of bright ‘frozen’ whirls within the consolidated melt pool, which were then ascribed to Cu segregations by the EDS map of Fig. 61b. The presence of copper segregations revealed the turbulent nature of the melt during solidification. Nevertheless, it was noted from Fig. 61b that Cu diffused everywhere at the melt pool scale.

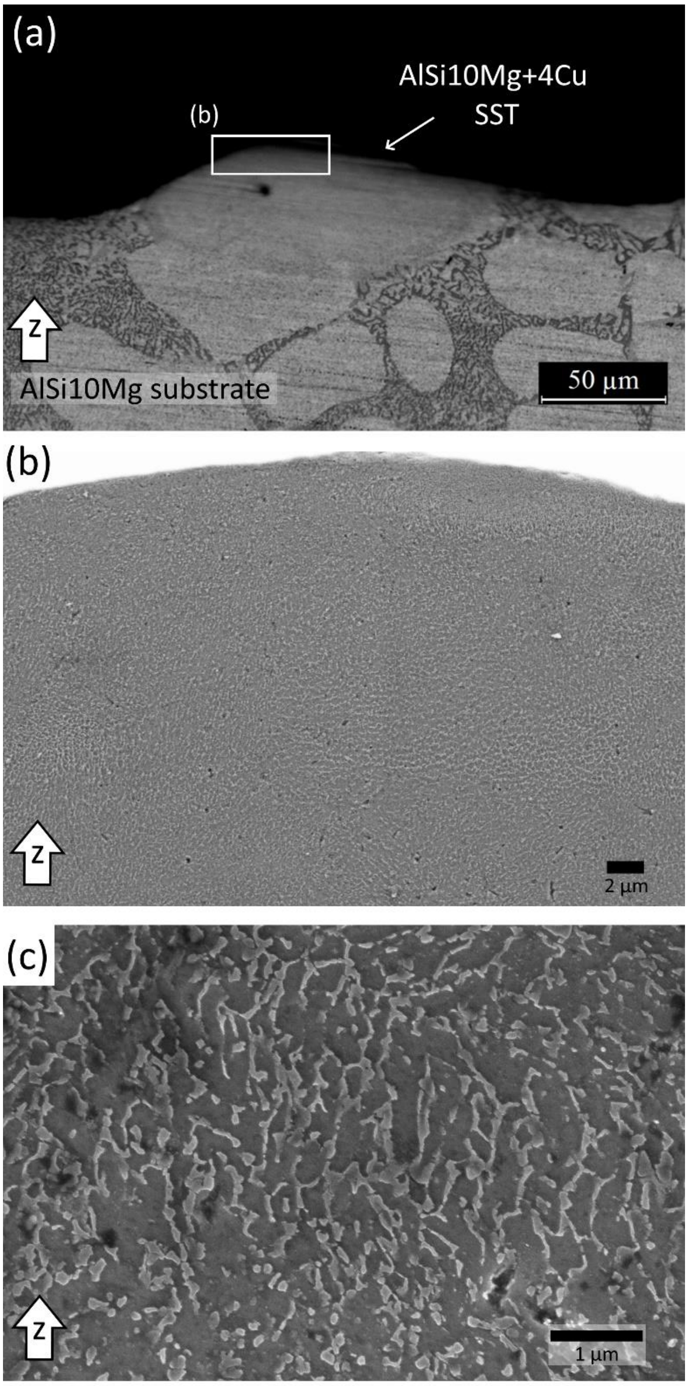

Fig. 60 (a) Low magnification and (b,c) high magnification micrographs showing the microstructure of a AlSi10Mg+4Cu melt pool.

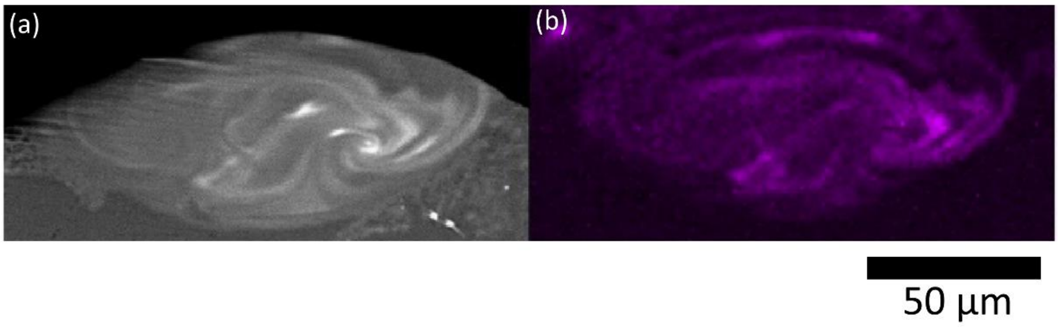

Fig. 61 Results of the EDS investigation on a melt pool cross-section of Fig. 60: (a) BSE-SEM micrograph and (b) the corresponding EDS map with Cu distribution.

3.3.1.3 Melt pool nano-hardness

Nanoindentation tests were performed along the melt pool cross-sections with the purpose of investigating the hardening effect produced by adding Cu. Nanoindentation grids were carried out on both AlSi10Mg and AlSi10Mg+4Cu melt pools in order to assess the whole melt pool surface. Nanoindentation results were reproduced in Fig. 62 by using colored contour maps to visually evaluate the distribution of the nano-hardness values.

The average nano-hardness value of AlSi10Mg+4Cu was about 2.4 ± 0.5 GPa, compared to the 1.8 ± 0.3 GPa of AlSi10Mg alloy. Therefore, Cu addition markedly increased the average hardness of the base AlSi10Mg alloy. It was also noted that there is a change of the hardness value distribution after mixing AlSi10Mg and Cu powders (Fig. 62). In this regard, the hardness distribution of AlSi10Mg (Fig. 62a) was more homogeneous than that measured on the AlSi10Mg+4Cu melt pool (Fig. 62b). In the latter case, indeed, red areas at higher hardness values ($H \geq 2.7$ GPa) were detected across the melt pool surface. The origin of such hardness peaks was investigated by testing a melt pool cross-section in terms of nano-hardness, chemical composition, and microstructure. Results are discussed in Section 3.4.5.

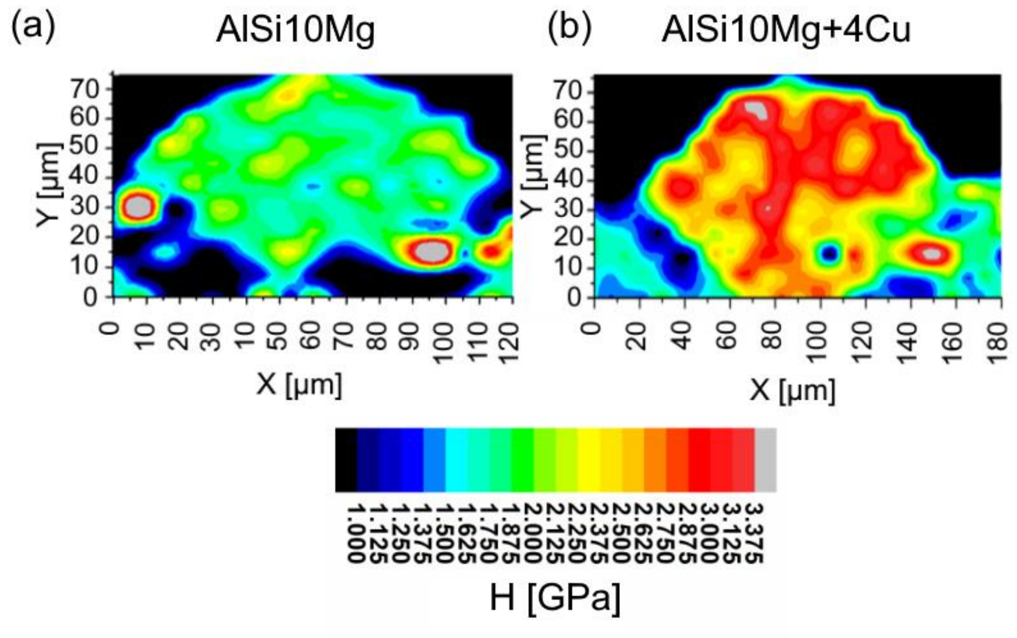

Fig. 62 Nano-hardness contour maps performed on the melt pool cross-sections of as-built (a) AlSi10Mg and (b) AlSi10Mg+4Cu alloys. Colored maps are continuous representations of nano-hardness values, which refer to the nano-hardness scale reported on the right side of the image.

3.3.2 Bulk samples

3.3.2.1 Density optimization

Being all the single scan tracks of the second job regular and continuous (Fig. 59a), the h_d values of 0.08, 0.12 and 0.14 mm were selected by using the SSTs width value $\overline{w}$ of 131 µm in Eq. (3.1). Bulk samples with unidirectional scanning strategy were produced to evaluate density and overlapping grade of nearby laser scans.

Density results are given in Table A 2. Densities ranged from 95.66% to a maximum of 99.30%. The analysis of variance (ANOVA) was then performed on the porosity content, and the statistical results are provided in Table A 3, Fig. 63 and Fig. 64. As can be noticed from Table A 3, the influence of power and hatching distance on porosity was highly significant since they returned low p-values. This is evident when the main interaction plots for porosity are considered (Fig. 63 and Fig. 64). In Fig. 63, it can be seen an increment of porosity by increasing the scanning speed. Still on Fig. 63, it can be noticed that the porosity level of samples manufactured with 160 W was always the highest at each scanning speed. Besides, when the power is increased at a fixed speed, porosity gradually reduced. In Fig. 64, the main interaction plot of porosity vs. hatching distance is provided. It was observed that the highest porosity of each power series was reached when a h_d of 0.08 mm was employed. By increasing the h_d, porosity appreciably decreased for 170 W and 180 W power series.

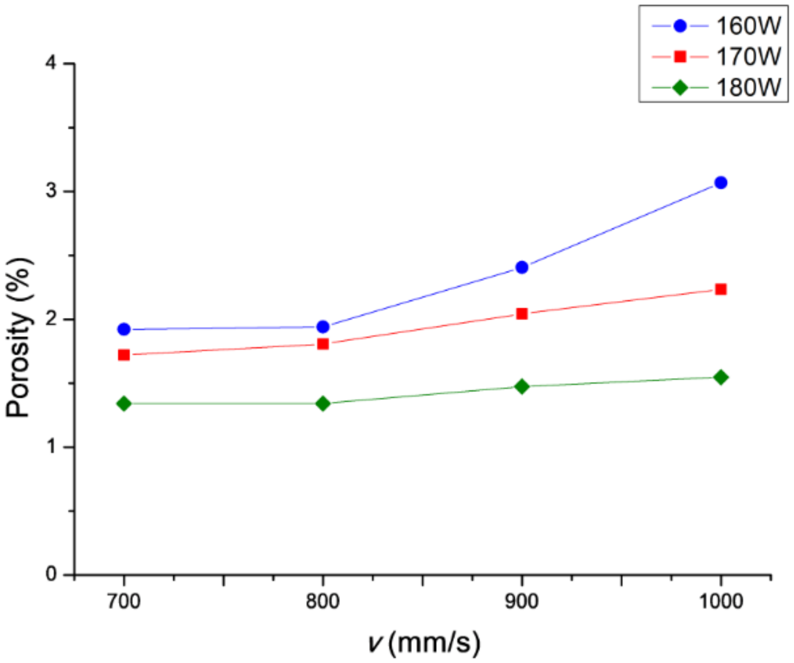

Fig. 63 Main interaction plots for porosity upon ANOVA analysis. The effect of scanning on porosity at varied power levels.

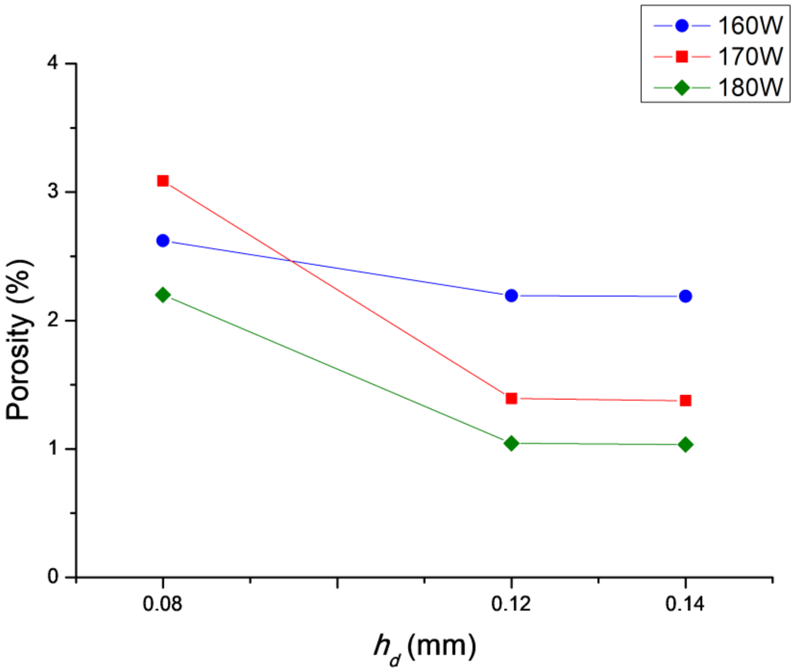

Fig. 64 Main interaction plots for porosity upon ANOVA analysis. The effect of hatching distance on porosity at varied power levels.

Overlapping φ values of neighboring laser scans were calculated by using the SSTs widths w_i labeled in Fig. 59, and then summarized in Table A 2. Overlapping values were related with porosity results in Fig. 65. Based on φ values, three overlapping scenarios were superimposed on Fig. 65, namely not-overlapped, partially overlapped and completely overlapped. A closer examination of the graph suggests that the higher densities values fell within the partially overlapped scenario. On the other hand, the highly porous samples were mostly manufactured with the process parameters belonging to the not-overlapped or the completely overlapped regions. A possible densification theory will be described in Section 3.4.1 by considering both the iso-power and iso-hatching behaviors of the alloy depicted in Fig. 65.

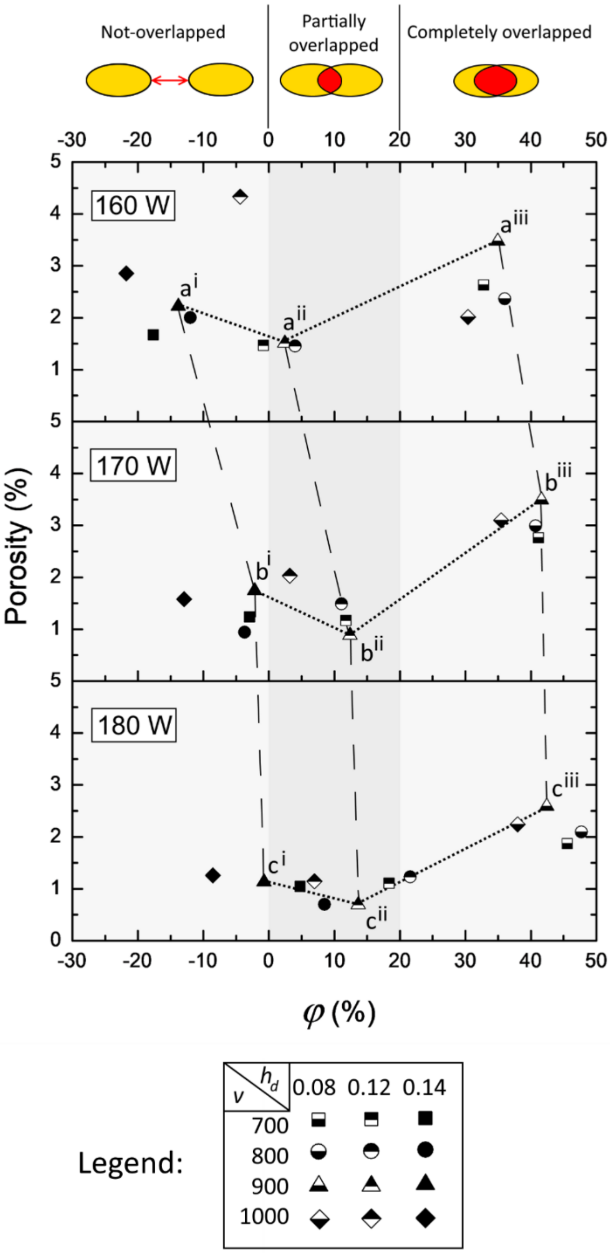

Fig. 65 Effect of φ on porosities of bulk samples produced with unidirectional scanning strategy. Dotted and dashed lines are referred to the iso-power and iso-hatching behaviours at 900 mm/s.

Fig. 66 plots the representative cross-sections of specimens built at 900 mm/s as a function of power and hatching distance. It can be noticed from Fig. 66 that elongated porosities are displaced along the Z direction of samples built in the not-overlapped condition. Columnar pores were in fact clearly observed in the polished cross-section of sample a^i. The origin of these pores can be mainly attributed to a lack of fusion during LPBF, owing to the scarce overlapping between adjacent scan tracks. This assumption was confirmed by the SEM micrograph of Fig. 67, which revealed the presence of un-melted powder particles within pores. On the other hand, pores with irregular shape arose at each power level by using the lowest hatching distance (see a^{iii}-c^{iii} samples). In these cases, an excessive laser re-melting induced by the high scan tracks overlapping could generate unstable molten pools and non-homogenous consolidation, thus forming irregular porosities.

Based on the results presented so far, P and h_d of 160 W and 0.08 mm were excluded for the production of bulk samples with 67° rotated scanning strategy, since they lead to a porosity content higher than 1.50 % (Table A 2). All the v values, instead, were kept since the effect on density was negligible in the selected range of scanning speeds.

Table A 4 summarized the density results of bulk samples produced with 67° rotated scanning strategy. Densities were comprised in a narrow range and varied from 98.62 to 99.16%. The corresponding residual porosity values were plotted in Fig. 68 according to the applied scanning speed. As can be seen from the graph, it would appear that the effect of P, v and h_d on porosity was not significant. This observation was later confirmed by the ANOVA analysis of Table A 5. Therefore, it is though that all these P, v and h_d combinations can be used to manufacturing components of AlSi10Mg+4Cu.

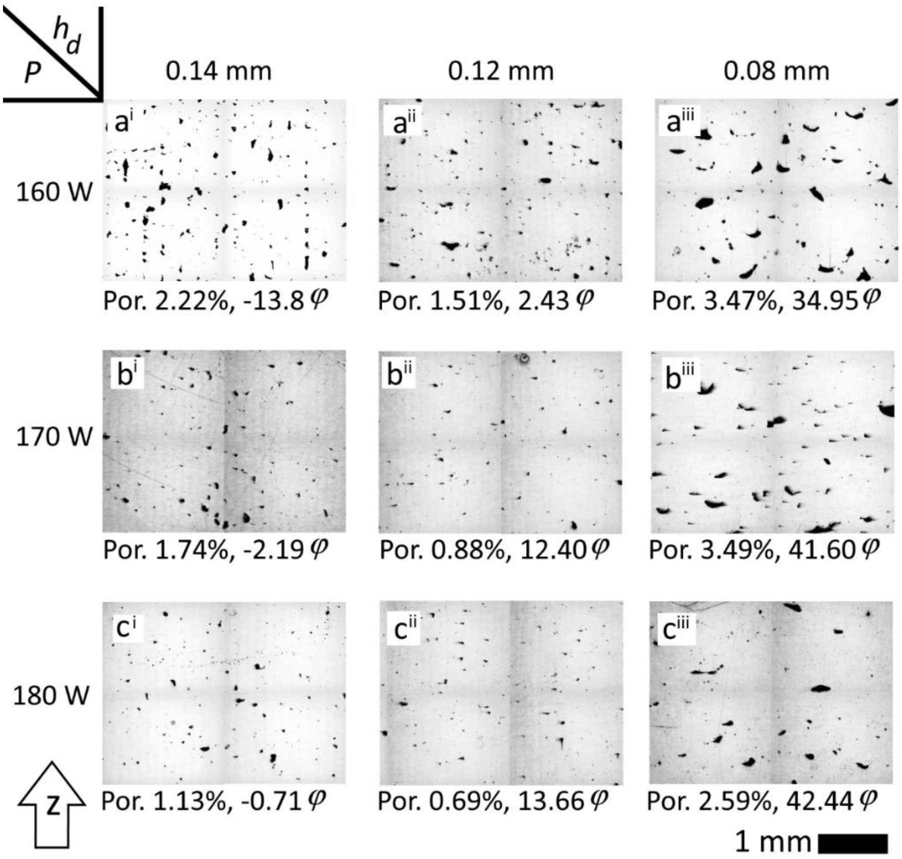

Fig. 66 OM micrographs taken along the XZ plane of bulk samples built with unidirectional scanning strategy at 900 mm/s. The label on the top-left of each image is referred to the labeled points of Fig. 65.

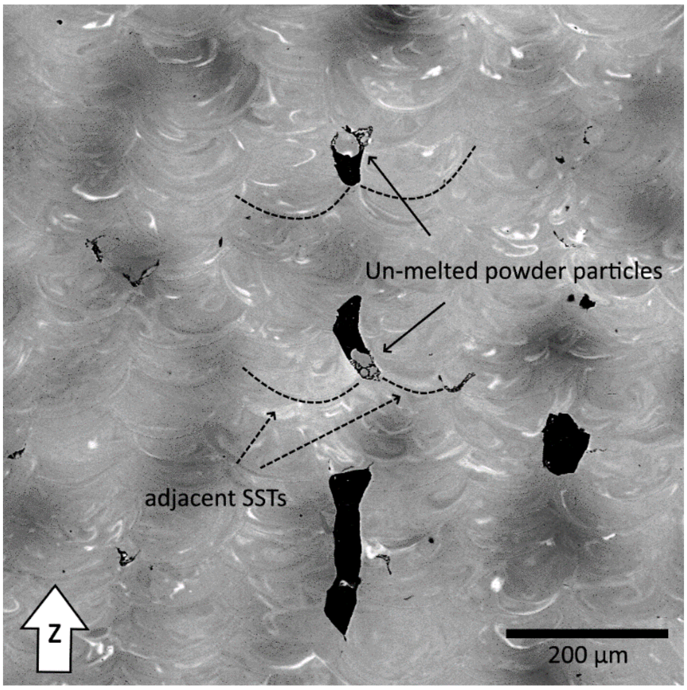

Fig. 67 Columnar porosities identified on a specimen produced with parameters belonging to the not-overlapped scenario. The lack of fusion pores were found in correspondence of adjacent laser scans.

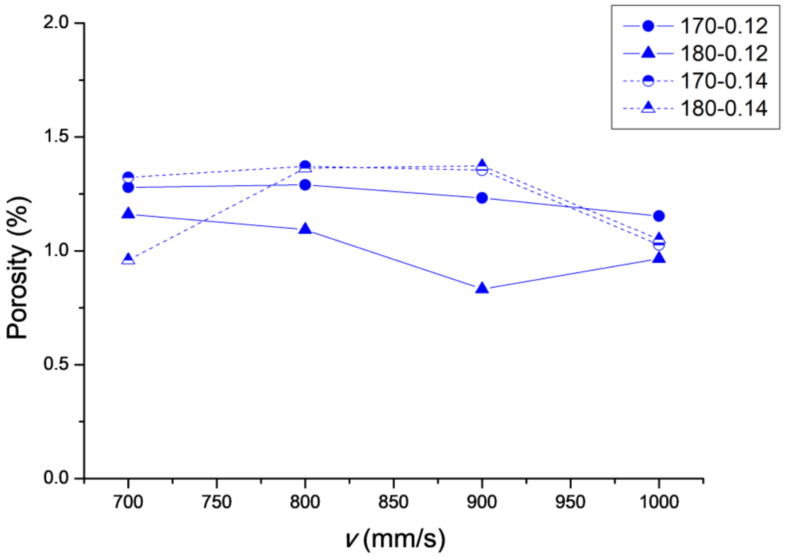

Fig. 68 Variation of porosity with scanning speed for bulk samples manufactured with a 67° rotated scanning strategy.

3.3.2.2 Microstructure

Fig. 69 shows the low magnification macrostructure of the as-built AlSi10Mg+4Cu alloy across his longitudinal plane. The alloy displays the typical morphological texture observed for other LPBF*ed* Al alloys [46,76]. A ‘fish scale’ pattern formed by piled-up melt pools is revealed. Melt pools with half-cylindrical shape were oriented following the laser scanning direction imposed by the rotated scanning strategy. Besides, it was possible to appreciate a good degree penetration of melt pools into the layers underneath as well as a proper overlapping of nearby single scan tracks. Porosities with size in the range between 10 and 30 μm were also detected.

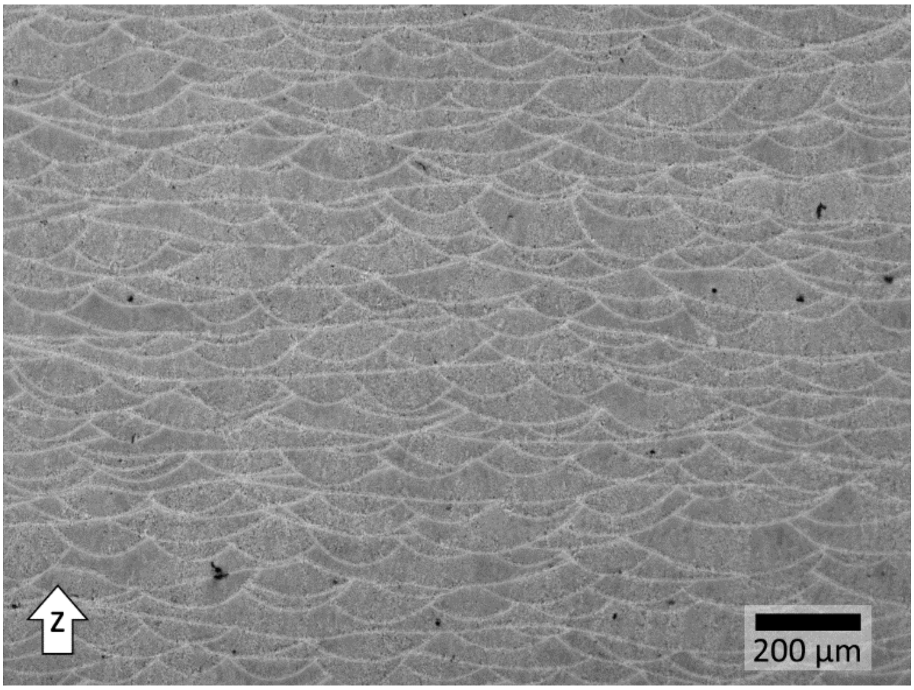

Fig. 69 Fish scale macrostructure of the as-built AlSi10Mg+4Cu alloy produced using 67° rotated scanning strategy. The observed macrostructure was observed along the building direction (Z-axis).

A representative micrograph retrieved by FESEM investigation on the AlSi10Mg+4Cu microstructure is reported in Fig. 70. The microstructure reveals the extremely fine cellular/columnar dendritic architecture induced by the severe constitutional undercooling stored during the rapid cooling from the melt. Dendrites epitaxially grew at the melt pool boundary and are oriented towards the melt pool centre, opposite to the heat flux extraction.

In Fig. 70, it is possible to distinguish the two typical zones of a melt pool. These zones are the melt pool core (‘MP core’), which is the inner part of a melt pool, and the melt pool boundary (‘MP boundary’), which is the overlapping area with previous/subsequent consolidated melt pools. The latter is, in turn, constituted by an external remelted area, also known as heat affected zone (‘HAZ’), and an adjacent region with a coarser microstructure (‘MP coarse’).

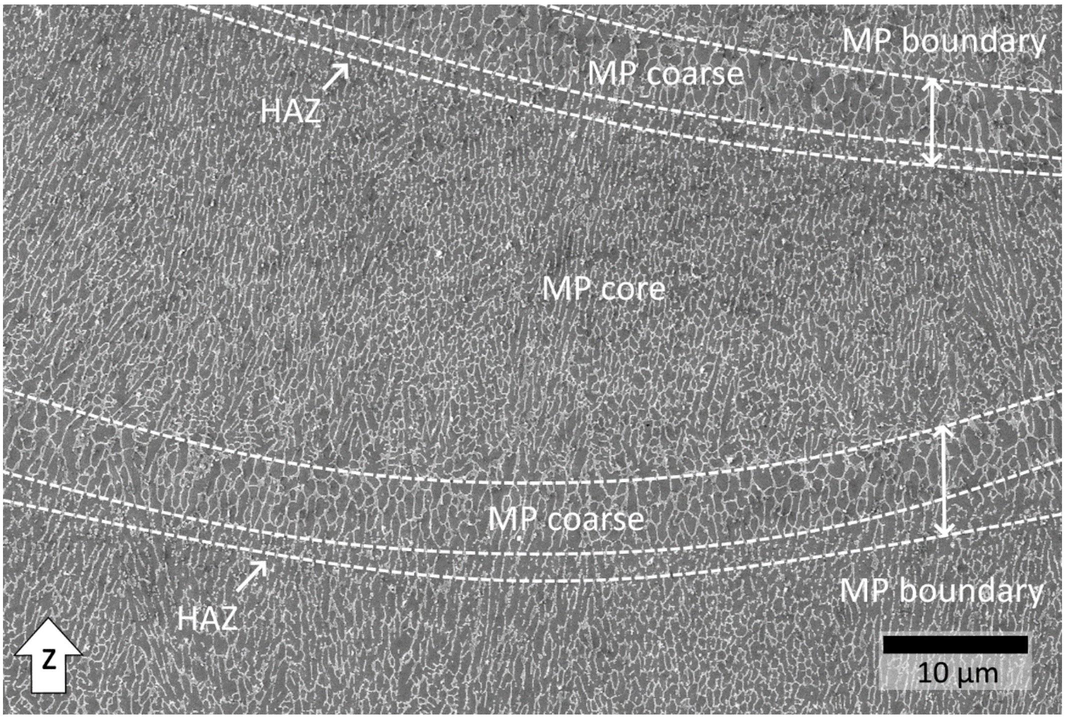

Fig. 70 FESEM micrograph showing the different zones of a melt pool along the building direction.

Moving from the core to the boundary of a melt pool, a variation of the microstructural features can be noticed. In the melt pool core, indeed, the solidification mode was mainly cellular-dendritic, resulting in a continuous eutectic architecture with fine cells of size 0.8 ± 0.4 µm (Fig. 71a). The fineness of cells gradually increased towards the melt pool boundary, where a coarser texture was observed in correspondence of the 'MP coarse' zone. Here, the solidification mode was cellular/columnar dendritic, as can be observed in Fig. 71b. The eutectic pattern was still discernible, although network interruptions and dendrite sided branches were observed to a large extent. Lastly, in the HAZ zone, the eutectic architecture was definitely broken into several particles due to the laser remelting occurred during manufacturing (Fig. 71c).

The cooling rate experienced by the melted alloy during solidification played a key role to determine the gradient and the fineness of the observed microstructure [160,162]. As previously described in Section 1.4.5, the cooling rate is defined as the product of G and R ($G \times R$), where G is the thermal gradient and R is the growth rate.

The thermal gradient G refers to the temperature variation in a space interval of a melt pool ($\frac{dT}{dx}$) and its value varies inside the melt pool. This fact was addressed to the Gaussian distribution of the laser energy deployed during printing. As a consequence of this, the melt temperature was much higher at the MP core rather than at the boundary, thus leading to a high thermal gradient over the MP core region. On the other hand, the growth rate R, which corresponds to the displacement of the crystal solidification front in the time unit ($\frac{dx}{dt}$), depends on the laser speed v and the angle θ formed with the melt pool border ($R =$

$V \cos\alpha$). It follows that, similarly to the G values distribution, the maximum R value was reached at the fusion centerline (α = 0°, R = 1), which corresponds to the MP core area, and R value decreased towards the MP boundary (α = 90°, R = 0). Therefore, a very high cooling rate occurred at the MP core reducing the energy barrier for crystal nucleation and, consequently, promoting the formation of fine cells [76]. Then, moving from the melt pool core to the boundary, the product G×R decreased and the eutectic cells size became coarser [155].

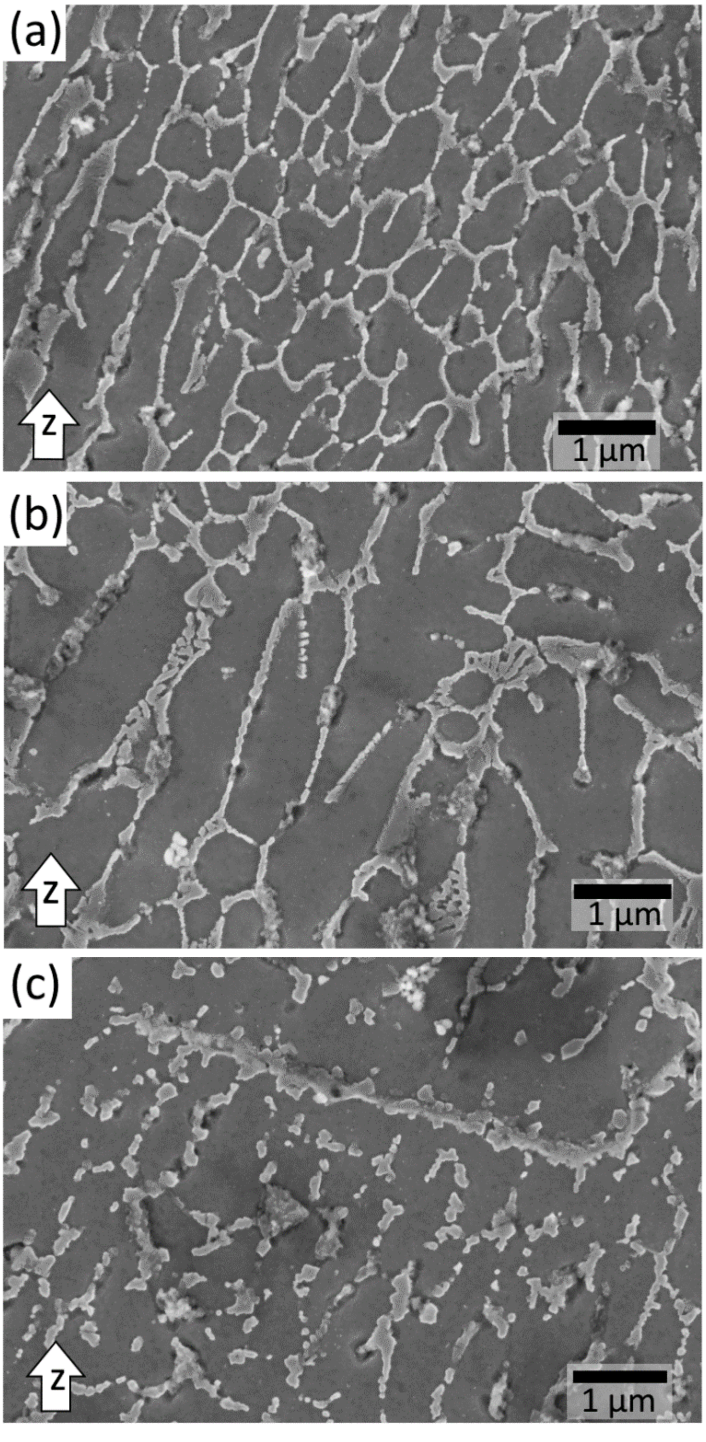

Fig. 71 High magnification FESEM images showing the gradient of microstructure within the a melt pool. The images refer to (a) MP core, (b) MP coarse and (c) HAZ zones.

Fig. 72 depicts the EDX maps conducted on a portion of the eutectic network of Fig. 71a. Results revealed the presence of Si in proximity of the eutectic architecture. Moreover, Cu was found to be preferentially located in the areas outside α-Al cells and interconnected to the eutectic Si. Therefore, differently from Al-Si-Mg alloys [190], it might be reasonable to consider the eutectic fraction of AlSi10Mg+4Cu alloy as an intermixing of eutectic Si particles and Al_2Cu phase (see XRD pattern of Fig. 73).

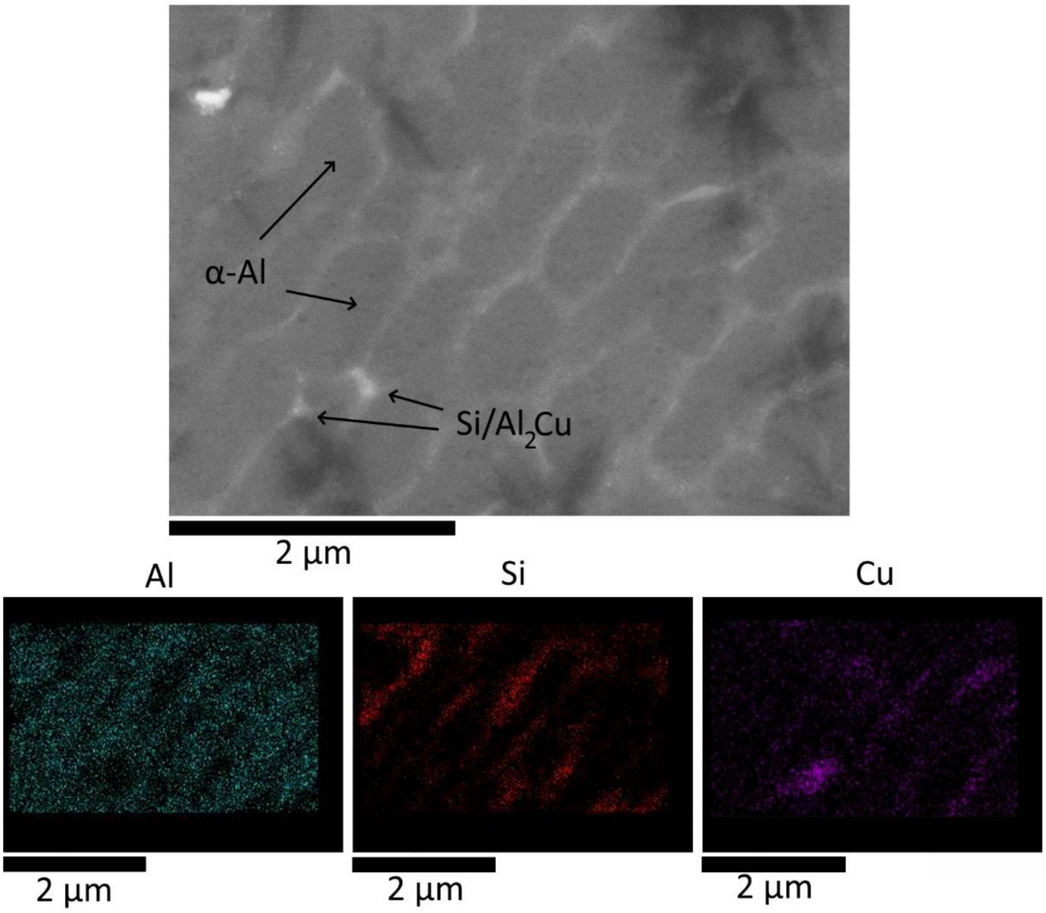

Fig. 72 EDX investigation on the eutectic network of the as-built AlSI10Mg+4Cu alloy.

3.3.2.3 Phase identification

The XRD analysis was performed on the XZ plane of an as-built bulk sample produced with a rotated scanning strategy, and the patterns were displayed in Fig. 73. XRD reflections revealed the presence of *fcc*-Al, diamond cubic Si and tetragonal Al_2Cu phase (θ phase).

The lattice parameter of *fcc*-Al phase was determined using cosθcotθ method to evaluate the extent of supersaturation. The calculated lattice value was compared with that of an AlSi10Mg+4Cu sample subjected to annealing at 300 °C for 24 h. Temperature and time of annealing were chosen to have the minimum content of solutionized atoms. Results are displayed in the inset of Fig. 73. As can be noticed, the value of Al lattice parameter (0.40433 nm) is lower than the one corresponding to the annealed sample (0.40498 nm). This fact suggests the presence of solutes trapped within the Al matrix after rapid cooling. Both Si and Cu, indeed, typically contribute to the reduction of the Al lattice parameter following the Vegard's law. However, Si and Cu decreased the Al lattice constant with a different efficacy [307]. The Si and Cu contributions to the reduction of Al lattice parameter were estimated to be of 1.74×10^{-4} nm/at% and 4.77×10^{-4} nm/at%, respectively [307]. Therefore, under the assumption that Si supersaturation was similar to that of master AlSi10Mg alloy (4 at% in Ref. [196]), the Cu supersaturation in *fcc*-Al phase might be in the range of 0.75 and 1 at%. Based on this result, it can be inferred that Cu supersaturation was partly limited by copious precipitation of Cu transition phases, such as Al_2Cu (θ phase), during printing.

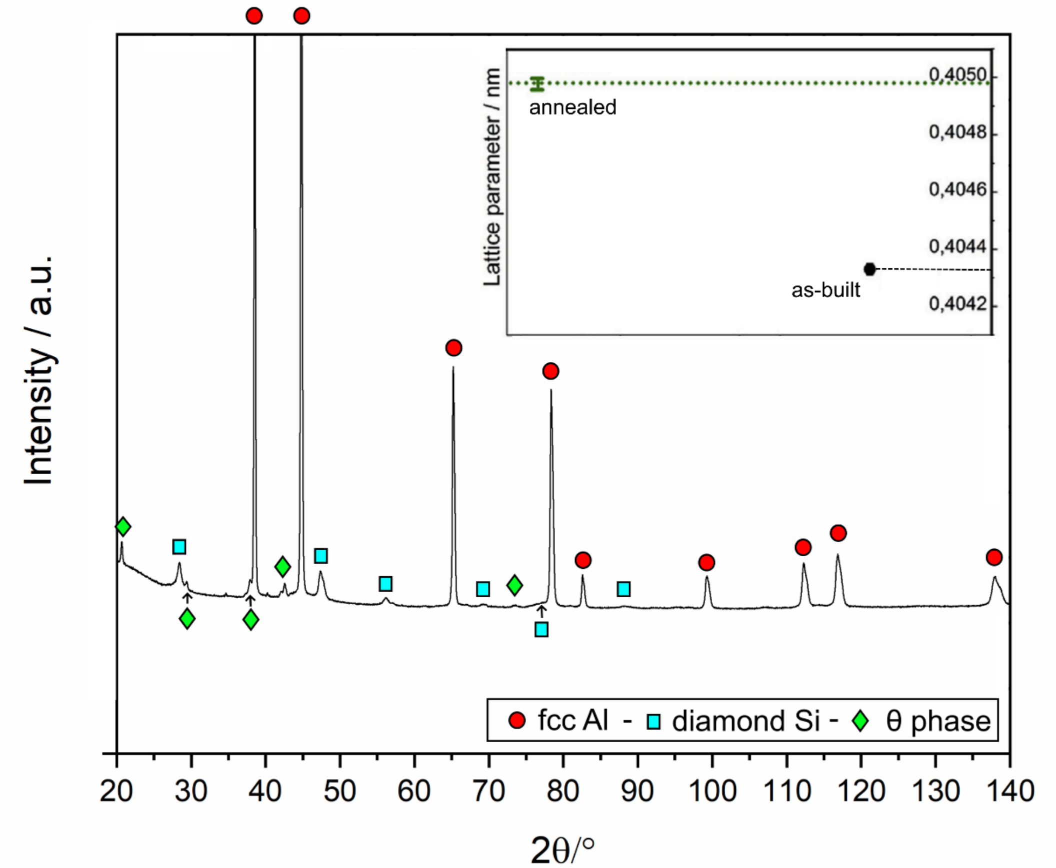

Fig. 73 XRD patterns of the as-built AlSi10Mg+4Cu alloy. The inset depicts the variation of the Al lattice parameter between as-built and annealed conditions reported by Marola et al. in Ref. [308].

3.3.2.4 Thermal behaviour

As described in Section 2.3.1, the precipitation reactions from a supersaturated solid solution are triggered by heating the alloy. For this reason, a DSC scan was performed on the as-built alloy to investigate the thermal behavior and, eventually, determine the aging temperature for the AlSi10Mg+4Cu system.

The DSC scan of AlSi10Mg+4Cu is depicted in Fig. 74. Two distinct exothermic signals were identified. The temperatures of these peaks are in agreement with those recorded for an LPBF*ed* AlSi10Mg alloy in a recent research [196]. The first most intense peak is centered at 225 °C. The exothermic nature of the peak indicated that some precipitation reactions occurred between 175 °C (onset temperature) and 275 °C. As evidenced in an as-built AlSi10Mg alloy [196], this signal accounted for Si diffusion and precipitation from the supersaturated solid solution. However, this exothermic peak might also account for the formation of other precipitates. In fact, transition intermetallic phases such as θ'-Al_2Cu [309], β''-Mg_2Si [222,228], and S'-Al_2CuMg [310] form within a similar temperature range. Therefore, it might be probable that their corresponding precipitation signals contributed to the intensity of our first exothermic peak.

The enthalpy unleashed during the first exothermal reaction was nearly 26 ± 3 J/g. By using the thermodynamic databases of the binary Al-Si and Al-Cu systems [311], the transformation enthalpy (ΔH) between supersaturated solid solution and equilibrium phase mixtures was determined. The values corresponded to 229 J/at% (8.5 J/g) and 633 J/at% (23.5 J/g), respectively, for Al-Si and Al-Cu systems. Hence, considering that $\Delta H_{Al\text{-}Cu}$ is three times of $\Delta H_{Al\text{-}Si}$, there is the evidence to indicate that the precipitation of Cu phases did contribute to the first exothermic signal.

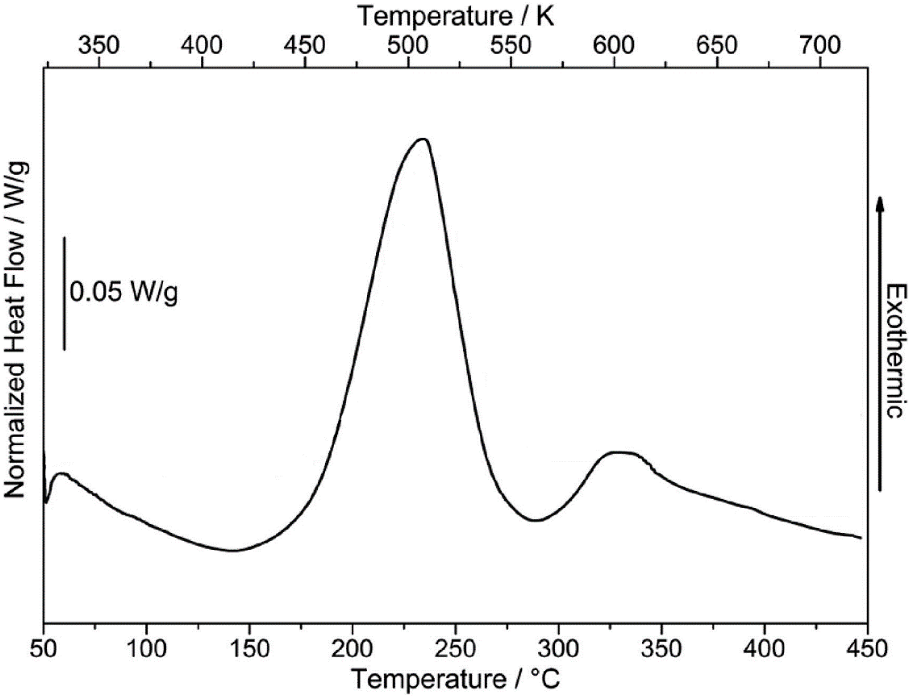

Fig. 74 DSC signals of the as-built AlSi10Mg+4Cu alloy.

By increasing the temperature, a less intense signal centered at around 330 °C is encountered. In this case, the peak was related to the precipitation of Mg_2Si and phases containing impurity elements [196].

By further increasing the temperature, the melting of AlSi10Mg+4Cu alloy occurred between 545 ± 5 and 585 ± 3 °C. These temperatures are in agreement with solidus and liquidus temperatures of a recently studied Al-Si-Cu ternary phase diagram [312]. A cooling scan of the melted alloy showed that the alloy started the solidification at 562 ± 1 °C and ended at 545 ± 3 °C. Therefore, a narrow melting/solidification range characterized this alloy, which is the fundamental requirement to prevent the risk of liquation cracking during manufacturing, as described in Section 1.5.2. Regarding this, no cracks were detected on the polished cross-sections of the as-built bulk samples (see Fig. 66).

3.3.2.5 Nano-hardness

Similarly to what has been performed on the melt pool cross-sections (Section 3.3.1.2), nano-hardness tests were performed on bulk samples to investigate the effect of Cu addition on the local hardness. A grid of 384 indentation marks (4 along X and 96 along Z, 10 μm from each other) was performed to cover the full cross-section height of the sample. Two representative indentation grids are visually represented in the form of maps in Fig. 75. The average nano-hardness value was equal to 2.4 ± 0.8 GPa, which was higher than the value found for the base AlSi10Mg alloy, i.e. 1.8 ± 0.2 GPa. Therefore, the average hardness of AlSi10Mg+4Cu suggests that the addition of Cu effectively strengthened the base AlSi10Mg alloy. However, it is possible to notice that there is a fluctuation of hardness along the building direction. The hardness variation does not appear to follow any trend, and it might be related to the different distribution of Cu powder.

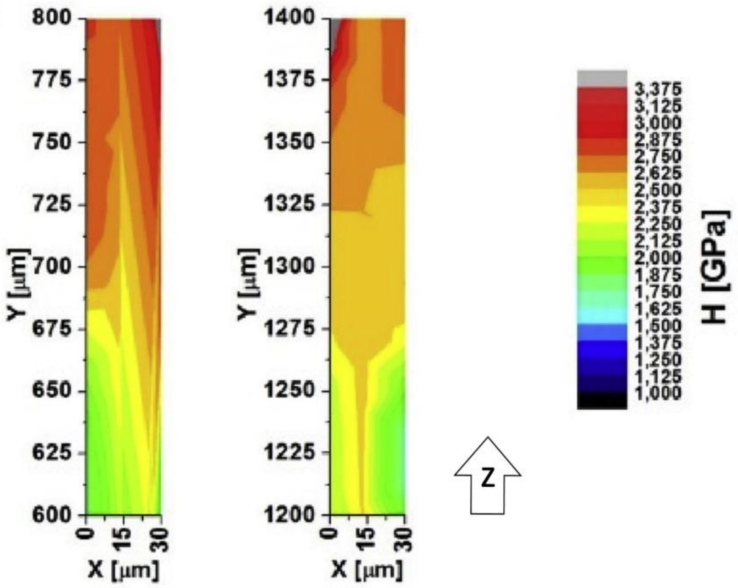

Fig. 75 Representative nanoindentation contour maps of the hardness distribution along the building direction of the as-built AlSi10Mg+4Cu alloy.

3.3.2.6 Macro-hardness and productivity

Since hardness showed fluctuations at the nano-scale, it was decided to assess the bulk samples hardness via Brinell hardness tests in order to evaluate a macro-portion of the specimen. Therefore, Brinell hardness (HB10) tests were performed, and a wider area of the sample was investigated. Five indentation marks were considered for each sample according to the ASTM E10-18 standard. Brinell tests were conducted on bulk samples with porosity less than 1.5 % (see Fig. 68). HB10 mean values are listed in Table A 4. Hardness ranged from 137 ± 2.3 to 149.2 ± 2.0 HB. It is thought that this hardness variation cannot be solely ascribed to the different porosity content of tested samples (Fig. 68). Considering the reference hardness of AlSi10Mg, which is 128.6 ± 1.9 HB [66], a hardness increment between 6.5 and 16 % was achieved upon mixing AlSi10Mg with Cu powders.

Brinell hardness values were then plotted against the volumetric energy density (VED) and the build-up rate ($\dot{V}$), also referred to as productivity, in Fig. 76. VED and $\dot{V}$ values were determined according to Eq. (3.2) [69] and (3.3) [313], and summarized in Table A 4 .

$$VED = \frac{P}{v \cdot h_d \cdot t} \quad \left[\frac{J}{mm^3}\right] \tag{3.2}$$

$$\dot{V} = v \cdot h_d \cdot t \quad \left[\frac{cm^3}{h}\right] \tag{3.3}$$

where P, v, and h_d are respectively the laser power, scanning speed, and hatching distance values used to manufacture the tested samples (Table A 4), whereas t refers to the layer thickness, which was fixed at 30 μm in this work.

Results of Fig. 76 revealed a general hardness reduction with the increase in *VED*. Moreover, it was found that the higher the *VED*, the lower was the productivity. Considering both hardness and productivity values as a function of *VED*, three different scenarios were identified. First, where relatively small *VED* values were used (VED < 50 J/mm^3), high hardness was combined with suitable productivity. By further increasing *VED* in the range between 50 and 60 J/mm^3, the process resulted in slightly lower build-up rates and different hardness values. Lastly, by using the higher energies (VED > 60 J/mm^3), hardness varied from medium to low values, whereas the productivity was the lowest.

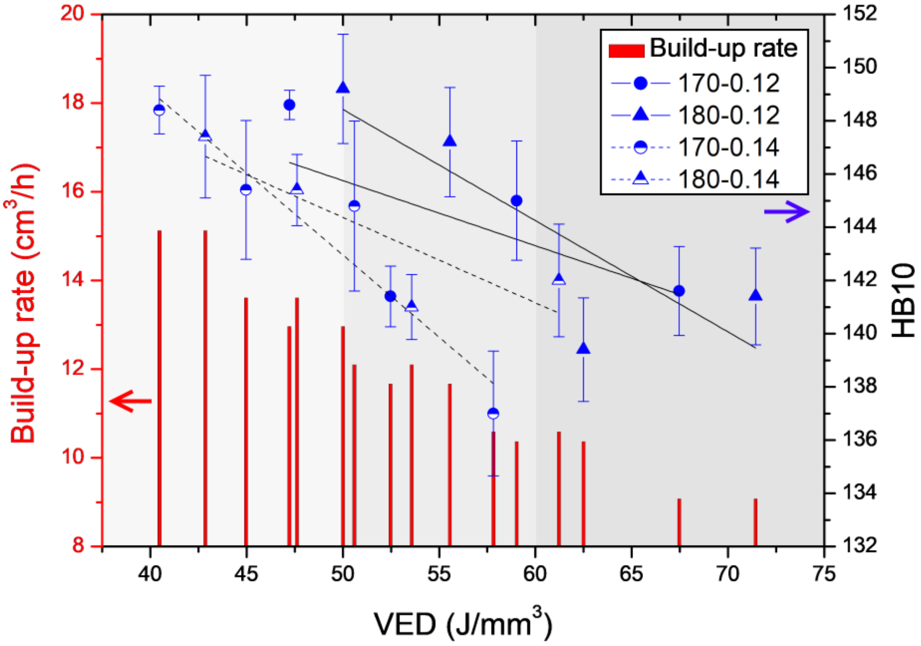

Fig. 76 Relationships between hardness, build-up rate, and *VED* for AlSi10Mg+4Cu bulk samples.

3.4 Discussion

3.4.1 Processability

Single scan tracks of mixed AlSi10Mg+4Cu powder were firstly manufactured to quickly assess the alloy processability and determine the good P-v combinations for the production of stable and regular SSTs (Fig. 58) [51,68,288]. Afterward, an additional job of SSTs was carried out to finely tune the process parameters and find the alloy process window. The SSTs widths w_i were then retrieved from on-top micrographs reported in Fig. 59. It was noticed that, for a given scanning speed, w_i values increased as the power increased, as shown by plots in Fig. 77 [63]. Due to this variability of w_i values, it was decided to adopt the mean width value $\overline{w}$ ($\sum w_i/12$) of all SSTs to define the three h_d values used for manufacturing bulk samples.

The unidirectional scanning strategy was employed at first with the aim of evaluating the overlapping φ of adjacent SSTs. For this reason, the porosity data of Fig. 65 were assessed, focusing the attention on the iso-power and iso-hatching behaviors represented respectively by dotted and dashed lines.

Considering iso-power behaviors, porosity achieved its minimum in the partially overlapped scenario for each P series (see a^{ii}, b^{ii} and c^{ii} points in Fig. 65). In fact, when the not-overlapped scenario was reached, aligned porosities arose as a consequence of farther scan tracks (Fig. 67) [40]. On the opposite, irregularly shaped pores occurred working in a completely overlapped scenario (Fig. 66). The presence of such porosities might be induced by an excessive laser remelting of former tracks owing to a large φ [168].

Considering the iso-hatching behaviors, it can be argued that overlapping φ increased as the used P increased. Interestingly, this behaviour can be correlated with the linear relationship of w_i with P reported in Fig. 77. By keeping constant h_d and increasing P, indeed, the scan track width w linearly increases and, consequently, the extent of overlap φ also increases. Increasing P and, thus, increasing φ was beneficial for the density to a large extent. A porosity reduction from 2.22% of a^{i} to 1.13% of c^{i} was found by following the iso-hatching behavior at 0.14 mm (Fig. 65). Similarly, porosity values below 1.50 % were always obtained along the iso-hatching line at 0.12 mm. Eventually, a higher presence of porosities was detected in the case of iso-hatching at 0.08 mm, since it was worked far away from the optimum overlapping condition.

Porosity results of Fig. 68 indicate that the process window selected for manufacturing bulk samples with the rotated scanning strategy allowed the production of near fully dense samples in all cases. Hence, the choice of the proper parameters was based on the final aim: hardness or productivity? As reported in Fig. 76, h_d of 0.14 mm and v of 1000 mm/s can be used when high productivity is desired. On the other hand, if a high hardness in the as-built condition is wanting, P of 180 W, h_d of 0.12 mm and v of 1000 mm/s must be used.

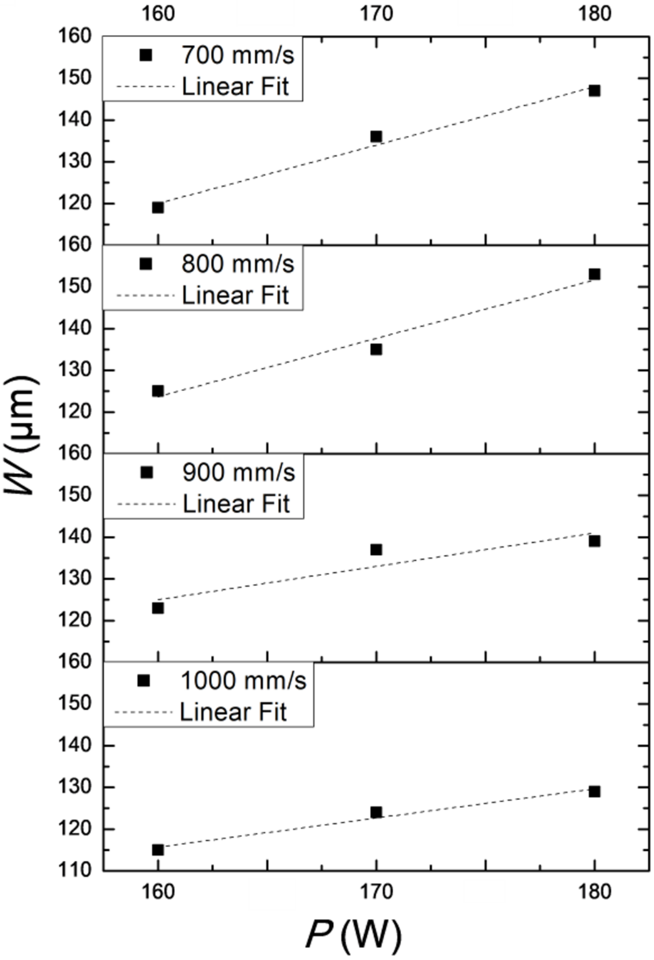

Fig. 77 Relationship between the SST width and laser power at varied scanning speeds.

3.4.2 A new method for the definition of LPBF parameters

"*At posteriori* analysis of results presented in Sections 3.3 and 3.3.2 supports the definition of a method for a time and cost-effective identification of the main process parameters to manufacture new alloys for LPBF. According to the particle size distribution of the powder, the layer thickness is fixed. After that, as already demonstrated in literature [44,64,67,100,180,298,299], the proper P-v combinations are identified through the SSTs approach. Furthermore, in the work of Nie et al. [64], the process window is then completed by producing and characterizing multi-tracks for the definition of the hatching distance. On the other hand, according to the innovative methodology proposed in this study, through SST jobs also the h_d value is defined.

As previously demonstrated, h_d can be calculated by using the reverse function of Eq. (3.1), i.e. the following Eq. (3.4):

$$h_d = w \cdot \left(1 - \frac{\varphi}{100}\right) \tag{3.4}$$

To minimize residual porosity, it is necessary to stay in the partially overlapped scenario (see Fig. 65). For this reason, by using in Eq. (3.4) φ values between 0 and 20% and the specific SST width w_i, taking into account the correlation between scan width and *P*-*v* combinations (Fig. 77), h_d values can be identified. In this way, just through SSTs characterization, a narrow process window for the production of bulk samples with 67° rotated scanning strategy can be selected. *P*, *v* and also h_d to be used in DoE are then defined without producing samples with unidirectional scanning strategy, minimizing the number of samples produced and accelerating times (Fig. 78).

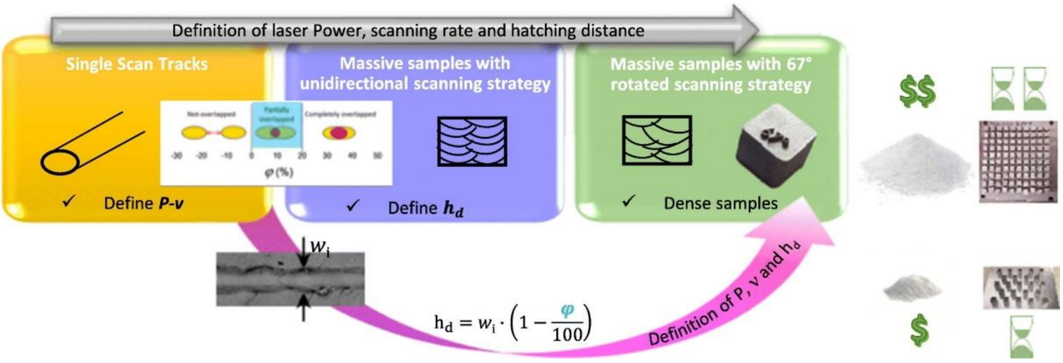

Fig. 78 Schematic representation of the proposed method for a time-saving identification of the alloy process parameters.

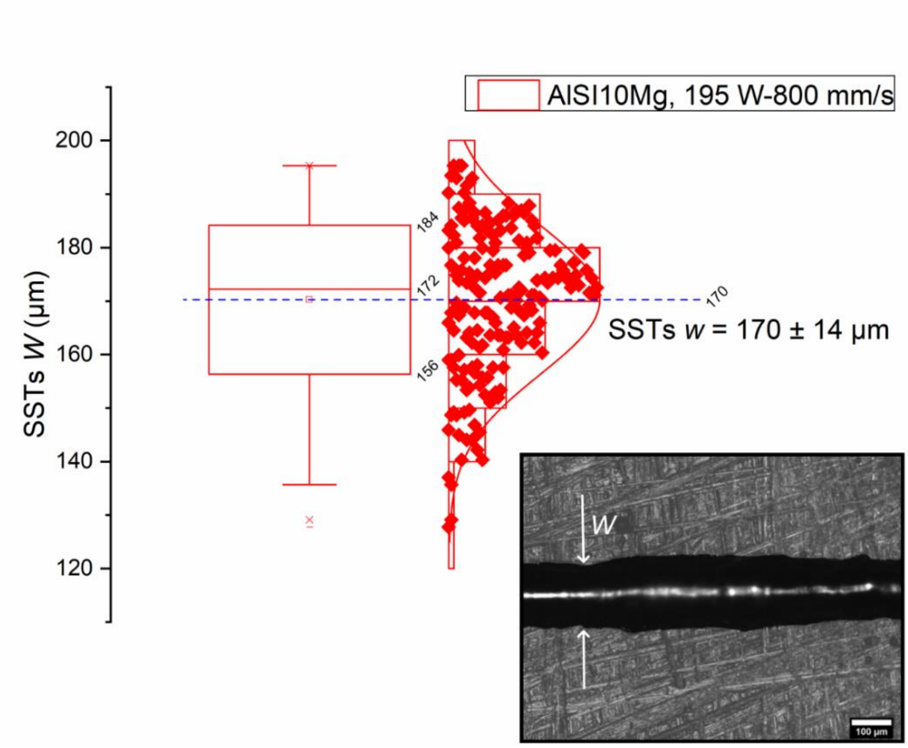

Fig. 79 Whisker plot of SST width measured on a single scan track of AlSi10Mg produced with optimized process parameters.

To validate this methodology, the main process parameters adopted in previous studies for AlSi10Mg powder processed with the same LPBF system were considered. Hence, a single scan track of AlSi10Mg was produced at 195 W and 800 mm/s with the procedure explained in Section 3.2.2. Then, SST width was determined and its value was found to be 170 ± 14 μm, Interestingly, by using in Eq. (3.1) the determined SST width and h_d of 0.17 mm, a φ value of 0% was obtained, confirming the role of the overlapping here suggested [53].” ® 2019 Materials & Design

3.4.3 Microstructure

In this work, the microstructure of a mixed AlSi10Mg+4Cu alloy was investigated on the longitudinal cross-sections of both single scan track and bulk samples (see Fig. 60c and Fig. 71a, respectively). In both conditions, primary Al columns/cells were decorated by a eutectic architecture, revealing the peculiar microstructure of LPBF*ed* parts reported by previous researchers [56,76]. The origins of these microstructures were deeply explained in Sections 1.4.5 and 2.2.1, considering the different solidification modes from the melt [162]. Briefly, the severe constitutional undercooling induced by rapid cooling promoted the growth of α-Al cells/columns into the liquid area of the melt pool according to a cellular/columnar dendritic solidification mode. Then, solute atoms in excess, mainly Si in Al-Si alloys [217], were rejected from the solidification front to the liquid nearby, leading to the formation of an extremely fine eutectic network rich of solute elements [216,314].

Despite the presence of a dendritic structure in both conditions, substantial differences emerged when the microstructures of melt pool and bulk samples are compared (Fig. 60c, Fig. 71a). First, eutectic was significantly fibrous in the case of SST, whereas it exhibited a lamellar shape in bulk samples. Second, the cell morphology of SST was rather inhomogeneous compared to the bulk sample counterpart. Third, the fineness of α-Al cells was more pronounced in single scan tracks. The average cell diameter, indeed, increased from the value of 0.4 ± 0.3 μm in SST to 0.8 ± 0.4 μm in bulk LPBF*ed* sample. Therefore, previous observations seem to suggest that the solidification within the single laser track occurred in the presence of a turbulent melt. In fact, the local temperature fluctuations arising during laser melting of a SST, likely created a surface tension gradient on the hemispheric cap of the molten pool, therefore triggering strong thermocapillary flows, as the ones observed in Fig. 61a [141,145]. Then, the convective motion of the melt presumably promoted the re-nucleation of crystals and their growth in different directions, leading to the fibrous eutectic of Fig. 60c [4,315]. On the opposite, the regular eutectic network of bulk samples in Fig. 71a indicates that solidification likely occurred from a relatively quiescent melt. During the production of a bulk samples, indeed, the molten pool remained in close contact with the underlying scan tracks throughout the whole cooling time. Therefore, previously consolidated layers acted as a heat sink, providing a continuous heat transfer to the molten pool and promoting the formation of a well-defined eutectic architecture (Fig. 71a).

Apart from these differences, SST and bulk sample microstructures showed a similar eutectic fraction, which ranged from 25 ± 4% to 27 ± 1%. It was noticed that these values were higher than the eutectic fraction calculated in the master AlSi10Mg alloy, which was nearly 17% [196]. This was due to the fact that Cu atoms were only partly supersaturated in the α-Al phase. As retrieved by the Al lattice parameter value of Fig. 73, Cu supersaturation ranged between 0.75 and 1%. Hence, it is thought that the remnant fraction of Cu was segregated at the cell boundaries during the latest stage of cooling, and remained in the eutectic zone as Al-Cu precipitates, thus rationalizing the overall increment of eutectic fraction. The compositional mapping performed on AlSi10Mg+4Cu eutectic confirmed that Cu preferentially located along the cell boundaries (see Fig. 72). Later, the phase investigation revealed the presence of the θ-Al_2Cu phase in the as-built state (Fig. 73 and Fig. 74). Therefore, it can be concluded that the eutectic structure of AlSi10Mg+4Cu was formed by an intermixing of Si precipitates and Al_2Cu phase.

3.4.4 Effect of *in-situ* alloying on chemical composition and microstructure

In-situ alloying of powder blends is an effective strategy to develop new Al alloys by LPBF, as recently demonstrated in Refs. [286–288]. However, the manufacturing of parts with homogeneous chemical composition was found to be an important challenge [66,169,285]. Therefore, in this work, a comprehensive chemical composition mapping was carried out on both SSTs and bulk sample cross-sections.

In a single scan track, the representative EDS map of Cu provided by Fig. 61b revealed the presence of Cu segregations within the melt pool. Segregations were oriented along with varied directions, forming bright bands. Closer investigations on these areas mainly showed fibrous structures with sided branches enriched of Cu, as the ones depicted in Fig. 80. Occasionally, un-melted Cu particles of large size were also detected within melt pools (Fig. 81). In this regard, it is worth noting that similar observations were recently reported by Cattano et al., after mixing AlSi10Mg and HX powders [285]. Apart from un-melted agglomerates of HX particles, they observed banded structures mainly composed of the constitutive transition metals of HX powder, i.e., Ni, Cr, and Fe. The origin of these bands was ascribed primarily for the very short lifetime of the melt pool (≈ 3 ms [316]), which not allowed the complete melting of the larger particles, and hampered the diffusion of solutes at long distances. This seems to be partially confirmed by the Cu bands observed in Fig. 61, which mainly tracked the turbulent motion of Marangoni flows that were suddenly ‘frozen’ by the rapid cooling. However, not only the fast cooling but also the different physical properties of the starting powders (reported in Table 16) could explain the formation of the observed Cu segregations.

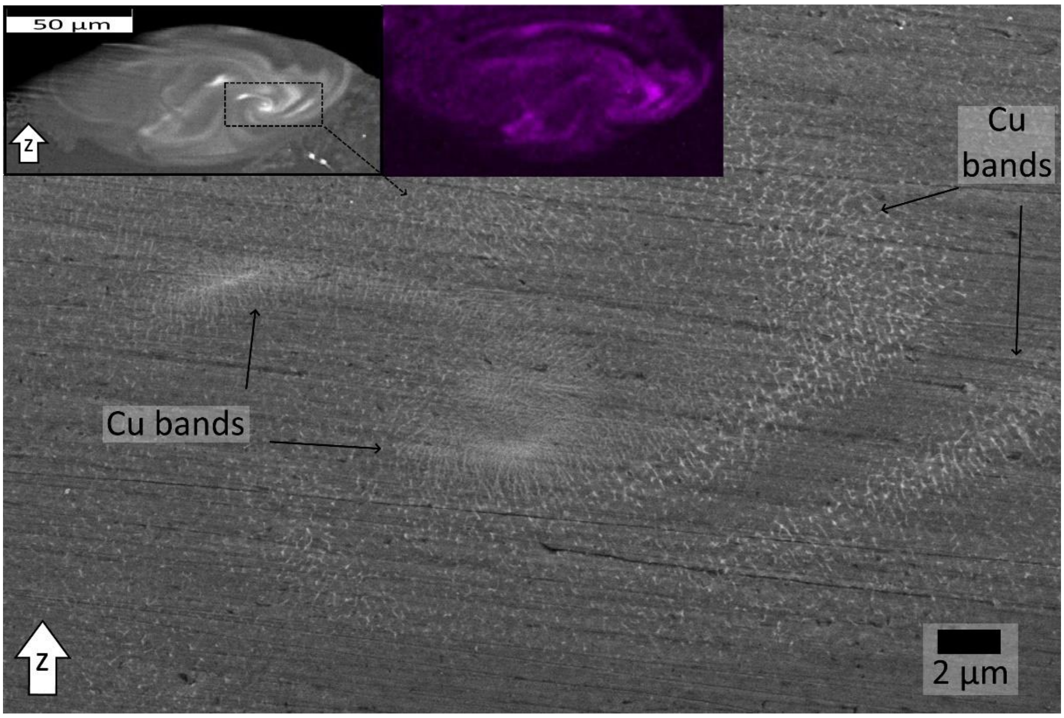

Fig. 80 FESEM micrograph of Cu segregations detected in the melt pool of Fig. 61.

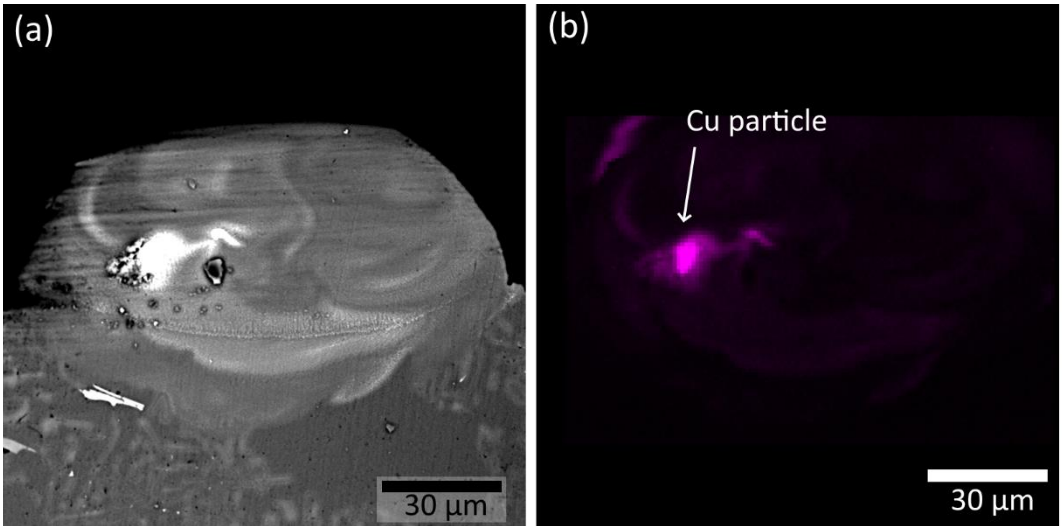

Fig. 81 Partially melted Cu particle embedded in a melt pool cross-section: (a) BSE-SEM micrograph and (b) the corresponding EDS map with Cu distribution.

It is widely known from the literature that the relatively high thermal conductivity of Al alloys requires the adoption of a high power laser to melt the starting powder completely [41,42]. Thus, the even higher thermal conductivity of Cu, which is almost the double of the AlSi10Mg one (see Table 16), could have enhanced the heat dissipation significantly from the melt pool core to the surrounding areas, leading eventually to the incomplete melting of the large Cu particles. Besides, another aspect to consider is the relatively low absorptance of Cu to the infrared radiation [39]. In previous research, indeed, the absorptance of a pure Cu powder bed irradiated by a laser wavelength of 1060 nm was estimated to be less than 1% [317].

Table 16 Physical properties of AlSi10Mg and pure Cu powders [318,319].

Alloy	density, [g/cm^3]	thermal conductivity, [W/m·K]	Specific energy, [J/mm^3]	Melting range [°C]
AlSi10Mg	2.67	130 - 190	2.9	570-590
Cu	8.96	384	6.1	1063

Table 16 also reports the specific energy values required to melt a volume unit of AlSi10Mg and Cu alloy. As can be observed, the energy input to melt a unit volume of Cu needs to be 2 times higher than the one required to melt a similar volume of AlSi10Mg. Hence, it was likely probable that, by using a laser power value between 160 and 180 W and speeds between 700 and 1000 mm/s (Fig. 59), the input energy was adequate to fully melt AlSi10Mg powder but not enough for the complete melting of Cu powder. Furthermore, the partial melting of Cu particles could have been induced even by the significant melting temperature difference of the starting powders (Table 16).

Under these conditions, when the laser irradiated AlSi10Mg+4Cu powder to form a single scan track, AlSi10Mg powder completely melted earlier than Cu. Therefore, immediately upon irradiation, the molten pool was likely formed by a liquid phase constituted by AlSi10Mg and Cu, and semi-solid Cu particles. At this point, the temperature gradient, generated during laser melting, induced the formation of turbulent convective flows [142]. Thus, it is believed that fluid flows driven by Marangoni convection contributed to the *in-situ* alloying of AlSi10Mg and Cu mixture [320]. In fact, the stirring of the melt pool likely enhanced the mixing of semi-solid Cu particles with the AlSi10Mg+Cu liquid phase. Furthermore, it was also possible that part of these Cu particles was progressively fused by the local heat flow released by the surrounding melt, being the amount of un-melted Cu particles quite limited. Then, Fig. 61 indicated that Cu was either conveyed into the Marangoni flows or de-mixed from the liquid phase due to the higher density of Cu (Table 16), falling at the bottom of the molten pool. Thus, both scenarios lead to the formation of Cu segregations. During cooling, Cu atoms diffused from Cu segregations into surroundings liquid areas and, then, precipitated out from supersaturated solid solution upon consolidation, forming the Cu bands with a dendritic structure observed in Fig. 80.

Despite the presence of Cu segregations, the EDS map of Cu provided by Fig. 61b confirmed the fact that Cu diffused everywhere at the melt pool scale. However, it must be underline that the AlSi10Mg substrate used for single scan tracks production has a dissimilar chemical composition compared to AlSi10Mg+4Cu. Therefore, since the laser energy involved the melting of a substrate portion during single scans consolidation [321], it might be possible that a Cu dilution occurred near the melt pool boundary/substrate interface, thus creating local fluctuations of the melt pool chemical composition. Nevertheless, the Cu wt.% concentration was measured in five points along the melt pool cross-section outside Cu segregations, and the average value was found to be 4.56 ±

0.22 wt.%, pointing that a substantial *in-situ* alloying was achieved to a large extent upon LPBF of a single scan track [288].

Similarly, Cu concentration was evaluated in bulk samples using EDS maps randomly performed on the longitudinal cross-sections. Five maps of 400×400 μm^2 each were considered. Results showed a Cu concentration of 3.96 ± 0.26 wt.%, which was in good agreement with the expected Cu concentration in the alloy, i.e. 4 wt.%. However, the representative Cu distribution map of Fig. 82 indicated the presence of Cu segregations mainly located in correspondence of the overlapping regions between adjacent melt pools. The origin of the observed Cu distribution can be explained considering the thermal effect produced by the fusion of subsequent scan tracks or layers [287]. When scan tracks/layers were scanned, the energy input was transferred to the previous laser tracks by conduction, and a remelting zone formed in the overlap area of adjacent SSTs [76]. Therefore, the diffusion of Cu atoms located near overlap regions was triggered. Cu locally diffused towards the overlapping areas following the preferential diffusional paths tracked by the local heat flux and forming, eventually, Cu segregations at the melt pool boundaries.

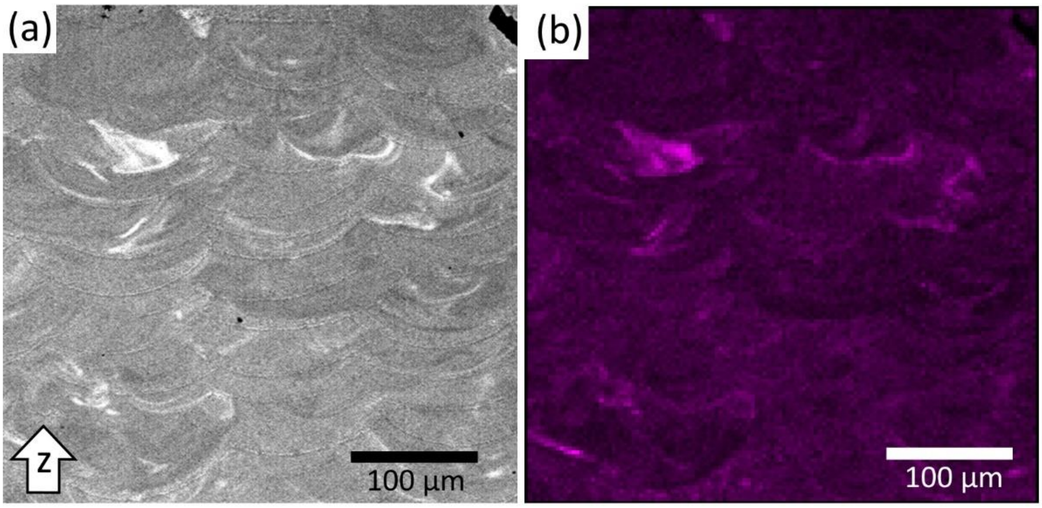

Fig. 82 The Cu distribution detected along the longitudinal plane of an as-built sample.

The progressive Cu diffusion induced by the local remelting influenced the alloy microstructure in correspondence of the areas enriched of Cu, as reported by Fig. 83. Here, the regular eutectic network observed in Fig. 71a was significantly interrupted by the presence of an un-melted Cu particle (Fig. 83). In this case, Cu abundantly diffused around the un-melted Cu particle (see inset of Fig. 83), creating a Cu-rich gradient structure. In this region, being the thermal conductivity of Cu higher than AlSi10Mg (Table 16), a steeper thermal gradient was expected, and, consequently, robust dendritic protrusions mostly enriched of Cu grew radially for roughly 2 µm, following the direction of the heat flux [158,162]. By moving farther from the Cu particle, a pronounced Cu gradient occurred (Fig. 83b), owing to the limited diffusivity of Cu in Al ($\approx 3.5 \times 10^{-9}$ m^2/s) [322]. Thus, a thinner dendritic microstructure formed by Al cells depleted of Cu and progressively enriched of Si was encountered at around 8 µm from the Cu particle center (Fig. 83b). Beyond the gradient structure, Cu wt.% concentration returned close to the standard value, i.e., 3.85 ± 0.3 wt.%.

In conclusion, considering the results presented so far, *in-situ* alloying was found to be an efficient way to manufacture SST and bulk samples of AlSi10Mg+4Cu alloy. The chemical composition analyses conducted on both melt pool and bulk samples longitudinal cross-sections revealed a Cu concentration very near to the theoretical one. However, the chemical homogeneity was partly affected by Cu segregations, which locally modified the microstructure forming Cu-rich bands (Fig. 80), or gradient structures (Fig. 83) around the un-melted Cu particles.

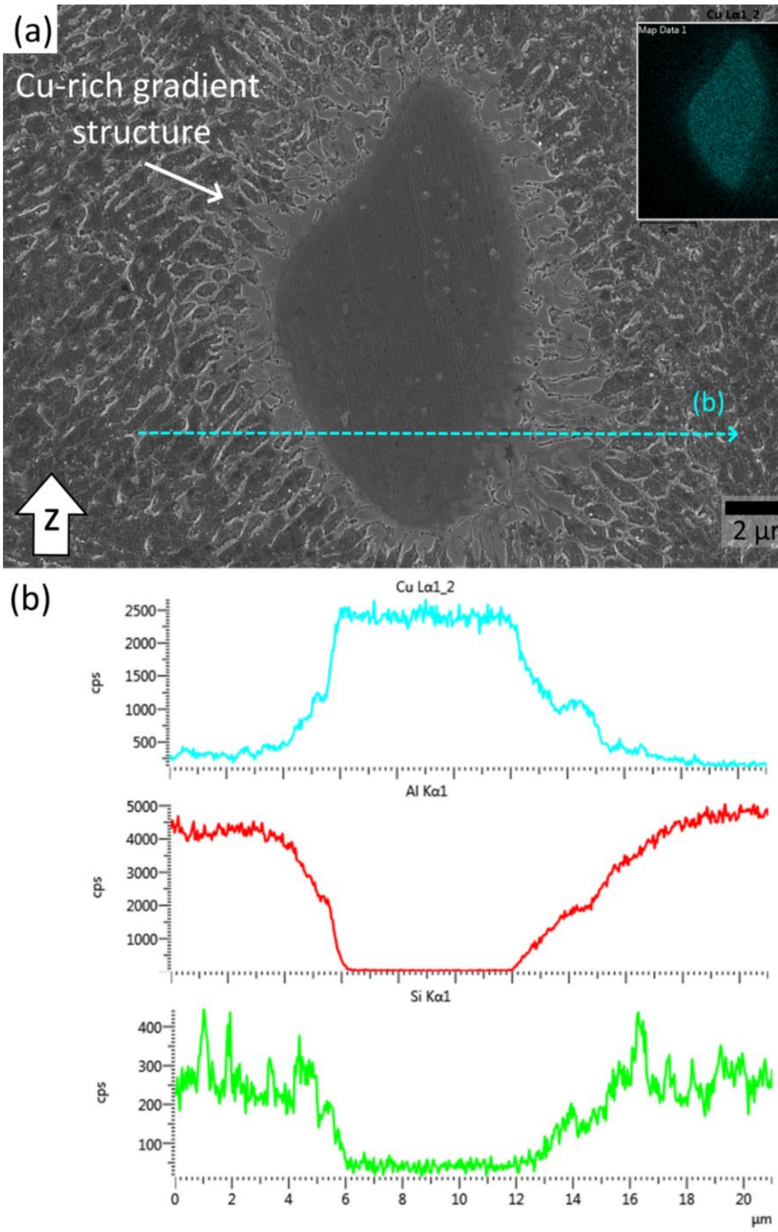

Fig. 83 (a) Un-melted Cu particle and its gradient structure primarily enriched of Cu. The inset reports the EDS map of Cu. (b) Results of the EDS line investigation conducted across the un-melted particle.

3.4.5 Effect of Cu addition on nano-hardness distribution

In Al alloys, Cu is used as alloying element due to its hardening effect mainly due to solid solution and precipitation strengthening [204,213]. In this work, 4 wt.% of Cu was added to AlSi10Mg alloy to increase the hardness and static strength of the base AlSi10Mg alloy. Results demonstrated the effective impact of Cu on hardness, showing a hardness increase of about 33% at the nano-scale (Section 3.3.1.3 and 3.3.2.5).

The hardness map retrieved from a SST of AlSi10Mg+4Cu (Fig. 62b) showed a hardness distribution less homogeneous than that of AlSi10Mg (Fig. 62a). Hardness peaks position of Fig. 62b resembled the distribution of Cu segregations in the melt pool of Fig. 61, i.e., tracking the circular motion of Marangoni flows. To deeply investigate the correlation between hardness and Cu, the same melt pool cross-section was studied in terms of nano-hardness and Cu distribution. The results were summarized in Fig. 84.

As can be seen from Fig. 84a, a hardness variation between cast-substrate and melt pool was noticed. Considering the nano-hardness values on cast substrate, an average hardness of 1.3 ± 0.4 GPa was found. However, there were several peaks (pointed by black arrows) showing hardness values higher than 6 GPa. EDS maps performed on these areas revealed the occurrence of precipitates rich in Mg and Fe (see supplementary compositional maps reported in Fig. A 1). According to the literature, these precipitates can be minor phases typically found in cast Al-Si-Mg alloys [68,206,323]. Depending on the Mg level, they can be ascribed either to the Chinese script like π-AlFeMgSi or the β-AlFeSi phase [323]. Moving towards the melt pool boundary, results revealed a slight hardness increase, although the dilution of AlSi10Mg+4Cu alloy into the AlSi10Mg substrate was not clearly noticed. Then, a significant hardness increase to 2.3 ± 0.3 GPa was revealed when the AlSi10Mg+4Cu melt pool surface was encountered. Three main contributions can be the cause of the observed hardness increment. First, the rapid cooling peculiar of LPBF process resulted in the formation of extremely fine Al grains (i.e., 0.4 ± 0.3 μm, Section 3.4.3) and, consequently, in a higher average hardness according to the Hall Petch equation [200,201]. Besides, the presence of trapped Si and Cu solutes into the α-Al solid solution, due to rapid cooling (Section 3.3.2.3) [204], caused the deformation of Al lattice and the formation of local residual strains, which effectively pinned the dislocation motion increasing the local hardness value [200]. Last, the precipitation strengthening also contributed to the hardness increment owing to the formation of a mix of partly coherent θ'- and θ-Al_2Cu phases, respectively detected by DSC and XRD [213]. Furthermore, the increment of hardness could be ascribed to the presence of Al-Si-Mg-Cu, Mg_2Si, and Si nano-precipitates, but there were no evident clues with the employed characterization techniques [190,219].

Considering the hardness distribution on the melt pool cross-section (Fig. 84a), it was found that hardness was homogeneously distributed with the sole exception of spots at higher and lower hardness, respectively indicated by green and red arrows. In this regard, it is interesting to observe that the harder point corresponded to a Cu segregation. In contrast, the lower hardness spot was found near a Cu-depleted area (Fig. 84a,b). Moreover, as can be noticed in Fig. 84b, the investigated hardness/compositional fluctuations occurred at a short distance from each other. Hence, it was possible that the investigated Cu/hardness fluctuations were caused by a local de-mixing of Cu from AlSi10Mg+Cu liquid, which in turn sunk to the bottom of the melt pool due to its higher density, and formed Cu segregation.

A similar study was conducted on a portion of the bulk sample (Fig. 85). BSE-SEM micrograph and corresponding Cu map pointed out the presence of regions at a high concentration of Cu (Fig. 85a,b). The nano-indentation test of Fig. 85c was performed on a sector containing Cu-rich segregations (black box of Fig. 85b) and revealed a quite homogeneous hardness distribution with hardness values between 2.750 and 3.375 GPa. However, similarly to SST cross-sections, some hardness fluctuations were identifiable. A lower hardness (≤ 2.750 GPa) was found in the correspondence of areas with less concentration of Cu, or the presence of pores (green-blue spot of Fig. 85c). On the other hand, hardness peaks (≥ 3.375 GPa) occurred over areas enriched of Cu, as the one indicated by the black arrow. The FESEM investigation of Fig. 85d revealed that the microstructure beneath the harder nanoindentation marks was constituted by a fine Si + Al_2Cu eutectic, as shown previously in Fig. 72.

Reported results evidenced the hardening effect induced by Cu. The impact of Cu on nano-hardness was twofold. On the one side, considering the mean hardness value, Cu addition increased the overall hardness of SSTs and bulk samples of about 33% compared to AlSi10Mg. On the other hand, nano-indentation and compositional maps pointed out that the presence of Cu segregations induced the formation of local regions at higher hardness. Nevertheless, thanks to the additional diffusion of Cu during LPBF manufacturing, the nano-hardness distribution in bulk samples (Fig. 75 and Fig. 85) was more homogeneous than the SSTs one (Fig. 62b).

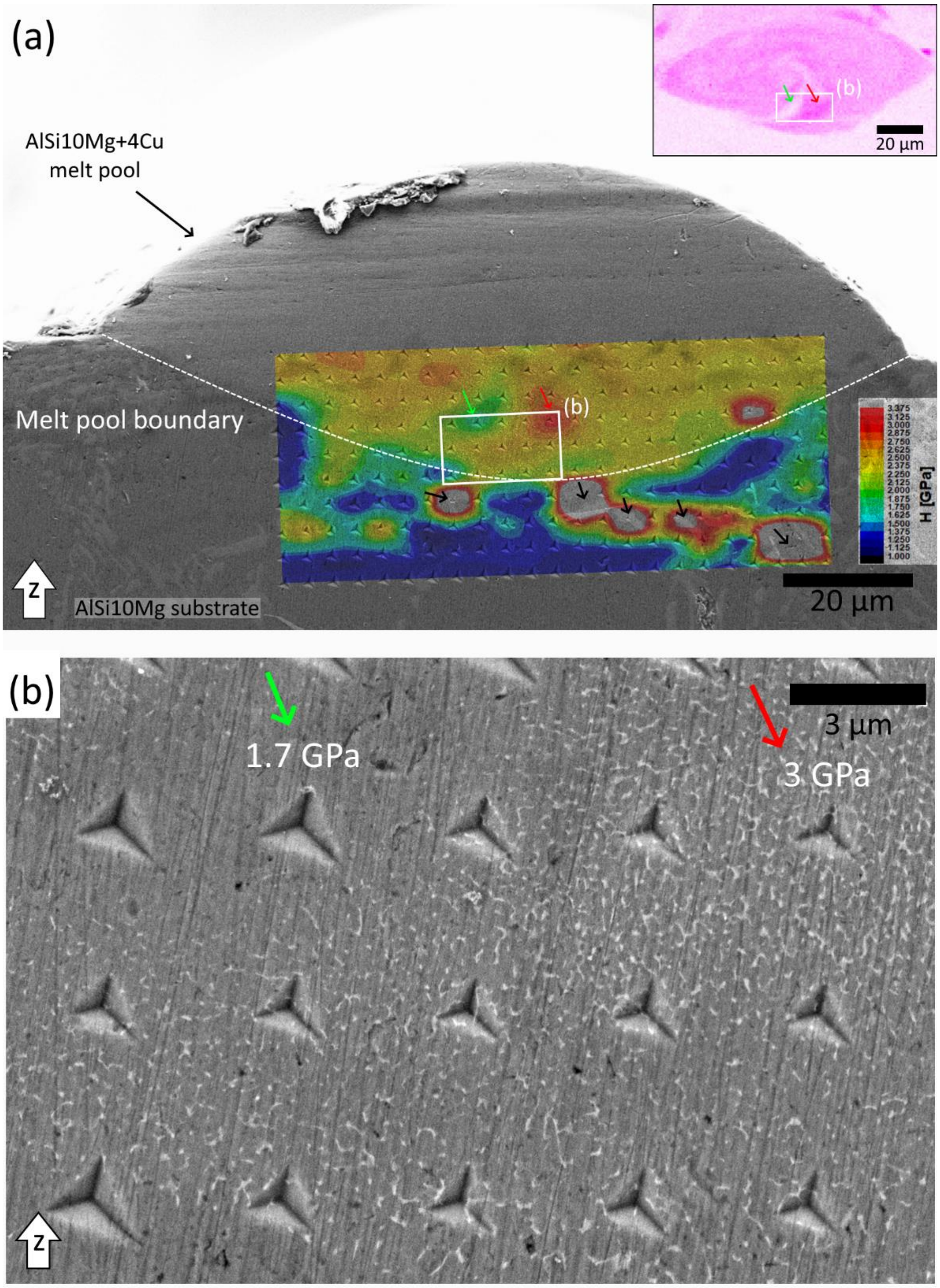

Fig. 84 (a) Results of a nanoindentation test conducted on a melt pool cross-section. The colored nanoindentation map was superimposed to the indentation grid. The inset depicts the EDS map of Cu. (b) High magnification micrograph showing the investigated indentation mark.

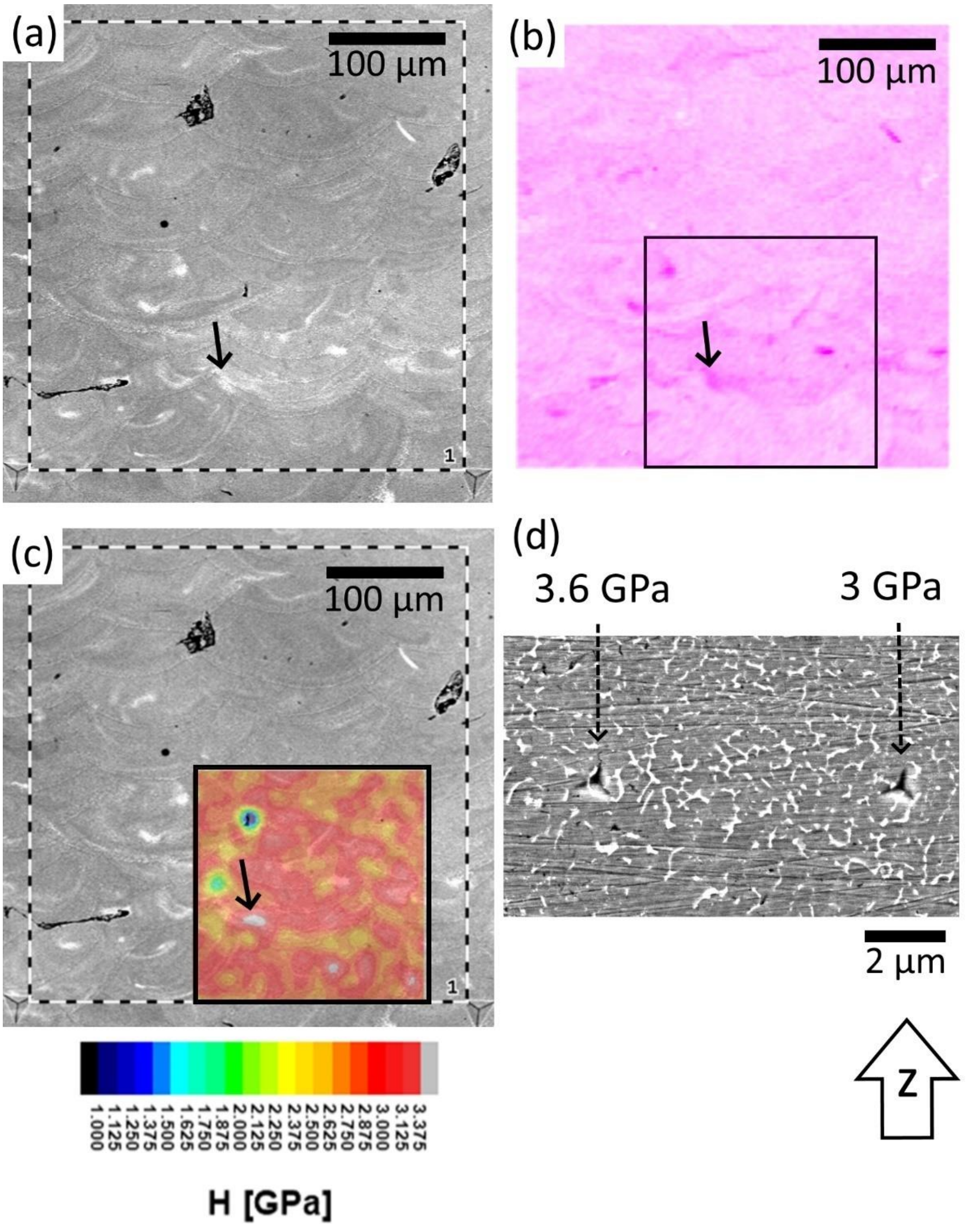

Fig. 85 (a) BSE-SEM micrograph of the as-built AlSi10Mg+4Cu alloy; (b) the Cu distribution obtained on the same micrograph by EDS analysis; (c) the superimposed nanoindentation map and (d) the microstructure beneath the harder indentation marks

3.5 Summary and conclusions

In this chapter, Laser Powder Bed Fusion was employed to *in-situ* synthetize an AlSi10Mg+4Cu alloy starting from mixed powder.

The processability of the selected composition was evaluated by producing SSTs and then bulk samples. In the beginning, a reliable P-v process window was quickly determined through the characterization of on-top and cross-section surfaces of single scan tracks. Stable SSTs and regular melt pools were selected to identify the process window. Therefore, the h_d was defined on the basis of melt pools overlapping φ, and bulk samples with unidirectional scanning strategy were manufactured accordingly. Once discarded the process parameters giving porosity higher than 1.5%, an additional batch of bulk samples was produced using the 67° rotated scanning strategy and φ values between 0 and 20%. Bulk samples showed a density level up to 99.16%. Lastly, macro-hardness and productivity were evaluated to select the optimum process parameters. If high productivity is desired, P of 170 W or 180 W, h_d of 0.14 mm and v of 1000 mm/s must be used. On the other hand, if the highest as-built hardness is wanted, a P of 180 W, v of 1000 mm/s and h_d of 0.12 mm must be used.

Based on the previous results, an accelerated method to define the main process parameters for LPBF is established. The method involves few steps, saving powder and working time. Indeed, by measuring the specific SST width w_i and imposing φ values between 0 and 20%, h_d values can be easily defined instead of performing time-consuming DoE experiments. In this way, the main process parameters (P, v, h_d) for the production of bulk samples are directly established only characterizing the single scan tracks.

Considering metallurgical aspects, the variation of microstructural features between SSTs and bulk samples revealed different solidification behaviors. The finer Al cells and the highly distorted eutectic fibers of SSTs indicate that solidification occurred in the presence of a turbulent melt. In contrast, the regular eutectic network observed in bulk samples can be ascribed to the relatively quiescent melt during LPBF manufacturing.

The microstructure morphology of bulk samples shows a dual eutectic formed by Si precipitates intermixed with Al_2Cu phase. Thus, a part of added Cu precipitates out during rapid cooling forming Al_2Cu phase, and the other fraction is hosted by Al lattice leading to a super-saturated solid solution with 0.75% - 1% of Cu. This contributes significantly to increase the hardness of the base AlSi10Mg alloy. A hardness increase of 33% was found at the nano-scale, whereas an increment between 6 and 16% was found at the macro-scale.

The Cu distribution is rather homogeneous on both SSTs and bulk samples cross-sections and reflects the nominal AlSi10Mg+4Cu composition, i.e. 4.56 ± 0.22 wt.% and 3.96 ± 0.26 wt.% for SSTs and bulk samples, respectively. This is due to the adequate mixing of the starting powder in the melt pool, promoted by the local convective flows arising during laser melting. However, as a consequence of the different physical properties of AlSi10Mg and Cu, Cu segregations form and slightly modify the local microstructure of AlSi10Mg+4Cu. Cu-rich bands and un-melted powder particles surrounded by a gradient microstructure interrupt the dual Si/Al_2Cu eutectic network. This, in turn, partly affects the local homogeneity of the chemical composition and nano-hardness distribution, which show higher values in correspondence of Cu segregations.

In conclusion, the modification of AlSi10Mg composition with Cu is effective in improving the as-built hardness of AlSi10Mg alloy. Besides, it is worth to mention that the *in-situ* alloying demonstrates to be a time-saving and cheap approach for starting the development of new alloys by LPBF. Future works should be focused on enhancing the overall homogeneity of chemical composition, minimizing the presence of Cu segregations.

3.6 Appendix

Table A 1 Results of the quantitative analysis performed on the melt pool cross-sections built in the first SSTs job. Geometrical characteristics were determined according to Fig. 50.

P [W]	*v* [mm/sec]	*LED* [J/mm]	*w* [µm]	*h* [µm]	*h/w* [-]	*g* [µm]	*d* [µm]	*g/d* [-]
100	300	0.33	134	92.56	0.68	70.26	22.3	3.15
	600	0.16	120	90.96	0.74	64.45	26.51	2.43
	800	0.12	96	61.45	0.63	37.94	23.51	1.61
	1200	0.08	107	87.35	0.81	67.55	19.8	3.41
	1500	0.06	45	13.43	0.3	6.1	7.33	0.83
130	300	0.43	128	91.93	0.7	54.65	37.28	1.47
	600	0.21	148	113.44	0.76	84.23	29.21	2.88
	800	0.16	101	50.33	0.49	37.09	13.24	2.8
	1200	0.1	78	63.29	0.82	47.29	16	2.96
	1500	0.08	91	31.12	0.34	12.21	18.91	0.65
160	300	0.53	169	74.28	0.44	33.52	40.76	0.82
	600	0.26	132	55.02	0.41	21.5	33.52	0.64
	800	0.2	120	62.36	0.51	32.12	30.24	1.06
	1200	0.13	95	54.75	0.57	29.77	24.98	1.19
	1500	0.1	91	36.02	0.39	8.18	27.84	0.29
180	300	0.6	168	88.1	0.52	39.72	48.38	0.82
	600	0.3	145	57.08	0.39	13.05	44.03	0.3
	800	0.22	155	83.92	0.54	44.77	39.15	1.14
	1200	0.15	111	46.81	0.42	15.23	31.58	0.48
	1500	0.12	108	50.25	0.46	28.7	21.55	1.33
195	300	0.65	187	131.44	0.7	41.15	90.29	0.46
	600	0.32	148	67.14	0.45	13.9	53.24	0.26
	800	0.24	156	66.59	0.43	19.39	47.2	0.41
	1200	0.16	117	73.36	0.62	38.55	34.81	1.11
	1500	0.13	109	82.15	0.75	50.77	31.38	1.62

Table A 2 Results of the density measurements performed on bulk samples built with unidirectional scanning strategy. The theoretical overlapping grade φ of adjacent SSTs measured by Eq. (3.1) is also reported.

P [W]	*v* [mm/s]	h_d [mm]	$\rho_{Arch.}$ [Kg/dm^3]	$\rho_{Rel.}$ [%]	Porosity [%]	φ [%]
160	700	0.08	2.67	97.38	2.62	32.77
		0.12	2.7	98.54	1.46	-0.84
		0.14	2.69	98.33	1.67	-17.65
	800	0.08	2.67	97.64	2.36	36
		0.12	2.7	98.55	1.45	4
		0.14	2.68	98	2	-12
	900	0.08	2.64	96.53	3.47	34.95

		0.12	2.7	98.49	1.51	2.43
		0.14	2.68	97.78	2.22	-13.82
	1000	0.08	2.68	97.99	2.01	30.44
		0.12	2.62	95.67	4.33	-4.35
		0.14	2.66	97.15	2.85	-21.74
170	700	0.08	2.66	97.25	2.75	41.18
		0.12	2.71	98.84	1.16	11.77
		0.14	2.71	98.77	1.23	-2.94
	800	0.08	2.66	97.01	2.99	40.74
		0.12	2.7	98.52	1.48	11.11
		0.14	2.71	99.06	0.94	-3.7
	900	0.08	2.64	96.51	3.49	41.6
		0.12	2.71	99.12	0.88	12.4
		0.14	2.69	98.26	1.74	-2.19
	1000	0.08	2.65	96.91	3.09	35.48
		0.12	2.68	97.98	2.02	3.23
		0.14	2.7	98.42	1.58	-12.9
180	700	0.08	2.69	98.13	1.87	45.58
		0.12	2.71	98.9	1.1	18.37
		0.14	2.71	98.96	1.04	4.76
	800	0.08	2.68	97.91	2.09	47.71
		0.12	2.71	98.78	1.22	21.57
		0.14	2.72	99.31	0.69	8.5
	900	0.08	2.67	97.41	2.59	42.44
		0.12	2.72	99.31	0.69	13.67
		0.14	2.71	98.87	1.13	-0.71
	1000	0.08	2.68	97.76	2.24	37.98
		0.12	2.71	98.86	1.14	6.98
		0.14	2.7	98.75	1.25	-8.53

Table A 3 Analysis of variance (ANOVA) on the porosity results of bulk samples manufactured with the unidirectional scanning strategy.

Source	DF	Sum of squares	F-value	p-value	Statistical significance ($p < 0.005$)
P	2	4.99	9.73	0.003	Significant
v	3	2.267	2.95	0.076	Not significant
h_d	2	9.647	18.82	0	Significant
$P \times v$	6	0.929	0.6	0.723	Not significant
$P \times h_d$	4	2.172	2.12	0.141	Not significant
$v \times h_d$	6	3.781	2.46	0.087	Not significant
Error	12	3.075			

Total	35	26.863

Table A 4 Porosity, hardness and build rate of bulk specimens produced with 67° rotated scanning strategy.

P [W]	v [mm/s]	h_d [mm]	VED [J/mm^3]	Build-up rate [cm^3/h]	$\rho_{Arch.}$ [Kg/dm^3]	$\rho_{Rel.}$ [%]	Porosity [%]	HB10
170	700	0.12	67.46	9.07	2.7	98.72	1.27	141.6 ± 1.6
	800		59.03	10.37	2.7	98.71	1.29	145.0 ± 2.2
	900		52.47	11.66	2.71	98.76	1.23	141.4 ± 1.1
	1000		47.22	12.96	2.71	98.84	1.15	148.6 ± 0.5
180	700		71.43	9.07	2.71	98.83	1.16	141.4 ± 1.8
	800		62.5	10.37	2.71	98.9	1.09	139.4 ± 1.9
	900		55.56	11.66	2.72	99.16	0.83	147.2 ± 2.0
	1000		50	12.96	2.71	99.03	0.96	149.2 ± 2.0
170	700	0.14	57.82	10.58	2.7	98.67	1.32	137.0 ± 2.3
	800		50.6	12.1	2.7	98.62	1.37	144.8 ± 3.1
	900		44.97	13.61	2.7	98.64	1.35	145.4 ± 2.6
	1000		40.48	15.12	2.71	98.97	1.02	148.4 ± 0.8
180	700		61.22	10.58	2.71	99.04	0.96	142.0 ± 2.1
	800		53.57	12.1	2.7	98.63	1.36	141.0 ± 1.2
	900		47.62	13.61	2.7	98.62	1.37	145.4 ± 1.3
	1000		42.86	15.12	2.71	98.95	1.05	147.4 ± 2.3

Table A 5 Analysis of variance (ANOVA) on the porosity results of bulk samples manufactured with the rotated scanning strategy.

Source	DF	Sum of squares	F-value	p-value	Statistical significance ($p < 0.005$)
P	1	0.09645	4.88	0.114	Not significant
v	3	0.10970	1.88	0.308	Not significant
h_d	1	0.04153	2.14	0.240	Not significant
$P \times v$	3	0.01678	0.29	0.833	Not significant
$P \times h_d$	1	0.02058	1.06	0.379	Not significant
$v \times h_d$	3	0.10579	1.82	0.318	Not significant
Error	3	0.05820			
Total	15	0.44723			

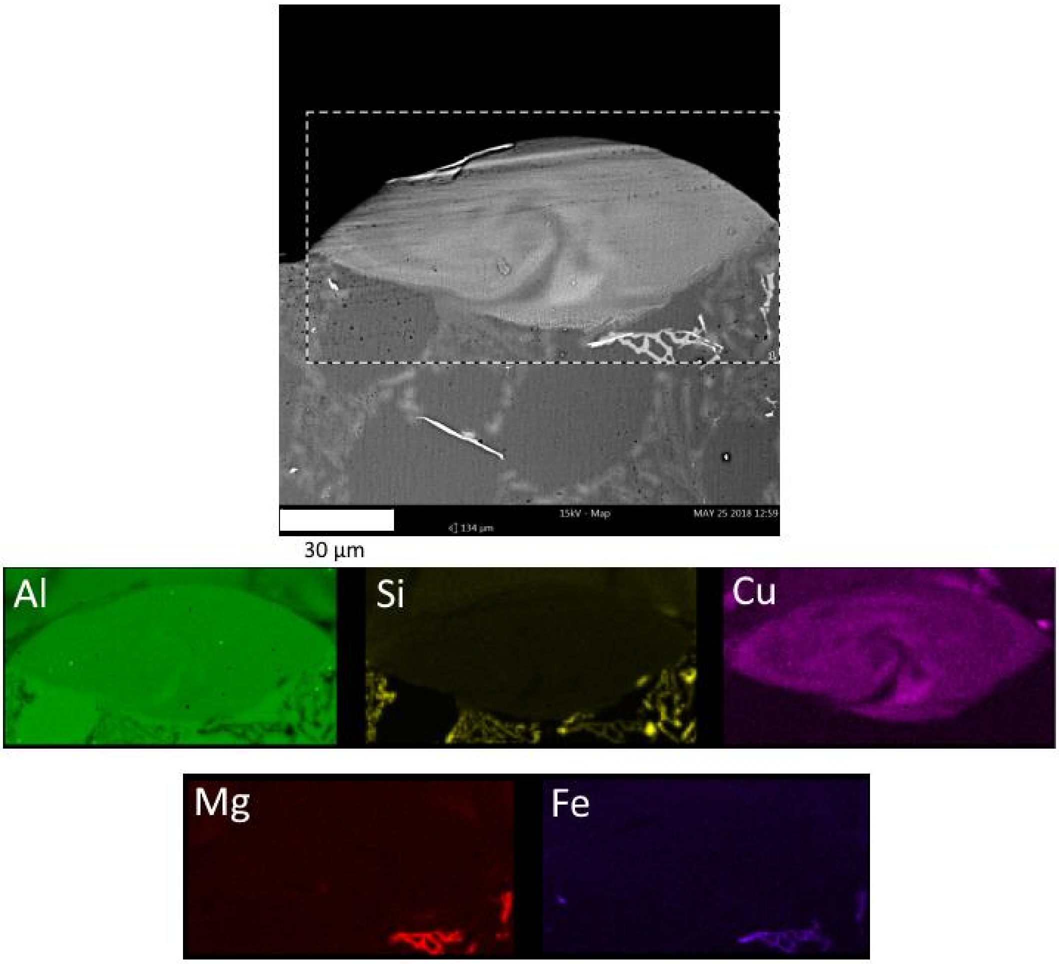

Fig. A 1 EDS compositional maps performed on the melt pool cross-section of Fig. 84 prior to nano-indentation tests.

Chapter 4

Direct aging of AlSi10Mg+4Cu alloy

4.1 Introduction

In the foundry industry, direct aging (T5 temper) is used as a regular heat-treatment strategy to heat-treat cast Al alloys [225]. According to the T5 protocol, the as-processed alloy is directly aged without the need of a previous solid solution heat-treatment. Hence, since the high level of supersaturated solid solution (SSSS) arising from the fast cooling of LPBF, direct aging has been recently adopted to age-harden Al alloys produced by LPBF [23].

To date, the direct aging response of LPBF*ed* Al-Si alloys has been widely investigated [221–223]. For instance, Aversa et al. were among the first LPBF users to directly age an as-built AlSi7Mg alloy produced by using platform heating temperatures between 100 and 190 °C [221]. They observed that the lower was the platform heating temperature, the higher was the hardening response of the alloy. In fact, after directly aging the alloy at 170 °C, a maximum hardness of 137 HV was measured on samples processed at 100 °C compared to the 115 HV of samples produced at 190 °C. The main reason for this was the impoverishment of the starting SSSS in samples fabricated with the higher platform heating temperature.

Similarly, other researchers pointed out that as-built Al-Si alloys with high solute content are inclined to be strengthened by direct aging [222,223]. In Ref. [222], AlSi7Mg alloy was heat-treated by both T5 and T6 heat-treatment strategies. It was found that direct aging heat-treatment returned the highest hardening response due to homogeneous precipitation of β''- Mg_2Si phase, which is enhanced by the high degree of supersaturation. Later, Rao et al. [223], by studying the precipitation pathway of an AlSi7Mg alloy directly aged at 165 °C, observed a copious number of nanometric Si particles at the peak-age condition. The Authors argued that such Si nano-particles are likely formed by the fast diffusion and the subsequent gathering of Si atoms during the early stage of direct aging.

Compared to the well-known direct aging behavior of Al-Si-Mg alloys [221–223], little work has been done to date on the aging response of LPBF*ed* Al-Si-Mg-Cu alloys. Regarding this, Roudnická et al. has recently investigated the age-hardening response of an AlSi9Cu3 alloy processed by LPBF [324]. After direct aging the alloy in the temperature range of 140-180 °C, the Authors observed an overall strengthening with a hardness and yield strength increment of 13÷18% and 36 %, respectively. In terms of metallurgical phases, a mix of θ'- Al_2Cu precipitates and Si platelets were revealed in the peak-aged condition.

To the best of the author’s knowledge, the state-of-art on the aging response of Al-Si-Mg-Cu alloys processed by LPBF is limited to the work of Roudnická et al. [324]. Therefore, this chapter aims at studying the direct aging behavior of the developed AlSi10Mg+4Cu alloy. Starting from the as-built condition, the alloy underwent direct aging heat-treatments at various temperatures, i.e. 160, 175, and 190 °C. The aging response was studied by tracking the hardness profile and, then, the significant direct aging conditions were investigated in terms of microstructure, thermal behavior, and tensile properties.

4.2 Materials and Methods

Gas-atomized powder of AlSi10Mg and high purity Cu were firstly mixed in a weight proportion of 96:4 through rotating jars and, then, *in-situ* alloyed during LPBF to synthesize the AlSi10Mg+4Cu alloy. The chemical composition of starting powders as well as the calculated composition of AlSi10Mg+4Cu is reported in Table 13 (Section 3.2.1). EDS analysis on bulk samples reported in Section 3.4.4 showed a Cu concentration of 3.96 ± 0.26 wt.%, which is in good agreement with the expected Cu concentration in the alloy, i.e. 4 wt.%.

An EOSINT M270 Dual-mode LPBF system was used to produce samples of AlSi10Mg+4Cu. To this end, the optimized process parameters for the productivity (see Section 3.4.1), namely P, v, and h_d of respectively 170 W, 1000 mm/s and 0.14 mm, were used. A rotating scanning strategy was adopted, changing the laser scanning direction of 67° after each layer. Produced samples revealed a densification level of 98.97 ± 0.21 % by image analysis, confirming that near fully dense samples can be successfully produced after a proper process parameter optimization.

Two types of samples were manufactured for this research (Fig. 86), namely cubes of $15\times15\times15$ mm^3 for the direct aging study and flat specimens for tensile tests with geometry according to ASTM E8/E8M-16a [325].

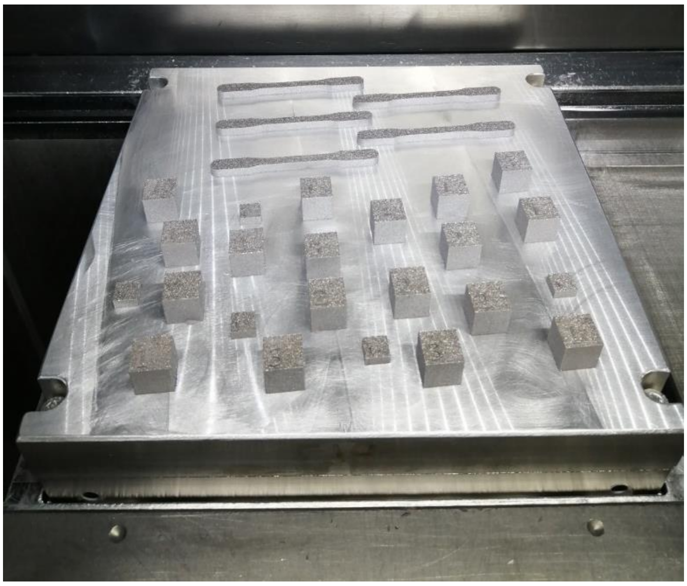

Fig. 86 Bulk samples of AlSi10Mg+4Cu used for the research study of this chapter.

The aging response of AlSi10Mg+4Cu was directly assessed starting from the as-built condition (without previous solutioning), following the protocol of the T5 temper [214] (Section 2.3.3). Direct aging heat-treatments were performed at 160, 175 and 190 °C for times ranging from 1 to 8 h. Aging temperatures were selected within the temperature range for the precipitation heat-treatments of age-hardenable aluminum alloys [225]. Heat-treatments were conducted in a heating oven (model BINDER FD56) with a temperature accuracy ΔT of ± 1.5 °C. Aging behaviors were evaluated by performing hardness measurements at fixed times, i.e. 1, 2, 4, and 8 h. Vickers micro-hardness tests (HV 0.5) were carried out by applying a static load of 0.5 Kg and a dwell time of 10 s using a HNVS-1000DX hardness tester. Five indentations were considered on each sample according to the ASTM E384-17 standard.

Phase identification was performed by X-Ray Diffraction (XRD) on the XZ cross sections of as-built and directly aged samples using a X-Pert Philips PW3040 diffractometer in Bragg Brentano configuration. A first batch of XRD patterns was obtained in the 2θ range from 20 to 100° at steps of 0.013°, and step duration of 25 s. After that, a second round of XRD analyses was performed between 42 and 48° using a finer step size (0.0033°) and an implemented duration time (60 s). The lattice parameter of the face centered cubic (*fcc*) Al was determined according to Eq. (4.1):

$$a = d_{hkl} \cdot \sqrt{h^2 + k^2 + l^2} \tag{4.1}$$

where d_{hkl} is the interplanar spacing and hkl are the Miller indexes.

A Setaram TGA 92 16.18 Differential Scanning Calorimeter (DSC) was used to investigate the thermal behavior of samples. DSC scans were carried out in the temperature range from 50 to 450 °C with an heating rate of 10 °C/min. To equilibrate the heat flux, an initial isothermal step of 15 min at 50 °C was performed before DSC scans.

Samples for microstructure investigation were prepared following the standard metallographic method down to 0.05 µm using colloidal silica. Etching was conducted in a diluted Keller solution (20% Keller reagents) for 10 s. Microstructural phases were then observed by a Field Emission Electron Microscope (FESEM) Zeiss SupraTM 40.

Finally, as-built and directly aged tensile specimens were tested by using a Zwick Z100 tensile machine applying a strain rate of 8×10^{-3} s^{-1}. All tests were carried out at room temperature. To ensure a representative behaviour, 3 samples for each condition were considered. Facture surfaces of tested samples were then observed by FESEM.

4.3 Results

4.3.1 Aging response

Aging curves of AlSi10Mg+4Cu alloy are depicted in Fig. 87. Before direct aging heat-treatments, as-built samples exhibited an average hardness of 142.3 ± 5.0 HV. In agreement with what was noticed for nano- and macro- hardness (Sections 3.3.2.5 and 3.3.2.6), the as-built hardness value of AlSi10Mg+4Cu was higher than the AlSi10Mg counterpart (i.e., 130.8 ± 3.1 HV), showing a hardness increment of nearly 8.8 % due to intrinsic hardening effect of Cu. On aging, micro-hardness followed different trends according to the used aging temperatures and times. When aging was conducted at 160 °C, hardness increased steadily up to 4 h. Then, beyond this point, the HV value reached a plateau of about 160.6 HV without showing a further hardness increment within the investigated time interval. Instead, by raising the aging temperature to 175 °C, a hardness peak of 163.9 HV was identified upon 1 h at 175 °C. Afterward, hardness slightly decreased at a higher aging time while remaining far above its as-built value. As far as the aging behavior at 190 °C is concerned, the aging curve went through a hardness peak after an elapsed time of 2 h. Then, a significative hardness drop was detected, suggesting a possible over-aging.

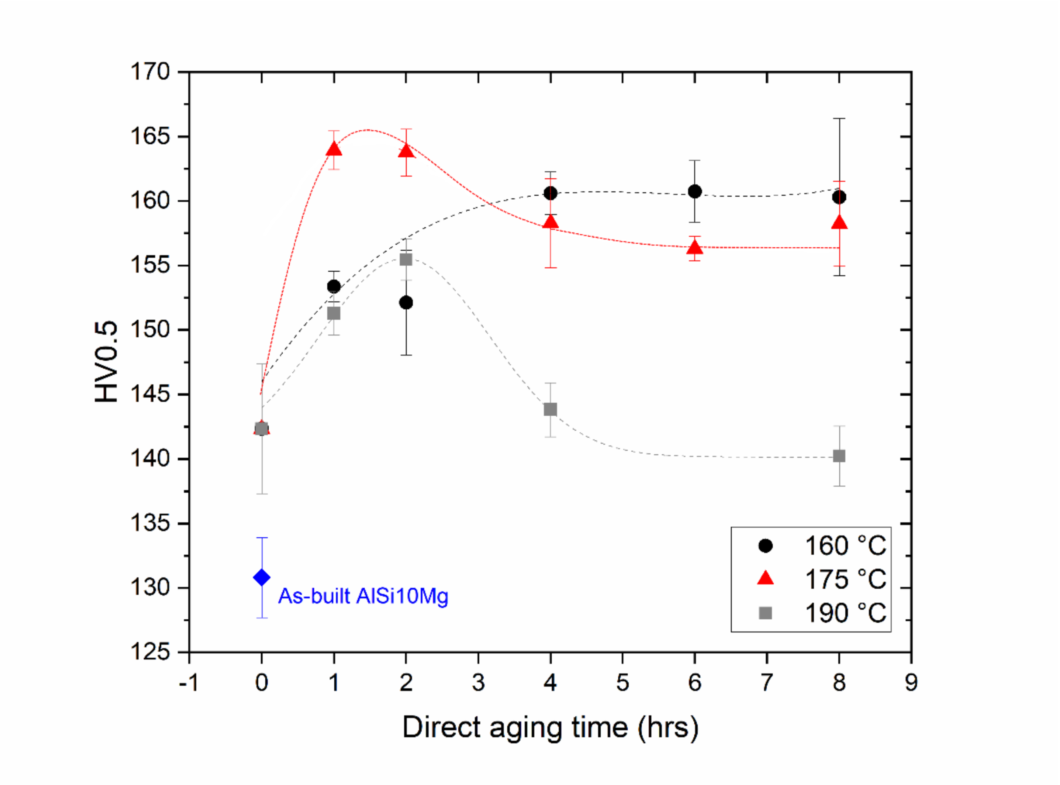

Fig. 87 Aging curves of AlSi10Mg+4Cu alloy at different temperatures and times.

Table 17 summarizes the maximum hardness (HV_{max}) obtained for each condition and the relative hardness increment (ΔHV_{max}) values, along with the time to reach them. As far as the aging temperature is raised above 160 °C, the time to HV_{max} decreased. It is also worth noting that the hardness increment at the peak age reduced when increasing the aging temperature from 175 to 190 °C. In conclusion, within the investigated temperature and time ranges, the highest hardness gain corresponded to the peak age achieved after 1 h at 175 °C with a ΔHV_{max} of + 21.61 HV.

Table 17 Temperature and time to the maximum hardness (HV_{max}), and the relative hardness increment (ΔHV_{max}) as compared to the as-built hardness value.

Aging temperature (°C)	Time to HVmax (h)	HVmax		ΔHVmax
		Mean	Dev.St.	
160	4	160.60	1.65	18.27
175	1	163.94	1.49	21.61
190	2	155.46	1.61	13.13

4.3.2 Phase Identification

The phase identification was conducted on the as-built and directly aged AlSi10Mg+4Cu samples. Results are summarized in Fig. 88 and Fig. 89.

Fig. 88 reports XRD patterns of samples showing the maximum hardness in the aging curves of Fig. 87 (see Table 17 for time and temperature conditions). As-built and heat treated samples at 8 h were also reported to detect the constitutional phase evolution during direct aging. Generally speaking, all XRD patterns revealed reflections due to the presence of *fcc* Al, diamond cubic Si, and tetragonal θ-Al_2Cu phases in agreement with the results presented in Section 3.3.2.3.

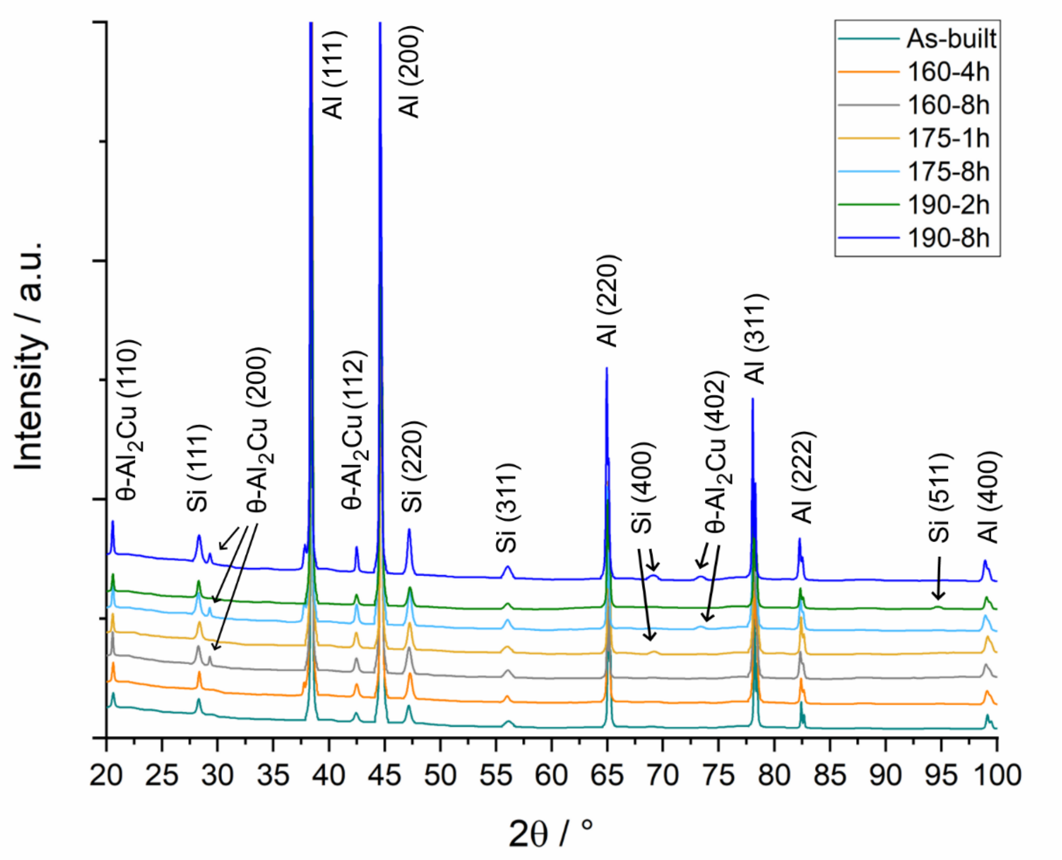

Fig. 88 XRD patterns of as-built and directly aged AlSi10Mg+4Cu samples.

From Fig. 88, it can be noticed that the position of Al peaks gradually shifted to lower angles by increasing the aging temperature and time. This trend was clearly observed for the Al (200) peak positions reported in Fig. 89a, and it could indicate a progressive impoverishment of the super-saturated solid solution formed by Si and Cu during the direct aging heat-treatment [227].

The intensities of diamond cubic Si signals were lower compared to those of *fcc* Al. However, Si reflections became sharper and more intense with the increasing of the aging temperature and time, as denoted by the Si (200) peaks of Fig. 89b. This corroborates the idea that, during aging, Si moved out of the super-saturated solid solution to precipitate at the Al cell boundaries [83,227].

A similar trend was found for the θ-Al_2Cu phase. At a constant aging temperature, indeed, higher peak intensities were detected at longer aging time, namely after 8 h, as observed in θ-Al_2Cu (112) reflections of Fig. 89c. Also, it must be noted that minor peaks referring to the θ-Al_2Cu phase, i.e. (200), (402) and (310) reflections, appeared after 8 h of heat-treatment (see Fig. 88 and Fig. 89).

The lattice parameter values for *fcc* Al of studied specimens are plotted against the direct aging times in Fig. 90. Results revealed a general broadening of the Al lattice parameter on the increasing aging time. Based on the linear behaviors, it could be inferred that within the investigated time interval and temperatures the higher the aging time, the larger is the Al lattice parameter. Lastly, the slope of the linear trends ranked in the sequence 160 < 175 < 190 °C, suggesting a possible influence of the aging temperature on the increment of the Al lattice parameter.

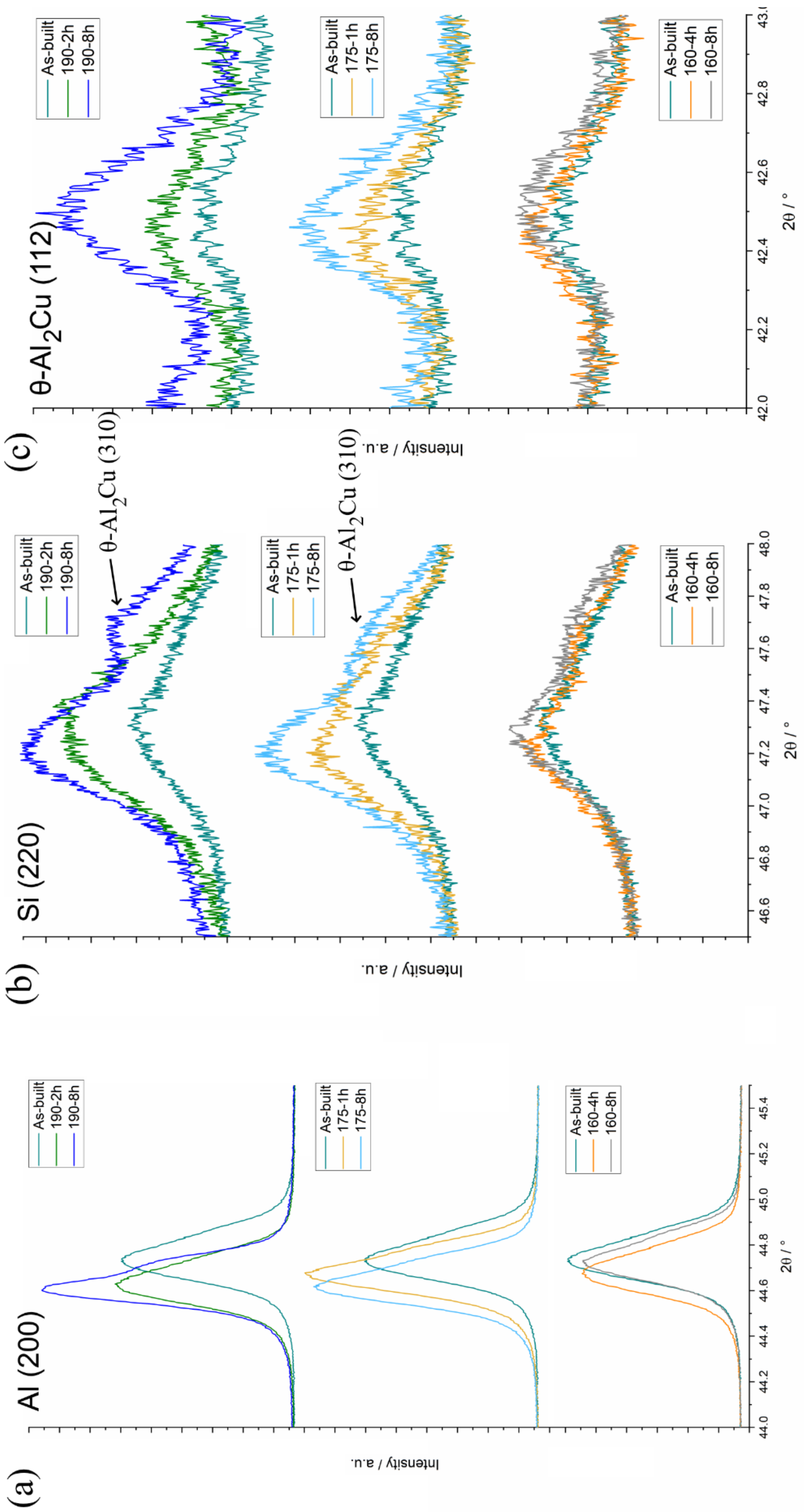

Fig. 89 Detail of (a) Al (200), (b) Si (200) and (c) (112) θ-Al_2Cu reflections.

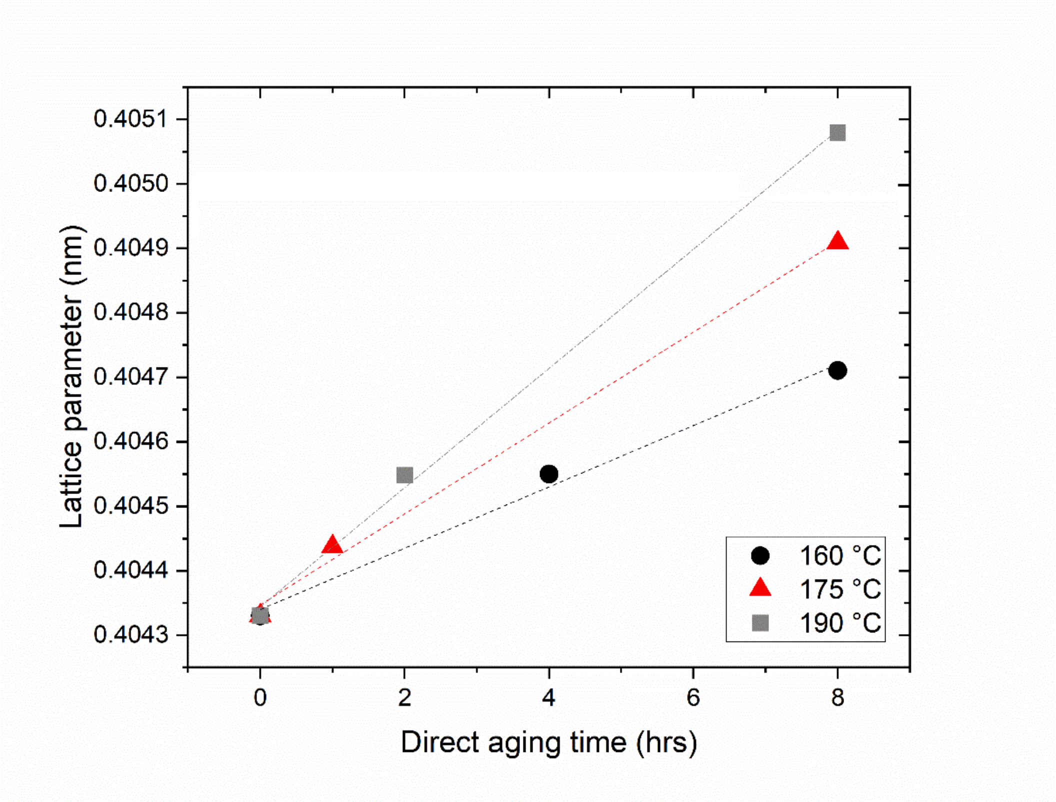

Fig. 90 Relationships between Al lattice parameter and the direct aging temperature.

4.3.3 Thermal behavior

In Fig. 91, the DSC scans of as-built and directly aged AlSi10Mg+4Cu specimens are reported.

As noticed in Section 3.3.2.4, the as-built sample showed two main exothermic peaks. The first one is centered at 238 °C, and it was associated with the precipitations of Si and θ'-Al_2Cu phase [308]. The second signal at 318 °C accounted for the formation of Mg_2Si and phases containing impurities [196,308]. The released enthalpies were 22.5 and 5.5 J/g, respectively.

After aging at 160 °C (Fig. 91a), the first exothermic signal slightly shifted at a higher temperature (~ 248 °C). Also, it must be pointed out that the peak intensity gradually decreased when increasing the aging time. Apart from the intensity variation, DSC scans did not show significant differences in the higher temperature range. Similarly, aging the alloy at 175 °C for 1 h reduced the first exothermic peak enthalpy from 22.5 to 12.9 J/g (Fig. 91b). However, after a direct aging time of 8 h, this peak completely disappeared, suggesting that Si and θ'-phase precipitation reactions already occurred during the direct aging heat-treatment. Finally, by further increasing the aging temperature to 190 °C (Fig. 91c), the first signal was still identifiable upon 2 h, although the released enthalpy was relatively low (~ 2.2 J/g), and then entirely disappeared after 8 h of direct aging.

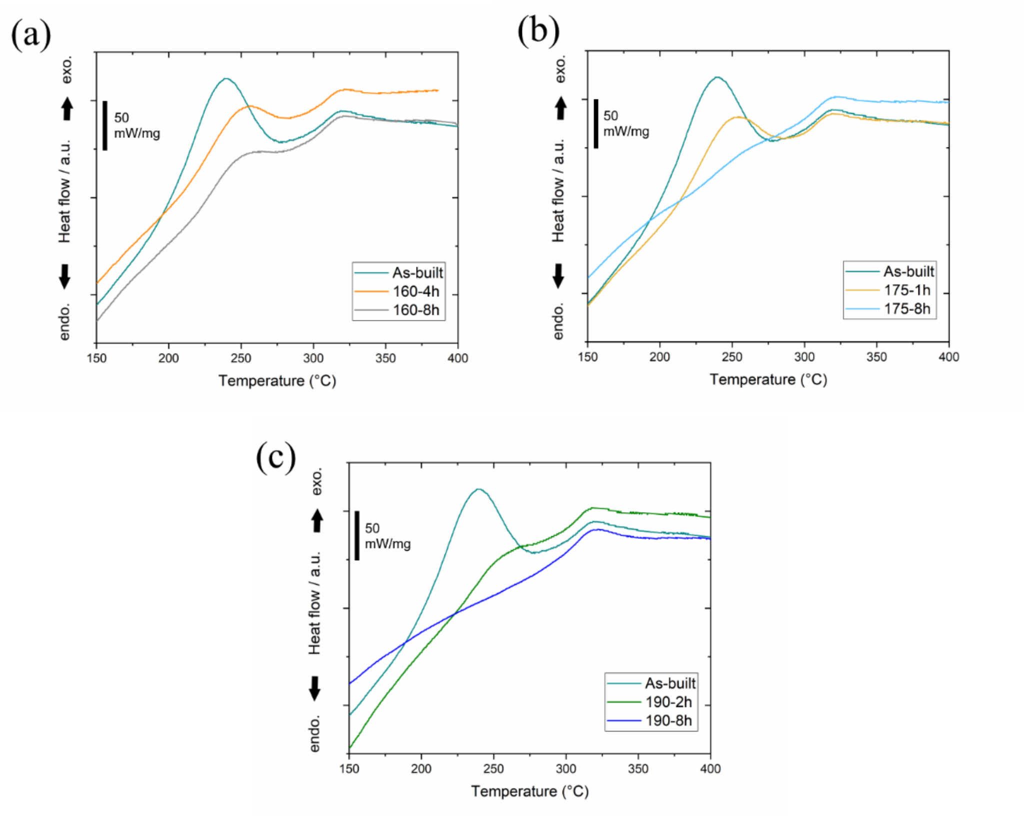

Fig. 91 Results of DSC scans performed on as-built and heat treated samples at (a) 160, (b) 175 and (c) 190 °C.

4.3.4 Microstructure

Fig. 92 reports the representative FESEM micrographs of AlSi10Mg+4Cu alloy before and after the direct aging heat-treatments. Prior to direct aging, as-built samples showed extremely fine α-Al cells surrounded by a fibrous eutectic architecture, as shown in Fig. 92a. The eutectic phase was constituted by Si particles intermixed with θ-Al_2Cu phase (see Section 3.3.2.2). Upon aging at 160 °C, microstructures of Fig. 92b,c did not show significant variations when compared to the as-built ones (Fig. 92a). By raising the aging temperature to 175 °C (Fig. 92d,e), the eutectic network was still identifiable. However, in Fig. 92e, it was noticed the presence of tiny particles within the α-Al cells, which likely precipitated out of the super-saturated solid solution during the aging heat-treatment. This was clearly observed after aging at 190 °C. In fact, micrographs in Fig. 92f,g were strewn with very fine precipitates randomly distributed on sample surfaces. Here, it must be also highlighted that the eutectic network was rather discontinuous likely due to the eutectic constitutive elements' diffusion through aging and the subsequent network spheroidization [216,228].

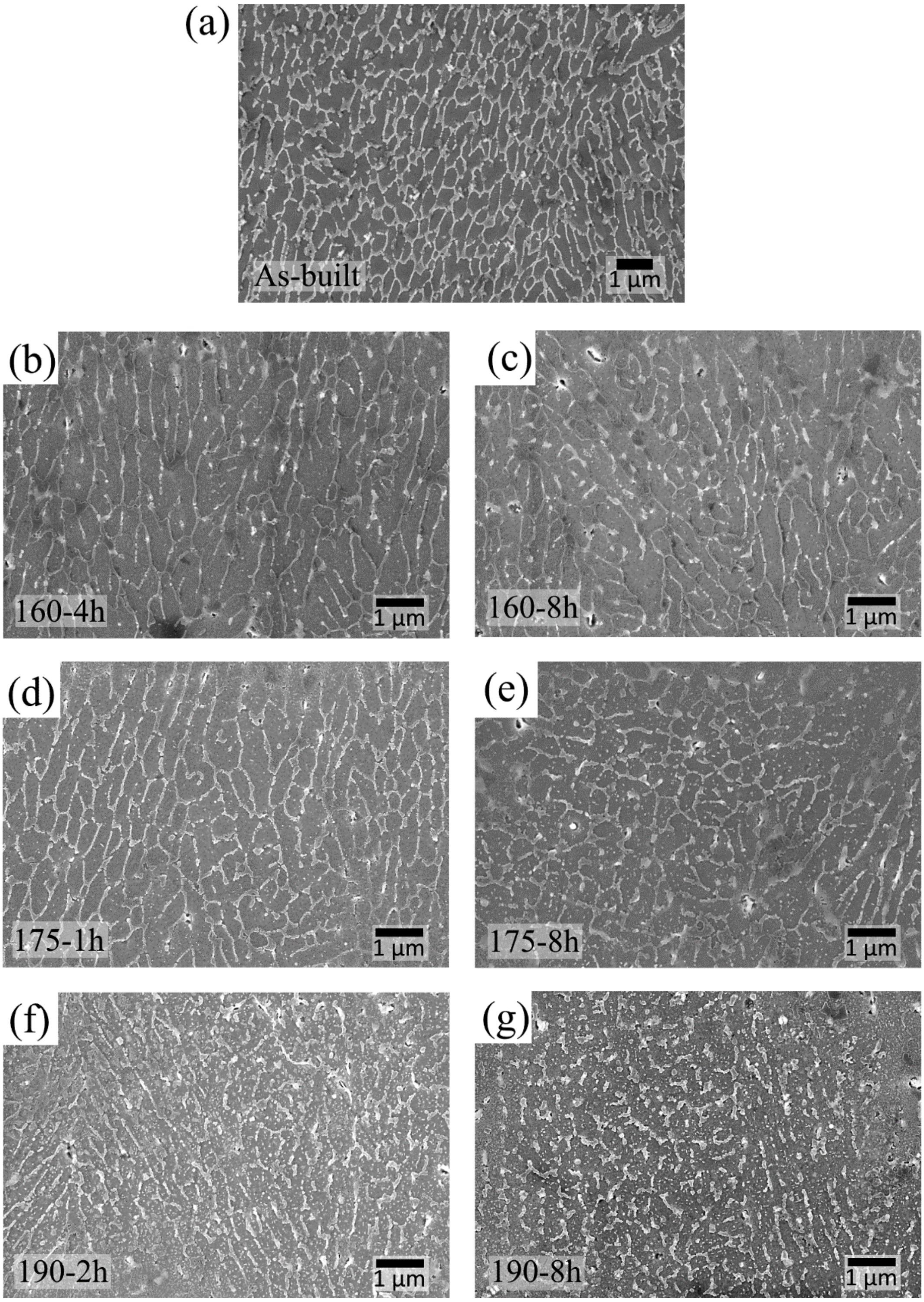

Fig. 92 The representative FESEM microstructures of (a) as-built and (b-g) directly aged specimens of AlSi10Mg+4Cu.

4.3.5 Tensile characterization and fracture analysis

Results of tensile tests conducted on the as-built (AB) and peak-aged AlSi10Mg+4Cu alloy are depicted in Fig. 93 and summarized in Table 18. The tensile curve of an as-built AlSi10Mg alloy produced by LPBF was reported for comparison. As can be noticed, the as-built AlSi10Mg+4Cu alloy shows higher yield strength (YS) and ultimate tensile strength (UTS) values compared to AlSi10Mg. In fact, by adding 4 wt.% of Cu to AlSi10Mg, an increment of YS and UTS of respectively 35 % and 19 % was achieved. However, the strengthening effect of Cu also induced a small ductility reduction from 3.3 % to 2.2 % (Table 18). As far as the peak-aged tensile curves of AlSi10Mg+4Cu are concerned, tensile curves were still higher than that of as-built AlSi10Mg but a slight decrease of YS and UTS was detected when comparing peak-aged curves with the AlSi10Mg+4Cu as-built ones (Fig. 93). Generally speaking, after directly aging the tensile samples to the peak-age, heat-treated specimens returned similar tensile behaviors. The premature failure for a tensile sample heat-treated at 175°C for 1 h was also noticed (see the red arrow in Fig. 93).

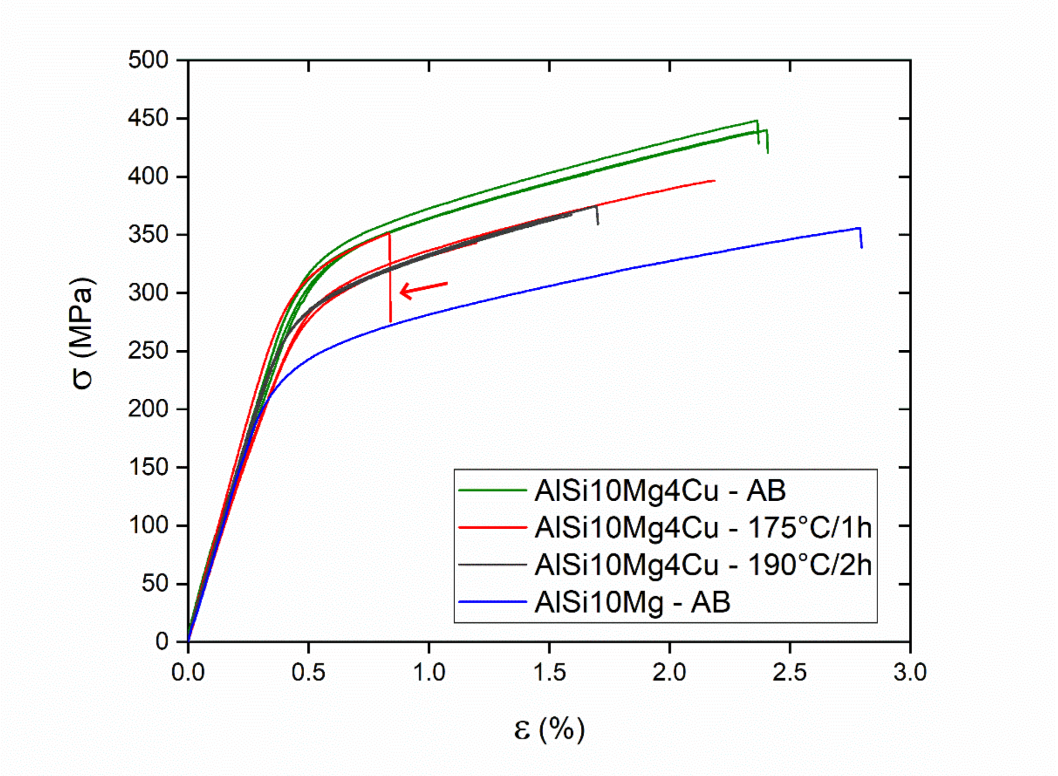

Fig. 93 Tensile curves of as-built and directly aged AlSi10Mg+4Cu samples. The tensile curve of an as-built AlSi10Mg specimen was reported as reference.

Table 18 Tensile test data for as-built and directly aged AlSi10Mg+4Cu and as-built AlSi10Mg.

	YS (MPa)	UTS (MPa)	ε (%)
AlSi10Mg4Cu - AB	339 ± 7	433 ± 4.6	2.19 ± 0.31
AlSi10Mg4Cu - 175°C/1h	314 ± 15	363 ± 28	1.4 ± 0.69
AlSi10Mg4Cu - 190°C/2h	301 ± 2.2	369 ± 4.6	1.6 ± 0.08
AlSi10Mg	250	362	3.3

Fracture surfaces of as-built and directly aged tensile samples were investigated by FESEM to figure out the prevailing failure mechanism. Before analyzing the results in more detail, it was observed that directly aged fracture surfaces resembled those of the as-built condition. Therefore, no significant differences were visible among the investigated tensile specimens.

The representative fracture surface topography of a tensile specimen was reported in Fig. 94a. A comprehensive observation of Fig. 94a revealed the presence of irregular and elongated cavities (pointed by black arrows), likely originated by lack-of-fusion regions between adjacent tracks or layers. Apart from these lack-of-fusion areas, fracture surfaces were dotted with several holes (pointed by red arrows) showing nearly spherical shapes. Fig. 94b provides a close-view of a spherical cavity, which exhibited a diameter of roughly 112 µm. A deep investigation inside the cavity evidenced the occurrence of brittle particles at the bottom, presumably oxides, and, occasionally, the presence of un-melted particles. By further increasing the magnification, it was possible to appreciate the nature of the failure micro-mechanisms. As can be observed in Fig. 94c, a combination of brittle and ductile fractures was locally found. In fact, a brittle area with a facet-like appearance likely originated from a cleavage fracture coexisted with a more ductile area, which showed very fine dimples with a size lower than 1 µm (see Fig. 94d). A close-view of the ductile region revealed the occurrence of nanometric precipitates within dimple cells as can be seen in Fig. 94e. These precipitates were observed both in as-built and directly aged specimens.

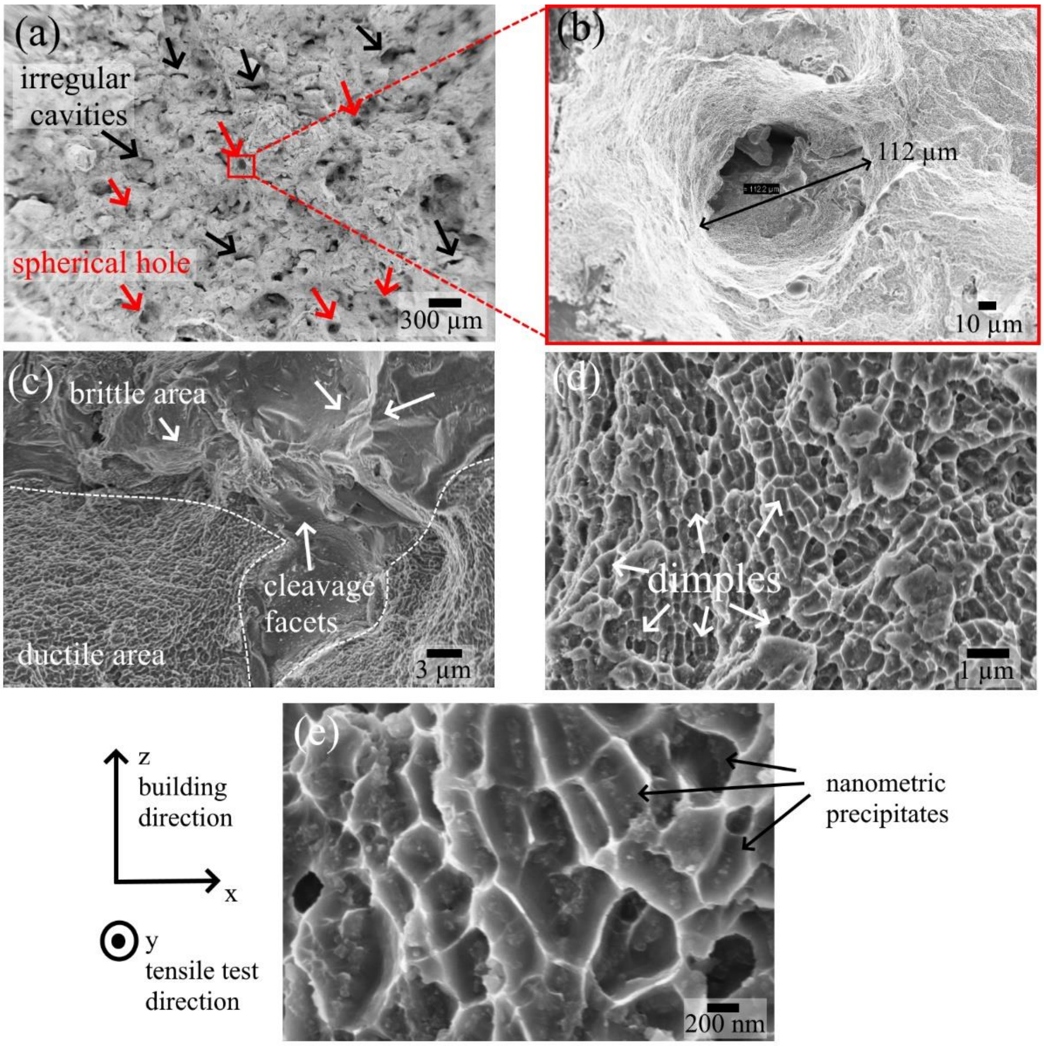

Fig. 94 (a-e) Representative micrographs of the FESEM investigation performed on the fracture surfaces of as-built and directly aged AlSi10Mg+4Cu specimens.

After FESEM investigation, EDS analyses were performed on the fracture surfaces to investigate the origins of the ductile-brittle areas visible in Fig. 94c. The compositional maps of Fig. 95 suggested that the investigated area was mainly constituted by Al, Si, and Mg, which indeed are the main chemical elements of AlSi10Mg+4Cu alloy. Moreover, brighter spots identified as pure Cu were embedded in the matrix. They could be powder particles of Cu not completely fused during LPBF. Finally, patches of oxygen were revealed in correspondence with the brittle facets indicated in Fig. 95.

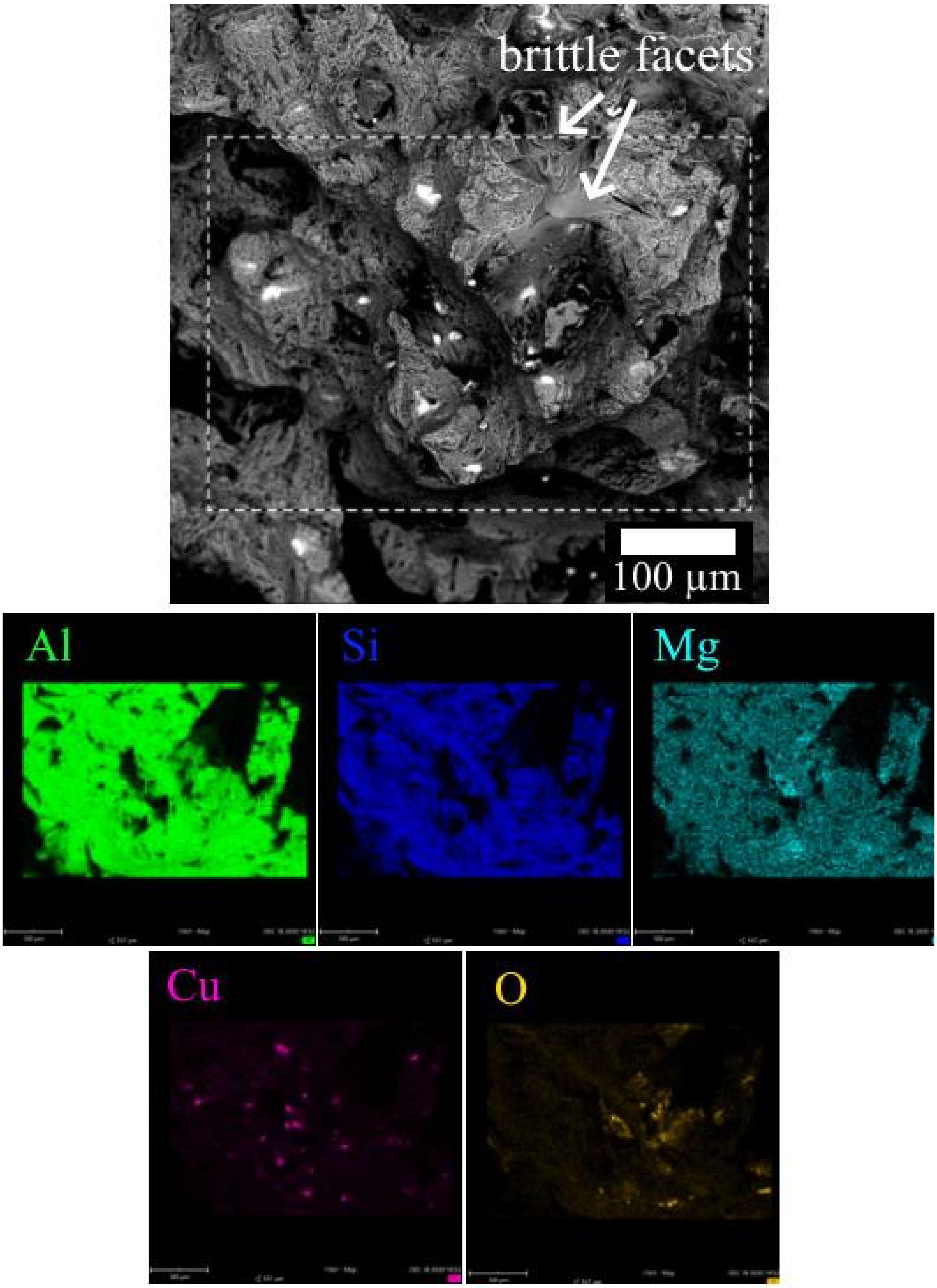

Fig. 95 Results of an EDS analysis conducted on a local area of the fractured surface.

4.4 Discussion

4.4.1 Hardness response and constitutional phase evolution during direct aging

LPBF has shown to be a unique additive manufacturing technique that develops very high heating and cooling rates (10^3-10^8 K/s) during the process [189]. These physical phenomena typically lead to the formation of extremely fine microstructures, metastable phases, and enhanced solid solubility, making possible to tailor novel alloy compositions for LPBF [224]. In this regard, Polmear et al. reported the solid solubility extension of the main Al solute elements in samples produced by rapid cooling techniques [200,204]. For instance, they showed how the solubility limit of Cu can be pushed to 42 wt.% in metastable conditions starting from the 5.65 wt.% reached at the equilibrium after a slow cooling process [204]. Hence, in this work, 4 wt.% of Cu powder was added to a commercial AlSi10Mg alloy in order to achieve a high super-saturated solid solution level after LPBF. Then, the precipitation potential of the as-built AlSi10Mg+4Cu samples was fully exploited by direct aging the alloy in order to increase its hardness.

By heating the alloy at temperatures between 160 and 190 °C, the age-hardening process occurred to a different extent based on the used aging temperature (Fig. 87). As can be noticed from the aging behaviors in Fig. 87, a limited hardening response was achieved at 190 °C, whereas higher strengthening was obtained at the lower temperatures, i.e. 160 °C and 175 °C. Generally speaking, this is in good agreement with what has been observed so far by heat-treating age-hardenable Al alloys [211,225]. However, former works also demonstrated that the higher the aging temperature, the lower is the peak-age time and its hardness intensity. Therefore, according to this, both peak-age time and hardness values detected in this work should increase in the order: 190 °C < 175 °C < 160 °C. This was ascribed to the fact that, by keeping the aging temperature below the metastable solvus line for the formation of GP zones, i.e. in the range of 140-160 °C for Al-Si alloys [223,225], the full precipitation sequence is exploited and, consequently, a delayed peak-age with higher hardness can be reached.

A detailed examination of results in Table 17 revealed two discrepancies with the afore mentioned criteria. First, aging at 160 °C did not show a hardness peak within the investigated time interval. On this point, it was thought that the peak-age condition might occur at a higher aging time, i.e. beyond 8 h. Still on this, aging at 160 °C should allow the nucleation of coherent metastable phases such as β''-Mg_2Si, θ'-Al_2Cu and Q''-$Al_5Mg_8Si_6Cu_2$ [312,326], thus reaching the highest hardening response among the tested aging temperatures. Second, the peak-age at 190 °C was reached at a higher aging time (2 h) than that of 175 °C (1h). In this case, it might be possible that the peak-age condition for 190 °C was already attained at aging time lower than 1 h. This would be in line with the theory that heat-treating beyond the GP zone solvus line might not have allowed a complete precipitation sequence leading to a poor an untimely hardening response.

To investigate these different hardening behaviors, the evolution of the constitutional phases of AlSi10Mg+4Cu during direct aging was assessed by coupling XRD, DSC, and FESEM results. Prior aging, as-built specimens exhibited a fibrous eutectic architecture formed by Si precipitates intermixed with θ-Al_2Cu phase, surrounding extremely fine α-Al cells (Fig. 92a). Despite the presence of Si and Al_2Cu precipitates in the as-built condition, it was demonstrated that Si and Cu atoms were still largely trapped into the *fcc*-Al lattice owing to the severe constitutional undercooling induced by LPBF (see Section 4.3.2). Therefore, this high grade of super-saturation provided a great driving force for Si and Cu solutes diffusion and nucleation of metastable phases [222].

By heating the alloy at the investigated aging temperatures, the precipitation process started with the diffusion of Si and Cu atoms within the α-Al matrix [216]. Apart from the heat given by the furnace, diffusion of solutes was accelerated by the high concentration of vacancies induced by the fast cooling, and, consequently, the nucleation of metastable phases occurred rapidly [222]. This was corroborated by the sudden reduction at short aging times of the released enthalpy associated with the precipitations of Si and the metastable θ'-Al_2Cu phase (see DSC scans of Fig. 91).

As the nucleation and growth of Si and Al_2Cu precipitates proceeded, the degree of super-saturation decreased accordingly, as proved by the increment of the Al lattice parameter with the direct aging time in Fig. 90. It was recently demonstrated by the Authors' previous work [308] that Si and Cu solutes contributed with a different efficacy to shrink the Al lattice constant of the as-built AlSi10Mg+4Cu alloy (Section 4.3.2). Therefore, as the aging time went by, the progressive diffusion of Si and Cu atoms from SSSS, and the consequent nucleation and growth of Si/Al_2Cu precipitates, induced a linear increase in the Al lattice parameter (Fig. 90). Solutes diffusion was found to be strictly related to the direct aging temperature [211]. Hence, the higher the aging temperature, the faster is the solutes diffusion from SSSS and, then, the nucleation of secondary phases containing Si and Cu.

The solutes diffusion dependence on the aging temperature can help to rationalize the different peak-age conditions achieved in Fig. 87. The adoption of temperatures relying on the low range of the age temperature interval for Al-Si alloys [225], such as 160 °C, enabled a slow solutes diffusion and a gradual and delayed hardening (Fig. 87). For this reason, it is thought that the alloy heat-treated at 160 °C did not yet completely reached the peak-age condition within the investigated time interval. This can be primarily explained by the fact that XRD reflections of Fig. 89 did not show significant changes in the intensity of Si (200)/θ-Al_2Cu (112) peaks, or shift to lower angles of Al (200) peak by increasing the direct aging time. Moreover, in line with our assumption, the work of

Roudnická et al. showed that the peak-age condition for an SLM*ed* AlSi9Cu3 alloy aged at 160 °C was reached at around 10 h, i.e. beyond the upper limit of our heat treatment time interval [324].

By increasing the aging temperature to 175 °C, a peak-age of 163 HV was achieved only after 1 h of aging time (Table 17). In this case, it is likely probable that Cu and Si atoms diffused rapidly from SSSS forming Si and a mix of $\theta''/\theta' + \theta$-Al$_2$Cu precipitates. Si and θ-Al$_2$Cu precipitations were confirmed by the more intense Si (200) and θ-Al$_2$Cu (112) reflections at 175 °C/1h when compared to the as-built ones (Fig. 89a-c). Instead, the lesser intense but still present exothermic peak of Si and θ' precipitations in the DSC scan measured for the sample aged at 175°C/1h could indirectly give the clue for the presence of a pre-existing θ' phase or, eventually, pioneers transition phases such as θ'' (Fig. 91b). Apart from the contribution of these precipitates to the overall hardness, it must be noted that, after 1 h at 175 °C, there still was a certain amount of solutes within the matrix, which brought a further strengthening by solid solution (see the lattice parameter value for 175 °C/1h in Fig. 90). Therefore, in this case, the proper balance between solid solution and precipitation strengthening mechanisms allowed to achieve the maximum hardness within a limited aging time.

By further increasing the aging temperature to 190 °C, the solutes diffusion and nucleation was further speed-up. Under this condition, since the applied aging temperature relies on the high range of the aging temperature interval [225], the formation of metastable phases θ''/θ' might have skipped or, whether they precipitated, quickly formed to a lower extent. In fact, the exothermic signal of Si + θ'-Al$_2$Cu was barely identifiable after just 2 h at 190 °C, thus pointing to an untimely formation of the stable θ-Al$_2$Cu phase (Fig. 91c). Furthermore, as can be deduced from Fig. 92f, Si and Cu solutes precipitated out from the eutectic breaking the fine network and forming idiomorphic precipitates. Considering also the appearance of minor reflections of Si and θ-Al$_2$Cu phases in the XRD results of samples aged at 190 °C (Fig. 88), it can be reasonable to conclude that these precipitates were mostly Si and θ-Al$_2$Cu particles. All these considerations can explain the lower strengthening reached by aging AlSi10Mg+4Cu at 190 °C (Fig. 87).

4.4.2 The superior tensile strength of AlSi10Mg+4Cu samples

As for hardness results of Fig. 87, the tensile properties of as-built and directly aged AlSi10Mg+4Cu samples were superior to the AlSi10Mg ones (Fig. 93). As can be deduced from Table 18, as-built AlSi10Mg+4Cu showed an increment of YS and UTS of respectively 35 % and 19 % with respect to the AlSi10Mg alloy. The improved strength of AlSi10Mg+4Cu can be entirely ascribed to the addition of Cu being both alloys processed by using the same LPBF machine and their optimum process parameters [196,308,327]. In this regard, it is thought that the presence of Cu had a beneficial effect on the alloy strengthening mechanisms. Previous works in literature, indeed, expressed the overall strength of Al alloys as the superimposition of the following contributing mechanisms [206,324]:

$$\sigma_{YS} = \sigma_{GBS} + \sigma_{sss} + \sigma_{PS} \tag{4.2}$$

where σ_{YS} is the yield strength of the alloy, σ_{GBS} the contribution of the grain boundary strengthening, σ_{sss} the contribution associated with the super-saturated solid solution, and σ_{PS} the contribution from precipitation strengthening.

The first contribution to the overall strength of as-built AlSi10Mg+4Cu was ascribed to the fine eutectic network obtained after rapid cooling (σ_{GBS}) (see Fig. 92a). However, since the mean size of α-Al cells in AlSi10Mg+4Cu was of the same order of magnitude of the as-built AlSi10Mg [196,308], this contribution did not justify the strength increment observed in AlSi10Mg+4Cu samples.

Among the various strengthening mechanisms, it was highly probable that σ_{sss} mainly contributed to increasing the strength of as-built AlSi10Mg+4Cu alloy. Under the assumption that the Si supersaturation content of AlSi10Mg+4Cu was similar to that of the master AlSi10Mg alloy [196], Cu atoms in solid solution induced an extra-distortion of *fcc* α-Al lattice, thus producing additional residual strains (Fig. 90). As a consequence, the dislocations motion could be effectively hindered by these solute-induced residual strains and the strength of the alloy could increase accordingly.

Apart from solutes strengthening, dislocations slip was also pinned by disseminated θ-Al_2Cu precipitates detected by XRD in as-built samples (Fig. 88), thus giving a further strengthening by precipitation (σ_{PS}). However, it must be highlighted that the specific contribution of the θ phase to the overall strength was limited since θ is typically characterized by a body-centered crystal structure, which is incoherent with the *fcc*-Al lattice [213]. As explained in Section 2.2.2.4, the higher strengthening contribution is achieved when gliding dislocations are forced to go through coherent precipitates. In this work, we did not clearly detect coherent transitions phases [211], but the exothermic signals associated with θ'-Al_2Cu and β-Mg_2Si precipitations in Fig. 91 could point to the presence of their pioneer transition phases (GP/θ''/θ'- Al_2Cu and GP/β''/β'- Mg_2Si) already in the as-built condition.

By directly aging AlSi10Mg+4Cu samples to the peak-age, a slight reduction of YS and UTS values can be noticed when they are compared to those before heat-treatment (Fig. 93). In this regard, it should be also noted that the alloy strengthening generally increases after direct aging heat-treatments as demonstrated by the direct aging hardness curves of Fig. 87. Therefore, higher YS and UTS values compared to the as-built ones were expected upon aging. Instead, the tensile results of Fig. 93 turned out the opposite. The reason for this is currently under investigation and further work should be done to completely address this point. However, the directly aged mechanical properties of

AlSi10Mg+4Cu were still much higher than AlSi10Mg counterparts, pointing that the additional strengthening contributions of Cu were still effective upon aging.

The reduction of YS and UTS might be caused by a change in the strengthening contribution mechanisms upon direct aging [206]. Starting from the evaluation of the grain size contribution (σ_{GBS}), FESEM microstructures of Fig. 92 suggested that the fineness of α-Al cells was preserved after aging heat-treatments. This was confirmed by the similar α-Al cell size values measured on the as-built (Fig. 92a) and directly aged micrographs (Fig. 92b-g), i.e. respectively of 0.8 ± 0.4 µm and 0.7 ± 0.5 µm. Therefore, the change in σ_{GBS} contribution with the direct aging can be considered negligible. Under this assumption, the decrease of YS and UTS can be attributable to a change of σ_{SSS} and σ_{PS} contributions after direct aging.

As pointed by the Al lattice constant values of Fig. 90, direct aging enhanced the solutes diffusion within Al matrix causing the relaxation of Al lattice. Thus, the σ_{SSS} contribution progressively decreased with increasing the aging temperature and time. At this point, the reduction of σ_{SSS} contribution should be counterbalanced by the precipitation strengthening mechanism. In line with this concept, the higher presence of Si and θ-Al_2Cu precipitates detected in the directly aged samples suggested an increment of σ_{PS} contribution after aging (Fig. 89). However, to properly quantify the amount of σ_{PS}, it is fundamental to consider also the size and the distribution of β/θ- nano-precipitates (Section 2.3.1). Therefore, future research works should be done to completely address this aspect and explain the reduction of YS and UTS after direct aging.

4.4.3 Fracture mechanisms

The representative features of the fracture surfaces of the as-built and directly aged AlSi10Mg+4Cu samples were reported in Fig. 94 and Fig. 95. As mentioned in Section 4.3.5, no significant differences were observed among the different samples. All the low-magnification topographies showed some irregular cavities stemming from lack-of-fusion porosities present in bulk samples, traces of oxides, and the occurrence of partially melted Cu particles (Fig. 94a,b and Fig. 95). This evidence suggested that the nucleation of the failure might have been located in correspondence with such defects. Moreover, all samples exhibited fracture surfaces strewn of several holes (Fig. 94a,b) with diameters of a size comparable to the laser scan track width (Section 3.3.1.1). It was also noticed that these defects were oriented along the Y direction, which was adopted as tensile direction during tensile tests (Fig. 94a,b). Therefore, considering that tensile samples were built on the XY plane and tested along the Y direction (Fig. 86, Fig. 94), these empty holes could have been originated from the detachment of laser scans aligned along the tensile direction. This assumption is consistent with the macro-fracture mechanism proposed by Rosenthal et al. for an as-built AlSi10Mg alloy produced by LPBF [242,328]. According to their theory, once the crack was randomly nucleated on the XZ surface of tensile samples, the crack propagated along the Z direction by cutting perpendicularly the pile-up layers. However, whenever a laser scan aligned favorably to the tensile direction was encountered, the crack propagation deviated around the track boundary instead of going through its core, thus leaving several empty cavities on the fracture surfaces (Fig. 94a,b).

Apart from the influence of laser scan tracks orientation, the crack propagation depended on the specific fracture mechanisms occurring at the microscopic scale [329]. Fig. 94c revealed the presence of a ductile-brittle fracture in AlSi10Mg+4Cu samples. This suggested that the crack propagation mainly accounted for two competing fracture micro-mechanisms [329]. On the one side, the crack propagation was likely promoted by the nucleation, growth, and coalescence of several micro-voids formed around nanometric precipitates as the ones identified in Fig. 94e. This micro-mechanism was predominantly ductile and led to the progressive formation of fine dimples (Fig. 94d). On the other side, the crack rapidly propagated by cleavage owing to the breakage of atomic bonds on specific crystallographic directions, which in turn induced the formation of cleavage facets (Fig. 94c). In this regard, it was highly probable that a brittle cleavage fracture occurred when the crack went through un-melted Cu particles or oxide skins (Fig. 95). This latter mechanism does not require plastic deformation and, therefore, it can rationalize the overall ductility reduction of AlSi10Mg+4Cu samples compared to AlSi10Mg alloy (Table 18).

From the previous findings, it can be inferred that the failure mode of AlSi10Mg+4Cu involves both ductile and brittle mechanisms [329]. Therefore, the higher the amount of brittle particles (un-melted Cu, oxides) or precipitates (residual Si) encountered by the crack during propagation, the less ductile is the tensile behavior of the alloy. This could partially explain the slightly lower elongation obtained upon direct aging (Table 18). In this context, we must reiterate that direct aging promoted the diffusion of Si from SSSS and, consequently, a higher residual Si was detected within the directly aged samples (Fig. 89b). Then, after direct aging, it might be possible that the crack propagation was further enhanced by the brittle skeleton of Si particles [83], besides the presence of un-melted Cu particles and oxides.

4.5 Summary and conclusions

In this chapter, the direct aging (T5 temper) was employed to fully exploit the precipitation potential of AlSi10Mg+4Cu samples without the need for previous solution heat-treatment.

By heating the alloy at temperatures between 160 and 190 °C, it was found that the age-hardening process was strictly dependent on the aging temperature. The maximum hardness increment was achieved by holding the as-built samples for 1 h in a furnace heated at 175 °C.

The microstructural and compositional evolution of AlSi10Mg+4Cu during direct aging was then tracked by coupling FESEM, XRD and DSC analyses and correlated to the hardness response. Generally speaking, the higher was the aging temperature, the faster was the diffusion of Cu and Si solutes from SSSS and, consequently, the nucleation of secondary phases, such as Si and θ-Al_2Cu precipitates. Aging at 160 °C enabled a slow solutes diffusion and a gradual and delayed hardening up to 160 HV without finding significant variations in XRD and DSC signals. By increasing the aging temperature to 175 °C, a mix of $\theta''/\theta' + \theta$-$Al_2Cu$ precipitates and Si phase returned the highest hardness (163 HV) at the peak-age (175 °C, 1h). Lastly, it was observed that a further increment of the aging temperature to 190 °C speeded-up the formation of the coherent θ-Al_2Cu phase achieving a lower hardening level.

The mechanical properties of as-built and directly aged samples of AlSi10Mg+4Cu were assessed via tensile tests. A superior tensile strength was obtained for AlSi10Mg+4Cu whether compared to AlSi10Mg alloy. This strength increment was attributable to the effect of Cu on the alloy strengthening mechanisms, mainly on the solid solution (σ_{SSS}) and precipitation strengthening (σ_{PS}) contributions.

Finally, the FESEM investigation on fracture surfaces of AlSi10Mg+4Cu revealed the presence of a ductile-brittle fracture in both as-built and directly aged specimens. The ductile fracture occurred primarily via nucleation, growth, and coalescence of voids, which likely formed near nanometric precipitates. On the other hand, the brittle facture was primarily ascribed to a cleavage mechanism through un-melted Cu particles and oxides skins.

Chapter 5

Manufacturing large-scale components of AlSi10Mg by LPBF

The content of this chapter is based on the following article:

- F. Bosio, H.P. Shen, Y. Liu, M. Lombardi, P. Rometsch, X.H. Wu, Y.M. Zhu, A.J. Huang, Production strategy for manufacturing large-scale AlSi10Mg components by Laser Powder Bed Fusion, JOM (2021), doi.org/10.1007/s11837-020-04523-8.

5.1 Introduction

The manufacturing of large-scale components by LPBF requires printing machines providing a high building volume. Therefore, since the majority of LPBF systems are equipped with a limited building chamber volume, producers have recently introduced to the market LPBF machines specifically designed for building large components. For example, the X Line 2000 R machine of GE Additive is endowed with a build volume of 800×400×500 mm^3, increasing six times the building volume of the previous Laser M2 Series 5 system [330,331].

Apart from the used LPBF system, manufacturing of large aluminum components involves crucial challenges to tackle before the production. In fact, the rapid solidification inevitably produces part bending, cracks, and distortions of supports that might cause the job failure [332]. Besides, the production of large components needs for long printing periods since LPBF is regarded as a slow process compared to the conventional foundry techniques [42]. Therefore, defects induced by internal residual stresses must be prevented to save powder and time. In this context, previous researches have proved that heating the building platform is an effective strategy to alleviate internal residual stresses and, thus, the deformation of components [333,334]. The main reason behind this was ascribed to the reduction of the solidification shrinkage thanks to the reduced thermal gradient during cooling (Section 1.5.2) [78,333].

Other than residual stress-related issues, it must be considered that platform heating can induce an *in-situ* age-hardening response of the Al alloy, if it belongs to the Al-Si age-hardenable alloys [225]. Hence, given that the manufacturing of large parts requires high printing time, there is the risk of an incipient over-aging. Recent works investigated the effect of the heated building plate on the microstructure and thermo-mechanical properties of Al-Si alloys [221][26][80]. Aversa et al. conducted differential thermal analysis (DTA) experiments on as-built specimens of A357 produced with an increased building platform heating [221]. Their results showed a decreased intensity of the thermal peak associated with Mg_2Si precipitates by increasing the heating platform temperature. The Authors attributed this phenomenon to the probable *in-situ* aging caused by heating the platform during printing. This hypothesis was in good agreement with the feeble differential scanning calorimetry (DSC) response of an AlSi10Mg alloy processed with a platform heated at 160 °C by Casati et al. [26]. In this study, Casati and co-workers advanced the idea that *in-situ* aging might depend on the elapsed time above the heated platform, the part volume, and the position along with the height of the investigated component. Nevertheless, they did not found any clear signals of age-hardening by studying the hardness profile of a cylindrical bar built at 160 °C. Recently, Rao et al. observed *in-situ* precipitation of nano-sized Si particles within A357 samples produced by heating the building platform at 80 °C [80]. Samples exhibited decent tensile properties. However, a relatively low hardness was found in both as-built and directly aged conditions, presumably owing to a reduced contribution of the solid solution strengthening. Besides, Buchbinder et al. investigated the impact of various platform heating temperatures on the distortions of AlSi10Mg cantilevers produced by SLM [25]. The Authors concluded that a platform heated at 250 °C was able to entirely prevent cracks and distortions, although quite low hardness (≈ 80 HV) was revealed. It is worth noting that this hardness impoverishment could be further exacerbated by the long holding time spent by the production of large components on the heated platform. Therefore, further research is desirable to tackle this issue.

In this chapter, two crucial design aspects involving the production of large aluminum components are addressed simultaneously (Fig. 96). The first aspect is the prevention of cracks formation and support distortions. To this purpose, varied platform heating temperatures were investigated and, then, the platform temperatures able to mitigate residual stresses were determined. The second aspect is the evaluation of the *in-situ* aging likely caused by the heated building platform. In this regard, the production of samples with heating temperature of 150 °C showed that *in-situ* aging is correlated with the holding time above the hot platform and the position along the building direction. Furthermore, the holding time limit to prevent *in-situ* over-aging at 150 °C is established. Lastly, by using a platform heating of 200 °C, it is shown that over-aging takes place during printing. A possible remedy to the *in-situ* overaging is explored by performing a T6-like heat-treatment after production.

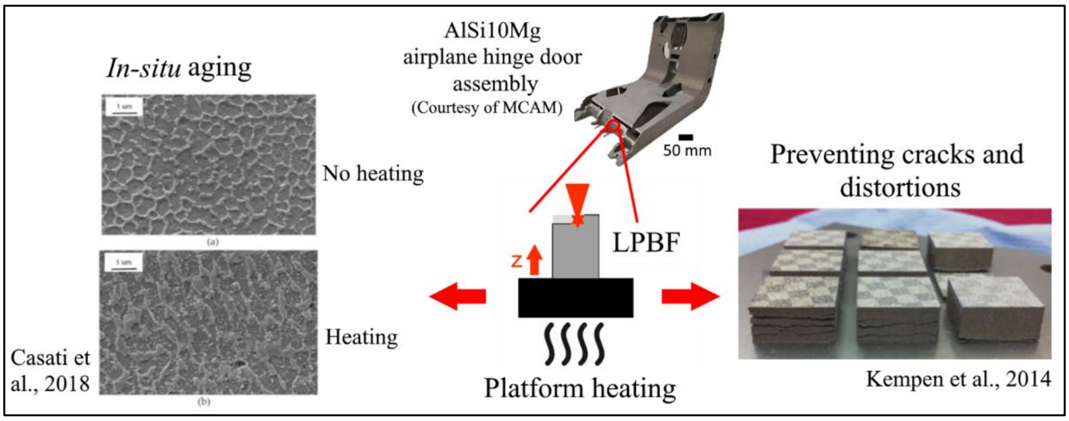

Fig. 96 The two aspects to be considered for the production of large aluminum parts via LPBF: prevention of cracks and distortions, and *in-situ* aging.

5.2 Materials and Methods

5.2.1 Powder and LPBF manufacturing

In this work, pre-alloyed gas-atomized powder of AlSi10Mg was employed (TLS Technik GmbH, Germany). Table 19 provides the chemical composition of the used powder. Metals elements were detected by direct current emission spectroscopy according to ASTM E 1097-12. Nitrogen and Oxygen were measured through inert gas fusion according to ASTM E 1019-11 standard. AlSi10Mg powder was firstly investigated by a Field Emission Gun Scanning Electron Microscope (FEGSEM) JEOL JSM-7001F to evaluate particle morphology. The laser diffraction analysis technique was then employed to measure the powder size distribution (PSD) by using a Malvern Mastersizer 2000 granulometer. The PSD curve was calculated by adopting the volumetric assumption. AlSi10Mg particles in Fig. 97 showed a spherical shape, although the presence of some irregularities, such as elongated particles, satellites, and, occasionally, particle agglomerates. Particles diameters corresponding to 10% (d_{10}), 50% (d_{50}) and 90% (d_{90}) of the cumulative PSD are, respectively, 18.2, 34.1, and 59.6 µm (Fig. 98).

Table 19 Chemical composition of the employed AlSi10Mg powder.

Element	Si	Mg	Fe	Ti	Ni	O	N	Al
wt %	10	0.49	0.17	0.014	0.005	0.091	< 0.001	Bal.

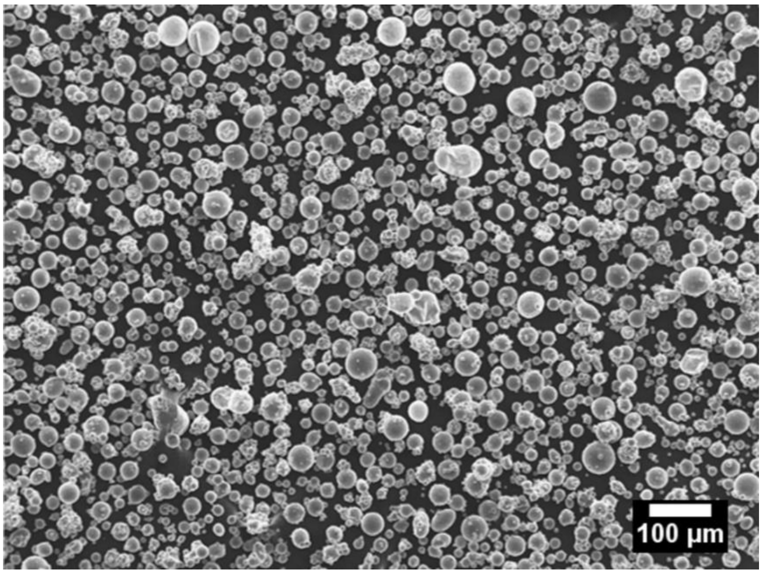

Fig. 97 Representative FEGSEM micrograph of AlSi10Mg powder provided by TLS Technik.

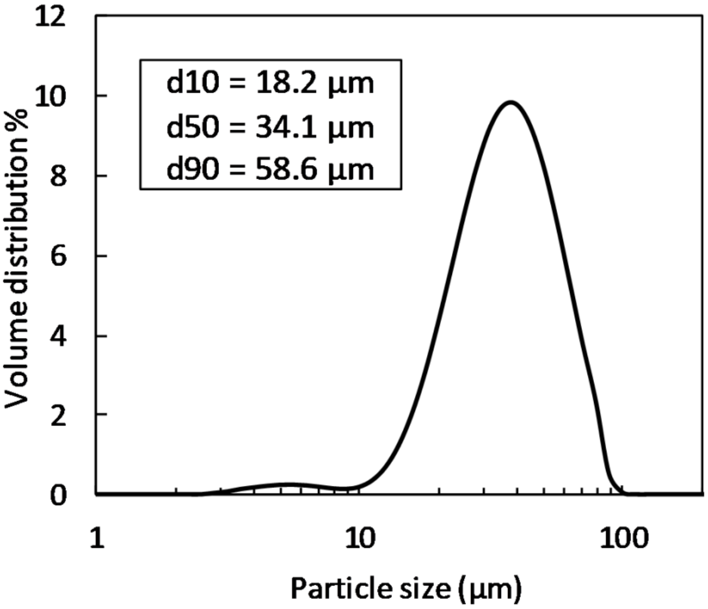

Fig. 98 The PSD curve calculated adopting the volumetric assumption.

An EOS M290 LPBF system (EOS Gmbh) was used to process AlSi10Mg powder. This system is equipped with a Yb-fiber laser with a wavelength of 1060-1100 nm, a laser spot of 100 µm, maximum nominal power of 400 W, and a scanning speed up to 7000 mm/s. The processing chamber was flushed with Ar to keep the oxygen level below 0.1% and to reduce the oxidation during manufacturing [125]. The specimens produced in this work were manufactured using the process parameters of Table 20. Process parameters were previously optimized by LPBF technicians at Monash Centre for Additive Manufacturing (MCAM). A value of 30 µm for the powder layer thickness was used considering the d_{50} value of PSD curve. A rotated scanning strategy (67°) was used to achieve more isotropic properties in the XY plane [46]. The building platform was heated to evaluate the impact on cracks/distortions and the *in-situ* aging of AlSi10Mg. It is worth noting that this strategy was not a simple platform pre-heating before manufacturing, but the platform was set at a fixed heating temperature (*T*) throughout the whole printing time. The uniformity of the temperature on the heated building platform was measured on 25 positions using a surface thermometer (TESTO 905-T2), revealing *T* fluctuations below 1 °C. The investigated temperatures were selected according to reference works in the literature of Al alloys [26,56,80,221]. The density of manufactured samples was determined via image analysis. Twenty micrographs were processed to calculate the average porosity. Results showed an average density of about 99.84 ± 0.15 %.

Table 20 Main process parameters adopted to manufacture AlSi10Mg specimens. (*) platform temperature without heating.

Laser power	370 W
Scanning speed	1300 mm/s
Hatching distance	0.17 mm
Spot size diameter	100 μm
Powder layer thickness	30 μm
Scanning strategy	Rotating - 67°
Building platform temperature, *T*	45^*, 100, 150, 200 °C

5.2.2 Cracks and distortions evaluation

The inevitable intrinsic residual stresses that arise during the progressive consolidation of layers lead to the severe distortions of supports, and the occurrence of cracks [74]. This is of particular importance when large components are produced by LPBF owing to the high volume of printed material. To alleviate these phenomena, heating the building platform during printing has been adopted as a preventive procedure over the years [25,81]. Thus, to have a safer route in the production of large-scale AlSi10Mg components, the impact of varied platform heating temperatures on the presence of cracks and distortions was studied at first. To this end, it was adopted the ‘twin cantilever’ method used in a previous research by Buchbinder et al. [25].

Therefore, cantilever samples with 3 mm of thickness and twin arms of 50 mm were produced using the fixed heating temperatures (Table 20). Afterward, the surface profiles were recorded by a CNC coordinate measuring machine (CRYSTA-Apex S700) with an accuracy of 1.7 μm in order to calculate the reference baseline (Fig. 99a,b). Then, specimen supports were cut near the building platform via electric wire. After the supports removal, all cantilever profiles were measured again to determine the extent of the arm deflection. The profile measurements were automatically performed using an *x*-step of 1 mm. For each heating temperature, five profiles were considered to calculate the overall deflection curve. In the end, the platform heating temperatures that returned the low extent of deflection were used for the *in-situ* aging study.

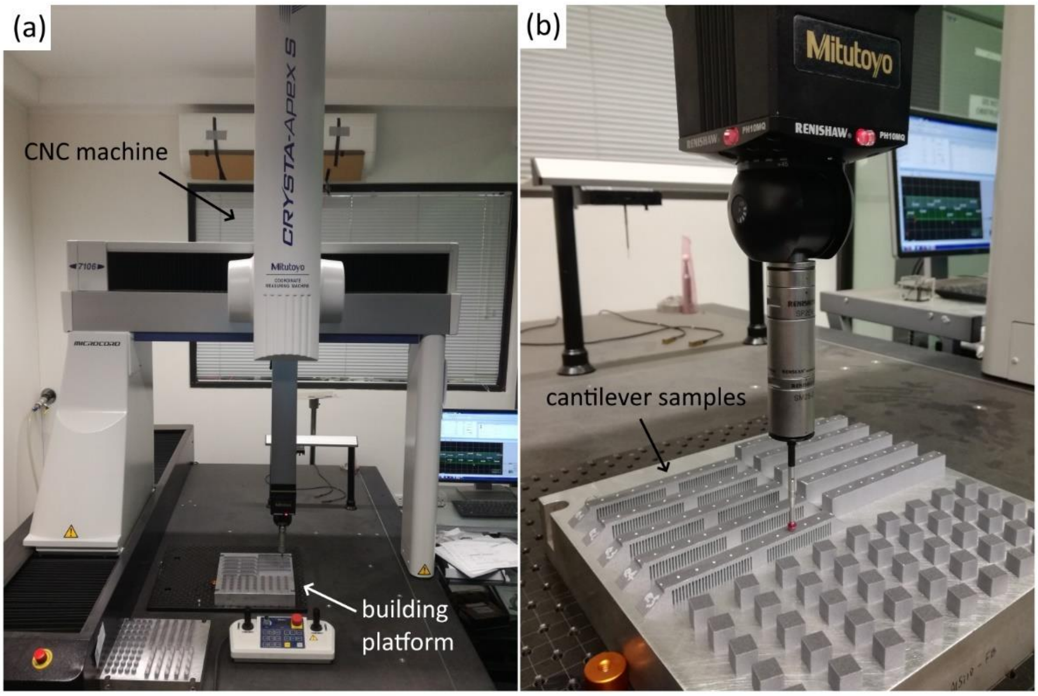

Fig. 99 (a) The CRYSTA-Apex S700 CNC machine used to determine cantilever profiles, and (b) a close-view on the building platform during a profile measurement.

5.2.3 *In-situ* aging evaluation

The production of large parts by LPBF may require extended printing periods, occasionally up to one working week. After the definition of the platform heating temperatures able to minimize distortions and cracks, it is necessary to find out if the long holding time elapsed on the heated platform can age or not AlSi10Mg parts. Besides, if *in-situ* aging takes place, the printing time limit beyond which overaging occurs should be estimated. The LPBF printing time t is the job length (hrs), which in turn depends on the process parameters (P, v, and h_d) and the volume of printed material. For this reason, two jobs with a low and high packing density of specimens, which corresponded respectively to a printing time t of 13.4 and 53 hrs, were designed (Fig. 100). AlSi10Mg parallelepiped samples of 11×85×35 mm^3 were manufactured using a platform heating of 150 °C. This temperature was adopted because being the more close among the investigated heating temperatures to the direct aging temperature of Al-Si alloys [225].

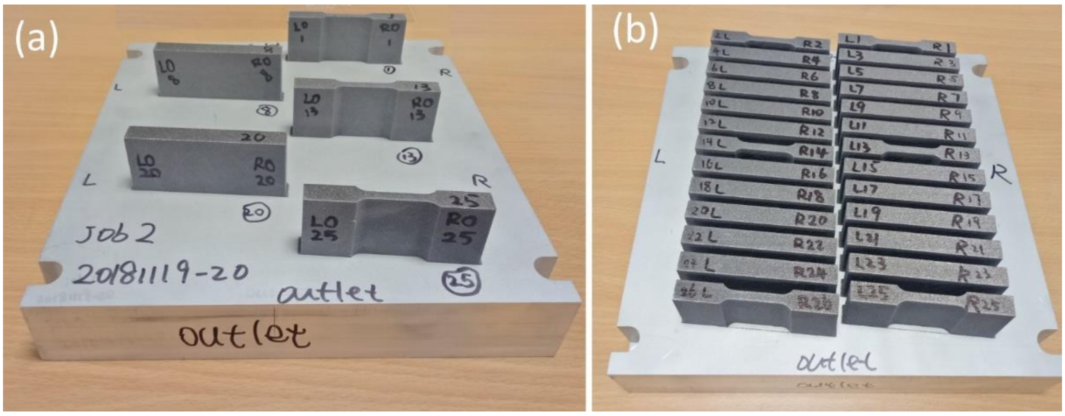

Fig. 100 (a) Low and (b) high packing density jobs corresponding to a total printing time t of 13.4 and 53 hrs, respectively.

At this point, micro-hardness was evaluated along the Z-axis of specimens. Vickers micro-hardness (HV0.5) tests were carried out by applying a static load of 0.5 Kg and a dwell time of 10 s using the Duramin A330 hardness tester. Six samples of each condition were evaluated to determine the overall hardness behavior. HV measurements were performed at specific height levels along the building direction, as depicted in Fig. 101. Thirty measures were considered at each height level to have a statistically significant value.

The LPBF holding time τ_i which is the time elapsed above the heated platform was retrieved by Eq. (5.1), and correlated to the hardness values:

$$\tau_i = \frac{(h - h_{i\_HV})}{h} \cdot t \tag{5.1}$$

where τ_i represents the holding time corresponding to the specific hardness tested level h_{i_HV}, h is the total height of samples (i.e., 35 mm) and t is the fixed printing time (i.e., 13.4 or 53 hrs).

Specimens were then polished down to a mirror-like surface and etched for 15 sec in Kroll's reagent to reveal the microstructural features. Microstructures were observed using the JEOL 7001F FEG-SEM. Investigations were conducted at a magnification of 20.000× along the building direction. Micrographs were taken within melt pool cores to avoid the microstructural inhomogeneities of melt pool borders [56].

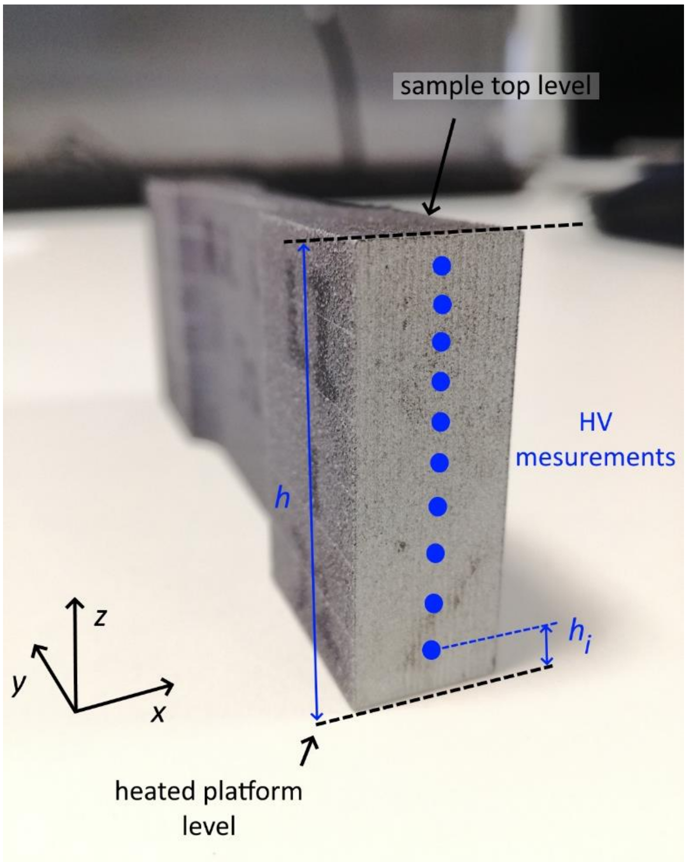

Fig. 101 Schematic representation of the investigated sample and position of HV tested points.

5.2.4 Heat-treatments

Bulk samples of 10×10×10 mm^3 were produced using a platform heating of 200 °C and a printing time of about 10 hrs. Long-term isothermal heat-treatment was performed at 200 °C for 100 hrs in order to mimic the heating effect of the building platform over long production time. The temperature of heat-treatment was fixed at the same platform heating T adopted during manufacturing. The temperature inside the furnace chamber was monitored by a thermocouple. Temperature fluctuations ΔT of ± 1 °C were revealed throughout heat-treatment. Later, the same samples underwent a T6-like heat-treatment to evaluate the impact on microstructure and hardness. T6 heat-treatment consisted of a solutioning at 520°C for 1 h, water quenching, and artificial aging at 160 °C for 6 h. The time interval between solutioning and artificial aging was kept below 30 min to avoid natural aging. On each sample, five hardness measurements were performed in the center of the XZ plane according to the ASTM E384-17 standard.

5.3 Results

5.3.1 Cracks and distortions

Platform heating temperatures able at preventing crack and distortions during manufacturing were firstly determined to uncover a safe route for the production of large-scale parts. The results are summarized in Fig. 102 and Fig. 103.

Fig. 102 depicts cantilever specimens manufactured at different platform heating temperatures before supports cutting. A close inspection of Fig. 102 shows that cracks and support distortions arose when a platform heating of 45 and 100 °C was adopted. The origin of such defects was found in the proximity of the first consolidated layer between supports and arms of the twin cantilever specimen. By increasing the heating temperature to 150 and 200 °C, cracks and distortions were reduced consistently.

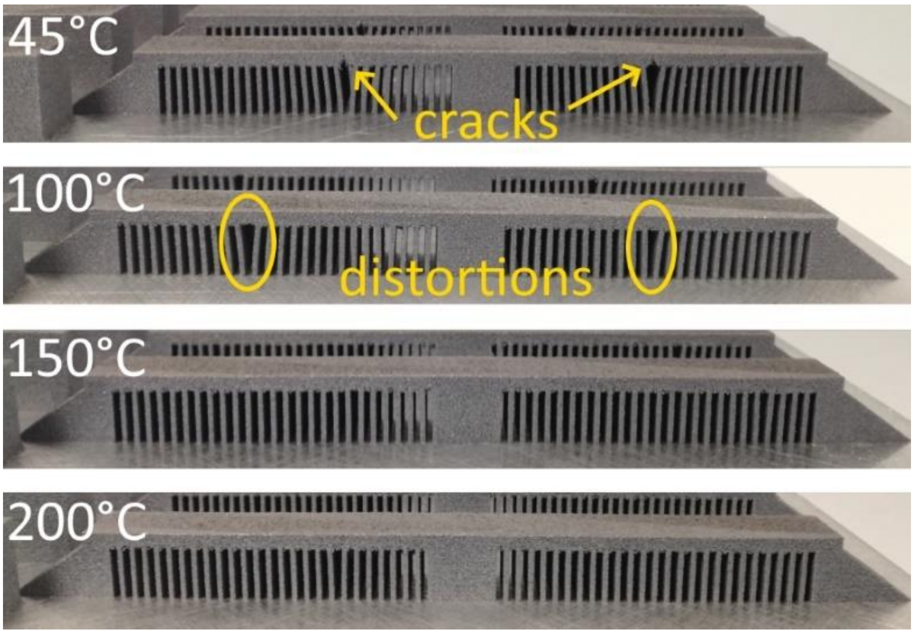

Fig. 102 Cracks and distortions identified on twin cantilever specimens produced according to varied platform heating temperatures.

Fig. 103 displays the number of cantilever deflections according to the applied platform heating temperature. Regardless of the heating temperature, it was observed that the majority of residual stresses generated during LPBF manufacturing was released after supports cutting and, consequently, bent deflections formed. Maximum deflection ΔZ was achieved at a platform heating of 45 °C in correspondence of the connection edge between platform and cantilever base. By increasing the heating temperature, deflection reductions of 34 % and 54 % were registered at the cantilever edge of samples built at 100 and 150 °C, respectively. By further increasing heating temperature up to 200 °C, deflections were not detected as a consequence of the shorten temperature gradient during manufacturing.

Therefore, based on the results presented so far, heating temperatures of 150 and 200 °C were considered for the in-situ aging study because they revealed a lower extent of bending, and prevented the formation of cracks and distortions in cantilever samples. This is, indeed, an essential requirement when large-scale components are manufactured by LPBF.

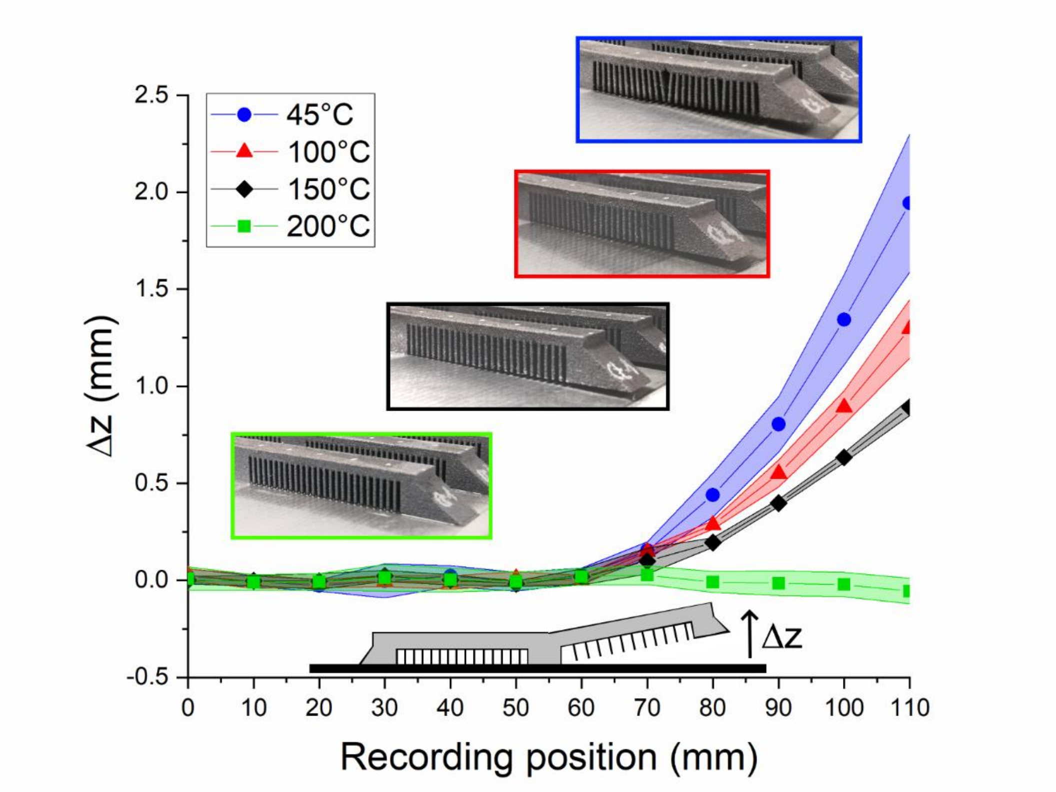

Fig. 103 Deflections (ΔZ) measured on twin cantilever samples built using different platform heating temperatures after support cutting. Colored bands represent standard deviations. Insets provide a qualitative interpretation of the results.

5.3.2 In-situ aging

In-situ aging experiments were performed at a platform heating of 150 °C, being this temperature the closer to the direct aging temperature for age hardenable Al-Si alloys [225]. The hardness and the microstructure evolution along the building direction of samples built at different printing times were investigated. The results are reported in Fig. 104 and Fig. 105, respectively.

Fig. 104 shows the hardness measured on samples with a height of 35 mm (Fig. 101) and manufactured with LPBF printing time t of 13.4 and 53 hrs on a building platform heated at 150 °C. Before exploring the results, it is worth to highlight that i-layer melted near the heated platform had experienced longer holding times (τ) that upper consolidated ones, thus by stacking layer on layer, the holding time of $i+1$ layer decreased. Thus, Y-axes of Fig. 104 can be read from bottom to top and vice versa.

As far as the hardness profile after 13.4 hrs of printing time is concerned, it was noticed that the hardness increased as the holding time τ increased. A significative hardness increment was detected up to τ of 2.5 hrs, which corresponded to the top part of samples. Then, hardness reached a plateau of about 137 HV throughout the remnant part of the sample down to the heated platform, i.e., between holding times of 2.5 and 12.4 hrs. Considering the hardness profile after 53 hrs of printing time, a hardness drop was observed, pointing a possible over-aging. By increasing τ, indeed, a hardness peak of 138.6 HV was found at τ of 13.6 hrs. Afterward, by further raising τ, hardness was remarkably reduced across the part of the sample that elapsed a longer time (up to 49.2 hrs) above the heated platform.

Thus, according to the results of Fig. 104, AlSi10Mg specimens built after 13.4 hrs were peak-aged to a large extent (up to h = 27 mm). On the other hand, it was highly probable that over-aging occurred after 53 hrs of printing time.

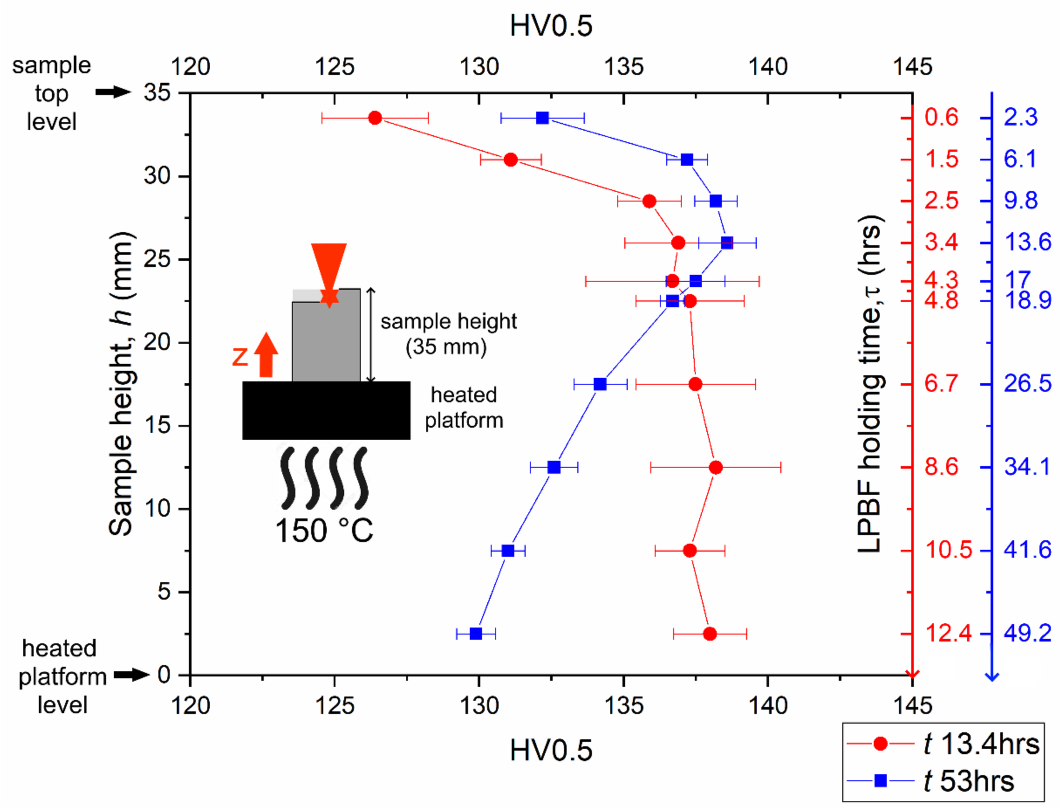

Fig. 104 Micro-hardness evolution of AlSi10Mg specimens manufactured after 13.4 or 53 hrs of printing time on a platform heated at 150 °C. Hardness data are plotted according to the sample height levels and the corresponding holding times.

Fig. 105 depicts the micrographs of specific positions along the building direction, which corresponded to the hardness data showed in Fig. 104. Based on the micrographs, the overall response of AlSi10Mg alloy to the rapid solidification generated very fine α-Al cells/columns decorated by a fibrous eutectic. The eutectic architecture was highly abundant in Si, as shown by EDS maps of Fig. 106. This was in good agreement with the literature on AlSi10Mg alloy processed by LPBF [76,190,196]. Furthermore, being AlSi10Mg very sensitive to precipitation hardening [215], a consistent presence of fine precipitates was found in sample positions which experienced higher holding times above the heated platform (i.e., Fig. 105e,f). Similarly, considering the same sample height but different printing time, a higher number density of precipitates was found in Fig. 105d-f compared to Fig. 105a-c. Instead, there were not any differences in dendrite width among the investigated samples (λ = 0.39-0.44 µm).

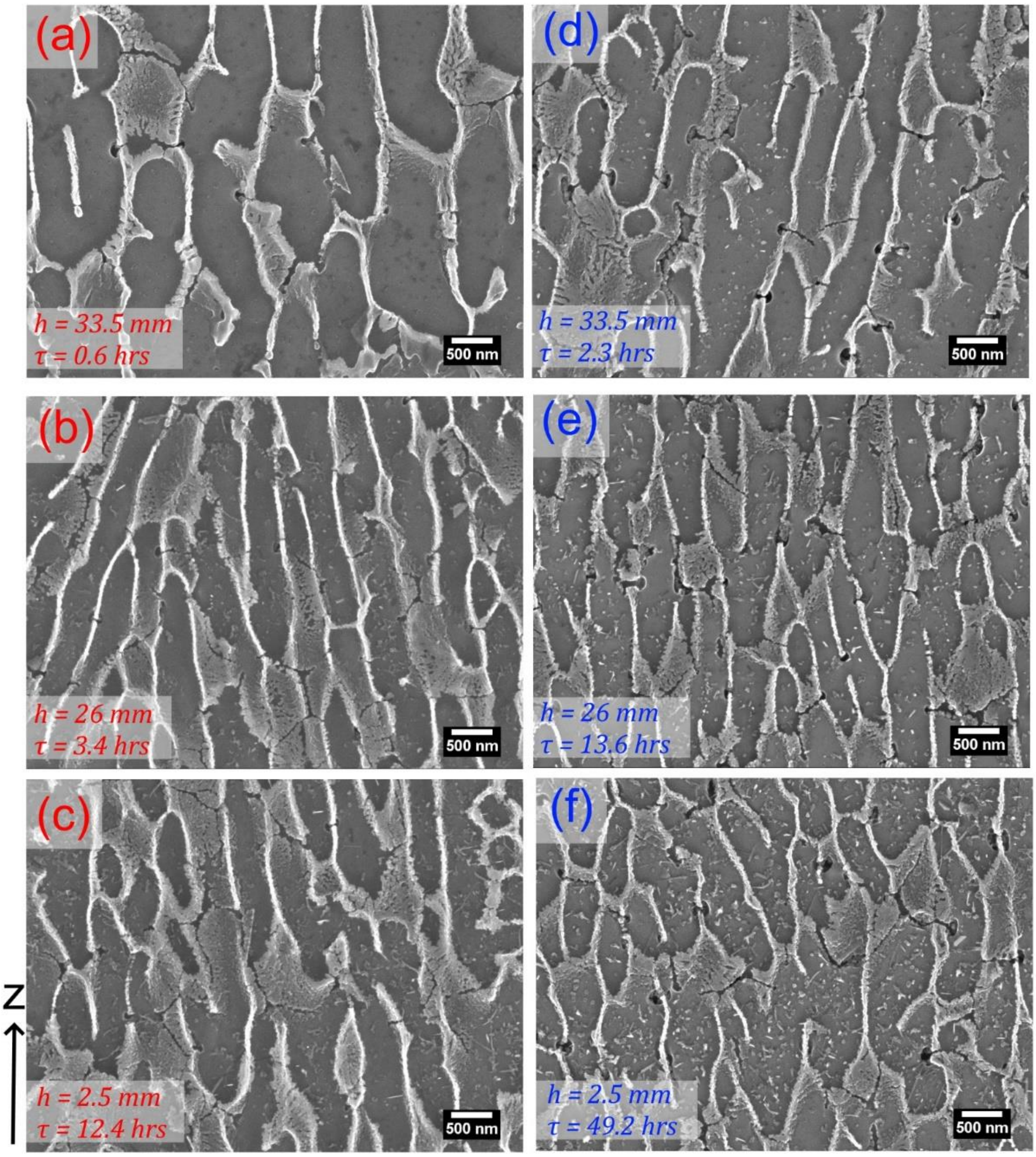

Fig. 105 Microstructure evolution along the building direction of specimens manufactured upon (a-c) 13.4 and (d-f) 53 hrs of printing time above a building platform heated at 150 °C. Micrographs were arranged according to increasing holding time and decreasing sample height. SEM investigations were conducted in a melt pool core next to the corresponding hardness measurement.

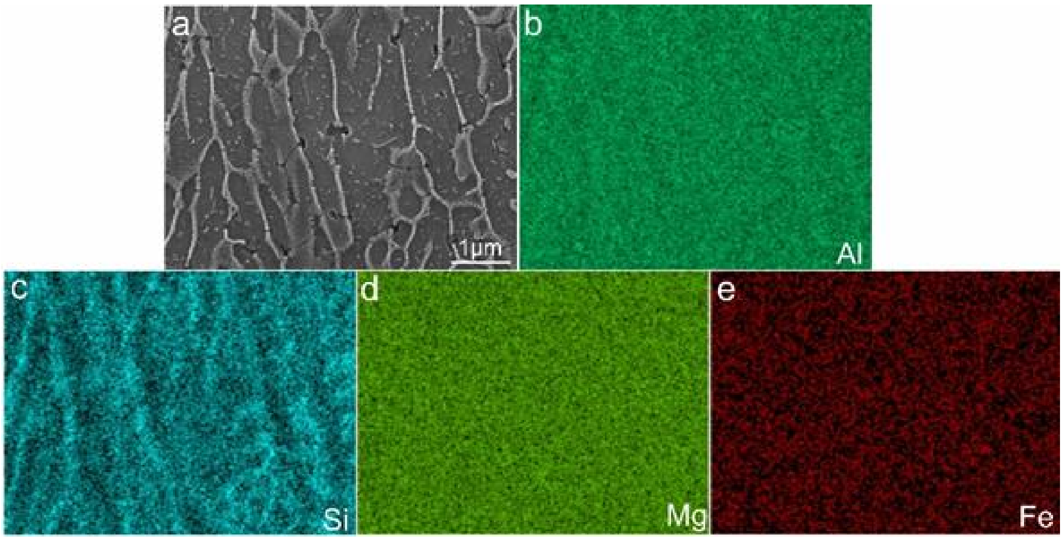

Fig. 106 (a) SEM micrograph and (b-e) corresponding EDS maps showing the enrichment of Si along the eutectic boundaries of Fig. 105f.

5.3.3 Heat-treatments

Fig. 107 reports the hardness values of bulk samples manufactured at a platform heating temperature of 200 °C after 10 hrs of printing time and various post-process heat-treatments. Specifically, two heat-treatments were designed. The first one was an extended isothermal treatment conducted at 200 °C to extend the effect of the heated platform at longer printing time (up to 100 hrs). The latter was a T6-like heat-treatment strategy.

Prior to whatever heat-treatment, the as-built samples showed an HV value of 100.5 ± 3.0, which is considerably lower than the as-built AlSi10Mg value reported in the literature (Section 2.4.1, Fig. 41). Thus, this results may suggest that AlSi10Mg samples were already overaged after 10 hrs on a heated platform at 200 °C. After 100 hrs at 200 °C, hardness decreased down to 91 ± 0.6 HV. However, when samples underwent T6-like heat-treatment, the mean hardness value increased of about 12 and 26 % for the as-built and isothermal heat treated samples, respectively. It is worthwhile to note that the hardness difference (≈ 10 HV) between as-built and iso-heat treated samples was balanced by T6 heat-treatment. Regarding this, all the measured hardness data were in the range of 111-118 HV, which is comparable to the peak-aged hardness value of Al-Si alloys after T6 heat-treatment (Section 2.4.1, Fig. 41).

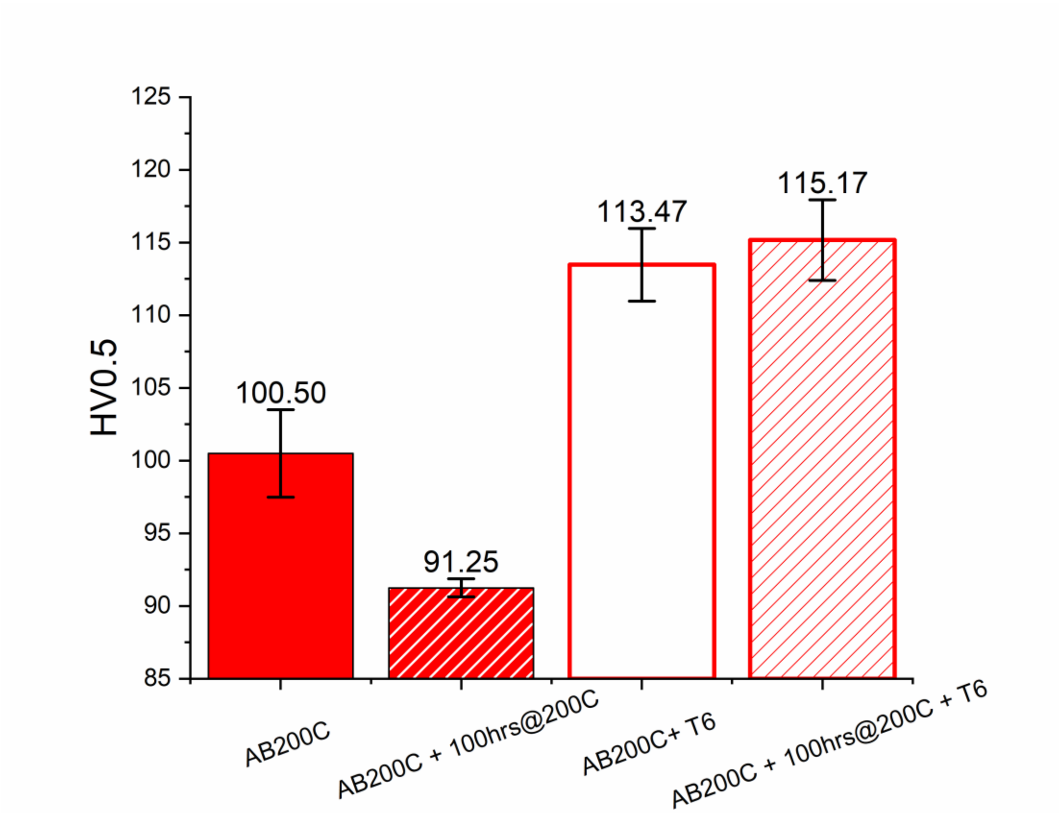

Fig. 107 Micro-hardness of as-built and heat treated bulk samples manufactured on a platform heated at 200 °C.

The microstructures of AlSi10Mg alloy under different heat-treatment conditions were then investigated (Fig. 108). Fig. 108a shows the overall microstructure after isothermal treatment at 200 °C for 100 hrs. As can be seen from Fig. 108a, AlSi10Mg still showed the typical ‘fish scale’ pattern microstructure constituted by dual-half cylindrical melt pools oriented along the scanning direction. Fig. 108b shows a high magnification micrograph of a melt pool core. It was found that the morphology of α-Al was mostly columnar owing to the heat flux directed towards the heated building plate. However, rounded cells of size of roughly 0.41 ± 0.03 µm were identifiable. Besides, it must be noticed the presence of tiny intracolumnar precipitates within the α-Al matrix, likely formed by Si diffusion and precipitation during isothermal heat-treatment.

The microstructure of AlSi10Mg samples after isothermal and T6-like heat-treatments are provided by Fig. 108c,d. In Fig. 108c, the ‘fish scale’ patterns almost disappeared due to the Si particles coarsening during heat-treatment, and the consequent eutectic network disruptions. However, few tracks pointed by black arrows resembled the original borders of a melt pool. When the high magnification microstructure of Fig. 108d is observed, Si particles with irregular rounded shapes and size between 0.3 and 4 µm were revealed. Apart from Si particles, the contours of elongated precipitates etched away by Kroll's reagents were also identified. They had a maximum longitudinal length of 12 µm and averaged thickness of 0.41 ± 0.12 µm. The EDS mapping of Fig. 109 evidenced that these precipitates were mainly enriched in Fe. Similar findings were reported by other researchers after heat treating LPBF*ed* AlSi10Mg via T6 strategy [190,240].

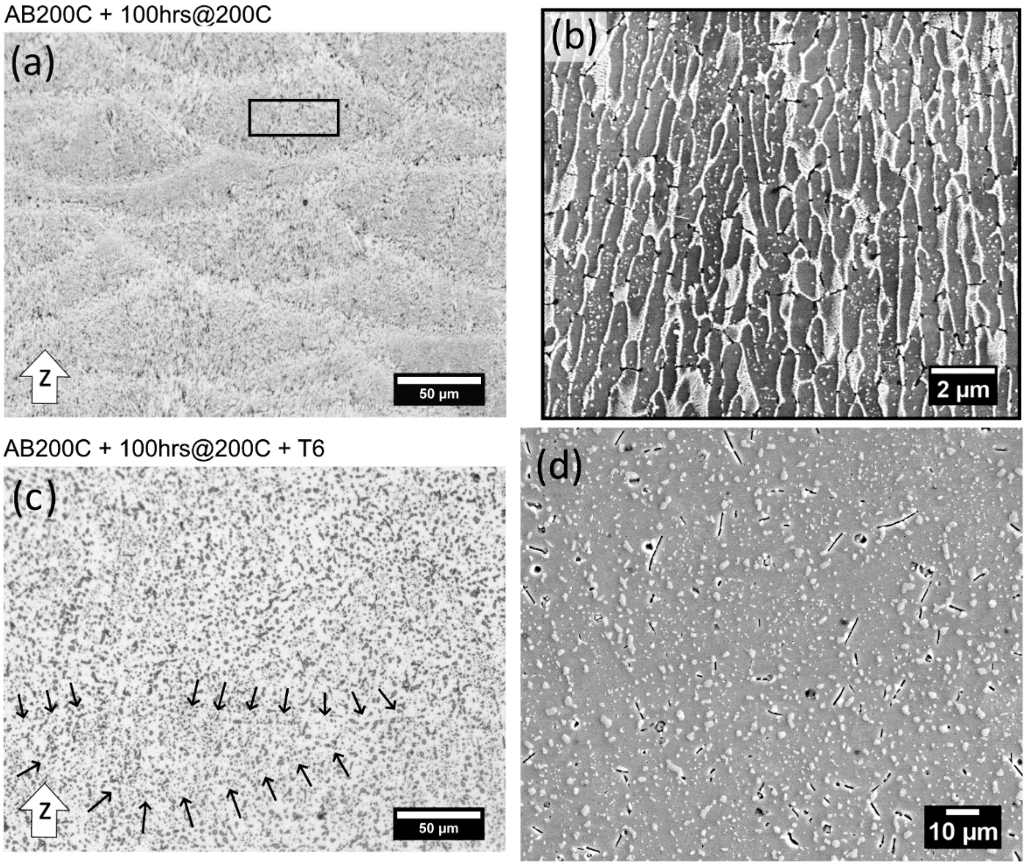

Fig. 108 (a) Low and (b) high magnification micrographs of AlSi10Mg bulk samples upon isothermal heat-treatment at 200 °C for 100 hrs; (c) low and (b) high magnification micrographs after isothermal heat-treatment + T6.

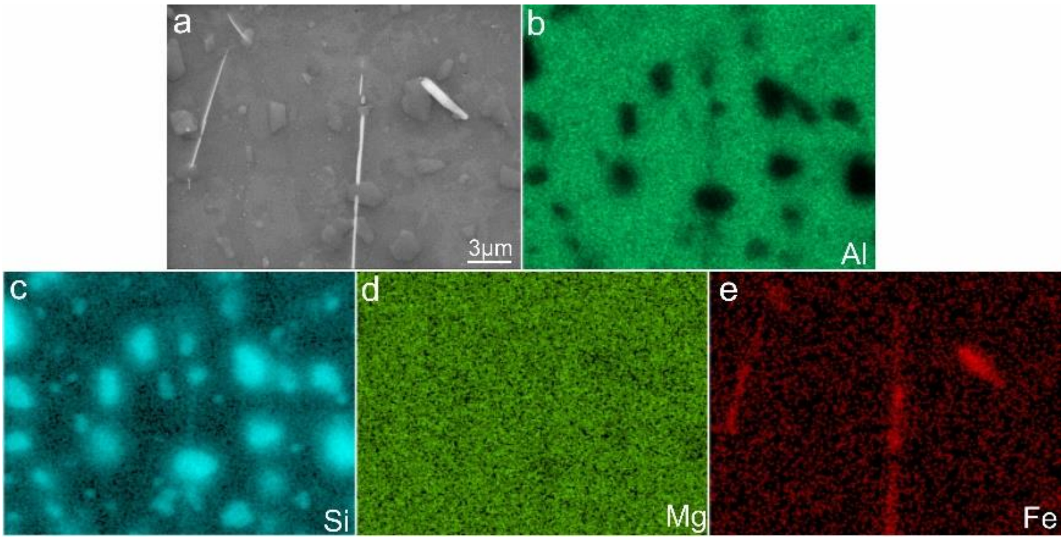

Fig. 109 (a) SEM micrograph and (b-E) corresponding EDS maps showing the Si particles and the plate-shaped precipitates enriched in Fe in Fig. 108d.

5.4 Discussion

5.4.1 Influence of platform heating on cracks and distortions

The production of large-scale components with complex shapes involves critical challenges to be tackled. The presence of internal residual stresses, which spontaneously arise upon rapid solidification, can lead to cracks formation, supports distortions, parts bending, and, in the worst case, to the job failure [78,333]. Therefore, the first aspect addressed in this work was the cracks prevention as well as the minimization of support distortions. To this purpose, the heated building platform strategy was employed during printing [25,80].

Four heating temperatures were investigated to find the temperature range minimizing cracks and distortions. Results of Fig. 102 showed that it is possible to prevent such defects in cantilever samples by using a platform heating temperature no less than 150 °C. This might be explained due to the fact that the shrinkage of parts is reduced at higher platform temperatures as a consequence of a shortened solidification range [333]. On the opposite, when relatively low temperatures are fixed ($T < 150$ °C), thermally induced tensile residual stresses form obvious cracks and distortions, as depicted in Fig. 102. In fact, when the first powder layer of the cantilever arm was melted, a spontaneous thermal expansion followed by compression after cooling was expected. Nevertheless, the shrinkage of the consolidated layer was hampered by the underlying support structure forming high tensile stresses in the opposite direction. Then, these residual stresses can lead to the fins bending and, eventually, to the crack initiation [25]. The evidence for this was obtained by cutting the cantilevers arms near the building plate. In fact, immediately after cutting, the tensile residual stresses were released and, thus, upward deflections occurred (Fig. 103). By increasing the platform heating from 45 to 200 °C, results of Fig. 103 suggest that cantilever arm deflection decreased at 150 °C and then became negligible at 200 °C. This is consistent with the absence of cracks and distortions observed before cutting in cantilevers manufactured at the same platform heating (Fig. 102), and with the previous work of Buchbinder et al. [25].

Based on the results, it can be concluded that raising the platform heating to 150 °C or more helps to alleviate cracks and distortions in AlSi10Mg parts. Therefore, the heating temperatures of 150 °C and 200 °C were taken into account for the production of large-scale components of AlSi10Mg.

5.4.2 *In-situ* aging via platform heating during LPBF

Once the proper platform heating temperature range to alleviate the internal residual stresses was identified, a second critical issue must be considered when facing the production of massive aluminum components. In this case, the issue is related to the intrinsic characteristics of the processed alloy. In fact, AlSi10Mg alloy is known to be very sensitive to precipitation hardening during aging heat-treatments performed above 160 °C [26,223]. Since the selected platform heating temperatures to prevent cracks were 150 and 200 °C, there could be the possibility to *in-situ* age parts during production. Therefore, it is technologically essential to evaluate if the long holding time elapsed on the heated platform by the large component can *in-situ* age and affect the mechanical properties of AlSi10Mg. In this regard, the hardness behaviors of AlSi10Mg specimens built with a platform heating of 150 °C after 13.4 and 53 hrs of printing time have revealed different responses to *in-situ* aging (Fig. 104).

On one side, considering a printing time of 13.4 hrs, the micro-hardness evolution along the building direction of parallelepiped samples is comparable with the aging response of a SLM*ed* A357 alloy characterized by Casati et al. [222]. It must be noted that, in their work, the direct aging was performed after LPBF manufacturing, showing a peak-age hardness value of 137 HV after 4 hrs at 160 °C. By comparison, the same hardness was achieved in this research at around 3.4 hrs with a platform heating of 150 °C. The overall hardness behavior reveals that the sample is peak-age to a large extent.

On the other side, considering a printing time of 53 hrs, hardness results indicate that over-aging takes place throughout the sample volume held for a longer time on the heated platform. Similarly, this aging response was comparable with the one found for a SLM*ed* AlSi10Mg alloy isothermally aged at 160 °C after manufacturing on a non-heated platform [26]. Besides, the microstructure of Fig. 105 provides clear evidence that over-aging mostly affects the volume of material built in the proximity of the heated platform. As widely reported in the literature, it is assumed that, immediately after melting, the solidification front propagated into the adjacent liquid in a dendritic mode [162]. Then, the constitutional undercooling promoted the formation of Si-supersaturated α-Al cells, still identifiable in Fig. 105f, and, subsequently, the segregation of Si atoms at the cell boundaries [216]. At this point, it was most likely that the high holding time in intimate contact with the heated platform triggered an untimely diffusion of Si atoms within α-Al cells [80]. This resulted in massive precipitation of very fine particles, and in the occasional disruptions of the eutectic network, which adversely affected the hardness. These fine precipitates were recently found to be pure Si precipitates in a directly aged A357 alloy processed by SLM [206].

Therefore, referring to the results of Fig. 108 and Fig. 109, it is believed that the synergism of the platform heating, set near the aging temperature of AlSi10Mg, with the holding time played a crucial role in determining the extent of the *in-situ* aging. Furthermore, it is advisable to use a platform heating of 150 °C when the built part requires a holding time of less than 13 hrs. In this way, it would be possible to prevent the over-aging and, simultaneously, to partially unleash the internal residual stresses without resorting to post-process heat-treatments. However, it should be considered that the build of large parts requires more than 13 hrs (up to one week, occasionally) and, consequently, the adoption of a platform heating higher than 150 °C would result in a severe over-aging phenomenon.

5.4.3 T6 heat-treatment: a remedy to over-aging

According to the results of Fig. 102 and Fig. 103, it is worth to reiterate that a platform temperature of 200 °C should be used for the production of large AlSi10Mg components to consistently alleviate the internal residual stresses and avoid the support breaking. However, results of Fig. 104 and Fig. 105 also indicate that over-aging occurs when manufacturing at the same temperature. A remedy to the over-aging phenomenon can be represented by post-process heat-treatments, such as the T6 solution. Therefore, bulk samples were manufactured with a platform heating of 200 °C at first. Then, to mimic *in-situ* aging, they were isothermally heat treated at 200 °C for 100 hrs in a furnace, and, lastly, underwent a T6 heat-treatment.

Considering the hardness results of Fig. 107, a relatively low hardness value (91.25 HV) showing that a microstructure punctuated by a consistent number of sub-micron particles was achieved after 100 hrs at 200 °C (Fig. 108b). The hardness weakening was likely attributed to the loss of Si from α-Al super-saturated solid solution [83], which resulted in the formation of fine precipitates within Al cells, and to the simultaneous low-temperature stress relieving [228,229]. Consequently, the solid solution contribution to overall strength was considerably reduced after this prolonged heat-treatment, resulting in a low hardness value (Fig. 107).

On the contrary, once performed the T6 heat-treatment, a significant increment of hardness (up to 115 HV) was obtained, making this value comparable to the cast counterparts [194,234]. As far as the contribution to strength is concerned, it is believed that the strengthening mechanism might be mostly ascribed to the dispersion of Si precipitates (identified in Fig. 107c,d), which pinned gliding dislocations [200]. This assumption is in good agreement with the literature works on T6 heat-treatment and Al-Si alloys [217,220]. Moreover, it must be pointed out that T6 led to a hardness increase with respect to the as-built condition. In contrast, other researches indicated a slight hardness impoverishment in the heat-treated state [194,206,217,220]. As an example, Aboulkhair et al. reported a hardness decrease from 125 to 103 HV after T6 [217]. Nevertheless, our as-built hardness exhibited a feeble HV value (100.5 HV) owing to the effect of the platform heating fixed at 200 °C. Thus, the only chance to partially recover the strength after LPBF manufacturing was to exploit the hardening effect brought by T6 heat-treatment. Besides, in sight of the production of highly performant aerospace components, T6 also contributes to enhancing the fatigue behavior [185].

In conclusion, based on the results presented in this section, it can be argued that the T6 heat-treatment is a viable solution to recover from the detrimental impact of *in-situ* over-aging during the production of large components by LPBF.

5.5 Summary and conclusions

In this chapter, the issues related to the production of large-scale AlSi10Mg components by LPBF have been addressed. On the one hand, there is the presence of internal residual stresses that can cause the premature rupture of part supports and, eventually, the job failure. On the other hand, one must cope with the *in-situ* aging of the processed aluminum alloy, which can potentially lead to over-aging.

According to previous investigations, the heating platform strategy was employed to define the temperatures clever at alleviating cracks and distortions. Afterward, these temperatures were used for *in-situ* aging experiments to evaluate the effect of a prolonged exposure above the heated plate on hardness and microstructure of the processed alloy.

It was found that, by using platform temperatures higher than 150 °C, part distortions and support breakages were partially or entirely prevented due to the mitigation of internal stresses. However, *in-situ* aging occurs when the platform is heated at 150 °C. Results showed that the peak-hardening is attained when the holding time τ ranges from 3.4 and 13.4 hrs. Further beyond this temperature range, over-aging starts to appear at $\tau \geq 13.6$ hrs. This latter value of holding time is regarded as the ultimate limit before incurring over-aging.

As far as the results of heat-treatment investigations are concerned, over-aging occurs both on the as-built and isothermal heat-treated samples manufactured on a platform heated at 200 °C, reaching lower hardness values compared to the ones in the literature. A good remedy for the recovering of over-aging was found to be the T6 heat-treatment. In fact, T6 can increase the hardness by 26% in the best scenario due to the beneficial effect brought by artificial hardening.

Finally, the results of this chapter pave the way for the definition of a production strategy for large-scale aluminum components (Fig. 110). If large parts with critic shapes are produced, a platform heated at 200 °C must be used to alleviate distortions and part bending throughout LPBF. However, the high holding time required by these components inevitably leads to over-aging. Thus, T6 heat-treatment must be conducted after printing to improve the hardness and making it comparable to the die-cast. On the other side, when smaller parts are produced at holding times lower than roughly 13 hrs, a platform heating fixed at the aging temperature for Al-Si alloys can be exploited to achieve peak-aged components without performing any further heat-treatments.

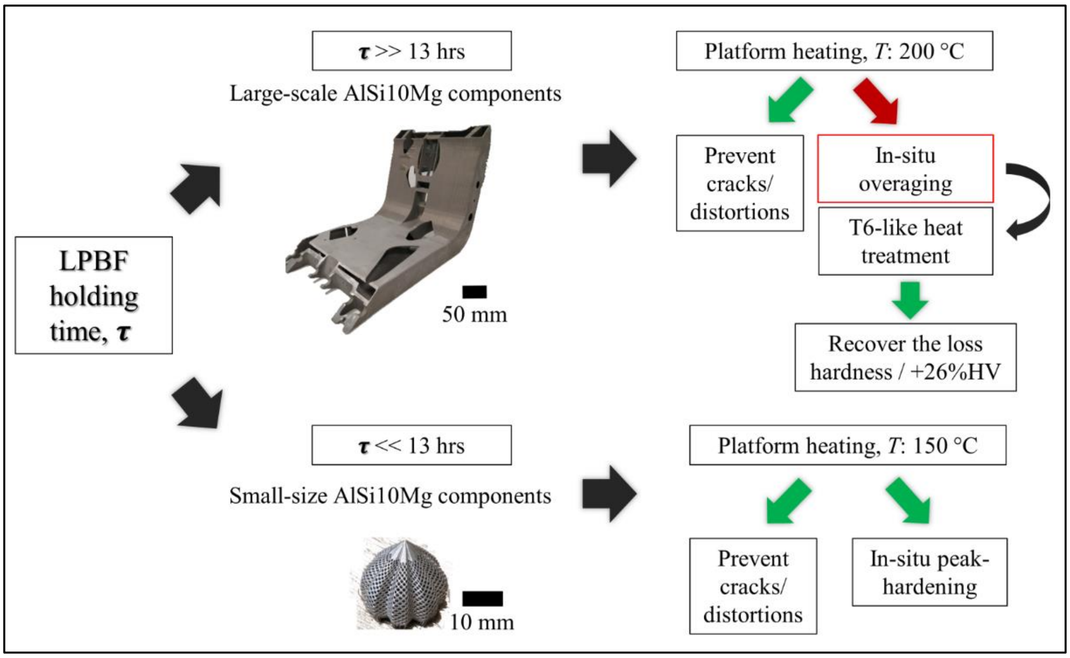

Fig. 110 Schematic representation of the production strategy proposed according to the findings of this work.

Chapter 6

Conclusions and future outlook

The limited material palette available for AM and the low productivity of additively manufacturing processes have been regarded as barriers to overcome for the global AM development. Therefore, the thesis has coped with these two critical challenges to contribute to the overall progress of the technology. On the one hand, an AlSi10Mg+4Cu mixed alloy was tailored for LPBF and characterized in terms of microstructure, chemical homogeneity, and mechanical behavior in the as-built and heat treated conditions. On the other hand, the thesis addressed the issues related to the manufacturing of large aluminum components by LPBF, defining a production strategy for massive aluminum parts.

The key findings of the thesis are concisely summarized in the following paragraphs.

6.1 Laser powder bed fusion of AlSi10Mg+4Cu alloy

The main focus of this research was to exploit the strengthening effect of Cu to improve the mechanical properties of an AlSi10Mg alloy by *in-situ* alloying Cu and AlSi10Mg powders during LPBF.

A powder blend was obtained by mixing AlSi10Mg and Cu powders and, then, an AlSi10Mg+4Cu alloy was synthesized *in-situ* exploiting the thermal effect of the laser energy. The alloy processability was studied by analyzing the properties of single fusion lines, also known as single scan tracks (SSTs). Then, the density, the microstructure, the chemical homogeneity, the phase composition and the hardness of as-built bulk samples were investigated. Once the proper process parameters were identified, bulk samples were heat-treated according to the T5 protocol with the purpose of fully exploiting the precipitation potential offered by the as-built AlSi10Mg+4Cu specimens. The directly aged samples were investigated in terms of phase composition, thermal behavior, and mechanical properties (i.e. hardness and tensile strength). The microstructure evolution during direct aging was correlated with the alloy age-hardening response.

The results of the investigation conducted on AlSi10Mg+4Cu alloy lead to the following conclusions:

- the SSTs approach was successfully used to quickly define a reliable P-v process window by studying the stability of SSTs on-top surfaces and their melt pool geometries.
- differently from earlier works, the h_d values used for the production of bulk samples were already fixed at the SSTs stage, considering the melt pools overlapping (φ).
- bulk samples built with a rotating scanning strategy (67°) and φ between 0 and 20 % showed a decent densification level (up to 99.16 %).
- besides density, the optimization of the process parameters was conducted considering both productivity and hardness. When the highest productivity is desired, one should use P of 170 W or 180 W, h_d of 0.14 mm and v of 1000 mm/s. If a high hardness is wanted, P, v and h_d of respectively 180 W, 1000 mm/s and 0.12 mm should be adopted.
- the processability study conducted on AlSi10Mg+4Cu alloy lays the foundation for defining a time-saving identification of the main process parameters, namely power, speed, and hatching distance, based on the evaluation of SSTs features.
- as proved by the variation in morphology of the eutectic network, a different solidification dynamic takes place during the production of SSTs and bulk samples.
- the microstructure morphology of AlSi10Mg+4Cu reveals the presence of fine α-Al cells surrounded by a dual eutectic of Si precipitates intermixed with Al_2Cu phase.
- the Cu addition was effective in improving the hardness of the base AlSi10Mg alloy; indeed a hardness increment of 33 % and between 6 and 16% was observed at the nano-scale and macro-scale, respectively. Precipitation strengthening as well as solid solution strengthening are likely the principal contributors to the hardness increment in AlSi10Mg+4Cu alloy.
- thanks to the mixing effect of the local convective flows arising during melting, the overall chemical composition of AlSi10Mg+4Cu reflects the nominal one to a large extent. However, local segregations of Cu

formed due to the different physical properties of AlSi10Mg and Cu powders creating local inhomogeneities, which in turn resulted in pronounced hardness peaks.

- the age-hardening response is strictly dependent on the aging temperature. A maximum hardness increment of 21 ΔHV was achieved after 1 h at 175 °C.
- results of XRD and DSC analyses indicate that higher aging temperatures boost the diffusion of Cu and Si solutes from the super-saturated solid solution and, consequently, the precipitation of Si and θ-Al_2Cu phases.
- aging the as-built specimens at 160 °C enables a slow solutes diffusion and a progressive hardening up to 160 HV. At the aging temperature of 175 °C, a peak-age of 163 HV is reached upon 1 h and the corresponding microstructure is constituted by a mix of $\theta''/\theta' + \theta$-$Al_2Cu$ precipitates and Si phase. Aging at 190 °C speeded-up the formation of the coherent θ-Al_2Cu phase leading to lower hardness.
- AlSi10Mg+4Cu alloy in the as-built or heat-treated condition exhibits a superior tensile strength compared to the AlSi10Mg counterpart. The main reason for this is ascribed to the additional strengthening effect of Cu via solid solution and precipitation strengthening.
- the tensile fracture mechanism of AlSi10Mg+4Cu is characterized by a ductile-brittle behavior.

Finally, a global view of this work supports the idea that the *in-situ* alloying of powder mixtures is a viable strategy to develop novel alloys by LPBF. By adopting this strategy, indeed, it is possible to have a comprehensive insight on the processability, microstructure, and mechanical properties of the synthesized alloy without involving important financial resources and a large amount of time to buy gas-atomized powders. However, the different properties of the starting powders and the rapid heating and fast cooling of LPBF can partially affect the alloy chemical homogeneity by forming segregations of constitutive element/s. In this respect, further research activities could be undertaken with the purpose of reducing the chemical inhomogeneities. Moreover, further work should be carried out to assess the effect of the conventional T6-like heat-treatment strategy on the mechanical properties of AlSi10Mg+4Cu. Lastly, it could be scientifically interesting to compare the microstructure, chemical composition, and mechanical properties of the *in-situ* alloyed AlSi10Mg+4Cu alloy with the pre-alloyed counterpart. The production of a gas-atomized AlSi10Mg+4Cu powder, indeed, can be carried out by using the gas-atomizer implant located at the Alessandria headquarter of Politecnico di Torino.

6.2 Manufacturing large-scale components of AlSi10Mg by LPBF

This work aimed at solving the issues related to the production of large aluminum parts by using the heated building platform strategy. Two main aspects were addressed: the inevitable presence of internal residual stresses that can cause the job failure during long printing time, and the *in-situ* aging of the processed alloy.

The main results of the research can be drawn as follows:

- building platform temperatures fixed at 150 °C and above can effectively alleviate the internal residual stresses and largely reduce the part distortions during extended LPBF jobs.
- by heating the platform at 150 °C, the *in-situ* aging of AlSi10Mg occurs. Hardness reaches the peak at a holding time between 3.4 and 13.4 hrs. Over-aging starts to appear at holding time higher than 13.4 hrs.
- as-built and isothermal heat treated samples manufactured at 200 °C show a clear over-aging response, reaching the lowest HV value after 100 hrs at 200 °C.
- T6-like heat-treatment can recover the loss of hardness caused by over-aging, increasing the HV value by 26 % in the best scenario.
- to produce large parts with critical shapes, a platform heating of 200 °C should be used to minimize distortions and parts bending during LPBF manufacturing. Nevertheless, the high holding time inevitably induces the over-aging, and the T6-like heat-treatment should be applied to achieve mechanical properties comparable to the cast counterparts.

At the end of this study, it can be concluded that the holding time, which is the time elapsed by the material onto the heated platform during LPBF, must be properly handled to avoid over-aging when processing age-hardenable aluminum alloys, such as AlSi10Mg and A357. In future, care should be taken when a consistent number of aluminum samples, which require a high printing time, are produced on a heated building platform. Further research might be scheduled to investigate the impact of the over-aging induced by high printing time on the tensile behavior and fatigue life of aluminum components.

References

[1] Andres Gameros, Additive Manufacturing: The Third Industrial Revolution, AZO Mater. (2015). https://www.azom.com/article.aspx?ArticleID=11885.

[2] ASTM International, F2792-12a - Standard Terminology for Additive Manufacturing Technologies, Rapid Manuf. Assoc. (2013) 10–12. doi:10.1520/F2792-12A.2.

[3] I. Gibson, D.W. Rosen, B. Stucker, Additive Manufacturing Technologies - Rapid Prototyping to Direct Digital Manufacturing, 2010.

[4] E.O. Olakanmi, R.F. Cochrane, K.W. Dalgarno, A review on selective laser sintering/melting (SLS/SLM) of aluminium alloy powders: Processing, microstructure, and properties, Prog. Mater. Sci. 74 (2015) 401–477. doi:10.1016/j.pmatsci.2015.03.002.

[5] D. Manfredi, F. Calignano, E.P. Ambrosio, M. Krishnan, R. Canali, S. Biamino, M. Pavese, E. Atzeni, L. Luliano, P. Fino, C. Badini, Direct Metal Laser Sintering: An additive manufacturing technology ready to produce lightweight structural parts for robotic applications, Metall. Ital. 105 (2013) 15–24.

[6] S.M. Thompson, L. Bian, N. Shamsaei, A. Yadollahi, An overview of Direct Laser Deposition for additive manufacturing; Part I: Transport phenomena, modeling and diagnostics, Addit. Manuf. 8 (2015) 36–62. doi:10.1016/j.addma.2015.07.001.

[7] D. Herzog, V. Seyda, E. Wycisk, C. Emmelmann, Additive manufacturing of metals, Acta Mater. 117 (2016) 371–392. doi:10.1016/j.actamat.2016.07.019.

[8] Final AM Motion - Roadmap: A strategic approach to increasing Europ's value proposition for additive manufacturing technologies and capabilities, Brussels, n.d.

[9] Aniruddha Srinath, Why is 2016 the year for additive manufacturing in the medical sector?, Med. Plast. News. (2016). https://www.medicalplasticsnews.com/why-is-2016-the-year-for-additive-manufacturing-in-the-medic/ (accessed September 14, 2020).

[10] Roland Berger Strategy Consultants, Additive manufacturing. A game changer for the manufacturing industry?, in: Munich, 2013: p. 33.

[11] R. DeSilva, Debunking the myths of Additive Manufacturing, Addit. Manuf. Summit. (2016). http://www.additivemanufacturingsummit.com/media/1003367/34746.pdf.

[12] Frost & Sullivan's Global 360° Research Team, Global Additive Manufacturing Market, Forecast to 2025, in: 2016: p. 61.

[13] Global Turbines Market: Overview, 2015.

https://www.transparencymarketresearch.com/turbines-market.html.

[14] E.E. Modic, Additive manufacturing orthopedic implants, Today's Med. Dev. (2018). https://www.todaysmedicaldevelopments.com/article/renishaw-additive-manufacturing-orthopedic-implants/.

[15] A. Bentur, Additive Manufacturing and Aviation – Certified, LeoLane. (2018). http://www.leolane.com/blog/additive-manufacturing-and-aviation-certified/ (accessed September 14, 2020).

[16] Grzegorz Moroz, How Additive Manufacturing is Reshaping the Auto Industry, Process Heat. (2018). https://www.process-heating.com/articles/92742-how-additive-manufacturing-is-reshaping-the-auto-industry (accessed September 14, 2020).

[17] Tyler Koslow, Siemens Making 3D Printed Gas Turbines & Parts for Nuclear Power Stations, All3DP. (2017). https://all3dp.com/siemens-nuclear-power/ (accessed September 14, 2020).

[18] AM PLATFORM, Additive Manufacturing: Strategic Research Agenda, 2014.

[19] AM PLATFORM, Additive Manufacturing: SASAM Standardisation Roadmap, 2015.

[20] K. Kempen, Expanding the materials palette for Selective Laser Melting of metals, KU Leuven, 2015.

[21] D. Bourell, M.. Leu, D.W. Rosen, Roadmap for additive manufacturing: Identifing the Future of Freeform Processing, 2009.

[22] S.A.M. Tofail, E.P. Koumoulos, A. Bandyopadhyay, S. Bose, L. O'Donoghue, C. Charitidis, Additive manufacturing: scientific and technological challenges, market uptake and opportunities, Mater. Today. 21 (2018) 22–37. doi:10.1016/j.mattod.2017.07.001.

[23] N.T. Aboulkhair, M. Simonelli, L. Parry, I. Ashcroft, C. Tuck, R. Hague, 3D printing of Aluminium alloys: Additive Manufacturing of Aluminium alloys using selective laser melting, Prog. Mater. Sci. 106 (2019) 100578. doi:10.1016/j.pmatsci.2019.100578.

[24] Q. Jia, P. Rometsch, S. Cao, K. Zhang, X. Wu, Towards a high strength aluminium alloy development methodology for selective laser melting, Mater. Des. 174 (2019) 107775. doi:10.1016/j.matdes.2019.107775.

[25] D. Buchbinder, W. Meiners, N. Pirch, K. Wissenbach, J. Schrage, Investigation on reducing distortion by preheating during manufacture of aluminum components using selective laser melting, J. Laser Appl. 26 (2014) 012004. doi:10.2351/1.4828755.

[26] M. Coduri, M. Hamidi Nasab, M. Vedani, R. Casati, V. Tirelli, Effects of Platform Pre-Heating and Thermal-Treatment Strategies on Properties of AlSi10Mg Alloy Processed by Selective Laser Melting, Metals (Basel). 8 (2018) 954. doi:10.3390/met8110954.

[27] ASTM International, Additive manufacturing — Design — Part 1 : Laser-based powder bed fusion of metals 1, ASTM Int. 2019 (2019) 1–15.

doi:10.1520/52911-1-19.2.

[28] S. Sun, M. Brandt, M. Easton, Powder bed fusion processes: An overview, Elsevier Ltd, 2017. doi:10.1016/B978-0-08-100433-3.00002-6.

[29] X.J. Wang, L.C. Zhang, M.H. Fang, T.B. Sercombe, The effect of atmosphere on the structure and properties of a selective laser melted Al-12Si alloy, Mater. Sci. Eng. A. 597 (2014) 370–375. doi:10.1016/j.msea.2014.01.012.

[30] H. Shen, P. Rometsch, X. Wu, A. Huang, Influence of Gas Flow Speed on Laser Plume Attenuation and Powder Bed Particle Pickup in Laser Powder Bed Fusion, Jom. 72 (2020) 1039–1051. doi:10.1007/s11837-020-04020-y.

[31] J.L. Bartlett, X. Li, An overview of residual stresses in metal powder bed fusion, Addit. Manuf. 27 (2019) 131–149. doi:10.1016/j.addma.2019.02.020.

[32] B. Zhang, L. Dembinski, C. Coddet, The study of the laser parameters and environment variables effect on mechanical properties of high compact parts elaborated by selective laser melting 316L powder, Mater. Sci. Eng. A. 584 (2013) 21–31. doi:10.1016/j.msea.2013.06.055.

[33] I. Yadroitsau, Selective laser melting: Direct manufacturing of 3D-objects by selective laser melting of metal powders, Lambert Academic Publishing, 2009.

[34] M. Brandt, The role of lasers in additive manufacturing, Elsevier Ltd, 2017. doi:10.1016/B978-0-08-100433-3.02001-7.

[35] D. Buchbinder, W. Meiners, K. Wissenbach, R. Poprawe, Selective laser melting of aluminum die-cast alloy—Correlations between process parameters, solidification conditions, and resulting mechanical properties, J. Laser Appl. 27 (2015) S29205. doi:10.2351/1.4906389.

[36] F. Calignano, G. Cattano, D. Manfredi, Manufacturing of thin wall structures in AlSi10Mg alloy by laser powder bed fusion through process parameters, J. Mater. Process. Technol. 255 (2018) 773–783. doi:10.1016/j.jmatprotec.2018.01.029.

[37] F. Calignano, D. Manfredi, E.P. Ambrosio, L. Iuliano, P. Fino, Influence of process parameters on surface roughness of aluminum parts produced by DMLS, Int. J. Adv. Manuf. Technol. 67 (2013) 2743–2751. doi:10.1007/s00170-012-4688-9.

[38] J.P. Kruth, X. Wang, T. Laoui, L. Froyen, Lasers and materials in selective laser sintering, Assem. Autom. 23 (2003) 357–371. doi:10.1108/01445150310698652.

[39] N.K. Tolochko, T. Laoui, Y. V. Khlopkov, S.E. Mozzharov, V.I. Titov, M.B. Ignatiev, Absorptance of powder materials suitable for laser sintering, Rapid Prototyp. J. 6 (2000) 155–160. doi:10.1108/13552540010337029.

[40] N.T. Aboulkhair, N.M. Everitt, I. Ashcroft, C. Tuck, Reducing porosity in AlSi10Mg parts processed by selective laser melting, Addit. Manuf. 1 (2014) 77–86. doi:10.1016/j.addma.2014.08.001.

[41] E. Louvis, P. Fox, C.J. Sutcliffe, Selective laser melting of aluminium

components, J. Mater. Process. Technol. 211 (2011) 275–284. doi:10.1016/j.jmatprotec.2010.09.019.

[42] D. Buchbinder, H. Schleifenbaum, S. Heidrich, W. Meiners, J. Bültmann, High power Selective Laser Melting (HP SLM) of aluminum parts, Phys. Procedia. 12 (2011) 271–278. doi:10.1016/j.phpro.2011.03.035.

[43] H. Schleifenbaum, W. Meiners, K. Wissenbach, C. Hinke, Individualized production by means of high power Selective Laser Melting, CIRP J. Manuf. Sci. Technol. 2 (2010) 161–169. doi:10.1016/j.cirpj.2010.03.005.

[44] K. Kempen, L. Thijs, J. Van Humbeeck, J.-P. Kruth, Processing AlSi10Mg by selective laser melting: parameter optimisation and material characterisation, Mater. Sci. Technol. 31 (2015) 917–923. doi:10.1179/1743284714Y.0000000702.

[45] A. Bin Anwar, Q.C. Pham, Selective laser melting of AlSi10Mg: Effects of scan direction, part placement and inert gas flow velocity on tensile strength, J. Mater. Process. Technol. 240 (2017) 388–396. doi:10.1016/j.jmatprotec.2016.10.015.

[46] D. Manfredi, F. Calignano, M. Krishnan, R. Canali, E.P. Ambrosio, E. Atzeni, From powders to dense metal parts: Characterization of a commercial alsimg alloy processed through direct metal laser sintering, Materials (Basel). 6 (2013) 856–869. doi:10.3390/ma6030856.

[47] M. Zavala-Arredondo, T. London, M. Allen, T. Maccio, S. Ward, D. Griffiths, A. Allison, P. Goodwin, C. Hauser, Use of power factor and specific point energy as design parameters in laser powder-bed-fusion (L-PBF) of AlSi10Mg alloy, Mater. Des. 182 (2019) 108018. doi:10.1016/j.matdes.2019.108018.

[48] L. Caprio, A.G. Demir, B. Previtali, Influence of pulsed and continuous wave emission on melting efficiency in selective laser melting, J. Mater. Process. Technol. 266 (2019) 429–441. doi:10.1016/j.jmatprotec.2018.11.019.

[49] M. Tang, P.C. Pistorius, J.L. Beuth, Prediction of lack-of-fusion porosity for powder bed fusion, Addit. Manuf. 14 (2017) 39–48. doi:10.1016/j.addma.2016.12.001.

[50] K. Wei, Z. Wang, X. Zeng, Preliminary investigation on selective laser melting of Ti-5Al-2.5Sn α-Ti alloy: From single tracks to bulk 3D components, J. Mater. Process. Technol. 244 (2017) 73–85. doi:10.1016/j.jmatprotec.2017.01.032.

[51] I. Yadroitsev, A. Gusarov, I. Yadroitsava, I. Smurov, Single track formation in selective laser melting of metal powders, J. Mater. Process. Technol. 210 (2010) 1624–1631. doi:10.1016/j.jmatprotec.2010.05.010.

[52] Z. Hu, B. Nagarajan, X. Song, R. Huang, W. Zhai, J. Wei, Formation of SS316L Single Tracks in Micro Selective Laser Melting: Surface, Geometry, and Defects, Adv. Mater. Sci. Eng. 2019 (2019) 1–9. doi:10.1155/2019/9451406.

[53] F. Bosio, A. Aversa, M. Lorusso, S. Marola, D. Gianoglio, L. Battezzati, P. Fino, D. Manfredi, M. Lombardi, A time-saving and cost-effective method

to process alloys by Laser Powder Bed Fusion, Mater. Des. (2019) 107949. doi:10.1016/j.matdes.2019.107949.

[54] Q. Guo, C. Zhao, M. Qu, L. Xiong, L.I. Escano, S.M.H. Hojjatzadeh, N.D. Parab, K. Fezzaa, W. Everhart, T. Sun, L. Chen, In-situ characterization and quantification of melt pool variation under constant input energy density in laser powder-bed fusion additive manufacturing process, Addit. Manuf. 28 (2019) 600–609. doi:10.1016/j.addma.2019.04.021.

[55] N.T. Aboulkhair, N.M. Everitt, I. Ashcroft, C. Tuck, Reducing porosity in AlSi10Mg parts processed by selective laser melting ☆, Addit. Manuf. 1–4 (2014) 77–86. doi:10.1016/j.addma.2014.08.001.

[56] H. Rao, S. Giet, K. Yang, X. Wu, C.H.J. Davies, The influence of processing parameters on aluminium alloy A357 manufactured by Selective Laser Melting, Mater. Des. 109 (2016) 334–346. doi:10.1016/j.matdes.2016.07.009.

[57] A.H. Maamoun, Y.F. Xue, M.A. Elbestawi, S.C. Veldhuis, Effect of selective laser melting process parameters on the quality of al alloy parts: Powder characterization, density, surface roughness, and dimensional accuracy, Materials (Basel). 11 (2018). doi:10.3390/ma11122343.

[58] W. Xiong, L. Hao, Y. Li, D. Tang, Q. Cui, Z. Feng, C. Yan, Effect of selective laser melting parameters on morphology , microstructure , densification and mechanical properties of supersaturated silver alloy, Mater. Des. 170 (2019) 107697. doi:10.1016/j.matdes.2019.107697.

[59] N. Read, W. Wang, K. Essa, M.M. Attallah, Selective laser melting of AlSi10Mg alloy: Process optimisation and mechanical properties development, Mater. Des. 65 (2015) 417–424. doi:10.1016/j.matdes.2014.09.044.

[60] S. Kumar, Selective Laser Sintering/Melting, Elsevier, 2014. doi:10.1016/B978-0-08-096532-1.01003-7.

[61] X. Su, Y. Yang, Research on track overlapping during Selective Laser Melting of powders, J. Mater. Process. Technol. 212 (2012) 2074–2079. doi:10.1016/j.jmatprotec.2012.05.012.

[62] M. Krishnan, E. Atzeni, R. Canali, F. Calignano, D. Manfredi, E.P. Ambrosio, L. Iuliano, On the effect of process parameters on properties of AlSi10Mg parts produced by DMLS, Rapid Prototyp. J. 20 (2014) 449–458. doi:10.1108/RPJ-03-2013-0028.

[63] I. Yadroitsev, I. Yadroitsava, P. Bertrand, I. Smurov, Factor analysis of selective laser melting process parameters and geometrical characteristics of synthesized single tracks, Rapid Prototyp. J. 18 (2012) 201–208. doi:10.1108/13552541211218117.

[64] X. Nie, H. Zhang, H. Zhu, Z. Hu, L. Ke, X. Zeng, Analysis of processing parameters and characteristics of selective laser melted high strength Al-Cu-Mg alloys: From single tracks to cubic samples, J. Mater. Process. Technol. 256 (2018) 69–77. doi:10.1016/j.jmatprotec.2018.01.030.

[65] A. Simchi, H. Pohl, Effects of laser sintering processing parameters on the microstructure and densification of iron powder, Mater. Sci. Eng. A. 359

(2003) 119–128. doi:10.1016/S0921-5093(03)00341-1.

[66] A. Aversa, M. Lorusso, G. Cattano, D. Manfredi, F. Calignano, E.P. Ambrosio, S. Biamino, P. Fino, M. Lombardi, M. Pavese, A study of the microstructure and the mechanical properties of an AlSiNi alloy produced via selective laser melting, J. Alloys Compd. 695 (2016) 1–9. doi:10.1016/j.jallcom.2016.10.285.

[67] I. Yadroitsev, I. Smurov, Selective laser melting technology: From the single laser melted track stability to 3D parts of complex shape, Phys. Procedia. 5 (2010) 551–560. doi:10.1016/j.phpro.2010.08.083.

[68] N.T. Aboulkhair, I. Maskery, C. Tuck, I. Ashcroft, N.M. Everitt, On the formation of AlSi10Mg single tracks and layers in selective laser melting: Microstructure and nano-mechanical properties, J. Mater. Process. Technol. 230 (2016) 88–98. doi:10.1016/j.jmatprotec.2015.11.016.

[69] E.O. Olakanmi, R.F. Cochrane, K.W. Dalgarno, Densification mechanism and microstructural evolution in selective laser sintering of Al-12Si powders, J. Mater. Process. Technol. 211 (2011) 113–121. doi:10.1016/j.jmatprotec.2010.09.003.

[70] J. Tyberg, J.H. Bohn, Local adaptive slicing for Layered Manufacturing, Rapid Prototyp. J. 4 (1998) 118–127.

[71] S. Das, Physical Aspects of Process Control in Selective Laser Sintering of Metals, Adv. Eng. Mater. 5 (2003) 701–711. doi:10.1002/adem.200310099.

[72] C. Qiu, C. Panwisawas, M. Ward, H.C. Basoalto, J.W. Brooks, M.M. Attallah, On the role of melt flow into the surface structure and porosity development during selective laser melting, Acta Mater. 96 (2015) 72–79. doi:10.1016/j.actamat.2015.06.004.

[73] D. Manfredi, F. Calignano, M. Krishnan, R. Canali, E.P. Ambrosio, S. Biamino, D. Ugues, M. Pavese, P. Fino, Additive Manufacturing of Al Alloys and Aluminium Matrix Composites (AMCs), Light Met. Alloy. Appl. (2014) 3–34. doi:10.5772/57069.

[74] P. Mercelis, J.P. Kruth, Residual stresses in selective laser sintering and selective laser melting, Rapid Prototyp. J. 12 (2006) 254–265. doi:10.1108/13552540610707013.

[75] L. Wang, X. Jiang, Y. Zhu, Z. Ding, X. Zhu, J. Sun, B. Yan, Investigation of Performance and Residual Stress Generation of AlSi10Mg Processed by Selective Laser Melting, Adv. Mater. Sci. Eng. 2018 (2018) 1–12. doi:10.1155/2018/7814039.

[76] L. Thijs, K. Kempen, J.P. Kruth, J. Van Humbeeck, Fine-structured aluminium products with controllable texture by selective laser melting of pre-alloyed AlSi10Mg powder, Acta Mater. 61 (2013) 1809–1819. doi:10.1016/j.actamat.2012.11.052.

[77] T. Kurzynowski, K. Gruber, W. Stopyra, B. Kuźnicka, E. Chlebus, Correlation between process parameters, microstructure and properties of 316 L stainless steel processed by selective laser melting, Mater. Sci. Eng. A. 718 (2018) 64–73. doi:10.1016/j.msea.2018.01.103.

[78] M.F. Zaeh, G. Branner, Investigations on residual stresses and deformations in selective laser melting, Prod. Eng. 4 (2010) 35–45. doi:10.1007/s11740-009-0192-y.

[79] L. Hitzler, C. Janousch, J. Schanz, M. Merkel, B. Heine, F. Mack, W. Hall, A. Öchsner, Direction and location dependency of selective laser melted AlSi10Mg specimens, J. Mater. Process. Technol. 243 (2017) 48–61. doi:10.1016/j.jmatprotec.2016.11.029.

[80] J.H. Rao, Y. Zhang, K. Zhang, X. Wu, A. Huang, Selective laser melted Al-7Si-0.6Mg alloy with in-situ precipitation via platform heating for residual strain removal, Mater. Des. 182 (2019) 108005. doi:10.1016/j.matdes.2019.108005.

[81] R. Mertens, S. Dadbakhsh, J. Van Humbeeck, J.P. Kruth, Application of base plate preheating during selective laser melting, Procedia CIRP. 74 (2018) 5–11. doi:10.1016/j.procir.2018.08.002.

[82] R. Mertens, B. Vrancken, N. Holmstock, Y. Kinds, J.P. Kruth, J. Van Humbeeck, Influence of powder bed preheating on microstructure and mechanical properties of H13 tool steel SLM parts, Phys. Procedia. 83 (2016) 882–890. doi:10.1016/j.phpro.2016.08.092.

[83] K.G. Prashanth, S. Scudino, J. Eckert, Defining the tensile properties of Al-12Si parts produced by selective laser melting, Acta Mater. 126 (2017) 25–35. doi:10.1016/j.actamat.2016.12.044.

[84] N. Kaufmann, M. Imran, T.M. Wischeropp, C. Emmelmann, S. Siddique, F. Walther, Influence of process parameters on the quality of aluminium alloy en AW 7075 using Selective Laser Melting (SLM), Phys. Procedia. 83 (2016) 918–926. doi:10.1016/j.phpro.2016.08.096.

[85] Z. Liu, C. Chua, K. Leong, K. Kempen, L. Thijs, E. Yasa, J. Van-Humbeeck, J. Kruth, A preliminary investigation on Selective Laser Melting of M2 high speed steel, Innov. Dev. Virtual Phys. Prototyp. (2011) 339–346. doi:10.1201/b11341-54.

[86] A.G. Demir, B. Previtali, Investigation of remelting and preheating in SLM of 18Ni300 maraging steel as corrective and preventive measures for porosity reduction, Int. J. Adv. Manuf. Technol. 93 (2017) 2697–2709. doi:10.1007/s00170-017-0697-z.

[87] B. Vrancken, S. Buls, J.-P. Kruth, J. Van Humbeeck, Preheating of Selective Laser Melted Ti6Al4V: microstructure and mechanical properties, (2016) 1269–1277.

[88] H. Ali, L. Ma, H. Ghadbeigi, K. Mumtaz, In-situ residual stress reduction, martensitic decomposition and mechanical properties enhancement through high temperature powder bed pre-heating of Selective Laser Melted Ti6Al4V, Mater. Sci. Eng. A. 695 (2017) 211–220. doi:10.1016/j.msea.2017.04.033.

[89] A. V. Müller, G. Schlick, R. Neu, C. Anstätt, T. Klimkait, J. Lee, B. Pascher, M. Schmitt, C. Seidel, Additive manufacturing of pure tungsten by means of selective laser beam melting with substrate preheating temperatures up to 1000 ∘ C, Nucl. Mater. Energy. 19 (2019) 184–188.

doi:10.1016/j.nme.2019.02.034.

[90] F. Bosio, Directed Energy Deposition of 316L Steel: Effect of Type of Powders and Gas Related Parameters, Proc. EURO PM2018. (2018) 1–6. doi:https://iris.polito.it/handle/11583/2715548.

[91] A. Saboori, A. Aversa, F. Bosio, E. Bassini, E. Librera, M. De Chirico, S. Biamino, D. Ugues, P. Fino, M. Lombardi, An investigation on the effect of powder recycling on the microstructure and mechanical properties of AISI 316L produced by Directed Energy Deposition, Mater. Sci. Eng. A. 766 (2019) 138360. doi:10.1016/j.msea.2019.138360.

[92] C. Pauzon, E. Hryha, P. Forêt, L. Nyborg, Effect of argon and nitrogen atmospheres on the properties of stainless steel 316 L parts produced by laser-powder bed fusion, Mater. Des. 179 (2019). doi:10.1016/j.matdes.2019.107873.

[93] C. Pauzon, P. Forêt, E. Hryha, T. Arunprasad, L. Nyborg, Argon-helium mixtures as Laser-Powder Bed Fusion atmospheres: Towards increased build rate of Ti-6Al-4V, J. Mater. Process. Technol. 279 (2020) 116555. doi:10.1016/j.jmatprotec.2019.116555.

[94] A. Ladewig, G. Schlick, M. Fisser, V. Schulze, U. Glatzel, Influence of the shielding gas flow on the removal of process by-products in the selective laser melting process, Addit. Manuf. 10 (2016) 1–9. doi:10.1016/j.addma.2016.01.004.

[95] T. Grünberger, R. Domröse, Direct Metal Laser Sintering: Identification of process phenomena by optical in-process monitoring, Laser Tech. J. 12 (2015) 45–48. doi:10.1002/latj.201500007.

[96] S.A. Khairallah, A.T. Anderson, A. Rubenchik, W.E. King, Laser powder-bed fusion additive manufacturing: Physics of complex melt flow and formation mechanisms of pores, spatter, and denudation zones, Acta Mater. 108 (2016) 36–45. doi:10.1016/j.actamat.2016.02.014.

[97] P. Bidare, I. Bitharas, R.M. Ward, M.M. Attallah, A.J. Moore, Fluid and particle dynamics in laser powder bed fusion, Acta Mater. 142 (2018) 107–120. doi:10.1016/j.actamat.2017.09.051.

[98] A. Bin Anwar, Q.C. Pham, Study of the spatter distribution on the powder bed during selective laser melting, Addit. Manuf. 22 (2018) 86–97. doi:10.1016/j.addma.2018.04.036.

[99] B. Ferrar, L. Mullen, E. Jones, R. Stamp, C.J. Sutcliffe, Gas flow effects on selective laser melting (SLM) manufacturing performance, J. Mater. Process. Technol. 212 (2012) 355–364. doi:10.1016/j.jmatprotec.2011.09.020.

[100] A. Aversa, M. Moshiri, E. Librera, M. Hadi, G. Marchese, D. Manfredi, M. Lorusso, F. Calignano, S. Biamino, M. Lombardi, M. Pavese, Single scan track analyses on aluminium based powders, J. Mater. Process. Technol. 255 (2018) 17–25. doi:10.1016/j.jmatprotec.2017.11.055.

[101] D. Gu, Y. Shen, Balling phenomena in direct laser sintering of stainless steel powder: Metallurgical mechanisms and control methods, Mater. Des. 30 (2009) 2903–2910. doi:10.1016/j.matdes.2009.01.013.

[102] E.O. Olakanmi, Selective laser sintering/melting (SLS/SLM) of pure Al, Al-Mg, and Al-Si powders: Effect of processing conditions and powder properties, J. Mater. Process. Technol. 213 (2013) 1387–1405. doi:10.1016/j.jmatprotec.2013.03.009.

[103] A. Simchi, Direct laser sintering of metal powders: Mechanism, kinetics and microstructural features, Mater. Sci. Eng. A. 428 (2006) 148–158. doi:10.1016/j.msea.2006.04.117.

[104] J. Ciurana, L. Hernandez, J. Delgado, Energy density analysis on single tracks formed by selective laser melting with CoCrMo powder material, Int. J. Adv. Manuf. Technol. 68 (2013) 1103–1110. doi:10.1007/s00170-013-4902-4.

[105] T. Kimura, T. Nakamoto, Microstructures and mechanical properties of A356 (AlSi7Mg0.3) aluminum alloy fabricated by selective laser melting, Mater. Des. 89 (2016) 1294–1301. doi:10.1016/j.matdes.2015.10.065.

[106] L. zhi Wang, S. Wang, J. jiao Wu, Experimental investigation on densification behavior and surface roughness of AlSi10Mg powders produced by selective laser melting, Opt. Laser Technol. 96 (2017) 88–96. doi:10.1016/j.optlastec.2017.05.006.

[107] H. Gong, K. Rafi, H. Gu, T. Starr, B. Stucker, Analysis of defect generation in Ti-6Al-4V parts made using powder bed fusion additive manufacturing processes, Addit. Manuf. 1 (2014) 87–98. doi:10.1016/j.addma.2014.08.002.

[108] U. Scipioni Bertoli, A.J. Wolfer, M.J. Matthews, J.P.R. Delplanque, J.M. Schoenung, On the limitations of Volumetric Energy Density as a design parameter for Selective Laser Melting, Mater. Des. 113 (2017) 331–340. doi:10.1016/j.matdes.2016.10.037.

[109] A.T. Sutton, C.S. Kriewall, M.C. Leu, J.W. Newkirk, Powder characterisation techniques and effects of powder characteristics on part properties in powder-bed fusion processes, Virtual Phys. Prototyp. 12 (2017) 3–29. doi:10.1080/17452759.2016.1250605.

[110] D. Herzog, V. Seyda, E. Wycisk, C. Emmelmann, Additive manufacturing of metals, Acta Mater. 117 (2016) 371–392. doi:10.1016/j.actamat.2016.07.019.

[111] R. Li, Y. Shi, Z. Wang, L. Wang, J. Liu, W. Jiang, Densification behavior of gas and water atomized 316L stainless steel powder during selective laser melting, Appl. Surf. Sci. 256 (2010) 4350–4356. doi:10.1016/j.apsusc.2010.02.030.

[112] J. Dawes, R. Bowerman, R. Trepleton, Introduction to the additive manufacturing powder metallurgy supply chain, Johnson Matthey Technol. Rev. 59 (2015) 243–256. doi:10.1595/205651315X688686.

[113] P. Sun, Z.Z. Fang, Y. Zhang, Y. Xia, Review of the Methods for Production of Spherical Ti and Ti Alloy Powder, Jom. 69 (2017) 1853–1860. doi:10.1007/s11837-017-2513-5.

[114] L.E. Murr, E. Martinez, J. Hernandez, S. Collins, K.N. Amato, S.M. Gaytan, P.W. Shindo, Microstructures and properties of 17-4 PH stainless

steel fabricated by selective laser melting, J. Mater. Res. Technol. 1 (2012) 167–177. doi:10.1016/S2238-7854(12)70029-7.

[115] T. Starr, K. Rafi, B. Stucker, C. Scherzer, Controlling phase composition in selective laser melted stainless steels, (2012) 439–446.

[116] M. Entezarian, F. Allaire, P. Tsantrizos, R.A.L. Drew, Plasma atomization: A new process for the production of fine, spherical powders, Jom. 48 (1996) 53–55. doi:10.1007/BF03222969.

[117] David Palousek, L. Pantelejev, T. Zikmund, D. Koutny, Processing of nearly pure iron using 400W selective laser melting - initial study, (2017) 1738–1743. doi:10.17973/MMSJ.2017.

[118] M. Letenneur, V. Brailovski, A. Kreitcberg, V. Paserin, I. Bailon-Poujol, Laser Powder Bed Fusion of Water-Atomized Iron-Based Powders: Process Optimization, J. Manuf. Mater. Process. 1 (2017) 23. doi:10.3390/jmmp1020023.

[119] I.E. Anderson, E.M.H. White, R. Dehoff, Feedstock powder processing research needs for additive manufacturing development, Curr. Opin. Solid State Mater. Sci. 22 (2018) 8–15. doi:10.1016/j.cossms.2018.01.002.

[120] S. Özbilen, Satellite formation mechanism in gas atomized powders, Powder Metall. 42 (1999) 70–78. doi:10.1179/pom.1999.42.1.70.

[121] A.B. Spierings, G. Levy, Comparison of density of stainless steel 316L parts produced with Selective Laser Melting using different powder grades, 20th Annu. Int. Solid Free. Fabr. Symp. SFF 2009. (2009) 342–353.

[122] J.H. Tan, W.L.E. Wong, K.W. Dalgarno, An overview of powder granulometry on feedstock and part performance in the selective laser melting process, Addit. Manuf. 18 (2017) 228–255. doi:10.1016/j.addma.2017.10.011.

[123] M. Simonelli, C. Tuck, N.T. Aboulkhair, I. Maskery, I. Ashcroft, R.D. Wildman, R. Hague, A Study on the Laser Spatter and the Oxidation Reactions During Selective Laser Melting of 316L Stainless Steel, Al-Si10-Mg, and Ti-6Al-4V, Metall. Mater. Trans. A Phys. Metall. Mater. Sci. 46 (2015) 3842–3851. doi:10.1007/s11661-015-2882-8.

[124] R. Li, J. Liu, Y. Shi, L. Wang, W. Jiang, Balling behavior of stainless steel and nickel powder during selective laser melting process, Int. J. Adv. Manuf. Technol. 59 (2012) 1025–1035. doi:10.1007/s00170-011-3566-1.

[125] M. Tang, P.C. Pistorius, Oxides, porosity and fatigue performance of AlSi10Mg parts produced by selective laser melting, Int. J. Fatigue. 94 (2017) 192–201. doi:10.1016/j.ijfatigue.2016.06.002.

[126] R.J. Hebert, Viewpoint: metallurgical aspects of powder bed metal additive manufacturing, J. Mater. Sci. 51 (2016) 1165–1175. doi:10.1007/s10853-015-9479-x.

[127] C. Weingarten, D. Buchbinder, N. Pirch, W. Meiners, K. Wissenbach, R. Poprawe, Formation and reduction of hydrogen porosity during selective laser melting of AlSi10Mg, J. Mater. Process. Technol. 221 (2015) 112–120. doi:10.1016/j.jmatprotec.2015.02.013.

[128] X.P. Li, K.M. O'Donnell, T.B. Sercombe, Selective laser melting of Al-12Si alloy: Enhanced densification via powder drying, Addit. Manuf. 10 (2016) 10–14. doi:10.1016/j.addma.2016.01.003.

[129] B.H. Rabin, G.R. Smolik, G.E. Korth, Characterization of entrapped gases in rapidly solidified powders, Mater. Sci. Eng. A. 124 (1990) 1–7. doi:10.1016/0921-5093(90)90328-Z.

[130] L.C. Ardila, F. Garciandia, J.B. González-Díaz, P. Álvarez, A. Echeverria, M.M. Petite, R. Deffley, J. Ochoa, Effect of IN718 recycled powder reuse on properties of parts manufactured by means of Selective Laser Melting, Phys. Procedia. 56 (2014) 99–107. doi:10.1016/j.phpro.2014.08.152.

[131] V. Seyda, N. Kaufmann, C. Emmelmann, Investigation of Aging Processes of Ti-6Al-4 v Powder Material in Laser Melting, Phys. Procedia. 39 (2012) 425–431. doi:10.1016/j.phpro.2012.10.057.

[132] A. Strondl, O. Lyckfeldt, H. Brodin, U. Ackelid, Characterization and Control of Powder Properties for Additive Manufacturing, Jom. 67 (2015) 549–554. doi:10.1007/s11837-015-1304-0.

[133] U. Tradowsky, J. White, R.M. Ward, N. Read, W. Reimers, M.M. Attallah, Selective laser melting of AlSi10Mg: Influence of post-processing on the microstructural and tensile properties development, Mater. Des. 105 (2016) 212–222. doi:10.1016/j.matdes.2016.05.066.

[134] A.H. Maamoun, M. Elbestawi, G.K. Dosbaeva, S.C. Veldhuis, Thermal post-processing of AlSi10Mg parts produced by Selective Laser Melting using recycled powder, Addit. Manuf. 21 (2018) 234–247. doi:10.1016/j.addma.2018.03.014.

[135] D.D. Gu, W. Meiners, K. Wissenbach, R. Poprawe, Laser additive manufacturing of metallic components: Materials, processes and mechanisms, Int. Mater. Rev. 57 (2012) 133–164. doi:10.1179/1743280411Y.0000000014.

[136] L. Thijs, Microstructure and texture of metal parts produced by Selective Laser Melting, 2014. doi:ISBN 978-94-6018-795-7.

[137] Marleen Rombouts, Selective laser sintering/melting of iron-based powders, 2006.

[138] X. Han, H. Zhu, X. Nie, G. Wang, X. Zeng, Investigation on selective laser melting AlSi10Mg cellular lattice strut: Molten pool morphology, surface roughness and dimensional accuracy, Materials (Basel). 11 (2018). doi:10.3390/ma11030392.

[139] N. Eustathopoulos, M.G. Nicholas, B.B. Drevet, Wettability at high temperatures, 1999. doi:0080421466.

[140] S. Schiaffino, A.A. Sonin, Molten droplet deposition and solidification at low Weber numbers, Phys. Fluids. 9 (1997) 3172–3187. doi:10.1063/1.869434.

[141] S. Lu, H. Fujii, K. Nogi, Marangoni convection and weld shape variations in Ar-O2 and Ar-CO2 shielded GTA welding, Mater. Sci. Eng. A. 380 (2004) 290–297. doi:10.1016/j.msea.2004.05.057.

[142] P. Yuan, D. Gu, Molten pool behaviour and its physical mechanism during selective laser melting of TiC/AlSi10Mg nanocomposites: Simulation and experiments, J. Phys. D. Appl. Phys. 48 (2015) 35303. doi:10.1088/0022-3727/48/3/035303.

[143] Marleen Rombouts, J.-P. Kruth, L. Froyen, P. Mercelis, Fundamentals of Selective Laser Melting of alloyed steel powders, CIRP Ann. Manuf. Technol. (2006) 187–192.

[144] X. Zhou, X. Liu, D. Zhang, Z. Shen, W. Liu, Balling phenomena in selective laser melted tungsten, J. Mater. Process. Technol. 222 (2015) 33–42. doi:10.1016/j.jmatprotec.2015.02.032.

[145] H.J. Niu, I.T.H. Chang, Instability of scan tracks of selective laser sintering of high speed steel powder, Scr. Mater. 41 (1999) 1229–1234. doi:10.1016/S1359-6462(99)00276-6.

[146] P.-G. de Gennes, Françoise Brochard-Wyart, David Quéré, Capillarity and Wetting Phenomena: Drops, Bubbles, Pearls, Waves, Springer, New York, NY, 2004.

[147] Chandrasekhar S, Hydrodynamic and Hydromagnetic Stability, Dover Publications, New York, 1981.

[148] C. Tang, K.Q. Le, C.H. Wong, Physics of humping formation in laser powder bed fusion, 149 (2020). doi:10.1016/j.ijheatmasstransfer.2019.119172.

[149] J.P. Kruth, L. Froyen, J. Van Vaerenbergh, P. Mercelis, M. Rombouts, B. Lauwers, Selective laser melting of iron-based powder, J. Mater. Process. Technol. 149 (2004) 616–622. doi:10.1016/j.jmatprotec.2003.11.051.

[150] S.I. Anisimov, Viktor A. Khokhlov, Instabilities in laser-matter interaction, (1995) 147.

[151] V. Semak, A. Matsunawa, The role of recoil pressure in energy balance during laser materials processing, J. Phys. D. Appl. Phys. 30 (1997) 2541–2552. doi:10.1088/0022-3727/30/18/008.

[152] Y. Zhang, J. Zhang, Modeling of solidification microstructure evolution in laser powder bed fusion fabricated 316L stainless steel using combined computational fluid dynamics and cellular automata, Addit. Manuf. 28 (2019) 750–765. doi:10.1016/j.addma.2019.06.024.

[153] L. Han, F.W. Liou, Numerical investigation of the influence of laser beam mode on melt pool, Int. J. Heat Mass Transf. 47 (2004) 4385–4402. doi:10.1016/j.ijheatmasstransfer.2004.04.036.

[154] E.H. Amara, R. Fabbro, Modelling of gas jet effect on the melt pool movements during deep penetration laser welding, J. Phys. D. Appl. Phys. 41 (2008). doi:10.1088/0022-3727/41/5/055503.

[155] S. Kou, Weld Metal Solidification I: Grain Structure, in: Weld. Metall., John Wiley & Sons, 2003: pp. 170–198.

[156] J. Zhang, B. Song, Q. Wei, D. Bourell, Y. Shi, A review of selective laser melting of aluminum alloys: Processing, microstructure, property and developing trends, J. Mater. Sci. Technol. 35 (2019) 270–284.

doi:10.1016/j.jmst.2018.09.004.

[157] M. Ma, Z. Wang, X. Zeng, A comparison on metallurgical behaviors of 316L stainless steel by selective laser melting and laser cladding deposition, Mater. Sci. Eng. A. 685 (2017) 265–273. doi:10.1016/j.msea.2016.12.112.

[158] P. D.A., E. K.E., Solidification, in: Springer Science (Ed.), Phase Transform. Met. Alloy., 1992: pp. 185–262. doi:10.1007/978-1-4899-3051-4.

[159] Z. Liu, L.C. Zhang, Y. Yang, Y. Jiang, G.W. Wang, Y.J. Liu, Gradient in microstructure and mechanical property of selective laser melted AlSi10Mg, in: J. Alloys Compd., Elsevier B.V, 2017: pp. 1414–1421. doi:10.1016/j.jallcom.2017.11.020.

[160] Sindo Kou, Weld Metal Solidification II: Microstructure withing Grains, in: Hohn Wiley & Sons (Ed.), Weld. Metall., 2003: pp. 199–215.

[161] P.A. Hooper, Melt pool temperature and cooling rates in laser powder bed fusion, Addit. Manuf. 22 (2018) 548–559. doi:10.1016/j.addma.2018.05.032.

[162] S. Kou, Basic Solidification Concepts, in: Weld. Metall., John Wiley & Sons, 2003: pp. 145–169.

[163] D. Gianoglio, S. Marola, L. Battezzati, A. Aversa, F. Bosio, M. Lombardi, D. Manfredi, M. Lorusso, Banded microstructures in rapidly solidified Al-3 wt% Er, Intermetallics. 119 (2020) 106724. doi:10.1016/j.intermet.2020.106724.

[164] W.A. Tiller, K.A. Jackson, J.W. Rutter, B. Chalmers, The redistribution of solute atoms during the solidification of metals, Acta Metall. 1 (1953) 428–437. doi:10.1016/0001-6160(53)90126-6.

[165] B. Zhang, Y. Li, Q. Bai, Defect Formation Mechanisms in Selective Laser Melting: A Review, Chinese J. Mech. Eng. (English Ed. 30 (2017) 515–527. doi:10.1007/s10033-017-0121-5.

[166] J.W. Elmer, J. Vaja, H.D. Carlton, R. Pong, The effect of Ar and N2 shielding gas on laser weld porosity in steel, stainless steels, and nickel, Weld. J. 94 (2015) 313s-325s.

[167] M.M. Collur, A. Paul, T. Debroy, Mechanism of alloying element vaporization during laser welding, Metall. Trans. B. 18 (1987) 733–740. doi:10.1007/BF02672891.

[168] K. Kempen, L. Thijs, E. Yasa, M. Badrossamay, W. Verheecke, J.P. Kruth, Process Optimization and micostructural analysis for Selective Laser Melting of AlSi10Mg, Solid Free. Fabr. (2011) 484–495.

[169] T.C. Dzogbewu, I. Yadroitsev, P. Krakhmalev, I. Yadroitsava, A. Du Plessis, Optimal Process Parameters for In Situ Alloyed Ti15mo Structures By Laser Powder Bed Fusion, 28th Annu. Int. Solid Free. Fabr. Symp. – An Addit. Manuf. Conf. (2017) 75–96. https://sffsymposium.engr.utexas.edu/sites/default/files/2017/Manuscripts/OptimalProcessParametersforInSituAlloyedTi1.pdf.

[170] W.E. King, H.D. Barth, V.M. Castillo, G.F. Gallegos, J.W. Gibbs, D.E. Hahn, C. Kamath, A.M. Rubenchik, Observation of keyhole-mode laser melting in laser powder-bed fusion additive manufacturing, J. Mater. Process. Technol. 214 (2014) 2915–2925. doi:10.1016/j.jmatprotec.2014.06.005.

[171] Q.C. Liu, J. Elambasseril, S.J. Sun, M. Leary, M. Brandt, P.K. Sharp, The effect of manufacturing defects on the fatigue behaviour of Ti-6Al-4V specimens fabricated using selective laser melting, Adv. Mater. Res. 891–892 (2014) 1519–1524. doi:10.4028/www.scientific.net/AMR.891-892.1519.

[172] S. Kou, Solidification and Liquation Cracking Issues in Welding, JOM. (2003) 37–42.

[173] T. Soysal, S. Kou, A simple test for assessing solidification cracking susceptibility and checking validity of susceptibility prediction, Acta Mater. 143 (2018) 181–197. doi:10.1016/j.actamat.2017.09.065.

[174] J.H. Martin, B.D. Yahata, J.M. Hundley, J.A. Mayer, T.A. Schaedler, T.M. Pollock, 3D printing of high-strength aluminium alloys, Nature. 549 (2017) 365–369. doi:10.1038/nature23894.

[175] G. Marchese, E. Bassini, A. Aversa, M. Lombardi, D. Ugues, P. Fino, S. Biamino, Microstructural evoultion of post-processed Hastelloy X alloy fabricated by Laser Powder Bed Fusion, Materials (Basel). 486 (2019). doi:https://doi.org/10.3390/ma12030486.

[176] M.L. Montero Sistiaga, R. Mertens, B. Vrancken, X. Wang, B. Van Hooreweder, J.P. Kruth, J. Van Humbeeck, Changing the alloy composition of Al7075 for better processability by selective laser melting, Elsevier B.V., 2016. doi:10.1016/j.jmatprotec.2016.08.003.

[177] M.V. R. Casati, M. Coduri, M.Riccio, A. Rizzi, Development of a high strength Al-Zn-Si-Mg-Cu alloy for selective laser melting, J. Alloy. Compd. Submitt. 801 (2018) 243–253. doi:10.1016/j.jallcom.2019.06.123.

[178] D. Dai, D. Gu, Influence of thermodynamics within molten pool on migration and distribution state of reinforcement during selective laser melting of AlN/AlSi10Mg composites, Int. J. Mach. Tools Manuf. 100 (2016) 14–24. doi:10.1016/j.ijmachtools.2015.10.004.

[179] S. Bagherifard, N. Beretta, S. Monti, M. Riccio, M. Bandini, M. Guagliano, On the fatigue strength enhancement of additive manufactured AlSi10Mg parts by mechanical and thermal post-processing, Mater. Des. 145 (2018) 28–41. doi:10.1016/j.matdes.2018.02.055.

[180] D. Gu, Y. Shen, Balling phenomena during direct laser sintering of multi-component Cu-based metal powder, J. Alloys Compd. 432 (2007) 163–166. doi:10.1016/j.jallcom.2006.06.011.

[181] K. Mumtaz, N. Hopkinson, Top surface and side roughness of Inconel 625 parts processed using selective laser melting, Rapid Prototyp. J. 15 (2009) 96–103. doi:10.1108/13552540910943397.

[182] M. Taheri Andani, R. Dehghani, M.R. Karamooz-Ravari, R. Mirzaeifar, J. Ni, A study on the effect of energy input on spatter particles creation during

selective laser melting process, Addit. Manuf. 20 (2018) 33–43. doi:10.1016/j.addma.2017.12.009.

[183] Y. Liu, Y. Yang, S. Mai, D. Wang, C. Song, Investigation into spatter behavior during selective laser melting of AISI 316L stainless steel powder, Mater. Des. 87 (2015) 797–806. doi:10.1016/j.matdes.2015.08.086.

[184] M. Taheri Andani, R. Dehghani, M.R. Karamooz-Ravari, R. Mirzaeifar, J. Ni, Spatter formation in selective laser melting process using multi-laser technology, Mater. Des. 131 (2017) 460–469. doi:10.1016/j.matdes.2017.06.040.

[185] N.T. Aboulkhair, I. Maskery, C. Tuck, I. Ashcroft, N.M. Everitt, Improving the fatigue behaviour of a selectively laser melted aluminium alloy : Influence of heat treatment and surface quality, JMADE. 104 (2016) 174–182. doi:10.1016/j.matdes.2016.05.041.

[186] J.E. Hatch, Properties of commercial casting alloys, in: Alum. Prop. Phys. Metall., ASM International, 1984: pp. 320–350. doi:10.1361/appm1984p001.

[187] T. Kimura, T. Nakamoto, T. Ozaki, K. Sugita, M. Mizuno, H. Araki, Microstructural formation and characterization mechanisms of selective laser melted Al–Si–Mg alloys with increasing magnesium content, Mater. Sci. Eng. A. (2019) 1–13. doi:10.1016/j.msea.2019.02.015.

[188] N.T. Aboulkhair, Additive manufacture of an aluminium alloy: processing, microstructure, and mechanical properties., University of Nottingham, 2015. http://eprints.nottingham.ac.uk/31152/1/Final_PhD Thesis_Nesma_Approved.pdf.

[189] X.P. Li, X.J. Wang, M. Saunders, A. Suvorova, L.C. Zhang, Y.J. Liu, M.H. Fang, Z.H. Huang, T.B. Sercombe, A selective laser melting and solution heat treatment refined Al-12Si alloy with a controllable ultrafine eutectic microstructure and 25% tensile ductility, Acta Mater. 95 (2015) 74–82. doi:10.1016/j.actamat.2015.05.017.

[190] L. Zhou, A. Mehta, E. Schulz, B. McWilliams, K. Cho, Y. Sohn, Microstructure, precipitates and hardness of selectively laser melted AlSi10Mg alloy before and after heat treatment, Mater. Charact. 143 (2018) 5–17. doi:10.1016/j.matchar.2018.04.022.

[191] H. Zhang, H. Zhu, T. Qi, Z. Hu, X. Zeng, Selective laser melting of high strength Al-Cu-Mg alloys: Processing, microstructure and mechanical properties, Mater. Sci. Eng. A. 656 (2016) 47–54. doi:10.1016/j.msea.2015.12.101.

[192] ASM International, Properties of Cast Aluminium Alloys, in: Prop. Sel. Nonferrous Alloy. Spec. Mater. - Vol. 2, ASM International, n.d.: pp. 569–666.

[193] ASM International, Properties of Wrought Aluminium and Aluminium Alloys, in: Prop. Sel. Nonferrous Alloy. Spec. Mater. - Vol. 2, ASM International, n.d.: pp. 222–483.

[194] L. Girelli, M. Tocci, M. Gelfi, A. Pola, Study of heat treatment parameters

for additively manufactured AlSi10Mg in comparison with corresponding cast alloy, Mater. Sci. Eng. A. 739 (2019) 317–328. doi:10.1016/j.msea.2018.10.026.

[195] T. Qi, H. Zhu, H. Zhang, J. Yin, L. Ke, X. Zeng, Selective laser melting of Al7050 powder: Melting mode transition and comparison of the characteristics between the keyhole and conduction mode, Mater. Des. 135 (2017) 257–266. doi:10.1016/j.matdes.2017.09.014.

[196] S. Marola, D. Manfredi, G. Fiore, M.G. Poletti, M. Lombardi, P. Fino, L. Battezzati, A comparison of Selective Laser Melting with bulk rapid solidification of AlSi10Mg alloy, J. Alloys Compd. 742 (2018) 271–279. doi:10.1016/j.jallcom.2018.01.309.

[197] Hugh Baker, Binary Alloy Phase Diagrams, in: A. International (Ed.), ASM Hanb. - Alloy Phase Diagrams, 1992: p. 52.

[198] R. Casati, M. Coduri, S. Checchia, M. Vedani, Insight into the effect of different thermal treatment routes on the microstructure of AlSi7Mg produced by laser powder bed fusion, Mater. Charact. 172 (2021) 110881. doi:10.1016/j.matchar.2021.110881.

[199] J.D. EMBURY, D.J. LLOYD, T.R. RAMACHANDRAN, Strengthening Mechanisms in Aluminum Alloys, 31 (1989) 579–601. doi:10.1016/b978-0-12-341831-9.50027-9.

[200] I. J. Polmear, Physical metallurgy of aluminium alloys, in: Light Alloy. From Tradit. Alloy. to Nanocrystals, Elsevier, 2006: pp. 29–96.

[201] K. Ma, H. Wen, T. Hu, T.D. Topping, D. Isheim, D.N. Seidman, E.J. Lavernia, J.M. Schoenung, Mechanical behavior and strengthening mechanisms in ultrafine grain precipitation-strengthened aluminum alloy, Acta Mater. 62 (2014) 141–155. doi:10.1016/j.actamat.2013.09.042.

[202] Y. Shi, K. Yang, S.K. Kairy, F. Palm, X. Wu, P.A. Rometsch, Effect of platform temperature on the porosity, microstructure and mechanical properties of an Al–Mg–Sc–Zr alloy fabricated by selective laser melting, Mater. Sci. Eng. A. 732 (2018) 41–52. doi:10.1016/j.msea.2018.06.049.

[203] Q. Jia, P. Rometsch, P. Kürnsteiner, Q. Chao, A. Huang, M. Weyland, L. Bourgeois, X. Wu, Selective laser melting of a high strength AlMnSc alloy: Alloy design and strengthening mechanisms, Acta Mater. 171 (2019) 108–118. doi:10.1016/j.actamat.2019.04.014.

[204] I. J. Polmear, Novel materials and processing methods, in: Light Alloy. From Tradit. Alloy. to Nanocrystals, Elsevier, 2006: pp. 367–412.

[205] T. Maeshima, K. Oh-ishi, Solute clustering and supersaturated solid solution of AlSi10Mg alloy fabricated by selective laser melting, Heliyon. (2019) e01186. doi:10.1016/j.heliyon.2019.e01186.

[206] K. V. Yang, P. Rometsch, C.H.J. Davies, A. Huang, X. Wu, Effect of heat treatment on the microstructure and anisotropy in mechanical properties of A357 alloy produced by selective laser melting, Mater. Des. 154 (2018) 275–290. doi:10.1016/j.matdes.2018.05.026.

[207] L.J. Colley, M.A. Wells, W.J. Poole, Microstructure-yield strength models

for heat treatment of Al-Si-Mg casting alloys II: Modelling microstructure and yield strength evolution, Can. Metall. Q. 53 (2014) 138–150. doi:10.1179/1879139513Y.0000000111.

[208] P.A. Rometsch, G.B. Schaffer, An age hardening model for Al-7Si-Mg casting alloys, Mater. Sci. Eng. A. 325 (2002) 424–434. doi:10.1016/S0921-5093(01)01479-4.

[209] S. Esmaeili, D.J. Lloyd, W.J. Poole, Modeling of precipitation hardening for the naturally aged Al-Mg-Si-Cu alloy AA6111, Acta Mater. 51 (2003) 3467–3481. doi:10.1016/S1359-6454(03)00167-8.

[210] M. Murayama, K. Hono, Three dimensional atom probe analysis of pre-precipitate clustering in an Al-Cu-Mg-Ag alloy, Scr. Mater. 38 (1998) 1315–1319. doi:10.1016/S1359-6462(98)00027-X.

[211] P. D.A., E. K.E., Diffusional Transformations in Solids, in: Springer science (Ed.), Phase Transform. Met. Alloy., 1992: pp. 291–308. doi:10.1007/978-1-4899-3051-4.

[212] M.F. Ashby, The light alloy, in: Eng. Mater. 2. An Introd. to Microstruct. Process. Des., Second edi, Butterworth Heinmann, 1999: pp. 100–132.

[213] S. J.M, H. T.J, H. H.K, Structural Ageing Characteristics of Aluminum-Copper Alloys, J. Inst. Met. 82 (n.d.) 239–248.

[214] ASTM International B917/B917M-12, Standard Practice for Heat Treatment of Aluminum-Alloy Castings from All Processes, ASTM B. Stand. 01 (2012) 1–11. doi:10.1520/B0917.

[215] S. Li, J. Liu, Y. Shi, Q. Wei, W. Li, A. Zhang, C. Yan, Y. Zhou, Effect of heat treatment on AlSi10Mg alloy fabricated by selective laser melting: Microstructure evolution, mechanical properties and fracture mechanism, Mater. Sci. Eng. A. 663 (2016) 116–125. doi:10.1016/j.msea.2016.03.088.

[216] K.G. Prashanth, S. Scudino, H.J. Klauss, K.B. Surreddi, L. Löber, Z. Wang, A.K. Chaubey, U. Kühn, J. Eckert, Microstructure and mechanical properties of Al-12Si produced by selective laser melting: Effect of heat treatment, Mater. Sci. Eng. A. 590 (2014) 153–160. doi:10.1016/j.msea.2013.10.023.

[217] N.T. Aboulkhair, I. Maskery, C. Tuck, I. Ashcroft, N.M. Everitt, The microstructure and mechanical properties of selectively laser melted AlSi10Mg: The effect of a conventional T6-like heat treatment, Mater. Sci. Eng. A. 667 (2016) 139–146. doi:10.1016/j.msea.2016.04.092.

[218] P. Wang, C. Gammer, F. Brenne, K.G. Prashanth, R.G. Mendes, M.H. Rümmeli, T. Gemming, J. Eckert, S. Scudino, Microstructure and mechanical properties of a heat-treatable Al-3.5Cu-1.5Mg-1Si alloy produced by selective laser melting, Mater. Sci. Eng. A. 711 (2018) 562–570. doi:10.1016/j.msea.2017.11.063.

[219] Y. Qi, H. Zhang, J. Zhu, X. Nie, Z. Hu, H. Zhu, X. Zeng, Mechanical behavior and microstructure evolution of Al-Cu-Mg alloy produced by laser powder bed fusion: Effect of heat treatment, Mater. Charact. 165 (2020) 110364. doi:10.1016/j.matchar.2020.110364.

[220] N.T. Aboulkhair, C. Tuck, I.A.N. Ashcroft, I.A.N. Maskery, N.M. Everitt, On the Precipitation Hardening of Selective Laser Melted AlSi10Mg, Metall. Mater. Trans. A. 46 (2015) 3337–3341. doi:10.1007/s11661-015-2980-7.

[221] A. Aversa, M. Lorusso, F. Trevisan, E. Ambrosio, F. Calignano, D. Manfredi, S. Biamino, P. Fino, M. Lombardi, M. Pavese, Effect of Process and Post-Process Conditions on the Mechanical Properties of an A357 Alloy Produced via Laser Powder Bed Fusion, Metals (Basel). 7 (2017) 68. doi:10.3390/met7020068.

[222] R. Casati, M. Vedani, Aging Response of an A357 Al Alloy Processed by Selective Laser Melting, Adv. Eng. Mater. 1800406 (2018) 1800406. doi:10.1002/adem.201800406.

[223] C.H.J. Davies, K. Zhang, J.H. Rao, X. Wu, A. Huang, Y. Zhang, Multiple precipitation pathways in an Al-7Si-0.6Mg alloy fabricated by selective laser melting, Scr. Mater. 160 (2018) 66–69. doi:10.1016/j.scriptamat.2018.09.045.

[224] P. Rometsch, Q. Jia, K. V. Yang, X. Wu, Aluminum alloys for selective laser melting – towards improved performance, Elsevier Inc., 2019. doi:10.1016/b978-0-12-814062-8.00016-9.

[225] H.A. Ferguson, Heat Treating of Aluminium Alloy, Heat Treat. Alum. Alloy. 4 (1991) 841–879. doi:10.1361/asmhba0001205.

[226] EOS GmbH - Electro Optical Systems, Material Data Sheet: EOS Aluminium AlSi10Mg, 49 (2014) 1–5. http://gpiprototype.com/images/PDF/EOS_Aluminium_AlSi10Mg_en.pdf.

[227] P. Ma, K. Prashanth, S. Scudino, Y. Jia, H. Wang, C. Zou, Z. Wei, J. Eckert, Influence of Annealing on Mechanical Properties of Al-20Si Processed by Selective Laser Melting, Metals (Basel). 4 (2014) 28–36. doi:10.3390/met4010028.

[228] J. Fiocchi, A. Tuissi, P. Bassani, C.A. Biffi, Low temperature annealing dedicated to AlSi10Mg selective laser melting products, J. Alloys Compd. 695 (2017) 3402–3409. doi:10.1016/j.jallcom.2016.12.019.

[229] J. Fiocchi, C.A. Biffi, Ad Hoc Heat Treatments for Selective Laser Melted Alsi10mg Alloy Aimed at Stress-Relieving and Enhancing Mechanical Performances, JOM. (2020). doi:10.1007/s11837-019-03973-z.

[230] J.R. Cahoon, W.H. Broughton, A.R. Kutzak, The determination of yield strength from hardness measurements, Metall. Trans. 2. (1971). doi:https://doi.org/10.1007/BF02913433.

[231] J.S. Zuback, T. DebRoy, The hardness of additively manufactured alloys, Materials (Basel). 11 (2018). doi:10.3390/ma11112070.

[232] A.H. Maamoun, Y.F. Xue, M.A. Elbestawi, S.C. Veldhuis, The effect of selective laser melting process parameters on the microstructure and mechanical properties of Al6061 and AlSi10Mg alloys, Materials (Basel). 12 (2018). doi:10.3390/ma12010012.

[233] F. Bosio, H. Shen, Y. Liu, M. Lombardi, P. Rometsch, X. Wu, Y. Zhu, A.

Huang, Production Strategy for Manufacturing Large-Scale AlSi10Mg Components by Laser Powder Bed Fusion, Jom. (2021). doi:10.1007/s11837-020-04523-8.

[234] L. Roger, Technical data sheets for heat treated aluminium high pressure die castings, CSIRO Light Met. Flagsh. (2008). http://csiro.au/science/ps1f1.html.

[235] Y. Bai, Y. Yang, Z. Xiao, M. Zhang, D. Wang, Process optimization and mechanical property evolution of AlSiMg0.75 by selective laser melting, Mater. Des. 140 (2018) 257–266. doi:10.1016/j.matdes.2017.11.045.

[236] K.G. Prashanth, B. Debalina, Z. Wang, P.F. Gostin, A. Gebert, M. Calin, U. Kühn, M. Kamaraj, S. Scudino, J. Eckert, Tribological and corrosion properties of Al-12Si produced by selective laser melting, J. Mater. Res. 29 (2014) 2044–2054. doi:10.1557/jmr.2014.133.

[237] K. Kempen, L. Thijs, J. Van Humbeeck, J.-P. Kruth, Mechanical Properties of AlSi10Mg Produced by Selective Laser Melting, Phys. Procedia. 39 (2012) 439–446. doi:10.1016/j.phpro.2012.10.059.

[238] I. Rosenthal, A. Stern, N. Frage, Microstructure and Mechanical Properties of AlSi10Mg Parts Produced by the Laser Beam Additive Manufacturing (AM) Technology, Metallogr. Microstruct. Anal. 3 (2014) 448–453. doi:10.1007/s13632-014-0168-y.

[239] N. Takata, H. Kodaira, A. Suzuki, M. Kobashi, Size dependence of microstructure of AlSi10Mg alloy fabricated by selective laser melting, Mater. Charact. 143 (2018) 18–26. doi:10.1016/j.matchar.2017.11.052.

[240] N. Takata, H. Kodaira, K. Sekizawa, A. Suzuki, M. Kobashi, Change in microstructure of selectively laser melted AlSi10Mg alloy with heat treatments, Mater. Sci. Eng. A. 704 (2017) 218–228. doi:10.1016/j.msea.2017.08.029.

[241] J. Rao, The influence of Processinf and Heat Treatment Parameters on Selective Laser Melted Aluminium Alloy A357, Monash University, 2017.

[242] I. Rosenthal, R. Shneck, A. Stern, Heat treatment effect on the mechanical properties and fracture mechanism in AlSi10Mg fabricated by additive manufacturing selective laser melting process, Mater. Sci. Eng. A. 729 (2018) 310–322. doi:10.1016/j.msea.2018.05.074.

[243] J.H. Rao, Y. Zhang, X. Fang, Y. Chen, X. Wu, C.H.J. Davies, The origins for tensile properties of selective laser melted aluminium alloy A357, Addit. Manuf. 17 (2017) 113–122. doi:10.1016/j.addma.2017.08.007.

[244] T.M. Mower, M.J. Long, Mechanical behavior of additive manufactured, powder-bed laser-fused materials, Mater. Sci. Eng. A. 651 (2016) 198–213. doi:10.1016/j.msea.2015.10.068.

[245] K. V. Yang, P. Rometsch, T. Jarvis, J. Rao, S. Cao, C. Davies, X. Wu, Porosity formation mechanisms and fatigue response in Al-Si-Mg alloys made by selective laser melting, Mater. Sci. Eng. A. 712 (2018) 166–174. doi:10.1016/j.msea.2017.11.078.

[246] S. Siddique, M. Imran, M. Rauer, M. Kaloudis, E. Wycisk, C. Emmelmann,

F. Walther, Computed tomography for characterization of fatigue performance of selective laser melted parts, Mater. Des. 83 (2015) 661–669. doi:10.1016/j.matdes.2015.06.063.

[247] A. Yadollahi, N. Shamsaei, Additive manufacturing of fatigue resistant materials: Challenges and opportunities, Int. J. Fatigue. 98 (2017) 14–31. doi:10.1016/j.ijfatigue.2017.01.001.

[248] S. Siddique, M. Imran, F. Walther, Very high cycle fatigue and fatigue crack propagation behavior of selective laser melted AlSi12 alloy, Int. J. Fatigue. 94 (2017) 246–254. doi:10.1016/j.ijfatigue.2016.06.003.

[249] E. Brandl, U. Heckenberger, V. Holzinger, D. Buchbinder, Additive manufactured AlSi10Mg samples using Selective Laser Melting (SLM): Microstructure, high cycle fatigue, and fracture behavior, Mater. Des. 34 (2012) 159–169. doi:10.1016/j.matdes.2011.07.067.

[250] L. Hitzler, J. Hirsch, J. Schanz, B. Heine, M. Merkel, W. Hall, A. Öchsner, Fracture toughness of selective laser melted AlSi10Mg, Proc. Inst. Mech. Eng. Part L J. Mater. Des. Appl. 233 (2019) 615–621. doi:10.1177/1464420716687337.

[251] J. Suryawanshi, K.G. Prashanth, S. Scudino, J. Eckert, O. Prakash, U. Ramamurty, Simultaneous enhancements of strength and toughness in an Al-12Si alloy synthesized using selective laser melting, Acta Mater. 115 (2016) 285–294. doi:10.1016/j.actamat.2016.06.009.

[252] L. Girelli, M. Giovagnoli, M. Tocci, A. Pola, A. Fortini, M. Merlin, G.M. La Vecchia, Evaluation of the impact behaviour of AlSi10Mg alloy produced using laser additive manufacturing, Mater. Sci. Eng. A. 748 (2019) 38–51. doi:10.1016/j.msea.2019.01.078.

[253] A.A. Raus, M.S. Wahab, Z. Shayfull, K. Kamarudin, M. Ibrahim, The Influence of Selective Laser Melting Parameters on Density and Mechanical Properties of AlSi10Mg, MATEC Web Conf. 78 (2016) 1–9. doi:10.1051/matecconf/20167801078.

[254] E. Zaretsky, A. Stern, N. Frage, Dynamic response of AlSi10Mg alloy fabricated by selective laser melting, Mater. Sci. Eng. A. 688 (2017) 364–370. doi:10.1016/j.msea.2017.02.004.

[255] N.E. Uzan, R. Shneck, O. Yeheskel, N. Frage, High-temperature mechanical properties of AlSi10Mg specimens fabricated by additive manufacturing using selective laser melting technologies (AM-SLM), Addit. Manuf. 24 (2018) 257–263. doi:10.1016/j.addma.2018.09.033.

[256] F. Bosio, E. Bassini, C.G. Oñate Salazar, D. Ugues, D. Peila, The influence of microstructure on abrasive wear resistance of selected cemented carbide grades operating as cutting tools in dry and foam conditioned soil, Wear. (2018). doi:10.1016/j.wear.2017.11.002.

[257] K.G. Prashanth, S. Scudino, A.K. Chaubey, L. Löber, P. Wang, H. Attar, F.P. Schimansky, F. Pyczak, J. Eckert, Processing of Al-12Si-TNM composites by selective laser melting and evaluation of compressive and wear properties, J. Mater. Res. 31 (2016) 55–65. doi:10.1557/jmr.2015.326.

[258] L. Xi, P. Wang, K.G. Prashanth, H. Li, H. V. Prykhodko, S. Scudino, I.

Kaban, Effect of TiB2 particles on microstructure and crystallographic texture of Al-12Si fabricated by selective laser melting, J. Alloys Compd. 786 (2019) 551–556. doi:10.1016/j.jallcom.2019.01.327.

[259] N. Kang, P. Coddet, C. Chen, Y. Wang, H. Liao, C. Coddet, Microstructure and wear behavior of in-situ hypereutectic Al-high Si alloys produced by selective laser melting, Mater. Des. 99 (2016) 120–126. doi:10.1016/j.matdes.2016.03.053.

[260] K. Schmidtke, F. Palm, A. Hawkins, C. Emmelmann, Process and mechanical properties: Applicability of a scandium modified Al-alloy for laser additive manufacturing, Phys. Procedia. 12 (2011) 369–374. doi:10.1016/j.phpro.2011.03.047.

[261] Y. Shi, P. Rometsch, K. Yang, F. Palm, X. Wu, Characterisation of a novel Sc and Zr modified Al–Mg alloy fabricated by selective laser melting, Mater. Lett. 196 (2017) 347–350. doi:10.1016/j.matlet.2017.03.089.

[262] Q. Jia, P. Rometsch, S. Cao, K. Zhang, A. Huang, X. Wu, Scripta Materialia Characterisation of AlScZr and AlErZr alloys processed by rapid laser melting, Scr. Mater. 151 (2018) 42–46. doi:10.1016/j.scriptamat.2018.03.035.

[263] E. V.I., Z. V.V., R. T.D., Scandium-alloyed aluminum alloys, Nonferrous Met. Alloy. 19 (1992) 709–715.

[264] K. V. Yang, Y. Shi, F. Palm, X. Wu, P. Rometsch, Columnar to equiaxed transition in Al-Mg(-Sc)-Zr alloys produced by selective laser melting, Scr. Mater. 145 (2018) 113–117. doi:10.1016/j.scriptamat.2017.10.021.

[265] Z. Horita, M. Furukawa, M. Nemoto, A.J. Barnes, T.G. Langdon, Superplastic forming at high strain rates after severe plastic deformation, Acta Mater. 48 (2000) 3633–3640. doi:10.1016/S1359-6454(00)00182-8.

[266] V. V. Zakharov, Combined Alloying of Aluminum Alloys with Scandium and Zirconium, Met. Sci. Heat Treat. 56 (2014) 281–286. doi:10.1007/s11041-014-9746-5.

[267] A.B. Spierings, K. Dawson, T. Heeling, P.J. Uggowitzer, R. Sch??ublin, F. Palm, K. Wegener, Microstructural features of Sc- and Zr-modified Al-Mg alloys processed by selective laser melting, Mater. Des. 115 (2017) 52–63. doi:10.1016/j.matdes.2016.11.040.

[268] A.B. Spierings, K. Dawson, K. Kern, F. Palm, K. Wegener, SLM-processed Sc- and Zr- modified Al-Mg alloy: Mechanical properties and microstructural effects of heat treatment, Mater. Sci. Eng. A. 701 (2017) 264–273. doi:10.1016/j.msea.2017.06.089.

[269] Y. Zhang, K. Gao, S. Wen, H. Huang, Z. Nie, D. Zhou, The study on the coarsening process and precipitation strengthening of Al3Er precipitate in Al-Er binary alloy, J. Alloys Compd. 610 (2014) 27–34. doi:10.1016/j.jallcom.2014.04.093.

[270] H. Li, Z. Gao, H. Yin, H. Jiang, X. Su, J. Bin, Effects of Er and Zr additions on precipitation and recrystallization of pure aluminum, Scr. Mater. 68 (2013) 59–62. doi:10.1016/j.scriptamat.2012.09.026.

[271] Y. Zhang, K. Gao, S. Wen, H. Huang, W. Wang, Z. Zhu, Z. Nie, D. Zhou, Determination of Er and Yb solvuses and trialuminide nucleation in Al-Er and Al-Yb alloys, J. Alloys Compd. 590 (2014) 526–534. doi:10.1016/j.jallcom.2013.11.211.

[272] R.A. Karnesky, D.C. Dunand, D.N. Seidman, Evolution of nanoscale precipitates in Al microalloyed with Sc and Er, Acta Mater. 57 (2009) 4022–4031. doi:10.1016/j.actamat.2009.04.034.

[273] Q. Jia, F. Zhang, P. Rometsch, J. Li, J. Mata, M. Weyland, L. Bourgeois, M. Sui, X. Wu, Precipitation kinetics, microstructure evolution and mechanical behavior of a developed Al?Mn?Sc alloy fabricated by selective laser melting, Acta Mater. 193 (2020) 239–251. doi:10.1016/j.actamat.2020.04.015.

[274] L. Pantělejev, D. Koutný, D. Paloušek, J. Kaiser, Mechanical and microstructural properties of 2618 Al-Alloy processed by SLM remelting strategy, Mater. Sci. Forum. 891 MSF (2017) 343–349. doi:10.4028/www.scientific.net/MSF.891.343.

[275] H. Zhang, H. Zhu, X. Nie, J. Yin, Z. Hu, X. Zeng, Effect of Zirconium addition on crack, microstructure and mechanical behavior of selective laser melted Al-Cu-Mg alloy, Scr. Mater. 134 (2017) 6–10. doi:10.1016/j.scriptamat.2017.02.036.

[276] A. Aversa, G. Marchese, D. Manfredi, M. Lorusso, F. Calignano, S. Biamino, M. Lombardi, P. Fino, M. Pavese, Laser powder bed fusion of a high strength Al-Si-Zn-Mg-Cu alloy, Metals (Basel). 8 (2018) 1–12. doi:10.3390/met8050300.

[277] L. Zhou, H. Pan, H. Hyer, S. Park, Y. Bai, B. McWilliams, K. Cho, Y. Sohn, Microstructure and tensile property of a novel AlZnMgScZr alloy additively manufactured by gas atomization and laser powder bed fusion, Scr. Mater. 158 (2019) 24–28. doi:10.1016/j.scriptamat.2018.08.025.

[278] S. Kumar, J.P. Kruth, Composites by rapid prototyping technology, Mater. Des. 31 (2010) 850–856. doi:10.1016/j.matdes.2009.07.045.

[279] X.P. Li, G. Ji, Z. Chen, A. Addad, Y. Wu, H.W. Wang, J. Vleugels, J. Van Humbeeck, J.P. Kruth, Selective laser melting of nano-TiB2decorated AlSi10Mg alloy with high fracture strength and ductility, Acta Mater. 129 (2017) 183–193. doi:10.1016/j.actamat.2017.02.062.

[280] Q. Han, R. Setchi, F. Lacan, D. Gu, S.L. Evans, Selective laser melting of advanced Al-Al2O3 nanocomposites: Simulation, microstructure and mechanical properties, Mater. Sci. Eng. A. 698 (2017) 162–173. doi:10.1016/j.msea.2017.05.061.

[281] D. Gu, H. Wang, D. Dai, P. Yuan, W. Meiners, R. Poprawe, Rapid fabrication of Al-based bulk-form nanocomposites with novel reinforcement and enhanced performance by selective laser melting, Scr. Mater. 96 (2015) 25–28. doi:10.1016/j.scriptamat.2014.10.011.

[282] A. Aversa, G. Marchese, M. Lorusso, F. Calignano, S. Biamino, E.P. Ambrosio, D. Manfredi, P. Fino, M. Lombardi, M. Pavese, Microstructural and Mechanical Characterization of Aluminum Matrix Composites

Produced by Laser Powder Bed Fusion, Adv. Eng. Mater. 19 (2017) 1–11. doi:10.1002/adem.201700180.

[283] F. Chang, D. Gu, D. Dai, P. Yuan, Selective laser melting of in-situ Al4SiC4 + SiC hybrid reinforced Al matrix composites: Influence of starting SiC particle size, Surf. Coatings Technol. 272 (2015) 15–24. doi:10.1016/j.surfcoat.2015.04.029.

[284] A. Aversa, G. Marchese, A. Saboori, E. Bassini, D. Manfredi, G. Marchese, A. Saboori, E. Bassini, P. Fino, M. Lombardi, D. Manfredi, S. Biamino, D. Ugues, P. Fino, Aluminum Alloys Specifically Designed for New Aluminum Alloys Specifically Designed for Laser Powder Bed Fusion, (2019). doi:10.3390/ma12071007.

[285] G. Cattano, Feasibility studies on Laser Powder Bed Fusion of powders mixtures based on Aluminium alloys or High Entropy Alloys, Politecnico di Torino, 2019. 11583/2750552.

[286] P. Vora, R. Martinez, N. Hopkinson, I. Todd, K. Mumtaz, Customised Alloy Blends for In-Situ Al339 Alloy Formation Using Anchorless Selective Laser Melting, Technologies. 5 (2017) 24. doi:10.3390/technologies5020024.

[287] P. Wang, K.G. Prashanth, S. Pauly, J. Eckert, S. Scudino, Microstructure and mechanical properties of Al-Cu alloys fabricated by selective laser melting of powder mixtures, 735 (2018) 2263–2266. doi:10.1016/j.jallcom.2017.10.168.

[288] K. Bartkowiak, S. Ullrich, T. Frick, M. Schmidt, New developments of laser processing aluminium alloys via additive manufacturing technique, Phys. Procedia. 12 (2011) 393–401. doi:10.1016/j.phpro.2011.03.050.

[289] T. DebRoy, H.L. Wei, J.S. Zuback, T. Mukherjee, J.W. Elmer, J.O. Milewski, A.M. Beese, A. Wilson-Heid, A. De, W. Zhang, Additive manufacturing of metallic components – Process, structure and properties, Prog. Mater. Sci. 92 (2018) 112–224. doi:10.1016/j.pmatsci.2017.10.001.

[290] G. Kasperovich, J. Haubrich, J. Gussone, G. Requena, Correlation between porosity and processing parameters in TiAl6V4 produced by selective laser melting, Mater. Des. 105 (2016) 160–170. doi:10.1016/j.matdes.2016.05.070.

[291] S. Liu, Y.C. Shin, Additive manufacturing of Ti6Al4V alloy: A review, Mater. Des. 164 (2018) 107552. doi:10.1016/j.matdes.2018.107552.

[292] D. Wang, C. Song, Y. Yang, Y. Bai, Investigation of crystal growth mechanism during selective laser melting and mechanical property characterization of 316L stainless steel parts, Mater. Des. 100 (2016) 291–299. doi:10.1016/j.matdes.2016.03.111.

[293] H. Choo, K.-L. Sham, J. Bohling, A. Ngo, X. Xiao, Y. Ren, P.J. Depond, M.J. Matthews, E. Garlea, Effect of laser power on defect, texture, and microstructure of a laser powder bed fusion processed 316L stainless steel, Mater. Des. 164 (2018) 107534. doi:10.1016/j.matdes.2018.12.006.

[294] V.A. Popovich, E. V. Borisov, A.A. Popovich, V.S. Sufiiarov, D. V. Masaylo, L. Alzina, Functionally graded Inconel 718 processed by additive

manufacturing: Crystallographic texture, anisotropy of microstructure and mechanical properties, Mater. Des. 114 (2017) 441–449. doi:10.1016/j.matdes.2016.10.075.

[295] S.A.M. Tofail, E.P. Koumoulos, A. Bandyopadhyay, S. Bose, L. O'Donoghue, C. Charitidis, Additive manufacturing: scientific and technological challenges, market uptake and opportunities, Mater. Today. 21 (2018) 22–37. doi:10.1016/j.mattod.2017.07.001.

[296] B. Vrancken, L. Thijs, J.P. Kruth, J. Van Humbeeck, Microstructure and mechanical properties of a novel β titanium metallic composite by selective laser melting, Acta Mater. 68 (2014) 150–158. doi:10.1016/j.actamat.2014.01.018.

[297] I. Yadroitsev, P. Krakhmalev, I. Yadroitsava, Hierarchical design principles of selective laser melting for high quality metallic objects, Addit. Manuf. 7 (2015) 45–56. doi:10.1016/j.addma.2014.12.007.

[298] C. Li, Y.B. Guo, J.B. Zhao, Interfacial phenomena and characteristics between the deposited material and substrate in selective laser melting Inconel 625, J. Mater. Process. Technol. 243 (2017) 269–281. doi:10.1016/j.jmatprotec.2016.12.033.

[299] P. Wei, Z. Wei, Z. Chen, J. Du, Y. He, J. Li, Y. Zhou, The AlSi10Mg samples produced by selective laser melting: single track, densification, microstructure and mechanical behavior, Appl. Surf. Sci. 408 (2017) 38–50. doi:10.1016/j.apsusc.2017.02.215.

[300] Z. Li, I. Kucukkoc, D.Z. Zhang, F. Liu, Optimising the process parameters of selective laser melting for the fabrication of Ti6Al4V alloy, Rapid Prototyp. J. 24 (2018) 150–159. doi:10.1108/RPJ-03-2016-0045.

[301] F. Trevisan, F. Calignano, M. Lorusso, M. Lombardi, D. Manfredi, P. Fino, Selective laser melting of chemical pure copper powders, Proc. Euro PM 2017 Int. Powder Metall. Congr. Exhib. (2017).

[302] B. Liu, R. Wildman, C. Tuck, I. Ashcroft, R. Hague, Investigaztion the effect of particle size distribution on processing parameters optimisation in selective laser melting process, 22nd Annu. Int. Solid Free. Fabr. Symp. - An Addit. Manuf. Conf. SFF 2011. (2011) 227–238.

[303] H. Yeung, B.M. Lane, M.A. Donmez, J.C. Fox, J. Neira, Implementation of Advanced Laser Control Strategies for Powder Bed Fusion Systems, Procedia Manuf. 26 (2018) 871–879. doi:10.1016/j.promfg.2018.07.112.

[304] ASTM B962, Standard Test Methods for Density of Compacted or Sintered Powder Metallurgy (PM) Products Using Archimedes Principle, ASTM Int. (2013) 1–7. doi:10.1520/B0962-13.2.

[305] D.R. Askeland, P.P. Fulay, W.J. Wright, The science and engineering of materials, Third S.I., 1998.

[306] ASTM E10-18, Standard Test Method for Brinell Hardness of Metallic Materials, ASTM Int. (2012) 1–36. doi:10.1520/E0010-15.

[307] V.A. Lubarda, On the effective lattice parameter of binary alloys, Mech. Mater. 35 (2003) 53–68. doi:10.1016/S0167-6636(02)00196-5.

[308] S. Marola, D. Gianoglio, F. Bosio, A. Aversa, M. Lorusso, D. Manfredi, M. Lombardi, L. Battezzati, Alloying AlSi10Mg and Cu powders in laser Single Scan Tracks, melt spinning, and Laser Powder Bed Fusion, J. Alloys Compd. 821 (2020) 153538. doi:10.1016/j.jallcom.2019.153538.

[309] G. Riontino, A. Zanada, Coupled formation of hardening particles on pre-precipitates in an Al-Cu-Mg-Si 2014 alloy, Mater. Lett. 37 (1998) 241–245. doi:10.1016/S0167-577X(98)00099-8.

[310] S.C. Wang, M.J. Starink, Precipitates and intermetallic phases in precipitation hardening Al-Cu-Mg-(Li) based alloys, Int. Mater. Rev. 50 (2005) 193–215. doi:10.1179/174328005X14357.

[311] I. Ansara, T. Dinsdale, M.H. Rand, Thermochemical database for light metal alloys, Belgium, 1998.

[312] S. Cui, I.H. Jung, Thermodynamic modeling of the quaternary Al-Cu-Mg-Si system, Calphad Comput. Coupling Phase Diagrams Thermochem. 57 (2017) 1–27. doi:10.1016/j.calphad.2017.02.002.

[313] M. Badrossamay, E. Yasa, J. Van Vaerenbergh, J.P. Kruth, Improving productivity rate in SLM of commercial steel powders, in: S. of M. Engineers (Ed.), Schaumburg, IL, USA, 2009: pp. 1–13.

[314] J. Wu, X.Q. Wang, W. Wang, M.M. Attallah, M.H. Loretto, Microstructure and strength of selectively laser melted AlSi10Mg, Acta Mater. 117 (2016) 311–320. doi:10.1016/j.actamat.2016.07.012.

[315] N. Kang, P. Coddet, H. Liao, C. Coddet, Macrosegregation mechanism of primary silicon phase in selective laser melting hypereutectic Al - High Si alloy, J. Alloys Compd. 662 (2016) 259–262. doi:10.1016/j.jallcom.2015.11.222.

[316] D. Dai, D. Gu, R. Poprawe, M. Xia, Influence of additive multilayer feature on thermodynamics, stress and microstructure development during laser 3D printing of aluminum-based material, Sci. Bull. 62 (2017) 779–787. doi:10.1016/j.scib.2017.05.007.

[317] F. Trevisan, Study and characterisation of different metal alloys processed through Laser Powder Bed Fusion, Politecnico di Torino, 2018. doi:10.6092/polito/porto/2709711.

[318] Sindo Kou, Heat Flow in Welding, in: Weld. Metall., John Wiley & Sons, 2003: pp. 46–64.

[319] Renishaw, Datasheet: AlSi10Mg-0403 powder for additive manufacturing H-5800-1084-01-B, 2001 (2001) 0–1.

[320] I. Yadroitsev, P. Krakhmalev, I. Yadroitsava, Titanium Alloys Manufactured by In Situ Alloying During Laser Powder Bed Fusion, Jom. 69 (2017) 2725–2730. doi:10.1007/s11837-017-2600-7.

[321] C. Böhm, M. Werz, S. Weihe, Dilution ratio and the resulting composition profile in dissimilar laser powder bed fusion of alsi10mg and al99.8, Metals (Basel). 10 (2020) 1–12. doi:10.3390/met10091222.

[322] H.B. Dong, P.D. Lee, Simulation of the columnar-to-equiaxed transition in directionally solidified Al-Cu alloys, Acta Mater. 53 (2005) 659–668.

doi:10.1016/j.actamat.2004.10.019.

[323] Q.G. Wang, C.J. Davidson, Solidification and precipitation behaviour of Al-Si-Mg casting alloys, J. Mater. Sci. 36 (2001) 739–750. doi:10.1007/s10853-006-1469-6.

[324] M. Roudnická, O. Molnárová, D. Dvorský, L. Křivský, D. Vojtěch, Specific Response of Additively Manufactured AlSi9Cu3Fe Alloy to Precipitation Strengthening, Met. Mater. Int. (2019). doi:10.1007/s12540-019-00504-y.

[325] T.O. Standard, A. American, N. Standard, Standard Test Methods for Tension Testing of Metallic Materials, (2018) 1–30. doi:10.1520/E0008.

[326] E. Sjölander, S. Seifeddine, The heat treatment of Al-Si-Cu-Mg casting alloys, J. Mater. Process. Technol. 210 (2010) 1249–1259. doi:10.1016/j.jmatprotec.2010.03.020.

[327] F. Bosio, A. Aversa, M. Lorusso, S. Marola, D. Gianoglio, L. Battezzati, P. Fino, D. Manfredi, M. Lombardi, A time-saving and cost-effective method to process alloys by Laser Powder Bed Fusion, Mater. Des. 181 (2019) 107949. doi:10.1016/j.matdes.2019.107949.

[328] I. Rosenthal, A. Stern, N. Frage, Strain rate sensitivity and fracture mechanism of AlSi10Mg parts produced by Selective Laser Melting, Mater. Sci. Eng. A. 682 (2017) 509–517. doi:10.1016/j.msea.2016.11.070.

[329] G.-V. Jorge Luis, Brittle and Ductile Fractures, in: Fractography Fail. Anal., 2018: pp. 60–70. doi:https://doi.org/10.1007/978-3-319-76651-5.

[330] GE Additive Machines, X Line 2000R, (n.d.). https://www.ge.com/additive/additive-manufacturing/machines/dmlm-machines/x-line-2000r (accessed August 31, 2020).

[331] GE Additive Machines, M2 Series 5, (n.d.). https://www.ge.com/additive/additive-manufacturing/machines/m2series5.

[332] F. Calignano, Design optimization of supports for overhanging structures in aluminum and titanium alloys by selective laser melting, Mater. Des. 64 (2014) 203–213. doi:10.1016/j.matdes.2014.07.043.

[333] P. Mercelis, J.P. Kruth, Residual stresses in selective laser sintering and selective laser melting, Rapid Prototyp. J. 12 (2006) 254–265. doi:10.1108/13552540610707013.

[334] K. Kempen, B. Vrancken, S. Buls, L. Thijs, J. Van Humbeeck, J.-P. Kruth, Selective Laser Melting of Crack-Free High Density M2 High Speed Steel Parts by Baseplate Preheating, J. Manuf. Sci. Eng. 136 (2014) 061026. doi:10.1115/1.4028513.